JAERI-Review
2004-023

ANNUAL REPORT OF NAKA FUSION RESEARCH ESTABLISHMENT FROM APRIL 1, 2003 TO MARCH 31, 2004

November 2004

Naka Fusion Research Establishment

日本原子力研究所
Japan Atomic Energy Research Institute

本レポートは、日本原子力研究所が不定期に公刊している研究報告書です。
入手の問合わせは、日本原子力研究所研究情報部研究情報課(〒319-1195 茨城県那珂郡東海村)あて、お申し越し下さい。なお、このほかに財団法人原子力弘済会資料センター(〒319-1195 茨城県那珂郡東海村日本原子力研究所内)で複写による実費頒布を行っております。

This report is issued irregularly.
Inquiries about availability of the reports should be addressed to Research Information Division, Department of Intellectual Resources, Japan Atomic Energy Research Institute, Tokai-mura, Naka-gun, Ibaraki-ken 〒319-1195, Japan.

編集兼発行　日本原子力研究所

JAERI－Review 2004－023

Annual Report of Naka Fusion Research Establishment from April 1, 2003 to March 31, 2004

Naka Fusion Research Establishment

Japan Atomic Energy Research Institute
Naka-machi, Naka-gun, Ibaraki-ken

(Received October 1, 2004)

This annual report provides an overview of research and development (R&D) activities at Naka Fusion Research Establishment, including those performed in collaboration with other research establishments of JAERI, research institutes, and universities, during the period from 1 April, 2003 to 31 March, 2004. The activities in the Naka Fusion Research Establishment are highlighted by researches in JT-60 and JFT-2M, theoretical and analytical plasma researches, research and development of fusion reactor technologies towards ITER and fusion power demonstration plants, and activities in support of ITER design and construction.

In the JT-60 research program, the pulse length of the tokamak discharge was extended successfully to 65 s (formerly 15 s) in order to demonstrate/study the high performance tokamak plasma in the time scale comparable to/longer than the relaxation time of the plasma current profile. The control systems, the power supply systems, the heating systems and the diagnostic systems of the JT-60 were modified successfully to accomplish the extended discharge. The H-mode was extended successfully up to 24 s with high normalized beta value β_N~2.0 after the extension of the pulse length. The duration is more than twice of the world record in such high beta region. On the research of the advanced steady state tokamak, a high equivalent fusion gain Q_{DT} was achieved with full non-inductive plasma current. A large bootstrap current fraction ~75% (larger than the expected value in the ITER steady state operation) was sustained for more than 7 s in the negative shear plasma. Also the plasma operation was extended to high density and high radiation loss region using the high-field-side pellet injection and inert gas injection. On the research of the MHD instabilities and control, an early injection of the electron cyclotron (EC) wave was found to be effective for the stabilization of the neoclassical tearing mode (NTM). The transport of the energetic ions at the Abrupt Large amplitude Events (ALE) was studied. On the research of the H-mode physics, a non-dimensional pedestal identity experiment was carried out between JT-60 and JET in ELMy H-mode plasmas. On the research of the current drive, the experimentally obtained EC current drive efficiency was compared to a nonlinear Fokker-Planck code calculation with the effect of the toroidal electric field included. Initial results on the real time control of the safety factor profile by the lower hybrid (LH) waves were obtained. On the research of the divertor / SOL plasmas and plasma wall interaction, studies on the transient heat and particle load by the ELMs, SOL flow and impurity transport with the newly installed Tungsten tiles in the divertor progressed.

Editors: Hoshino, K., Umeda, N., Tsuji, H., Yoshida, H., Nagami, M.

The design of the new National Centralized Tokamak (NCT), which is the modification of the JT-60 to the super conductor version, progressed both in physics and in engineering utilizing the previous JT-60SC design. Two different configurations with low aspect ratio are studied.

In the JFT-2M research program, the compatibility of the Ferrite inside wall (FIW) with high β_N plasma was demonstrated up to β_N~3.5. High β plasma was obtained with plasma even at the close wall case. In the study of the H-mode, an operational boundary of the high recycling steady (HRS) mode was identified, and the study of the characteristic oscillations in the edge transport barrier made a progress. Studies on divertor/SOL and compact toroid (CT) injection progressed.

A series of the experimental programs on the JFT-2M was completed at the end of this fiscal year after the 21 years operations since 1983, with the significant contribution to the controlled nuclear fusion research.

In the theoretical and analytical researches, significant progress was made in the studies of the H-mode power threshold, EC power necessary to stabilize the NTM, the effects of the ferromagnetic wall on the plasma stability and the effects of D shaping and rotation shear on the ballooning modes. In the project of numerical experiment of tokamak (NEXT), the studies of the ion temperature gradient driven trapped electron mode (ITG-TEM) turbulence, damping mechanism and global characteristics of the zonal flow progressed.

R&Ds of fusion reactor technologies have been carried out both to further improve technologies necessary for ITER construction, and to accumulate technological database to assure the design of fusion DEMO plants. For ITER superconducting magnets, the critical current density of a bronze processed Nb_3Sn strand has been improved by 14%, satisfying the specification of 700 A/mm^2 that was optimized for ITER. For development of ITER Neutral Beam Injector, H^- ion beam of 110 mA (80 A/m^2) was stably accelerated at the extraction voltage of > 5 kV. By the Cu coating on the bellows part of a 170-GHz gyrotron for ITER, the heating rate of the bellows was reduced to less than 1/10 of the original rate and 0.5-MW operation for 100 s was demonstrated successfully. For the Blanket fabrication technology, a joint technology between tungsten and F82H steel was developed using a solid state bonding method. The joining temperature and pressure were 960 °C and 50 MPa, respectively in order to obtain fine grained F82H. To examine applicability of the screw tube for the plasma facing component of a fusion DEMO plant, thermal fatigue experiment of divertor mockups with a screw tube made of F82H has been performed at heat flux conditions of 3 and 5 MW/m^2. For the structural material development, irradiation experiments of F82H steel by multiple ion beams have been carried out up to 100 dpa to investigate the radiation hardening of F82H at high doses. The radiation hardening with increasing dose was almost saturated at around 30dpa. As an advanced method for tritium removal from ITER Test Blanket Module, research on the electrochemical hydrogen pump using a ceramic protonic conductor has been carried out extensively. D-T neutronics experiments of blanket mock-up assemblies designed by JAERI were performed. The mock-up consisted of lithium-6 enriched Li_2TiO_3, beryllium, F82H and a SS-reflector. The Tritium Production rates (TPR) measured and the TPR obtained by design analysis agreed each other within 10 %.

In the ITER Program, along the work plan approved on February 2003 under the framework of the ITER Transitional Arrangements, the Design and R&D Task works started among the Participant Teams. JAERI has been in charge of seventeen Design Task works that make the implementation of preparing the procurement documents for facilities and equipments that are so scheduled as to be ordered at the early stage of ITER construction. The structure and management system and the staffing and resources of the ITER organization, the procurement allocation of ITER components and the site issue have been

continuously discussed among the delegations of six countries/area including South Korea that joined the Negotiation in June 2003.

Finally, in the fusion reactor design studies, the conceptual design of the economical and compact low aspect ratio (A~2) reactor (VECTOR) progressed. Researches on the physics related to the reactor design, liquid wall divertor and assessment of the fusion energy progressed.

Keywords; JAERI, Fusion Research, JT-60, JFT-2M, Fusion Technology, ITER, Fusion Power Demonstration Plants, Fusion Reactor

JAERI－Review 2004－023

那珂研究所年報（平成15年度）

日本原子力研究所
那珂研究所

（2004年10月 1日 受理）

日本原子力研究所（原研）那珂研究所における平成15年度（2003年4月～2004年3月）の研究開発活動について、原研内の他研究所および所外の研究機関さらに大学との協力により実施した研究開発も含めて報告する。原研那珂研究所の主な活動として、JT-60 と JFT-2M によるプラズマ実験研究、プラズマ理論解析、ITER 及び発電実証プラントに向けた核融合炉工学の研究開発、及びITERの設計と建設の支援が行われた。

JT-60 による研究開発では、プラズマの電流分布の緩和時間と同程度以上の時間スケールで高性能トカマクプラズマの実証と研究を行うために、トカマクプラズマ放電時間を 65 秒間に伸長することに成功した(従来は 15 秒間)。制御系、電源系、加熱系及び計測系の改造の成功がこの成果を生んだ。この放電時間の伸長後に、高い規格化ベータ値β_N~2.0 を維持しつつ、H モード(ELM 付き)を 24 秒間定常に維持することに成功した。これは、このような高ベータ領域では、従来の世界記録の 2 倍以上である。先進定常トカマクに関する研究では、完全非誘導電流駆動で高い等価核融合利得 Q_{DT} を達成した。負磁気シアプラズマで、全プラズマ電流のうち~75%をブートストラップ電流で 7 秒間以上流した(この割合は ITER の定常運転で想定される値以上である)。また、高磁場側からのペレット入射と不活性気体入射を用いることにより運転領域をより高密度、より高放射損失の領域に拡大した。MHD 不安定性とその制御の研究では、新古典テアリングモード(NTM)の抑制には、電子サイクロトロン(EC)波の早期入射が有効であることを実証した。急激な大振幅現象(ALE)時の高エネルギーイオンの輸送について解明した。H モード物理の研究では、ELM 付き H モードにつき、JET トカマクとの間で無次元ペデスタル比較実験結果を得た。電流駆動の研究では、実験的に得られた電流駆動効率とトロイダル電場を考慮した非線形フォッカープランクコード計算との比較を行った。低域混成(LH)波による安全係数分布の実時間制御の初期実験結果を得た。ダイバータ/SOL プラズマとプラズマ壁相互作用の研究では、ELM による過渡的な熱や粒子の負荷の解明、SOL 流や不純物輸送の解明を新たにダイバータに設置したタングステンタイルを用いることなどにより進めた。

JT-60 を超電導化改造する新しい国内重点化装置（NCT)の物理と工学設計を以前の JT-60SC 設計を利用して進めた。低アスペクト比の二案につき検討した。

JFT-2M による研究開発では、高ベータプラズマとフェライト鋼内壁(FIW)の整合性をβ_N~3.5 まで実証した。プラズマと壁の距離が近接している場合も高ベータプラズマを得た。H モード研究では、高リサイクル定常(HRS)モードの運転境界を得、周辺輸送障壁 での特徴的揺動の研究を進めた。ダイバータ/SOL とコンパクトトロイド(CT)入射の研究を進めた。

那珂研究所：〒311-0193 茨城県那珂郡那珂町向山801-1
編集者： 星野 克道、梅田 尚孝、辻 博史、吉田 英俊、永見 正幸

JFT-2M による実験研究は、1983 年に開始されたが、制御核融合研究に大きく貢献して、今年度末でその 21 年間の運転を終了した。

理論研究および解析研究では、H モード遷移パワー、NTM 安定化に必要な EC パワー、強磁性体壁のプラズマ安定性に対する影響、バルーニングモードへの D 型形状や回転のシアが与える影響などについての研究を進めた。トカマク数値実験プロジェクト(NEXT)では、イオン温度勾配駆動型捕捉電子モード(ITG-TEM)乱流の解明や帯状流の減衰機構と大域的特性の解明を進めた。

核融合炉工学の研究開発は、ITER の建設に必要な技術の更なる改良、及び発電実証プラントの設計に必要な技術データベースの蓄積という二つの目的に向けて推進された。ITER 用のマグネット用超伝導線材の一つであるブロンズ法で製作した Nb_3Sn 素線の臨界電流密度が、その製法の改良により 14%向上し、ITER 最適化設計により新たな仕様値となった 700 A/mm^2 の性能を満たした。ITER 用中性粒子入射技術開発では、電流値 110mA（電流密度 80 A/m^2）の水素負イオンビームが、5kV 以上の引き出し電圧により安定に加速されることを確認した。170GHz の周波数で動作する ITER 用ジャイロトロンのベローズ構造部について、銅の被覆を行うことによりこれまで長時間連続動作の障害となっていた異常な発熱率が 1/10 に減少し、0.5 MWの出力にて連続 100 秒間の動作実証に成功した。ブランケット製作技術の開発では、F82H 鋼とタングステンを固相拡散により接合する技術を開発した。拡散接合条件は、F82H 鋼の結晶の粗大化を避ける観点から温度 960 ℃、圧力 50 MPa に選定した。スクリュー型の冷却管が発電実証プラントのプラズマ対向機器にて使用可能かどうかを検証するため、F82H を材料とするスクリュー管を使用したダイバータ模擬体の熱疲労試験を 3 MW/m^2 及び 5 MW/m^2 の熱流束条件にて行った。構造材料の開発では、複数種のイオンビームを用いて、F82H の照射実験を照射量 100 dpa まで行い、高照射量における F82H 鋼の照射硬化特性を調べた。その結果、照射による材料の硬化現象は 30 dpa 前後において飽和する傾向が明らかとなった。ITER テスト・ブランケット・モジュールで生成されたトリチウムを回収するための先進技術として、セラミックのプロトン導電体を用いた電気化学水素ポンプの研究を重点的に進めた。また、原研で設計されたブランケットを模擬する試験体に D-T 反応により発生する中性子を入射する実験を行った。 この試験体は Li^6 の濃度を濃縮した Li_2TiO_3、ベリリウム、F82H 鋼とステンレス鋼の反射体から構成されている。本実験の結果、測定されたトリチウム生成率はこれまでの設計解析値と 10%の範囲内で一致することが確認された。

ITER 計画においては、ITER 移行措置の枠組みのもとで 2003 年 2 月に承認された作業計画に沿って、参加極チーム間で設計および R&D のタスク作業が開始された。原研は、建設の早い段階において発注が予定される設備と機器に関し、日本が担当して調達書類の準備を行う 17 件の設計タスク作業を進めてきた。この間、2003 年 6 月に韓国が参加極として交渉に加わり、六カ国／地域で引き続き、計画を実施する ITER 機関の体制や運営方法、人事や財源、機器製作の分担、及び建設サイトについて協議が進められた。

最後に、核融合炉設計研究では、経済的でコンパクトな低アスペクト比(A～2)核融合炉(VECTOR)の概念設計を進めた。核融合炉設計の物理、液体壁ダイバータ、核融合エネルギーの評価を進めた。

This is a blank page.

Contents

目次

FOREWORD

This report presents the results from research and development activities at Naka Fusion Research Establishment of Japan Atomic Energy Research Institute (JAERI) during the period from 1 April, 2003 to 31 March, 2004. The results are highlighted by researches in JT-60 and JFT-2M, research and development of fusion reactor technologies, and activities in support of ITER design and construction.

The research on the JT-60 made a remarkable progress in the extension of the discharge duration up to 65 s. Modifications of the control systems, power supply systems, heating systems and diagnostic systems enabled this accomplishment. The H-mode was extended up to 24 s maintaining high beta value and now we begin to study the high performance plasma in the time scale comparable to the relaxation time of the current profile. The design studies of the National Centralized Tokamak (NCT) which is the upgrade of the JT-60 progressed with the collaboration with the universities and industries. At the end of this fiscal year, a series of the experimental programs on the JFT-2M tokamak was completed after the 21years of operation, with the significant contribution to the controlled nuclear fusion research.

R&Ds of fusion reactor technologies have been carried out both to further improve technologies necessary for ITER construction, and to accumulate technological database to assure the design of fusion DEMO plants. The critical current density of a bronze processed Nb_3Sn strand for ITER magnets has been improved by 14%, satisfying the specification of 700 A/mm^2 that was optimized for ITER. As an advanced method for tritium removal from ITER Test Blanket Module, research on the electrochemical hydrogen pump using ceramic protonic conductor has been carried out extensively. In the Blanket R&D, the joint technology between tungsten and F82H was developed using a solid state bonding method with the temperature and pressure of 960 °C and 50 MPa.

As the implementation institute of ITA in Japan, JAERI has advanced the Design Task works in cooperation with the International Team. The site issue has been under discussion including further exploration of a broader project approach to fusion energy after the Ministerial Meeting for ITER held in December 2003. JAERI has been continuously supporting the international negotiation and also conducting a more detailed analysis of the Rokkasho candidate site from a technical viewpoint.

It should be emphasized that above results include those performed in collaboration with other research establishments of JAERI, research institutes, and universities. In view of these encouraging outcomes, I do expect with full confidence that the fusion research and developments will make a new and powerful take off towards the energy source for mankind when the construction of ITER is initiated in coming future.

関　昌弘

Masahiro Seki
Director General
Naka Fusion Research Establishment, JAERI

This is a blank page.

I. JT-60 PROGRAM

Objectives of the JT-60 project are to contribute to physics R&D of the International Thermonuclear Experimental Reactor (ITER), and to establish the physics basis for the tokamak fusion reactor.

In the fiscal year of 2003, the reactor-relevant performance progressed much with the collaboration with the universities and institutes.

This part is divided into the three chapters; Experimental Results and Analyses (Chap.1), Operation and Machine Improvements (Chap.2) and Design Progress of the National Centralized Tokamak Facility (Chap.3).

1. Experimental Results and Analyses

1.1 Long Pulse Operation and Extended Plasma Regimes

1.1.1 Extension of JT-60U Pulse Length

The JT-60U tokamak project has addressed major physics and technological issues for ITER and commercially attractive steady-state reactors. These experimental and demo reactors require simultaneous sustainment of high confinement, high normalized beta β_N, high bootstrap fraction, full noninductive current drive and efficient heat and particle exhaust in the steady-state. In such high β steady-state systems, the plasma current profile $j(\rho)$, where ρ is the normalized flux radius, plays a central role, and it is important to investigate how $j(\rho)$ evolves and then how the confinement and stability characteristics change in a long time scale compatible to characteristic relaxation time of the current profile, τ_R. In addition, it is important for realizing a steady-state operation to understand the change of plasma-wall interactions with a long time scale and its impact on the integrated performance.

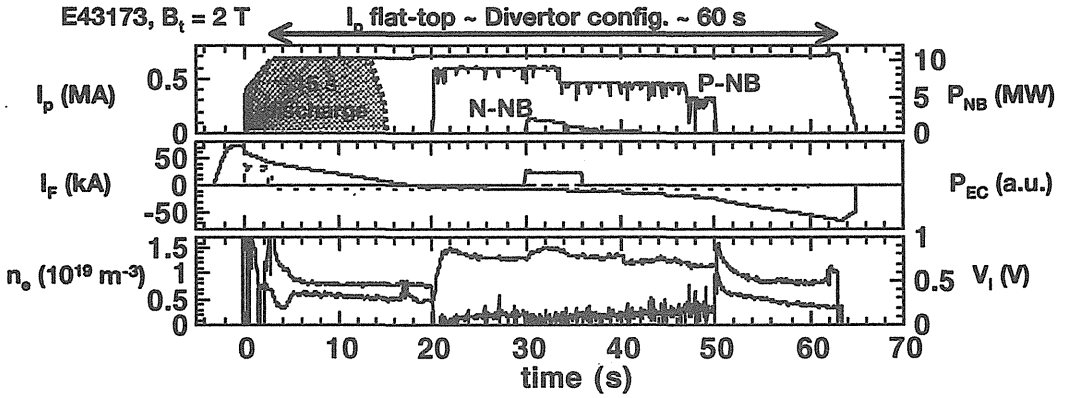

Fig. I.1.1-1 Time evolutions of a 65 s discharge.

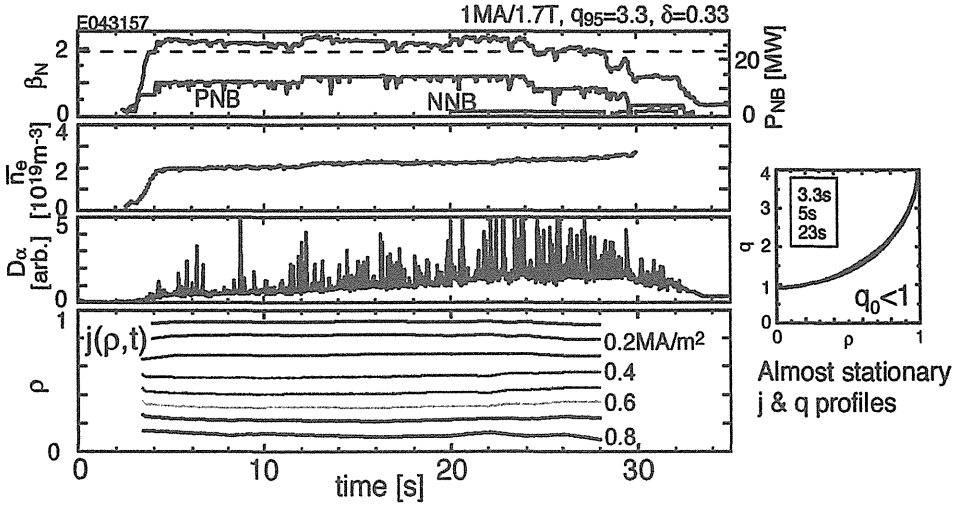

Fig. I.1.1-2 Time evolutions of a shot in which $\beta_N \geq 1.9$ was sustained for 24 s (Left figures). Current profile (Right).

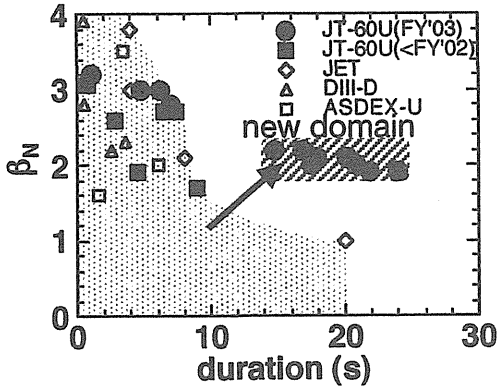

Fig. I.1.1-3. Progress of sustainment of β_N.

Towards this goal, the JT-60U pulse length is extended to 65 s (formerly 15 s) by modification in control systems in operation, heating and diagnostics systems without major hardware upgrade. Maximum duration of both parallel P-NB and N-NB (negative-ion source NB) injections have been extended to 30 s (formerly 10 s), while those of RF (ECRF and LHRF) pulses have been extended to 60 s. As the result, a 65 s discharge with ~60 s plasma current I_p flat top of 0.7 MA and a divertor configuration was successfully obtained as shown in Fig. I.1.1-1.

1.1.2 Sustainment of High Normalized Beta Value β_N

Sustainment of high β_N is one of the most important issues in developing compact fusion reactors, since fusion power density is proportional to the square of β_N. Although the highest attainable β_N can be beyond 3 - 4 which is limited ultimately by the ideal MHD stability, sustainable β_N tends to be limited much below due to the so called neo-classical tearing modes (NTMs). Since the stability of NTMs strongly depends on the alignment between j(ρ) and the pressure profile p(ρ), it is important to investigate the evolution of the plasma over τ_R. After the modification for the long pulse operation, sustainment of $\beta_N \geq 1.9$ for 24 s has been successfully demonstrated in JT-60U (Fig. I.1.1-2). Before this achievement, the sustainable time of such high β_N values had been limited up to about 10 s in the world. As shown in the figure, j(ρ) is almost saturated at the end of the high β_N stage in the discharge. In this discharge, no signature of NTM is observed. This can be attributed to good alignment between j(ρ) and p(ρ). Extension of the operational domain of the sustained β_N against the duration is summarized in Fig. I.1.1-3. Thus, a remarkable progress in sustainment of high β_N has been achieved after the long pulse modification..

1.1.3 Long Pulse High Recycling H-Mode

Another important issue in fusion research is the particle control. The particle controllability under saturated divertor plates, where the recycling ratio is unity, has not been well understood yet, and investigation has just started in long and high-power heated discharges in JT-60U. Saturation of the divertor plates affects not only the divertor plasma but also the main plasma. Figure I.1.1-4 shows the time evolution of the long-pulse ELMy H-mode plasma (I_p = 1.0 MA, B_t = 1.7 T). After $t \sim 10$ s, the deuterium flux, the carbon flux, and the radiation from the divertor plasma increased, while the radiation from the main plasma

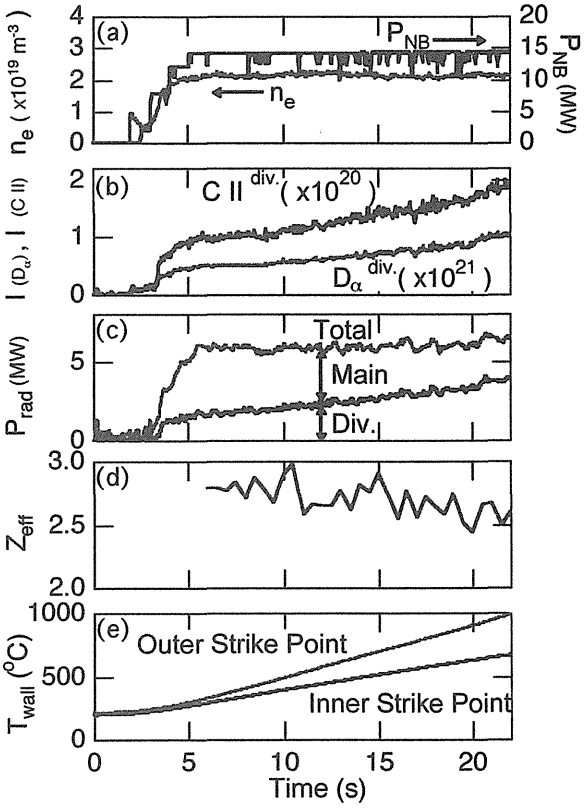

Fig. I.1.1-4 Time evolutions of (a) the line-averaged electron density, the NB-heating power, (b) D_α and C II brightness, indicating recycling flux and carbon release flux, (c) the total radiation power, the divertor radiation power, (d) Z_{eff} in the main plasma, and (e) the surface temperature around the inner and the outer strike point.

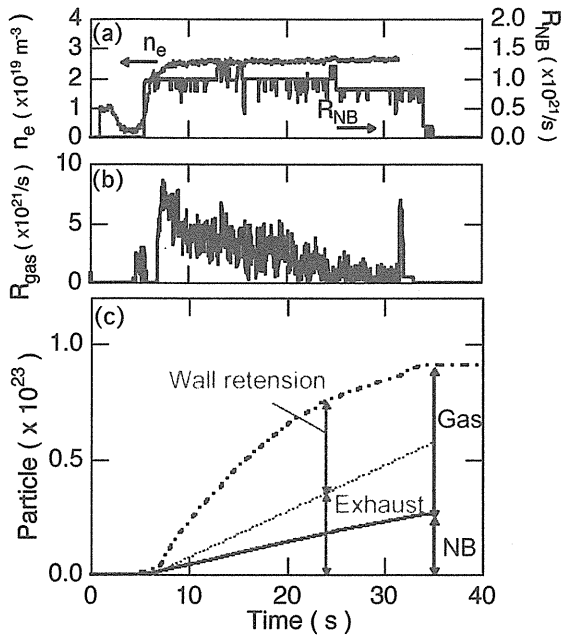

Fig. I.1.1-5. Time evolutions of (a) the line-averaged electron density, the NB-fuel rate, (b) the gas-puff rate, (c) the particle balance. The wall inventory was invoked from injected (Gas + NB) and exhausted (Exhaust) particle

decreased. This is probably because that the impurity shielding efficiency was enhanced due to the high recycling flux. The saturation of the divertor causes these changes. In addition, discharge history is found to be a key factor, in particular, when intense gas-puff was applied in consecutive discharges. Figure I.1.1-5 shows the particle balance of a high-density, steady-state ELMy H-mode plasma (I_p = 1.0 MA, B_t = 2.1 T). The gas-puff rate to keep the constant density decreased gradually. This decrease of the gas-puff rate implies reduction of the particle sink into the divertor plates, and the wall inventory seems to be saturated. Although the plasma density could be controlled by the feedback control system in this discharge, in the following discharge, the density went over the preprogrammed density. To keep the controllability of the plasma density with the divertor plates saturated, it is required to enhance the exhaust efficiency, which may be possible by optimization of the plasma configuration such as proximity of the divertor legs to the pumping slot.

1.2 Enhanced Performance and Steady State Research

1.2.1 Achievement of High Fusion Triple Product under Full Non-Inductive Current Drives [1.2-1]

High β_p ELMy H-mode plasmas are characterized by a weak positive magnetic shear profile with the central safety factor above unity [1.2-2], which is compatible with the standard and the hybrid operational scenarios in ITER. One of the key issues for obtaining a high-performance high-β_p H-mode plasma is to suppress the NTMs. In JT-60U, by decreasing the pressure gradient at the mode rational surface, NTM onset has been successfully avoided with good reproducibility. In addition, increase in the capacity of poloidal field coils by 20% , increase in beam energy E_{NNB} and injection power P_{NNB} of the negative-ion-based neutral beam (NNB) [1.2-3] enabled the high-triangularity operations and a high fraction of NB current drive, respectively.

The typical time evolutions of the high β_p ELMy H-mode discharge are shown in Fig. I.1.2-1, where plasma parameters are as follows: I_p=1.8 MA, B_t=4.1 T, R=3.23 m, a=0.78 m, q_{95}=4.1 and triangularity at the separatrix δ_x=0.34. In this discharge, NNB with E_{NNB}=402 keV and P_{NNB}=5.7 MW was injected from 5.7 s. At t=6.5 s, a high-performance plasma with the

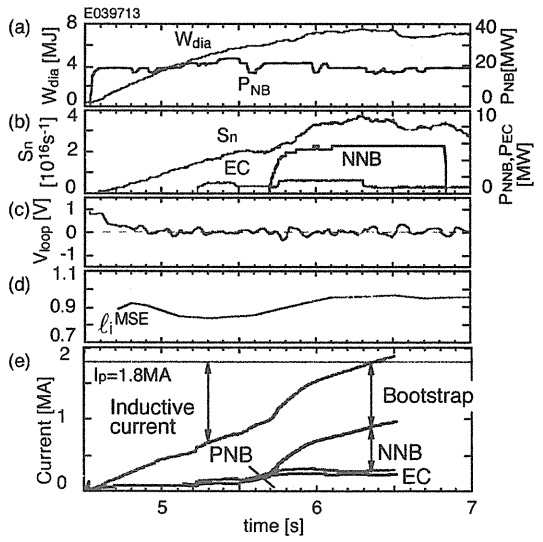

Fig. 1.1.2-1 Typical time evolutions of a high β_p ELMy H-mode discharge: (a) stored energy and injection power of PNBs, (b) neutron emission rate, injection power of EC and NNB, (c) loop voltage, (d) internal inductance evaluated with MSE diagnostics, (e) driven current calculated with TOPICS, where I_p=1.8 MA, B_t=4.1 T, major radius R=3.23 m, minor radius a=0.78 m, safety factor at 95% flux surface q_{95}=4.1 and triangularity at the separatrix δ_x=0.34.

following parameters was obtained: stored energy W_{dia}=7.5 MJ, H-factor H_{89PL}=2.5, HH-factor $H_{H98(y,2)}$= 1.2, β_p=1.7, β_N=2.4, fusion triple product $n_D(0)\tau_E T_i(0)$=

$3.1\times10^{20}m^{-3}\cdot s\cdot keV$ and equivalent fusion gain Q_{DT}^{eq}= 0.185. As shown in Figs. I.1.2-1(c) and (d), the loop voltage V_{loop} reaches zero, and internal inductance l_i evaluated with the motional Stark effect (MSE) diagnostic is almost constant in time after t~6.3 s, which suggests the full non-inductive current drive. The time evolution of the bootstrap current and the beam-driven current was simulated using the time-dependent transport code TOPICS. As shown in Fig. I.1.2-1(e), plasma current is fully maintained non-inductively. Slowing-down of the NNB fast ions was also simulated with the Orbit Following Monte-Carlo (OFMC) code, which indicates that about 95% of the energy and parallel momentum are transferred to the plasma within 0.8 s after the injection, suggesting that the high energy ion distribution is nearly in steady state at t=6.5 s. In order to visualize the integrated plasma performance, we have used the septangular plot (Fig.I.1.2-2), which contains β_N, HH_{y2}-factor (the confinement enhancement factor over the ITER ELMy

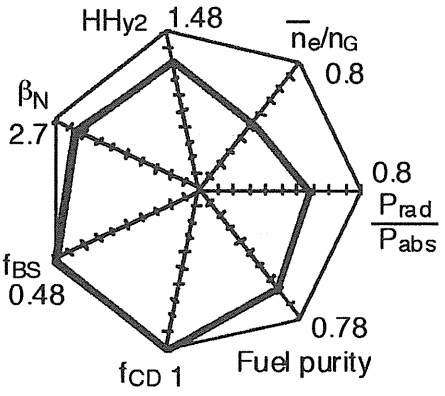

Fig. I.1.2-2 Septangular plot of E39713 data. Values in this figure correspond to those in the steady-state weak positive shear scenario in ITER.

H-mode scaling), $\bar{n}_e$ normalized by the Greenwald density n_G, ratio of radiation power P_{rad} to absorption power P_{abs}, fuel purity defined as the ratio of the number of deuterons to that of electrons, fraction of bootstrap current f_{BS}, and fraction of non-inductively driven current f_{CD}. In this plot, each value is normalized to that in one of the ITER steady-state scenarios. In E39713, $\bar{n}_e/n_G$=0.42, P_{rad}/P_{abs}=0.54, fuel purity=0.6, f_{CD}=1 and f_{BS}=0.49. As shown in this figure, the values of f_{CD} and f_{BS} meet the requirement in ITER, and β_N and $H_{H98(y,2)}$ are close to the requirement (~80%).

1.2.2 Sustainment of High-Beta Plasmas

Demonstration of a stationary high-beta discharge is important to clarify the physical issues relating to NTM and ideal MHD instabilities at high β_N. Previously, β_N~3 was sustained for 0.8 s with NNB in a high β_p H-mode discharge [1.2-4], where the duration was limited by onset of the m/n=2/1 NTM. The experiments to sustain the high β_N (~3) plasma have been performed. In this series of discharges, q_{95} was decreased below 3 aiming at arranging the q=2 surface at the peripheral region. By the discharge optimization, β_N~3 was sustained for ~6 s without destabilizing NTM. It is notable that no large sawtooth oscillation was observed in spite of very low-q (q_{95}~2.3) operation. This result is also remarkable in that β_N~3 can be sustained in the low-q regime.

1.2.3 Long Sustainment of Large Bootstrap Current

For the steady-state operation of the tokamak reactors, a large bootstrap current fraction (f_{BS}>70%) is required to reduce the circulating power for the non-inductive current drives. In JT-60U, a quasi-steady RS plasma

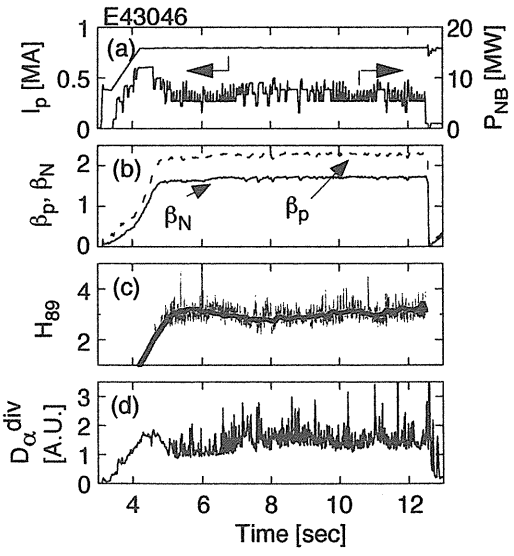

Fig.I.1.2-3 Typical time evolutions of a reversed shear ELMy H-mode discharge: (a) plasma current (I_p) and injected NB power (P_{NB}), (b) normalized beta (β_N: solid curve) and poloidal beta (β_p: dotted curve), (c) H factor (H_{89}) and (d) deuterium recycling emission at the divertor (D_α^{div}).

with the large f_{BS}~80% had been sustained for 2.7s ($<\tau_R$) [1.2-5]. The main objective of this study is to investigate whether the RS ELMy H-mode plasma is stable until the current and the pressure profiles become stationary. The typical time evolutions are shown in Fig. I.1-2-3 (I_p=0.8MA, B_T=3.4T, q_{95}~8.6, κ=1.6, and δ=0.42). The co-NB power of ~3.2MW was injected for the current drive, and the ctr-NB power of ~0.9MW was injected for the MSE measurement. Using the feedback control of the stored energy by the perpendicular NBs, β_N~1.7 (β_p~2.25) was maintained from t~5.1s until the end of the NB heating (t=12.5s). In this phase, the large f_{BS}~75% and the nearly full non-inductive current drive (f_{CD}>90%) were maintained for ~7.4s, which corresponds to16 times the energy confinement time. The high H_{89} of 3.0 (HH_{y2}~1.7) was obtained due to both internal and edge transport barriers. Figure I.1.2-4 shows the progress in the quasi-steady f_{BS} on various tokamak devices. The duration of the quasi-steady f_{BS} is defined as the pulse length where the plasma performance was maintained above 85% of the maximum stored energy [1.2-6]. The operational region of the large f_{BS} plasmas has been significantly extended, which is higher than the level of ITER steady-state operation and comparable to that of thesteady-state tokamak reactor (SSTR).

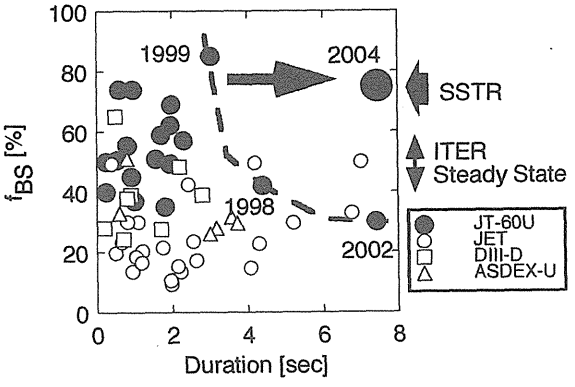

Fig. I.1.2-4 Progress in quasi-steady f_{BS} on various tokamak devices. The data from various confinement mode plasmas are plotted in this figure.

1.2.4 Compatibility of an Advanced Tokamak Plasma with High Density and High Radiation Loss Operation [1.2-7]

Operational region of an advanced tokamak plasma with internal transport barriers (ITBs) has been extended to high density and high radiation loss for

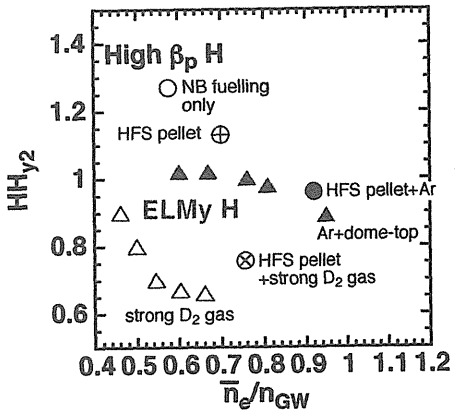

Fig. I.1.2-5 HH_{y2} as a function of $\bar{n}_e/n_{GW}$. Circles : high β_p H-mode plasmas. Triangles : ELMy H-mode plasmas.

establishment of a steady-state tokamak operation concept in a fusion reactor. In the high β_p ELMy H-mode plasmas with weak positive magnetic shear, the high confinement of HH_{y2}=1.1 has been achieved at $\bar{n}_e/n_{GW}$ of 70% and radiation loss fraction to the heating power of 60% by injecting high-filed-side (HFS) pellets [1.2-8].

In the high β_p ELMy H-mode plasmas (I_p=1.0 MA, B_T=3.6 T, q_{95}= 6.2, δ_x=0.37), $\bar{n}_e/n_{GW}$=0.92 has been achieved with a small confinement degradation (HH_{y2}=0.96) by injecting multiple HFS pellets and Ar gas together with small D_2 gas-puffing (Fig. I.1.2-5). In this plasma, total radiation loss power reaches to 90% of the heating power. When strong D_2 gas-puffing was applied in addition to the HFS pellets injection, the confinement degrades to HH_{y2}=0.75 at $\bar{n}_e/n_{GW}$=0.75. High confinement was obtained in the ELMy H-mode plasma without ITB by injecting Ar gas in the dome-top configuration, in which the outer strike point is located on the divertor dome (I_p=1.2 MA, B_T=2.5 T and q_{95}=4.2) [1.2-9].

The n_e profiles normalized by n_{GW} are shown in Fig. I.1.2-6 for the high β_p ELMy H-mode plasma

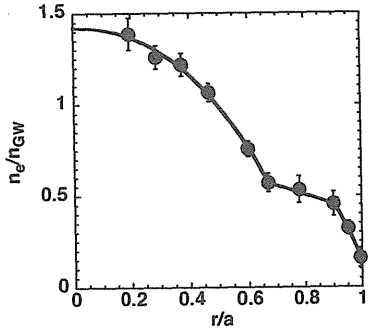

Fig. I.1.2-6 n_e profile normalized by n_{GW}.

with the HFS pellets and Ar injections at $\bar{n}_e/n_{GW}$=0.92. The clear density ITB is formed, and the peakedness increases in time after the Ar injection. Although the pedestal density is about 0.4-0.5n_{GW}, the central density exceeds n_{GW}. Therefore, the high ratio of $\bar{n}_e/n_{GW}$ is obtained due to the peaked density profile inside the ITB.

In order to understand the physical mechanisms for high confinement at high density, the core-edge parameter linkage is investigated. In JT-60U, a possible feedback loop among the edge and core parameters has been proposed in the ELMy H-mode and high β_p ELMy H-mode plasmas [1.2-10], where improved core confinement (high β_p) enhances the edge pressure, and the enhanced edge pressure improves the core confinement. In the high β_p ELMy H-mode plasma with the HFS pellets and Ar injections, β_p-ped is enhanced with β_p-tot. The parameter-linkage between the edge and core plasmas is consistent with the no Ar injection case, which indicates that the confinement improvement is not ascribed to the core confinement enhancement only. In this plasma, the high confinement is terminated by an n=1 MHD mode located around the ITB. During the confinement degradation, β_p-ped also decreases with β_p-tot. The change of the pedestal parameters such as density and temperature induced by the HFS pellet and Ar injections could trigger the positive feedback loop for higher β_p-ped and higher β_p-tot. The ITB degradation by the MHD mode could be related to the trigger of the negative feedback loop. The simple model suggests that the ITG mode is suppressed in r/a=0.4-0.65 by the density peaking and high Z_{eff} caused by the Ar injection during the high confinement phase. However, it also suggests the ITG mode suppression during the confinement degradation phase. The role of the ITG mode suppression in the feedback loop is not well understood yet.

The impurity accumulation was observed in the high β_p ELMy H-mode plasma with the peaked density profile [1.2-11]. The compatibility of the peaked density profile with impurity enhanced radiation loss is discussed. The radiation loss profile in the main plasma evaluated using Abel inversion technique is peaked in the high β_p ELMy H-mode compared to that in the ELMy H-mode with Ar injection. The ratio of the main plasma radiation loss (including the radiation loss in the SOL plasma) to the total radiation loss is estimated to be 0.65-0.7 for the high β_p ELMy H-mode. In the high β_p ELMy H-mode, the total radiation loss reaches to ~90% of the input power. The n_{Ar} profile is more peaked by a factor of ~2 than the n_e profile, and n_{Ar}/n_e reaches to about 1% in the central region. The 1-D impurity transport analysis in the main plasma suggests that the core radiation loss from the Ar impurity accumulated by a factor of 2 can be compensated with slightly enhanced confinement in a fusion reactor. For the modeling of Ar behavior in the divertor plasma, the radiation power calculated by 2-D fluid divertor code UEDGE considering the intrinsic C and seed Ar impurities is compared with the measurements. The calculated radiation loss power is smaller than the measurements and localized in the inner strike point. Further optimization of the input parameters is necessary to fit the calculation to the measurement.

References

1.2-1 Isayama, A. *et al., Nucl. Fusion* **43,** 1272 (2003).

1.2-2 Kamada, Y. *et al., Fusion Sci. Technol.* **43,** 185 (2002).

1.2-3 Umeda, N. *et al., Nucl. Fusion* **43,** 522 (2003).

1.2-4 Fujita, T. *et al., Nucl. Fusion* **43,** 1527 (2003).

1.2-5 Fujita, T. *et al., Phys. Rev. Lett.* **87,** 085001 (2001).

1.2-6 Litaudon, X. *et al., Plasma Phys. Control. Fusion* **46,** A19 (2004).

1.2-7 Takenaga, H. *et al.*, to be appeared in *Proc. 20th Int. Conf. on Fusion Energy 2004* (Vilamoura, 2004).

1.2-8 Takenaga, H. *et al., Phys. Plasmas*, **8,** 2217 (2001).

1.2-9 Kubo, H. *et al., Phys. Plasmas, 9, 2127* (2002).

1.2-10 Kamada, Y. *et al., Plasma Phys. Control. Fusion* **44,** A279 (2002).

1.2-11 Takenaga, H. *et al., Nucl. Fusion*, **43,** 1235 (2003).

1.3 MHD Instabilities and Control

1.3.1 Stabilization of the Neoclassical Tearing Mode

Stabilization of NTMs by the localized heating and/or current drive by electron cyclotron (EC) wave is important to sustain the high beta plasmas. In JT-60U, real-time NTM stabilization has been successfully

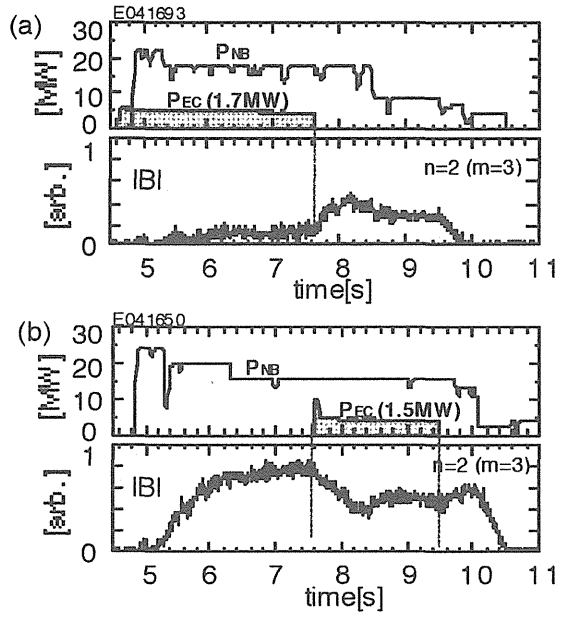

Fig. I.1.3-1 Typical waveform of an NTM stabilization experiment for the cases of (a) early ECCD and (b) late ECCD.

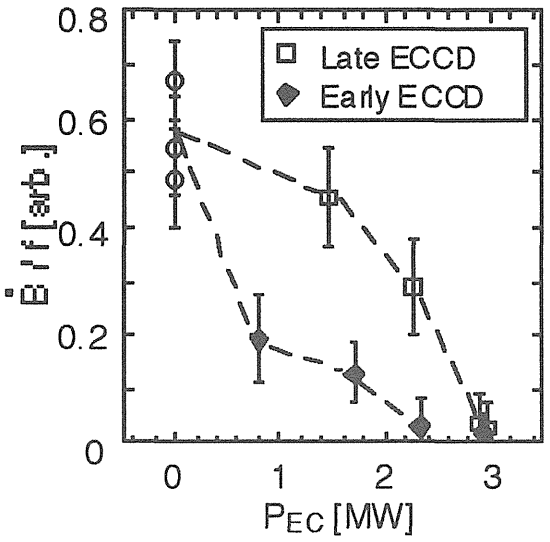

Fig. I.1.3-2 Dependence of amplitude of magnetic perturbations on EC wave power.

demonstrated [1.3-1]. As a new scheme, EC current drive (ECCD) before or just after the NTM onset ('early ECCD') has been performed aiming at stabilization with smaller amount of EC wave power [1.3-2]. Typical time evolutions in the early and the conventional late ECCD cases are shown in Fig. I.1.3-1. In the early injection case, the growth of the 3/2 NTM is suppressed during the EC phase. It is notable that the amplitude of magnetic perturbations in the early injection case is smaller than that in the late injection case throughout the discharge. This suggests that EC injection time affects the evolution of NTMs, possibly

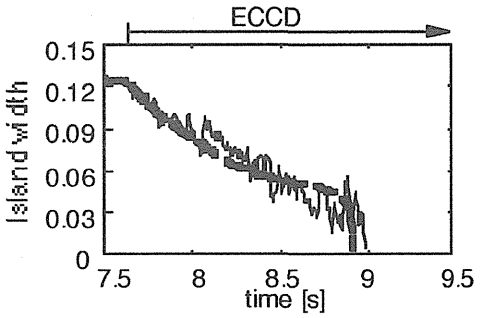

Fig. I.1.3-3 Time evolution of magnetic island width evaluated by magnetic perturbations (solid line) and TOPICS simulation (dotted line).

through the change in the current and temperature profiles. In Fig. I.1.3-2, amplitude of magnetic perturbations during EC injection is plotted as a function of EC injection power. In the late injection case, the amplitude gradually decreases with increasing EC power, and the NTM is completely stabilized at four-unit EC injection (~3 MW). In the early injection case, the mode amplitude significantly decreases even at one-unit EC injection (~0.8 MW), and complete stabilization is achieved at three-unit injection (~2.3 MW). This shows that EC power required for complete stabilization can be reduced by early injection. It is also found that the suppression effect significantly decreases with the deviation from the mode location. This shows that the injection angle must be precisely adjusted also in the early injection case.

To simulate the temporal evolution of NTMs, a code to consistently solve the modified Rutherford equation has been incorporated to the transport code TOPICS, where the change in the current profile and stability due to ECCD is also simulated (See also Sec. 2.2). Time evolution of the magnetic island width during ECCD is shown in Fig. I.1.3-3, where results from the TOPICS code and the amplitude of magnetic perturbation measured with saddle coils are compared. The simulation reproduces the experimental result quite

well, in particular, quick shrink from t= 8.8 s [1.3-3].

1.3.2 Energetic Ion Transport by Alfvén Eigenmode Induced by N-NB injection

In burning plasmas, Alfvén eigenmodes (AEs) can be destabilized by energetic ions, for example α - particles. The AEs can induce the enhanced transport of energetic ions from the core region, which can cause the degradation of the performance of a fusion reactor. The lost energetic ions may also damage the first wall. Thus, the understanding of energetic ion transport when AEs are destabilized is important. The AE experiments have been performed by using N-NB injection in JT-60. Neutron measurement and neutral particle measurement are utilized in order to investigate the energetic ion transport by AEs. Typical time evolutions during the NNB injection are shown in Fig. I.1.3-4, where B_T=1.2T, Ip=0.6MA. Figure I.1.3-4 (a) shows the magnetic fluctuation amplitude in the

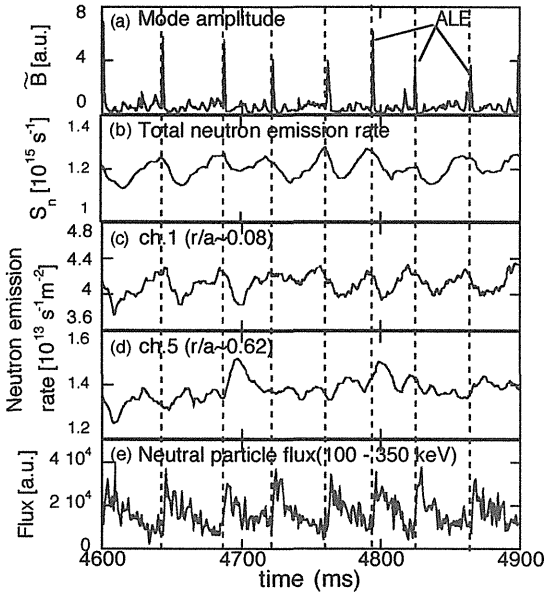

Fig.I.1.3-4 Time trace of (a) mode amplitude of magnetic fluctuation in the frequency range of 20-80 kHz, (b) total neutron emission, (c) and (d) signal of ch1(r/a~0.08) and ch5 (0.62) of neutron emission profile monitor, respectively, and (e) neutral particle flux with energy of 100-400 keV

frequency range of 20-80 kHz. Bursting modes called Abrupt Large-amplitude Events (ALEs) [1.3-4] are observed. Figure I.1.3-4 (b) shows the total neutron emission rate and Figures I.1.3-4 (c) and (d) show the signals from ch.1, ch5 of six channels neutron emission profile monitor [1.3-5]. The sight lines of ch.1 and ch.5 pass through r/a ~ 0.08 and 0.62, respectively. The total neutron emission rate reduces ~6 % on the occurrence of ALEs. The neutron emission signal of ch.1 is reduced on the occurrence of ALEs, while the signal of ch.5 is often increased. Figure I.1.3-4 (e) shows the neutral particle flux with energy of 100 ~ 400keV, measured by the newly installed natural diamond detector (NDD) [1.3-6]. When ALEs occur, the neutral particle fluxes are enhanced. The NDD detects the neutral particles whose pitch angles are almost the same as that of the energetic ions by the N-NB. The energetic ions are neutralized through a charge exchange reaction with the neutral particle D^0 or the hydrogen-like carbon ion C^{5+} and are emitted from the plasma as neutral fluxes. Figures I.1.3-5 (a) and (b) show the energy distribution of the neutral particle flux

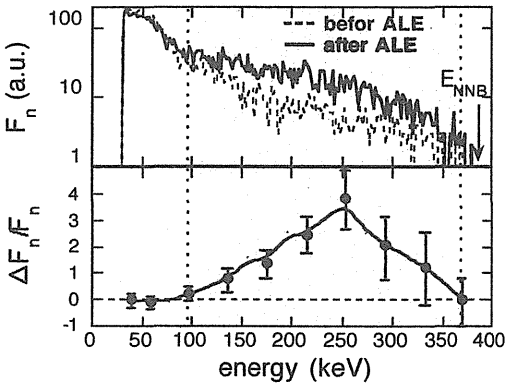

Fig.I.1.3-5 Energy distribution of (a) neutral particle fluxes before and after ALE, (b) the fraction of enhanced neutral particle fluxes by ALEs.

before and after the ALEs, and the fraction of the enhanced neutral particle flux by ALEs, respectively. Neutral particle flux in a limited energy range (100 ~ 370 keV) is enhanced by ALEs. Since the number of the beam-target neutrons is over 90% of the total number of the neutron emission according to the calculation by TOPICS code [1.3-7], and the energy range of enhanced neutral particles is over 100keV, the observed change in the neutron emission profile is attributed to the transport of energetic ions produced by N-NB injection. Thus, Fig. I.1.3-4 indicates that ALEs redistribute energetic ions from the core region to the outer region of the plasma. Furthermore, Fig. I.1.3-5 suggests that the emitted neutral particles satisfy the

resonance condition with the mode [1.3-8]. In the AE experiments using neutron emission profile measurement and neutral particle flux measurement, not only energetic ion transport but also the energy dependence of the transported energetic ions are clearly observed.

References

1.3-1 Isayama, A. *et al., Nucl. Fusion* **43**,1272 (2003).

1.3-2 Nagasaki, K. *et al., Nucl. Fusion* **43**, L7 (2003).

1.3-3 Hayashi, N. *et al.*, to be published in *J. Plasma Fusion Res.*

1.3-4 Shinohara, K. *et al., Nucl.Fusion* **41**,603 (2001).

1.3-5 Ishikawa, M. *et al., Rev. Sci. Instru.***73**, 4273 (2002).

1.3-6 Ishikawa, M, *et al.*, Submitted to *Rev. Sci. Instru.*

1.3-7 Shirai, H. *et. al., J. Phys. Soc. Jpn*, **64**, 4209 (1995).

1.3-8 White, R. B. *et.al. Phys. Fluids* **26**, 2958 (1983).

1.4 H-Mode and Pedestal Research

1.4.1 Dimensionless Pedestal Identity Experiments in JT-60U and JET in ELMy H-Mode Plasmas

In order to understand the physical mechanism to determine the pedestal and ELM characteristics, the dimensionless identity experiment has been started between JT-60U and JET. The dimensionless plasma parameters are normalized plasma pressure β, Larmor radius ρ*, and collisionality ν*.

The first comparison is performed with matched shape as shown in Fig. I.1.4-1 (a) (κ~1.45, δ~0.28) and I_p/B_T of 1.8 MA/3.1 T (JT-60U) and 1.9 MA/2.9 T (JET), corresponding to q_{95} = 3.1, to expect matched non-dimensional parameters at pedestal [1.4-1]. In contrast to expectations from the identity relations, the pedestal temperature of JT-60U plasmas is systematically lower than in JET, over the whole density range. For the case of plasmas with Type I ELMs, the resulting difference in pedestal electron pressure is up to a factor of 2.

A comparison between the ρ*, ν^*_e and $\beta_{p,ped}$ values obtained in the scans in the two devices is shown in Fig. I.1.4-1 (b)-(d). All dimensionless parameters are calculated at the pedestal top. The range of ρ* achieved in the two machines is comparable. Nonetheless, Fig. I.1.4-1(b) also shows that the match achieved in ν^*_e is not very good, with ν^*_e (JT-60U) ≈ 2 × ν^*_e (JET), for the same ρ*. This occurs because, for the same n_{ped}, T_{ped} is systematically lower in JT-60U than in JET plasmas. The fact that the pedestal temperatures in the two devices do not scale as expected is also reflected in the comparison of $\beta_{p,ped}$ as a function of ρ*, both toroidal and poloidal, as shown in Fig. I.1.4-1 (c) and (d).

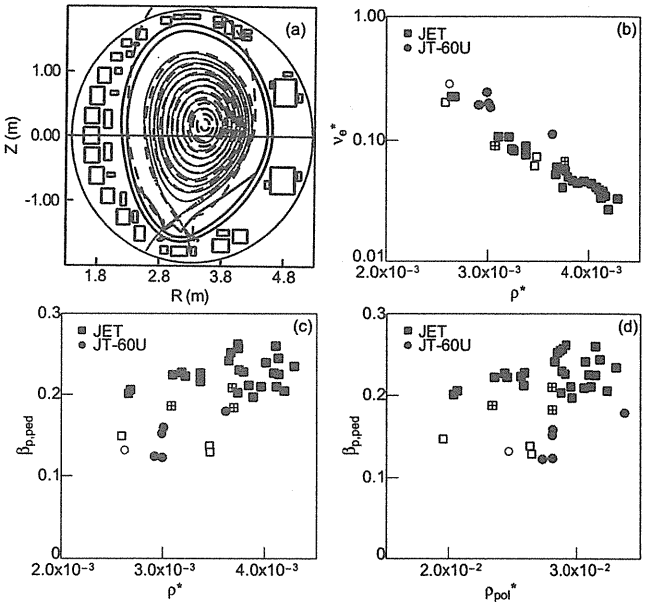

Fig. I.1.4-1. (a) Poloidal cross-section of a plasma discharge in JT-60U (continuous line) and one in JET (dashed line). (b)-(d) Comparison of the pedestal dimensionless parameters for the complete data set at the matched I_p/B_T in JET and JT-60U.

Possible reasons for the discrepancy in the pedestal parameters in the two experiments were considered. One is the effect of the mismatched inverse aspect ratio ε (ε = 0.29 in JET, while ε = 0.25 in JT-60U), which could cause a change in the MHD stability of the pedestal and therefore in the achievable pedestal pressure, ELM frequency and type. This was investigated by analyzing the variation of MHD stability in an 'aspect ratio scan', based on JET discharge. But the dependence of the pedestal MHD stability on inverse aspect ratio was found to be fairly weak and may not cause the large difference in pedestal pressure found experimentally between JET and JT-60U identity plasmas. The second difference between the JET and JT-60U plasmas is the toroidal field ripple at the plasma edge, which is <1% in JET, while in JT-60U it is ≈1%. Ripple-induced fast ion losses in JT-60U can produce a counter rotation source in the plasma edge, in particular for outer shifted plasmas with perpendicular beam injection, such as those used in this identity experiment. In order to confirm the

effect of toroidal rotation, new experiments were performed in two different plasma currents, 1.07MA and 1.8MA. When we switched the three perpendicular NBIs to Negative-Ion based NBI (N-NBI), we obtained less counter rotation with almost the same absorbed power. Then, in the low I_p case, the increase of the pedestal pressure by >40% was observed together with the clear change of the ELM behavior, where the ELM frequency was reduced and ELM amplitude was increased. In JET, on the other hand, the reduction of the edge pressure using combined heating of NBI and ICRH was observed with less co-rotation. The understanding of this improvement of the pedestal performance in JT-60U is left for the future work.

1.4.2 Impact of the Toroidal Rotation on the ELM Behavior [1.4-2]

The ELMy H-mode operation is intended as a standard scenario for ITER. Such ELMy H-mode plasmas possess high levels of thermal confinement, however, large ELMs release high levels of heat and particle fluxes. It is therefore important to control the pulsed ELM heat and particle loads.

By using various combinations of NBI lines in JT-60U, it has been possible to investigate the impact of toroidal rotation velocity on ELM behavior by changing the toroidal momentum input in a detailed manner for similar absorbed NB heating power. Five combinations of different tangential NBs were utilized for various toroidal rotation scans: (a) two units of co-NBs (COx2); (b) one unit of co-NB (COx1); (c) one unit of co-NB and one unit of ctr-NB (BAL); (d) one unit of ctr-NB (CTRx1), and ; (e) two units of ctr-NBs (CTRx2). Perpendicular NBs were added to each combination of tangential NB. The discharge conditions were: B_T=2.1T, I_P=1.0MA, q_{95}=3.3, κ=1.4, δ=0.3, plasma volume V_P~60m^3, n_e/n_{GW}~0.4 and the ion grad B drift was towards the divertor.

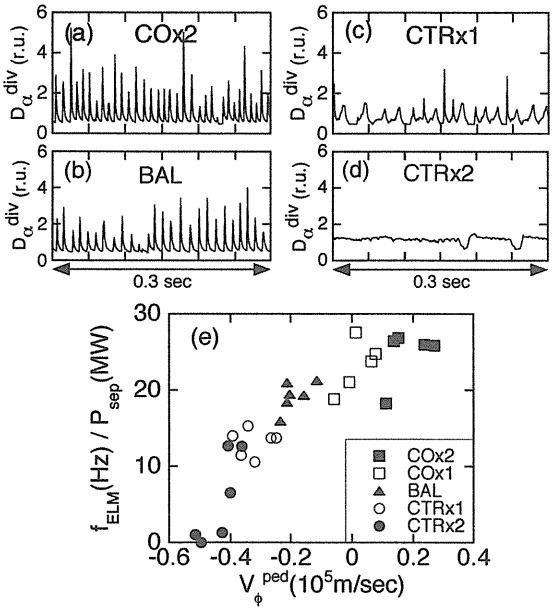

Fig. I.1.4-2 D_α signals at the divertor in the cases of (a) COx2, (b) BAL, (c) CTRx1, (d) CTRx2. (e) Relation between the ELM frequency normalized by P_{sep} and pedestal toroidal rotation velocity estimated at a normalized minor radius of 0.9.

The profiles of n_e, T_e and T_i were similar in all these cases, even in the pedestal region. However, the toroidal rotation velocity and its shear were significantly different for each case. The D_α^{div} signals reveal that the ELM behavior is significantly different for each combination of tangential NBs, as can be seen in Fig. I.1.4-2 (a)-(d). The ELM frequency in the case of CTRx1 is smaller than that for the COx2 and BAL cases, and also the magnitude of the D_α^{div} spikes induced by the ELMs decreases. Since the level of D_α^{div} signal is larger than the base level of D_α^{div} signal in ELMy phase, some mechanism that enhances the particle transport at the plasma edge may exist. Figure I.1.4-2 (e) shows the relation between the ELM frequency normalized by P_{sep} and pedestal toroidal rotation velocity estimated at a normalized minor radius of 0.9. The ELM frequency decreases significantly with increased toroidal rotation velocity in the counter direction in the case of CTRx2 and CTRx1 and for BAL and COx1, where the values of toroidal rotation velocity are negative or almost zero. The ELM frequency normalized by P_{sep} is almost constant for positive value of toroidal rotation velocity. There may be a critical value of the toroidal rotation velocity required for the disappearance of ELMs. The above results indicate that the ELM frequency and pulsed ELM heat load onto the diverter plates can be actively controlled by the toroidal momentum input.

References

1.4-1 Saibene, G, *et al.*, *Plasma Phys. Control. Fusion* **46**, A195 (2004).

1.4-2 Sakamoto, Y, *et al.*, *Plasma Phys. Control. Fusion* **46**, A299 (2004)

1.5 Current Drive Research

1.5.1 Current Drive by Electron Cyclotron Waves [1.5-1]

Current profile control by the electron cyclotron current drive (ECCD) has been used to achieve a high performance plasma. For example, an increase of the β_N was observed by stabilizing NTMs when the ECCD compensates a missing bootstrap current produced by the flattening of the plasma pressure profile in the magnetic islands [1.5-2]. The calculation based on the linear ECCD theory well agrees with the experiment under the condition in which the effects of the distortion of the electron distribution function f_e is small due to collision relaxation [1.5-3], validation of ECCD theory is currently underway with the effects of the distortion. Such a distortion can be produced by the toroidal electric field E_ϕ of a tokamak discharge, and by the oscillating RF electric field by the EC waves. Theoretical works [1.5-4,5] predicted that both of the effects become prominent in a high T_e plasma. Recent progress of the EC systems in JT-60U made it possible to study ECCD under the high T_e condition exceeding 20keV. In the strong distortion regime, distortion of electron distribution function should be treated non-linearly in solving the Fokker-Planck equation.

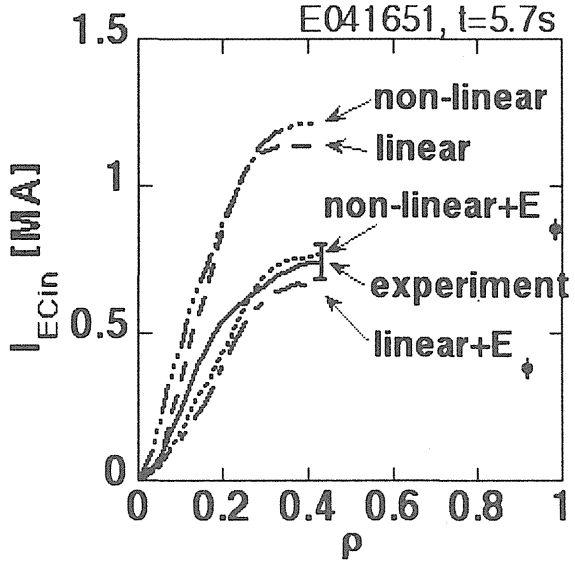

Fig. I.1.5-1: Profiles of EC driven current enclosed in a magnetic surface I_{ECin}. EC driven current obtained by experiment (solid curve) and by various calculations are shown; dashed curve: linear calculation without E_ϕ, dot-dashed curve: linear calculation with E_ϕ, three-dots-dashed curve: non-linear calculation without E_ϕ, dotted curve: non-linear calculation with E_ϕ. Non-linear calculation with E_ϕ agrees the closest with the experimental result concerning to the EC driven current.

Comparison of the experimentally observed EC driven current to calculation results has been made in regard to the toroidal electric field and the EC power density. We employed two codes to calculate the EC driven current profile; a linear code without E_ϕ (RADAR code) and a non-linear code with E_ϕ (CQL3D code [1.5-6]). The calculated EC driven currents in various conditions are shown in Fig. I.1.5-1, in comparison with the experimental result. The EC driven current I_{EC} was evaluated by the loop-voltage profile analysis [1.5-3]. While the total measured I_{EC} is 0.74±0.06MA, the linear calculation predicts 1.1MA, overestimating the I_{EC} by 48% [1.5-7]. When we compare the linear calculation without E_f (I_{EC}=1.1MA) to that with E_ϕ (I_{EC}=0.66MA), the EC driven current decreases by a factor of 1.7. The strong reduction of I_{EC} by E_ϕ is also seen in a comparison of the non-linear calculation with (I_{EC}=0.76MA) / without E_ϕ (I_{EC}= 1.2MA). On the other hand, a smaller non-linear power effect can be seen in a comparison of the linear and non-linear calculations. The E_ϕ effect was significant under the experimental condition. Thus the non-linear calculation taking into account the E_f best agrees with the experiment. It has been found that consideration of both of the non-linear effect and the toroidal electric field effect is necessary.

1.5.2 Real-Time Control of Safety Factor Profile

The plasma current profile, and hence the safety factor profile $q(\rho)$ plays an essential role in regard to confinement and stability in a tokamak plasma. A real-time $q(\rho)$ control system has been developed; this system enables real time evaluation of $q(\rho)$ by MSE diagnostic and control of CD location by adjusting the parallel refractive index $N_{//}$ of lower-hybrid (LH) waves through the change of phase difference ($\Delta\phi$) of LH waves between multi-junction launcher modules [1.5-8]. Relation between $\Delta\phi$ and LHCD location (ρ_{CD}) has been experimentally determined. The control system determines ρ_{CD} (or $\Delta\phi$) in such a way to minimize the weighted difference between the real-time evaluated $q(\rho)$ and the reference $q_{ref}(\rho)$. For the first time, $q(\rho)$ has been evaluated in real time from the local measurement of pitch angle by MSE. The equilibrium was not reconstructed in real-time with

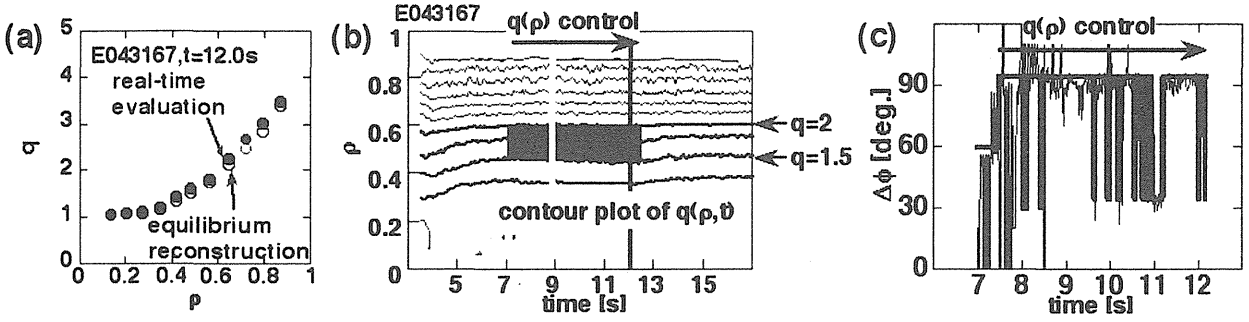

Fig. I.1.5-2: (a) Comparison of q(r) by the real-time calculation (closed circles) and q(r) by an equilibrium reconstruction with MSE (open circles). They show a good agreement. (b) Temporal evolution of q(r) evaluated in real-time. Shrinkage of q=1.5 surface during 7s<t<12.2s, but no shrinkage of q=2 surface, exhibits spatially localized LHCD in the shaded region (0.45<r<0.6). (c) Temporal evolution of Δφ (thick curve: command value from the q(r) control system, thin curve: output from the LH system). The output traces the command value.

MSE, but q(ρ) was directly estimated under an assumption that the shapes of internal magnetic surfaces are the same as the shape of the last closed magnetic surface. Figure I.1.5-2(a) shows a q(ρ) profile by real-time evaluation, in comparison with that by equilibrium reconstruction. They show a good agreement. Temporal evolution of the real-time q(ρ) is shown in Fig. I.1.5-2(b), showing penetration of current (t<7s). Co-LHCD (injection power P_{LH}=0.6MW) has been applied during 7s<t<12.2s, and real-time control of q(ρ) has started at t=7.5s. The control system itself determined $N_{//}$ (or directly controllable Δφ) after t=7.5s to raise the safety factor at the plasma center q(0). Figure I.1.5-2(c) shows the temporal evolution of Δφ. The output from the LH system traces the command value from the q(ρ) control system. During the control, the current stopped penetrating within ρ<0.45, and the safety factor even increased. The safety factor profile did not reach the reference $q_{ref}(\rho)$, since the available LH power was limited up to 0.6MW in this discharge. The change in q(ρ) indicates the LHCD current was localized at ρ=0.45-0.6. After the end of LHCD, and hence, after the end of q(ρ) control (t>12.2s), the current started to penetrate again.

References

1.5-1 Suzuki, T., *et al.*, *J. Plasma Fusion Res.* **80**, 511 (2004).

1.5-2 Isayama, A., *et al.*, *Plasma Phys. and Controlled Fusion* **42**, L37 (2000).

1.5-3 Suzuki, T., *et al.*, *Plasma Phys. and Controlled Fusion* **44**, 1 (2002).

1.5-4 Dnestrovskij, Y. N., *et al.*, *Nuclear Fusion* **28**, 267 (1988).

1.5-5 Harvey, R. W., *et al.*, *Phys. Rev. Lett.* **62**, 426 (1989).

1.5-6 Harvey, R. W. and McCoy, M. G., 1993 *Proc. IAEA Technical Committee Meeting (Montreal, 1992) (Vienna: IAEA)* p498.

1.5-7 Suzuki, T., *et al.*, *Nuclear Fusion* **44**, 699 (2004).

1.5-8 M. Seki *et al.*, *Fusion Sci. and Tech.* **42**, 452 (2002).

1.6 Divertor / SOL Plasmas and Plasma-Wall Interaction

1.6.1 ELM Plasma Study in SOL and Divertor

Transient heat and particle loading on the plasma facing components caused by ELM events is crucial for the ITER. Radial and parallel transport of the ELM plasma at the SOL and divertor was investigated, using fundamental edge diagnostics such as Langmuir probes at poloidal locations (Low-Field-Side midplane and just below X-point) and magnetic pick-up coils [1.6-1]. Time lag from the start of magnetic fluctuations and the first peak of the ion saturation current j_s, at the LFS divertor (130 – 210 μs) was explained by the parallel convection from midplane to the divertor: transport time of the convection flow is L_{para}/C_s ~130 μs. However, time lag of the start of j_s enhancement (70-130 μs) was shorter than the convection transport time. At HFS (High-Field-Side) and LFS divertor strike-points, j_s enhanced simultaneously, and strong enhancement of *negative* j_s was found at the private

flux region. Transport of the ELM plasma in the private region is also important.

The radial velocity was evaluated by the time lag, t_{perp}^{mid}, from the start of magnetic fluctuations to the first peak of j_s as shown in Fig.I.1.6-1(a): i.e. $V_{perp}^{mid} = \Delta r^{mid}/\tau_{prep}^{mid}$, where Δr^{mid} is distance between the separatrix and midplan Mach probe location. Figure I.1.6-1(b) shows that V_{perp}^{mid} was generally proportional to Δr^{mid}, and V_{perp}^{mid} = 1.7 km/s was determined with large variation between 1 and 2.5 km/s. These velocities were relatively higher than those measured in other tokamaks: 1 km/s (JET), 0.6 km/s (DIII-D), 0.75 km/s (MAST).

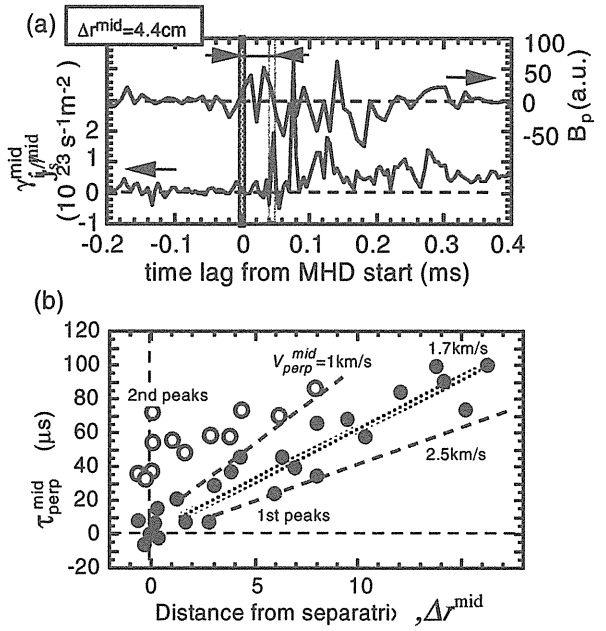

Fig.I.1.6-1 (a) time evolutions of magnetic fluctuation (MF) and ion saturation current at midplane (j_s^{mid}). (b) Time lags between MF start and first j_s^{mid} peak as a function of Mach probe location.

Characteristics of the density and floating potential fluctuations were statistically analyzed in order to investigate intermittent transport (IPO) between ELMs and ELM transport itself. Probability distribution function (PDF) analysis shows that intermittency in the midplane SOL was larger than that in divertor [1.6-2].

1.6.2 SOL Flow and Impurity Transport

Understanding of influences of gas-puff location on SOL flow and impurity shielding was progressed by code analyses on "puff and pump" experimental results [1.6-3].

Parallel and perpendicular transport of IPOs, and the relation between IPOs and ELM are in future work. multi-machine collaboration work.

Measured SOL flow velocities were subsonic ($M_{//}$ = 0.4-0.5) at HFS SOL (above the HFS baffle) and at the LFS divertor entrance (just below X-point). The SOL flow increased during gas-puff from the plasma top (M-GP), in particular, at HFS SOL, where the flow velocity and density increased significantly. The Carbon concentration in the main plasma (n_C/n_e ~0.8% for M-GP) was lower than 1.2% for gas-puff from the divertor (D-GP).

Figure I.1.6-2 (a) shows T_e, T_i and $M_{//}$ at HFS divertor calculated by Simple Divertor Code. Predicted $M_{//}$ (0.1-0.2) was smaller than the measured. Impurity Monte-Carlo code (IMPMC) calculation resulted in a converse prediction: larger n_C/n_e for M-GP than for D-

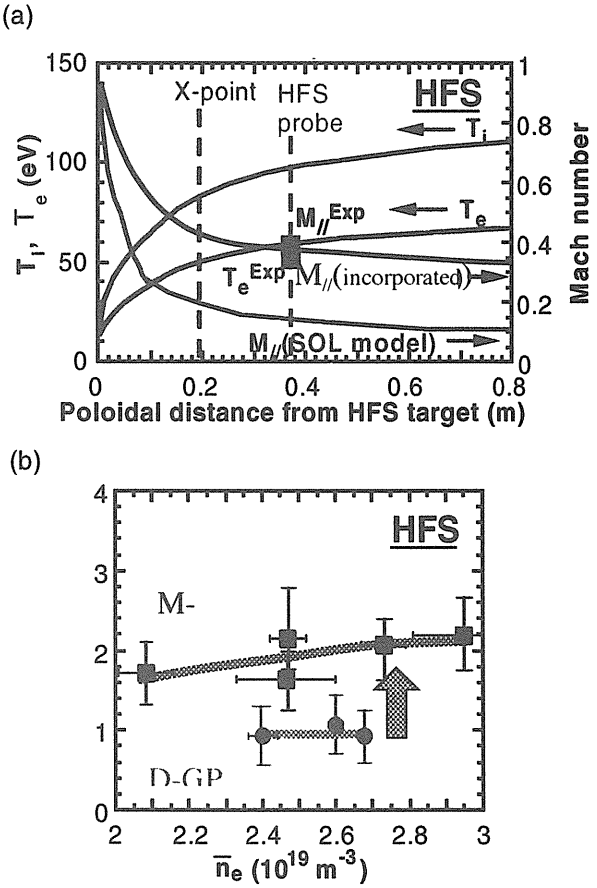

Fig. I.1.6-2 (a) distributions of T_e, T_i and $M_{//}$ (Simple Divertor Code prediction and incorporation with measurement) at HFS divertor for M-GP. (b) Ratio of friction force to ion thermal force as a function of line-averaged main plasma density for main and divertor gas puff cases.

GP [1.6-4]. Measured subsonic Mach flow was incorporated in Simple Divertor Code as shown in Fig. I.1-6.2 (a). Friction-force in the subsonic SOL flow increased compared to that for the original model. Ratios of the friction-force to the thermal force for M-GP and D-GP cases were shown in Fig. I.1-6.2 (b). For the case of M-GP, ion friction-force becomes larger than ion thermal-force at HFS SOL. This would explain improvement of the carbon shielding during the puff and pump. The simulation also indicated that poloidal distributions of the highly charged carbon ions such as C^{4+} and C^{5+} around the main plasma were changed by the incorpolation of the measured subsonic SOL flow velocity. Role of the SOL flow and ion temperature distributions should be investigated in experiment and modeling in future.

1.6.3 Carbon Transport and Ion Temperature in the Divertor

The spatial distribution of C^{3+} density and C^{3+} temperature in divertor plasmas has been investigated in order to understand the transport of carbon ions and to determine D^+ temperature [1.6-5]. Simultaneous measurement of three spectral lines, C IV ($3s^2S_{1/2}$ - $3p^2P_{3/2}$), C IV (n = 5 - 6), and C IV (n = 6 - 7), provided the population densities, $C^{3+}(3p^2P_{3/2})$, C^{3+} (n = 6), and C^{3+} (n = 7), respectively. From analyses using two-dimensional transport codes and a collisional-radiative model code, it is concluded that C^{3+} (n = 7) is predominantly excited from the ground-state of C^{3+} by electron collision in all the regions of the divertor plasma under the attached condition. Hence, the C^{3+} density and the C^{3+} temperature can be measured from the brightness and the Doppler width of the CIV (n=6-7) spectral line, respectively.

Regression analysis of the spectrum resulted in two C^{3+} temperature components. The higher C^{3+} temperature ranged from 50 to 150 eV, the lower around 20 eV as shown in Fig. I.1.6-3. From the results of the code analyses, it is concluded that the higher and the lower C^{3+} temperature correspond to the C^{3+} temperature of the common flux plasma and of the private plasma, respectively. For the inner divertor, the code analyses indicate that C^{3+} temperature is close to D^+ temperature, and that the C IV spectral line is predominantly emitted around the inner divertor leg.

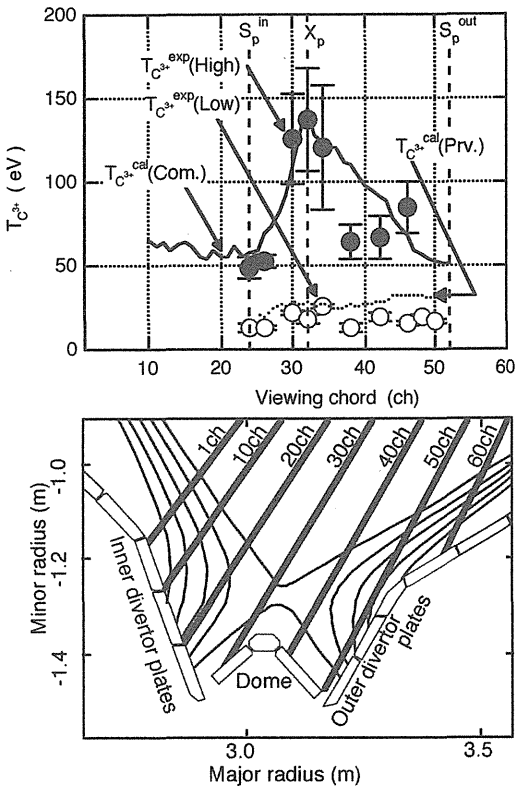

Fig. I-1.6-3 Comparison of measured and calculated C^{3+} temperatures as a function of viewing chord, shown in the bottom figure. T_{C3+}^{exp}(High) and T_{C3+}^{exp}(Low) indicate the measured C^{3+} temperature of the high and the low temperature component, respectively. T_{C3+}^{cal}(Com) and T_{C3+}^{cal}(Prv) indicate the calculated C^{3+} temperature of the common and the private region, respectively. S_p^{in}, S_p^{out} and X_p indicate the inner and the outer strike point, and the X-point, respectively.

1.6.4 Hydrogen Molecule Behavior in the Divertor Plasmas

Understanding of H_2 molecule behavior in the divertor plasma is essential to establish the heat and particle control using the divertor. The H_2 molecules play an important role as a source of the H^+ ions, and they may play a role as a sink of the H^+ ions by the molecular assisted recombination. The H_2 molecule behavior has been spectroscopically studied in attached and detached divertor plasmas of JT-60U [1.6-6].

The decay lengths of the H_2 Fulcher line intensity in the attached and the detached divertor plasma were ~1 cm and ~4 cm, respectively (Fig.I.1.6-4 (a)). It suggested that the H_2 molecules penetrated more deeply in the detached divertor plasma than in the attached divertor plasma. Since the rate of the molecular assisted recombination increases with

vibrational excitation of the ground state of the H_2 molecules, it is important to estimate the vibrational population of the ground state. From the vibrational population ratios of the upper state of the Fulcher transition: d $^3\Pi_u$ (Fig. I.1.6-4 (b)), using a coronal model, the vibrational temperature of the ground state was estimated to be ~1eV.

The H_2 molecule behavior and the Fulcher line emission were simulated with a three-dimensional neutral transport code and a collisional-radiative model code. For the attached divertor plasma, the background plasma parameters were determined using Simple Divertor Code from the electron temperature and density measured with the Langmuir probes at the divertor plates. As shown in Fig. I.1.6-4 (a), the fall in intensity of the H_2 Fulcher lines with distance from the divertor plates was reproduced by calculation using a neutral transport and a collisional radiative model code. It suggested that the H_2 molecule density distribution was well reproduced by the neutral particle transport calculation. For the detached divertor plasma, since it is difficult to obtain the spatial distribution of the plasma parameters from the Langmuir probe measurement, a two-dimensional fluid code was used to obtain the background plasma. The relative observed profile of the Fulcher line intensity was reproduced by the calculation with the ground-state vibrational temperature of 0.5 eV. The calculated vibrational temperature agreed well with the vibrational temperature estimated from the vibrational population ratios of the d $^3\Pi_u$ state considering uncertainty. In the detached divertor plasma, the molecular assisted recombination rate was estimated to be as large as the H^+-e recombination rate.

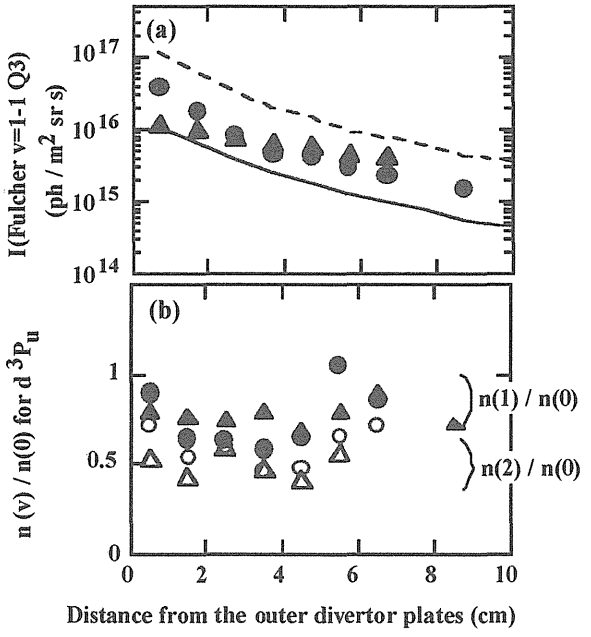

Fig. I.1.6-4 (a) Intensity of Fulcher v=1-1 Q3 line and (b) vibrational population ratios (closed symbols: $n(v=1)$ / $n(v=0)$, open symbols: $n(v=2)$ / $n(v=0)$) of the d ^3P_u state as a function of the distance from the outer divertor plates. Circles and triangles indicate the attached and the detached divertor plasma, respectively. The lines indicate the intensity calculated for the attached divertor plasma. The continuous and the broken line are the calculations with and without considering the dissociative attachment from the n=3 state.

1.6.5 Tungsten Tile Study in ELMy H-mode PlasmasTungsten is a candidate of plasma facing materials in fusion devices because of high heat conductivity, small erosion rate and low hydrogen retention. In order to investigate compatibility with plasma and tungsten, 13 tiles of outer divertor tiles (about 1/18 toroidal section) have been replaced with W-coated CFC tiles as shown in Fig. I.1.6-5. W layer with rhenium multi-layers is formed on CFC tiles by vacuum plasma spray coating and the thickness of W layer is 50 μm. In the ELMy H-mode plasmas with $\bar{I}_p$ = 1 MA, B_t < 2.0 T, NB-heating power ~6.5 MW, $\bar{n}_e$ = 1.9 -2.2 x 10^{19} m^{-3}, the outer strike point was swept from CFC tiles to W tiles shown in Fig. I.1.6-5. Figure I.1.6-6 shows time trace of W I line intensity (wavelength: 400.9 nm) measured with a visible

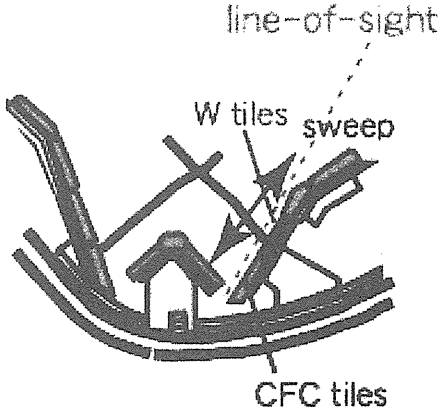

Fig.I.1.6-5 Poloidal cross-section of the divertor

spectrometer (line-of-sight of the spectrometer is shown in Fig. I.1.6-5) together with NB-heating power and the location of the outer strike point. The W I line intensity increased when the outer strike point set on the W tiles. The W sputtering yield against ion flux was estimated to ~10^{-4} (preliminary) and similar to the results in ASDEX Upgrade. From ELMy H-mode plasmas with NB-heating power up to ~15 MW, some

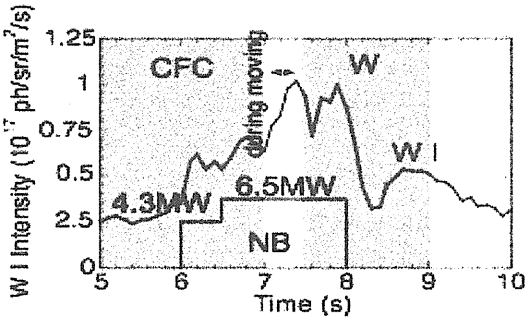

Fig.I.1.6-6. Time trace of W I line intensity, NB-heating power. Location of the outer strike point is also shown.

W lines near 5 ~6 nm in the VUV region (W^{28+}, W^{29+}, W^{44+}, etc) were observed. But the soft X-ray signal was too weak to analyze W transport/accumulation because only a small amount of W seemed to generate and penetrate to the main plasma. Experiments with higher NB-heating power are planned.

1.6.6 Local Gas-Puff in the Divertor

Chemical sputtering of carbon divertor plates is crucial because the lifetime of the divertor plates depends on the chemical sputtering and carbon co-deposition can increase tritium retention. The parameter dependence of chemical sputtering has been energetically investigated by spectroscopic technique [1.6-7]. In this technique, it is essential to determine D/XB value, the number of dissociation events per a photon, and the ratio of the loss rate of the molecule to the emission rate of the observed molecular band under the real divertor conditions. For determination of the D/XB value, a gas-puff system was installed at a poloidal section of the outer divertor where viewing chords for spectroscopic diagnostics were positioned. The D/XB values for CD_4, CH_4, C_2H_6, C_3H_8 will be determined from the puff rates and the emission intensities.

References

1.6-1 Asakura, N., *et al.*, "Parallel and radial trasnport of ELM plasma in SOL and divertor on JT-60U", submitted to *J. Nucl. Mater.*

1.6-2 Uesugi, Y., *et al.*, *20th annual meeting of Japan Soc. Plasma Sci. Nucl. Fus. Res. Mito*, 28pA03 (2003).

1.6-3 Asakura, N., *et al. Nucl. Fusion*, **44** (2004) 503.

1.6-4 Asakura, N., *et al. Proc. 30th Eur. Conf. St. Petersburg, 2003*, Vol.**27A** (2003) 2-153.

1.6-5 Nakano, T., *et al., J. Plasma Fusion Res.* **80**, 500 (2004).

1.6-6 Kubo, H., *et al.*, "Spectroscopic study of hydrogen particle behavior in attached and detached divertor plasmas of JT-60U", submitted to *J. Nucl. Mater.*

1.6-7 Roth, J., *et al.*, submitted to *Nucl. Fusion.*

1.6-8 Nakano, T., *et al., Nucl. Fusion* **42**, 689 (2002).

1.6-9 Nakano, T., Kado, S., *J. Plasma and Fusion* Res. **80**, 91 (2004). (*in Japanese*)

2. Operation and Machine Improvements

2.1 Tokamak Machine

2.1.1 Operation Status

The operation and maintenance of JT-60U was carried out in this fiscal year. In the maintenance period, some improvements towards long pulse operation have been made in JT-60 tokamak machine. Conducting capability of DCW (Disruption Control Windings) magnetic field coil was changed from 40kA-8sec to 30kA-20sec. The temperature rise of the feeders was, therefore, controlled with a newly installed air cooling fan so as not to exceed the limit (around 70 degrees Celsius) against stress concentration caused by thermal expansion during the long time operations. Software improvements have been made in gas injection and pellet injection control systems to match injection timing with long discharge. A start timing signal of the pellet injection was shifted, and sampling period and elapsed time for gas injection data gathering were extended.

Understanding of tritium removal characteristics and de-tritiation rates in the carbon-based plasma facing material is of crucial importance for the nuclear fusion reactor operation. From this point of view, initial measurements of exhaust gas from the vacuum vessel were conducted in JT-60 deuterium discharges following the installation of some exhaust gas analysis systems [2.1-1]. Tritium was measured with an ion chamber and a water bubbler. Exhausting gas composition and chemical form were measured with a micro gas-chromatograph and a residual gas analyzer. De-tritiation rates in three types of discharges; plasma discharges, Taylor discharge cleanings and glow discharge cleanings, were estimated. It was found that the most effective method for de-tritiation was the glow discharge cleaning with H_2 gas. The chemical forms of the removed tritium mainly consisted of elemental gas.

2.1.2 Tungsten Coated CFC Tiles

In order to apply tungsten divertor tile for JT-60, the heat load tests of three types of tungsten-coated CFC tiles were conducted at JAERI Electron Irradiation Stand (JEBIS). The types were (1) 3 μm-thick physical vapor deposition (PVD), (2) 50 μm-thick vacuum plasma splay (VPS) coating, (3) 500 μm-thick VPS coating. (2) and (3) tiles have 16 μm W/Re multi-layer (Fig. I.2.1-1) between each CFC substrate and tungsten coating layer to prevent the formation of carbides in the main tungsten layer. The heat load tests of 7-8 MW/m^2 x 5 s showed that 3 μm PVD and 50 μm VPS coating tiles withstood for 230 cycles, while 500 μm VPS coating tile suffered damage due to crack formation after 85 cycles.

As the results of the heat load tests, we have selected the 50 μm VPS coating as the divertor target tile. In Aug. 2003, 13 tiles were installed in the upper part of the outer divertor in JT-60, as shown in Fig. I.2.1-2, and study on the tungsten transport and accumulation experiments has started.

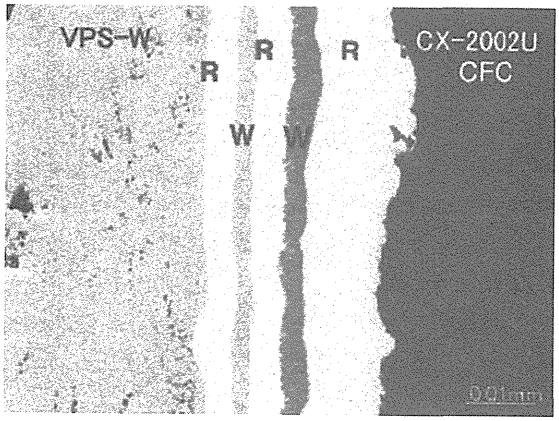

Fig.I.2.1-1 W/Re multi-layer between CFC substrate and tungsten coating layer.

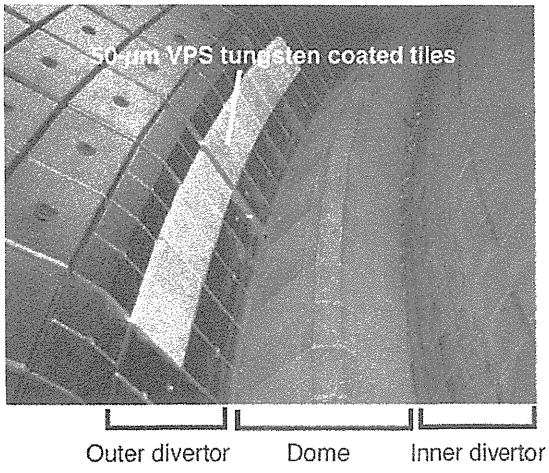

Fig. I.2.1-2 Tungsten coated tiles installed in the outer divertor.

2.1.3 Study of the Plasma-Surface Interaction

The cooperative research program between JAERI and universities using the JT-60 first wall tile was initiated in2001. Under the program, various studies on the plasma facing materials have been progressed [2.1-2], [2.1-3]. Major research activities conducted in FY 2003 are as follows:

(1)Tritium Retention by IP

Tritium depth profile in the dome top tile used in the JT-60 deuterium experiments was measured with an imaging plate (IP) technique and a tritium survey monitor [2.1-4]. The tritium profile in depth direction measurements showed that the

amount of the tritium within 1 μm depth from the surface was small, while it increased in the area more than 1 μm depth. In JT-60, roughly half of the tritium produced by D-D nuclear reaction escapes from plasma due to ripple loss, and implants deeply into the plasma-facing wall with an energy level of 1 MeV. Since the tritium retained in such deep position is hard to be removed, the retention of the implanted tritium could be a long-term potential issue.

(2) Deuterium Depth Profiles by NRA

Deuterium concentrations and depth profiles in the divertor tiles were investigated by nuclear reaction analysis (NRA) [2.1-5]. The highest deuterium concentration ($D/^{12}C$ of 0.053) was found in the outer dome wing tile, while peak of tritium concentration was observed in the dome top tile. It was also found by SEM observation that slight re-deposition layers existed in the outer dome wing tile which was located on the opposite side of the eroded outer divertor tiles. On the other hand, the OFMC simulation showed that energetic deuterons caused by the neutral beam injection were intensively implanted into the dome top area or upper part of the outer dome wing tile. Therefore another accumulation process such as the deuterium-carbon co-deposition is considered other than the implantation of energetic deuterons in the outer dome wing tile.

(3) Low-Z Impurity Deposition

Low-Z impurity (^{7}Be) on the JT-60 divertor tiles was analyzed to study the impurity behavior in the divertor region [2.1-6]. The amount of the ^{7}Be increased approximately one hundred times after B_4C-tile installation in the outer divertor. The ^{7}Be was probably produced by $^{10}B(p, \alpha)^7Be$ nuclear reaction on the divertor tiles in the hydrogen experiment with ion cyclotron range of frequency heating. The ^{7}Be was distributed asymmetrically in the poloidal and the toroidal direction. The highest ^{7}Be concentration was found at the inner divertor, though its boron content, B/(B+C), was ~20%, which was lower than that of the B_4C tiles (~80%) of the outer divertor. This fact shows the impurity moves from the outer divertor to the inner divertor.

(4) Observation of Re-deposition Layers

Transmission Electron Microscopy (TEM), Selected Area Electron Diffraction (SAD) and Energy Dispersive X-ray spectroscopy (EDX) measurements were made on carbon deposition layers formed on graphite armor tiles used in the lower X-point divertor region of JT-60 [2.1-7] with the hydrogen discharge in 1988-1990. Some redeposition layers gathered at poloidal and/or toroidal sections of the inboard side of the inner-separatrix strike point were measured with the TEM. Images of 0 - 6 μm subsurface layers were correlated to the last 30-shots in the 1988 experimental campaign.

Fig. I.2.1-3 shows a TEM image of the redeposition layers at a toroidal section on the inboard side, at 20 - 30 mm apart from the strike point. Two columnar layers correspond to successive normal and disruptive divertor discharges of

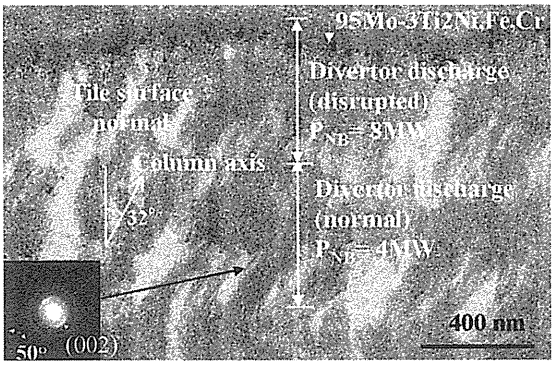

Fig. I.2.1-3 TEM image of redeposition layers at toroidal section with an insertion of a SAD pattern from columns showing oriented graphenes structure of the columns.

relatively lower NBI power at 4 and 8 MW, respectively. Columnar structure is formed onto relatively lower temperature substrate and by inclined incidence angle of adatoms against the substrate (Fig. I.2.1-4). In Fig. I.2.1-3, it was found column axis in the deposition layers was oriented at around 32 degree to the surface normal (β), while a SAD pattern, inserted in Fig. I.2.1-3, indicated that graphene sheet was oriented at 50 degrees on average. Relation between the column axis orientation (β) and graphene one (α) was found to roughly match "tangent rule", $\tan\alpha = 2\tan\beta$ (Fig.I.2.1-4). Also in the SAD pattern, diffused and elongated (002) diffraction spots in Fig. I.2.1-3 show less crystallized graphitic structure, and indicate the lower deposition temperature for those shots. A codeposition layer of the graphene with Mo-Ti-Ni/Fe/Cr particulates from TiC coated Mo liners was found corresponding to plasma disruption.

(5) Depth Profile and Retention of Hydrogen Isotopes

Hydrogen isotope distributions of the graphite tiles in the W-shaped divertor were studied. The tiles used in the studies were set in the JT-60 between 1997 - 1999. Just before the removal of the tiles form the vacuum vessel, hydrogen

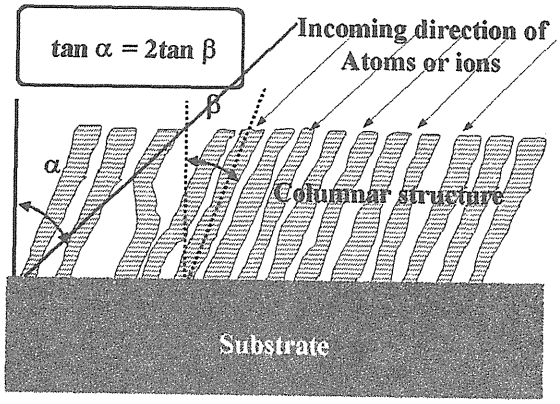

Fig. I.2.1-4 A schematic diagram for columnar structure formation. Column axis orientation angle (α) and angle of incoming direction of adatoms (β) follows "tangent rule".

discharge experiments were conducted. In the studies, the depth profiles of deuterium (D) and hydrogen (H) in graphite tiles were measured through SIMS. Erosion depth and deposition layer thickness measurements were made by a dial gauge and a Scanning Electron Microscope (SEM). Chemical state for tile surfaces was also analyzed with a X-ray Photoelectron Spectroscopy (XPS).

It was found that retention of H and D in the sub-surface layer (0 - 2 μm) of the thick deposition layers on the inner divertor tile was quite small, even smaller than those in the erosion dominated outer divertor tile. The reason seems to because the poor adhesion or porous structure of the deposited layers inhibited the heat flow from the plasma to the substrate, resulting in temperature increases at the surface of the deposited layer. Hydrogen discharges, employed for reduction of tritium, seemed to be effective to exchange most of deuterium retained in the near surface regions [2.1-8].

In the outer target tiles, it was found that the largest deuterium concentration was found around the slot-entrance zone of the tile where re-deposition layers of thickness less than 5 μm were observed. On the other hand, the concentration of the deuterium was the lowest and no re-deposition layers were found in the middle zone of the tile, where the frequency of the separatrix strike point hitting was the largest and erosion was dominant [2.1-9].

(6) Dust Analysis

Dusts in the JT-60 vacuum vessel were corrected under the collaboration between JAERI and INEEL (Idaho National Engineering and Environmental laboratory) [2.1-10]. The dust of 170 mg in total was corrected at sampling area inside the vacuum vessel. The dust at the locations not exposed to plasma was larger than that at the positions exposed to plasma. Dust particles analysis with SEM/EDX showed that most of the dust was carbon. Average particle size at all location was 3.08 μm. Specific surface area of the dust was 0.28 - 1.18 m^2/g. These results of specific surface area measurements for dust in JT-60 were consistent in magnitude with that obtained in other fusion machines. The average surface mass density was 37.4 mg/m^2 at all sampling surface. The total dust inventory extrapolated from the surface mass densities of each sampling locations and total surface area of inside the vessel was ~7 g. This amount of the dust in JT-60 was considerably smaller than that observed in other tokamaks.

References

2.1-1 Kaminaga, A., et al., *Proc. 20th SOFE* (2003).
2.1-2 Masaki, K., et al., *Proc.16th PSI, J. NuclMater.*, to be published.
2.1-3 Miya, N., et al., *11th ICFRM* (2003), *J. Nucl. Mater.*, to be published.
2.1-4 Sugiyama, K. et al., *ibid.*
2.1-5 Hayashi, T. et al., *J. Nucl. Mater.*, to be submitted.
2.1-6 Masaki, K., et al., *11th ICFRM* (2003), *J. Nucl. Mater.*, to be published.
2.1-7 Gotoh, Y., et al., *ibid.*
2.1-8 Hirohata, Y., et al., *ibid.*
2.1-9 Oya., Y., et al., *Phsica Scripta.* **T108**, 57 (2004).
2.1-10 Shape, J.P.Y., et al., *Proc. 16th PSI, J. NuclMater.*, to be published.

2.2 Control System

2.2.1 Modification of the control system for long -pulse discharge

Since it was required that a pulse length of the plasma discharge was extended up to 65-sec long enough for saturation of plasma current profiles, the following changes and modifications have been made to the JT-60 control system.

1) To collect entire discharge data due to the pulse length extension
2) To add consistency checks among discharge parameters relating to a pulse length extension
3) To re-engineering discharge interval control functions to secure the average heat load of field coils and power supplies within an allowable limit

Two choices were possible for data storage in the long pulse operation. (1) Increase data amounts; (2) increase a sampling interval. For some new or modified systems were applicable to increase their data amount due to enough data

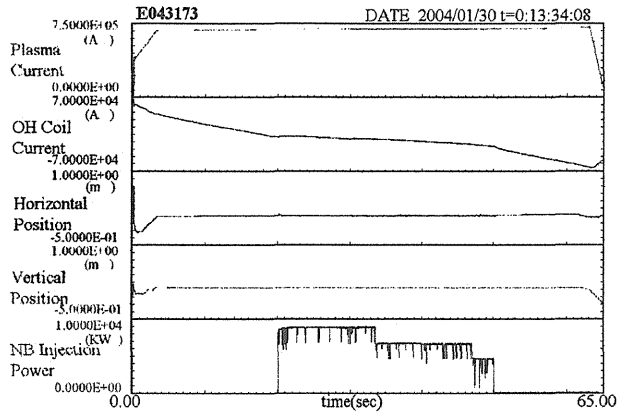

Fig.I.2.2-1 A typical data in a 65-sec plasma discharge

storage area. However, for old CAMAC modules, there was no extra memory and storage. Therefore, data sampling interval change was applied to the old systems to maintain same data amounts.

The allowable heat load on toroidal and poloidal field coils and power supplies have to be consistent with their design limit even in the long-pulse operation. The heat load of the toroidal/poloidal field coils can be estimated by means of time integral calculation of Joule heating. ZENKEI, the supervisory control system of JT-60, provide prediction function for toroidal field pre-programmed waveform, and real-time protection function for poloidal field coils. In addition, discharge interval control has been added to keep an average heat load under the design specification. Based on the integrated time of coil current excitation and coil surface temperature monitoring, plasma discharge operation is restricted until reaching adequate coil surface temperature.

For the NB injection system, the modification of the power supply system has been performed for 30-sec long NB injection (four positive-ion based NB units). One of the two negative-ion based NB unit was modified to be capable of 30-sec injection with 2 MW at maximum. The rest of PNB units (seven perpendicular units) were modified to be provided 10-sec injection within a period of 30-sec in a shot. Human interface system setting for discharge parameters was also modified. A number of control algorithms, such as neutron yield feedback control and stored energy feedback control, are capable to select by respective NB units simultaneously.

All of the modifications have been successfully completed, and followed by the plasma commissioning with 65 sec discharge (1MA, 2.1T with 30-sec NB injection) in November 2003. Figure I.2.2-1 shows a typical data of the time evolution in a 65-sec plasma discharge.

2.2.2 Development of plasma current profile control system

A feedback control system of plasma current profile has been newly developed. This control employs the LHRF as a current

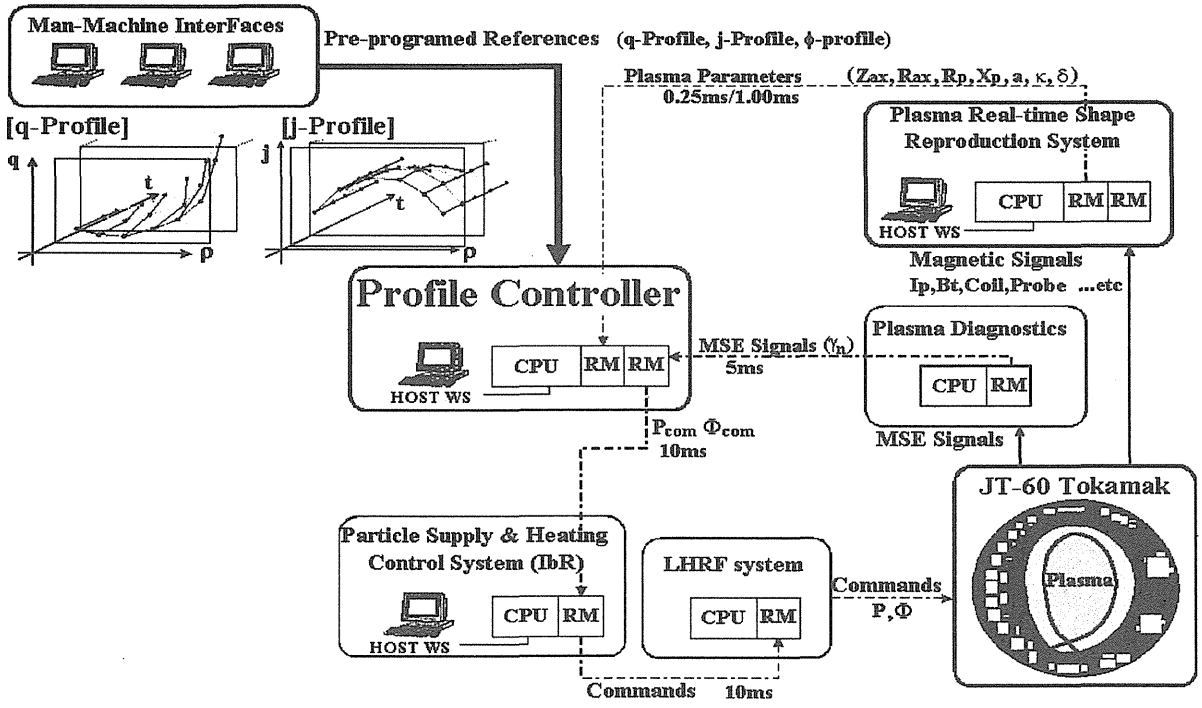

Fig.I.2.2-2 Schematic Diagram of the Current Profile Control System

drive (CD) actuator and a measurement system based on motional stark effect (MSE) as a current profile detector. Basically three profile references; current profile, q-profile and magnetic flux profile can be chosen in this profile control system. The q-profile control has been selected as the first trial. Plasma equilibrium parameters are calculated by the real-time plasma shape reproduction system based on the CCS method [2.2-1]. The phase and power of the LHRF are manipulated to control the position and increase extent of current drive.

A schematic diagram of the new plasma current profile control system is shown in Figure I.2.2-2. The profile controller, consists of compact PCI modules, executes profile reproduction with MSE diagnostic (current-profile and q-profile), and gives a command to the LHRF system. A reflective memory module is employed for high-speed data communication of control and diagnostics data.

The first feedback control was executed for 3sec at shot #E043172, where target q-surface was ~1.5, LH power use around 1MW, and calculated output commands were oscillated between 90 degree and 30 degree. To avoid control command oscillation, improvements of control logic and more LH injection power would be necessary to demonstrate clear current drive at target plasma horizontal position.

References

2.2-1 Kurihara, K., *Fusion Eng. Des.*, **51-52** 1049 (2000).

2.3. Power Supply System

2.3.1 Remodel of Toloidal Field Coil Power Supply (TFPS) for Long Pulse Discharge

(1) New control system for TFPS.

The control system for TFPS was remodeled for long pulse plasma operation up to 65 s. The former system could control toroidal field coil (TF-coil) current only for 15 s. The TFPS is composed of both the system directly supplied from 275 kV power grid and toroidal filed coil power supply motor generator (T-MG) of 215 MVA. The TFPS is controlled by two ways; the preset one shot control of four diode rectifiers and the field control of the T-MG. The simplified main circuit diagram is shown in Fig. I.2.3-1. The new control system for the TFPS is composed of WS and VME (Versa Module Europe) modules. *VxWorks* is adopted as Real-time OS for the system. In the system, about 50 programs to control each device of the TFPS are set in VME. These tasks are activated by command messages from the toroidal host WS and started a sequence control.

In the case of plasma discharge experiment, the host WS of the TFPS receives a command message from ZENKEI, the order computer of JT-60. The command message is analyzed by the toroidal host WS and the task program corresponded to the message is started.

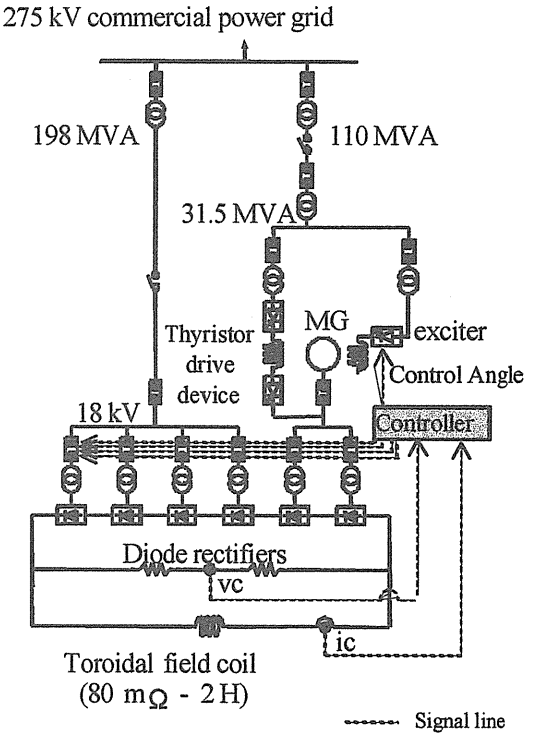

Fig. I.2.3 - 1 Simplified main circuit diagram of the TFPS

(2) New coil current control system.

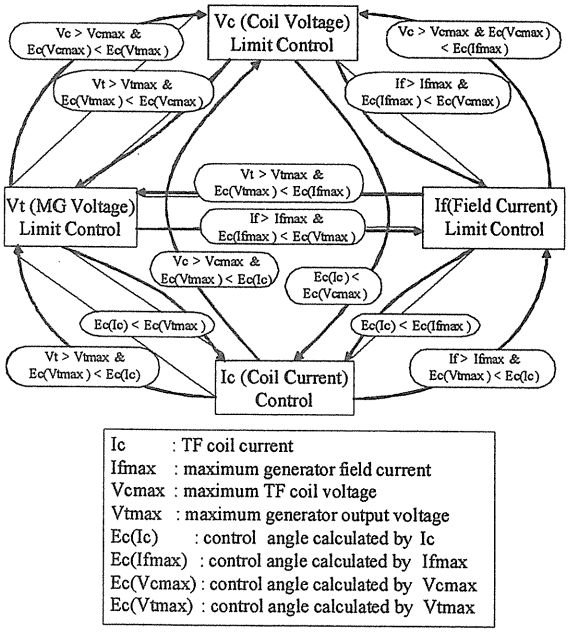

Fig. I.2.3 - 2. Coil current control with added limit function.

The new control system of the AVR for the toroidal field coil power supply motor generator (T-MG) is supervised by AVR-VME, the part of the control system of the TFPS. In the AVR, a TF-coil current and a generator output voltage are controlled by a generator field current through a control angle for the exciter. Since the TF-coil circuit is a second-order time lag circuit, a state feedback control method was adopted to stabilize and improve the response time as a new coil current control. [2.3-1]

In the coil current control system, the generator field current, generator output voltage and TF-coil voltage limit function are activated when those are required. The flow diagram is shown in Fig. I.2.3-2. By these limit functions, the operation of the TF-coil can be kept safety within the finite capacity of the TFPS even if the signal lines of the TF-coil current, the TF-coil voltage, generator field current, and generator output voltage are disconnected through a trouble.

A coil abnormal detection function moreover is introduced into the system for coil protection. For example, a short-circuited unit coil can be detected by this function in real-time. The normal state of the coil can be detected by comparing the measured coil current with the calculated value from the coil voltage using the follow equation.

$$I_{Coil} = I_{preCoil} + \frac{\Delta T}{L}\left(V_{Coil} - R \times I_{preCoil}\right)$$

where I_{coil} is the expected coil current, $I_{preCoil}$ is the coil current before one sample period, V_{coil} is the applied voltage, L is the coil inductance, R is the coil resistance, and $\_T$ is the sampling time of 10ms.

When the difference between the calculated and the measured coil currents exceeds 20 %, an abnormal state is identified and then the experiment will be terminated immediately.

(3) Simulations of the new coil control system.

The performance of the new coil current control system was evaluated by a simulation code of PSCAD/EMTDC before operation tests of the TFPS. The simulation results of coil current control are shown in Fig. I.2.3-3.

The initial magnetization period for the plasma discharge is 30 s and magnetization is continued for the 65 s plasma experiment. The toroidal magnetic field increases from 1 T to 2 T during the shot. The rotational speed of the T-MG is simulated based on the experiment. The feedback control gains are optimized so as to deter overshoot of the coil current. As a result this system could control the coil

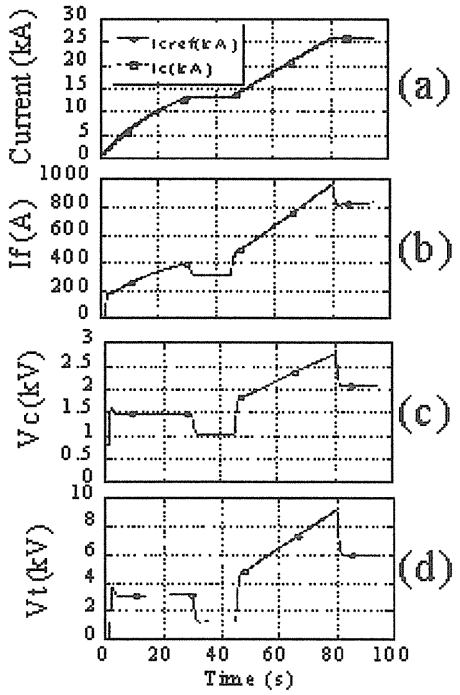

Fig. I.2.3 -3 Simulation results
(a) Simulated TF-coil current
(b) Simulated generator field current
(c) Simulated TF-coil voltage
(d) Simulated generator output voltage

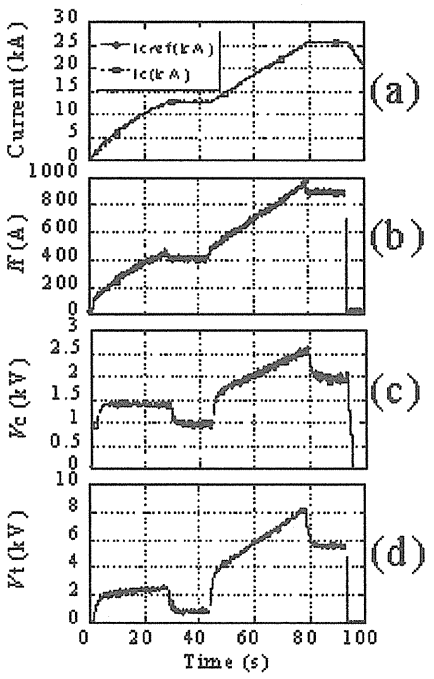

Fig. I.2.3-4 Operational test results
(a) Measured TF-coil current
(b) Measured generator field current
(c) Measured TF-coil voltage
(d) Measured Generator output voltage

current plateau with requisite accuracy and stability.

Moreover the performance of the limit functions was also evaluated by the simulation. It was found these limit functions were obtained successful results. [2.3-1]

(4) Operation Test of the TFPS.

The control system developed was tested with the TFPS. The results are shown in Fig.I.2.3-4. The initial magnetization period for the plasma discharge is 30 s, while the plasma operation period lasted for 65 s. The toroidal magnetic field is ramped from 1 T to 2 T in the plasma experiment. This system could control TF-coil current corresponded to the coil reference current as similar as the simulation results, and the operation tests of TFPS were completed satisfactorily.

2.3.2 Remodel of Poloidal Field Coil Power Supply for Long Pulse Discharge

A minor modification of the JT-60 poloidal field coil power supply (PFPS) has been carried out to cope with the prolongation of the plasma discharge duration from 15 s to 65 s. Concerning the long pulse operation, the F-coil power supply unit (F-PS) of the PFPS has already achieved 70 s as the maximum for the pulse operation test of the ITER CS model coil with the reduced Motor-Generator (MG) output voltage of 11 kV, while the rated output voltage is 18 kV. [2.3-2] By this modification, the temperature rise of the field winding of the MG and the snubber resistances of thyristor converters for F-PS could be suppressed within the limits. The modification for the pulse prolongation of whole of the PFPS was based on the successful experience of the CS model coil operation.

(1) Rearrangement of the main circuit

Due to the limitation of available power of Poloidal MG (P-MG: 500MVA/1.3GJ), the divertor coil power supply unit (M-PS) has been powered separately from Heating MG (H-MG: 400MVA/2.6GJ). This time, the M-PS has been changed the connection to P-MG from H-MG because the long pulse operation of M-PS is common to the other poloidal field coil power supplies. Figure I.2.3-5 shows the simplified main circuit diagram.

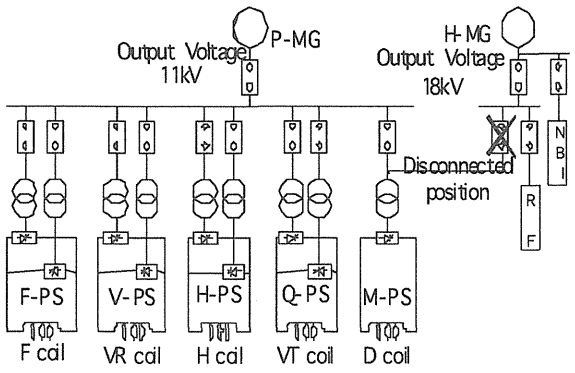

Fig. I.2.3-5 Main Circuit Diagram of PFPS.

In addition, the following reengineering was conducted:

(a) Since the P-MG shall trip in the case the rotating speed decreases lower than that limit, a new interlock to avoid the P-MG trip was added in the control system of the PFPS.

(b) Temperature rise of the AC equipments during the plasma experiment was evaluated for the long pulse operation. As the result, the output bus-bar and the field winding of the P-MG have the largest temperature rises in the AC equipments. However, these temperature rises are acceptable in the case of this operation.

(c) The I^2t of Q-PS for the VT-coil (triangularity control coil) was expanded to 50 kA - 7.2 s from the original value of 50 kA – 6 s for long pulse operation. For this modification, the pulse interval was changed from 15 min to 30 min.

(d) The I^2t of M-PS (divertor coil power supply) was expanded to 110 kA - 8 s from the original value of 110 kA – 6 s for the long pulse operation. For this modification, the pulse interval was changed from 15 min to 30 min.

(e) The temperature rise of the DC equipments during the plasma experiment was evaluated for the long pulse operation. As the result, the DC feeder of the F-PS has the large temperature rise in the DC equipments. However, it is acceptable in the case of the pulse interval of 30min.

(f) Some control signals for switch gear and circuit breaker for the M-PS were modified to receive electrical power from the P-MG.

(g) The detection system of rotating speed of the P-MG was added into the original control system for the new interlock.

(h) The amount of data storage was improved for the long pulse operation.

(i) The real-time detection functions of the I^2t and pulse duration are appended into the coil current control system for the long pulse operation.

Reference

2.3-1 Shimada, K., et al., *Proc. Int. Conf. on Electrical Engineering* **2**, 777 (2004)

2.3-2 Terakado, T., et al., JAERI-Tech 2001-056 (2001)

2.4 Neutral Beam Injection System

2.4.1 Beam Steering for Negative-Ion Based NBI

In the Negative-ion Based NBI (N-NBI) system for JT-60U [2.4-1], the goal target is to inject neutral deuterium beam of 10MW at 500keV for 10 sec with two large ion sources. Until 2003, beam injections of 5.8MW at 400keV with deuterium and 10 sec injection of 2.6MW with hydrogen have been achieved. To reach the injection goal some improvements have been conducted. One issue for increasing injection power is to reduce the beam loss in its passage through the ion source and the beamline. To reduce the beam loss, it is important to investigate the beam characteristics such as beam divergence and beam deflection. Therefore the steering of both single beamlet and multiple beamlets was studied experimentally.

The negative ion beam is usually extracted from a 45 x 110 cm^2 area divided into five segments. There are 216 (horizontally 24 and vertically 9 rows) aperture holes in each segment. In this study, multiple beamlets were extracted from only the center segment and some single beamlets were extracted from the adjacent segment. The other plasma grid segments were masked. Extracted negative ions are accelerated in three stage electrostatic accelerator.

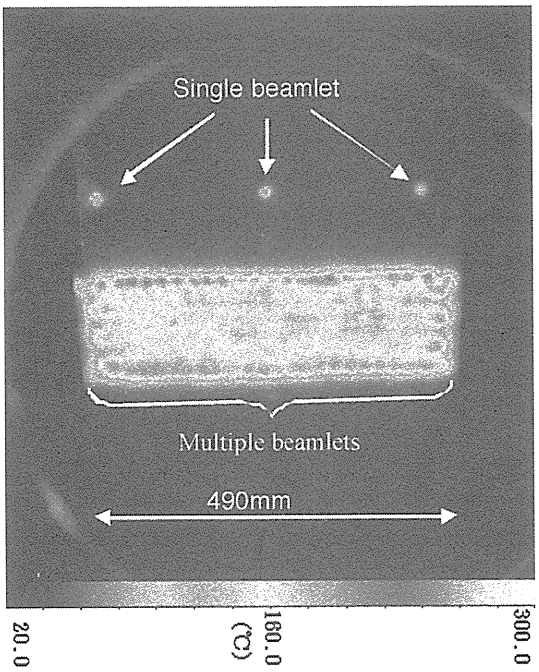

Fig. I.2.4-1 Beam footprint measured by infrared camera. Single and multiple beamlets were extracted from the center and the adjacent segments, respectively.

The aperture displacement method, based on the thin lens theory, is utilized in order to converge the beam envelope from the wide extraction area to the narrow injection port. The aperture axis of the grounded grid (GRG) is displaced against those of upstream grids, so beam is steered in the opposite direction from the offset. The aperture displacement changes according to aperture position and the apertures at the edge area need large displacement. Two types of grids with different aperture displacements were examined. One was a

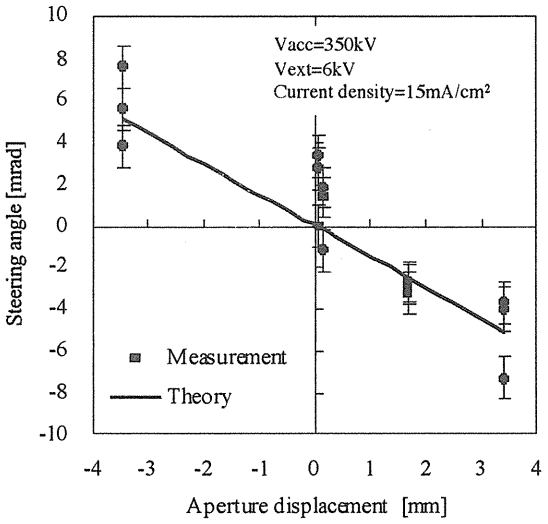

Fig.I.2.4-2. Correlation between aperture displacemen

grid in which the maximum displacement was 3.4 mm in the horizontal direction and 1.2 mm in the vertical direction at the outermost aperture, which were decided by the thin lens theory. The other had half the displacement of that one. In this experiment, the maximum steering angle was supposed to be 5.2mrad with 3.4mm aperture displacement.

Figure I.2.4-1 shows the temperature profile footprint measured by the infrared camera on the target plate set at 3.5m away from the GRG. Multiple beamlets in the center area and three single beamlets are seen in Fig.I.2.4-1. The steering angle of each single beamlet was evaluated from its peak position of the temperature profile and aperture position of the GRG. The beam steering angles were measured with two types of the GRGs in order to obtain the correlation between aperture displacement and steering angle. Figure I.2.4-2 shows the correlation between aperture displacement and steering angle in the horizontal direction. Though the data is dispersed a little,

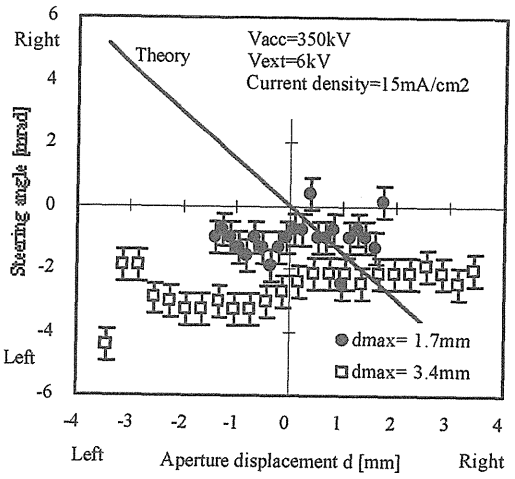

Fig. I.2.4-3. Correlation between aperture displacement and steering angle for the multiple beamlets

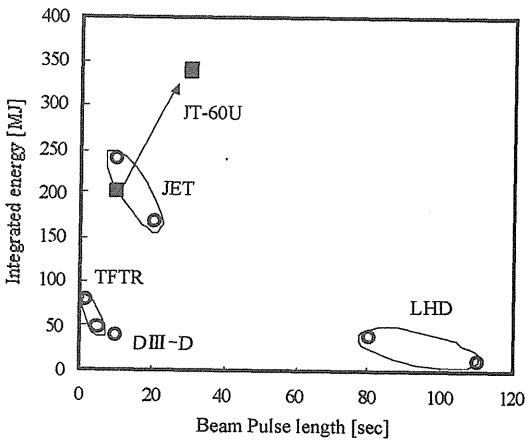

Fig. I.2.4-4 Integrated beam injection energy versus beam pulse length for the fusion device in the world.

the measured steering angle is in good agreement with the value of the thin lens theory.

Figure I.2.4-3 shows the horizontal steering angle of the multiple beamlets. Two types of the GRGs were used as well as the single beamlet. Measured steering angles were largely different from the theoretical values, and most of the steering angles were around -2mrad, which meant 2mrad to left direction. This means that the beam axis is shifted about 2mrad and most of the beamlets are extracted almost parallel. There was little difference between the results for the two GRG configurations. Thus, the steering angle of the single beamlet agrees with the thin lens theory, but that of the multiple beamlets does not. It is thought that the multiple beamlets are repulsed each other by the space charge effect of beamlets in the accelerator.

2.4.2 Extension of Pulse Length of Positive and Negative Ion Based NBI Systems

In order to investigate the behavior of high performance plasma for continuous discharge, it is necessary to make the pulse length of plasma heating system longer. In the NBI system, the pulse length has been limited by both electrical capability of the power supply and temperature rise of the beam limiters installed at the NBI injection port without active cooling. The limiter prevents damage of the NBI port from the beam bombardment.

To extend the pulse length in both P- and N-NBI systems, capability of key components of the power supply was enhanced in addition to modification of the control system. The beam limiter at the NBI port was redesigned to suppress the temperature rise on its surface. In design, the area of the limiter surface exposed to the beam was expanded by increasing the obliqueness of the limiter surface along the beam direction. The volume of the limiter was also enlarged to increase the heat capacity.

Four tangential injection units of P-NBI system were modified for extension of the pulse length. Operation of other units leaves the pulse length of 10sec as it is. In the N-NBI system, it is necessary to reduce the excess heat load on acceleration grids in addition to the modification mentioned above. One cause of the heat load is excessive stripping of the negative ions in their passage through the grid structure due to the collision with residual gas molecules [2.4-2]. It is generally considered that the heat loading of the grids is due to acceleration of the electrons stripped from negative ions. The accelerated electron hits downstream grid by its deflection due to the magnetic field that is generated by current flowing in a plasma grid (PG filter). This current forms a magnetic filter of fast electrons in the source plasma to produce negative ions efficiently. To minimize the stripping loss, the top and bottom segments out of five accelerating grid segments were replaced to the plates that have a big hole to exhaust the residual gas for lowering gas pressure in the acceleration part. As a result the ratio of the heat load to the accelerating beam power decreased from 8 % to 6 % under the optimum condition.

After the conditioning of the injection port for reducing re-ionizing loss, 30 sec operation of P-NBI was achieved at 8 MW for four units. 17 sec operation of N-NBI was also attained at 366 keV so far. The pulse length was limited by the excessive arc discharge current due to no adjustment of the filament voltage. As a result of the long injection pulse , 360 MJ of the integrated energy was injected to the JT-60 plasma by both NBI

systems. This is the maximum in record in the world by using NBI system as shown in Fig.I.2.4-4

References

2.4-1 M. Kuriyama ,et al, *Fusion Sci. Technol.*, **42**, 410 (2002)

2.4-2 T.Yamamoto, et al, *J.Plasma Fusion Res.* **Series 5**, 474 (2002)

2.5 Radio-Frequency Heating System

Performance of the JT-60U radio-frequency (RF) heating system has been constantly improved to open up new experimental regions. In FY 2003, major improvements of the JT-60U RF heating system were progress in operation of the electron cyclotron heating (ECH) system and modification of the lower hybrid (LH) launcher.

2.5.1 Progress in Operation of the ECH System

Two types of power injection modes of the ECH system have been required for realizing a variety of experiments in JT-60U. One mode is called a high power mode where the injected power is about 3 MW for 2 - 3 s. This mode has been used mainly for experiments of the neoclassical tearing mode (NTM) stabilization and strong electron heating of high performance plasmas. The other mode is called a long pulse mode where the pulse width is 10 - 30 s at about 0.6 MW of the injected power. This long pulse mode has been used for long pulse discharges of JT-60U, which are enabled up to 65 s, to perform local current drive or electron temperature profile control. The long pulse mode has been developed intensively while the high power mode had already been developed by FY2002 [2.5-1]. A key point for the long pulse mode is to control the oscillation of high power gyrotrons at 110 GHz, which are the most important component of the ECH system. Extension of the pulse width was limited by sudden stop of the gyrotron oscillation due to decrease of the gyrotron beam current about 10%. This decrease is due to the cathode cooling caused by thermoelectron emission from the cathode. There are several methods to continue the gyrotron oscillation. Among them, a conventional method of controlling the heater current was adopted in order to compensate the decrease of the beam current. In addition, a new method of controlling the voltage has been developed and was tried independently or together with the conventional method. The new method changes electron velocity distribution by the anode voltage to keep the oscillation condition as the beam current decreases, and therefore features faster response than the heater current control. Adjusting the oscillation condition like this can be done only in the JT-60U ECH system whose gyrotron has a triode-type

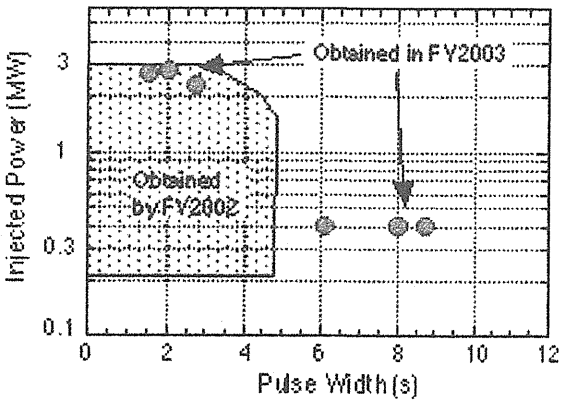

Fig. I.2.5-1 Injected power as a function of pulse width. Progress is made at longer pulse width.

electron gun while the other gyrotrons in the world have a diode-type one. Figure I.2.5-1 shows progress of the injected power as a function of the pulse width. In the long pulse mode, the pulse width 8.7 s was obtained at 0.4 MW with one gyrotron and the heater current control, where the heater current was increased at most by 50%. The anode voltage control has been tested with a dummy load. Preliminary test showed extended oscillation up to 16 s at 0.4MW with the anode voltage control by the voltage change only 2 - 3 %. The adjustment of oscillation conditions is being continued to achieve the objective pulse width 30 s.

2.5.2 Modification of the LH Launcher with Thin Carbon Grills

The LH launcher, installed at the equatorial port P18, consists of eight multi-junction grills made of stainless steel [2.5-2]. Each grill is divided into twelve rectangular channels with thin septa, forming sub-waveguides. Their dimensions are 12 mm wide and 120 mm high, and width of the septum is 2.5 mm. The launcher had been damaged by energetic ion and electron bombardment or by RF breakdown near the launcher surface. Some parts of its surface were melted 1 - 5 mm deep. Therefore the power injection capability had been degraded for these several years. Eight thin carbon grills (15 mm deep) were designed, fabricated, and connected with the original multi-junction grills [2.5-3] because the launcher could be moved by 50 mm in the major radius direction. Carbon was adopted as grill materials since it was high heat-resistant and it quite less degrades plasma performances than stainless steel if it were melted or sublimated into plasmas. Two types of carbon materials, graphite and carbon fiber composite (CFC) were used. Six graphite and two CFC grills were connected with the original launcher, as shown in Fig. I.2.5-2. The most important point of this modification is to keep sufficient electric

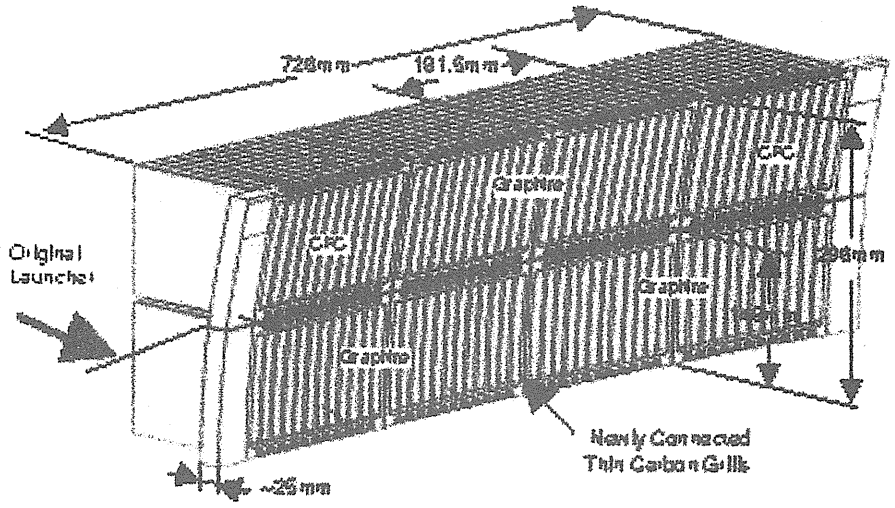

Fig. I.2.5-2 Outline of the modified LH launcher with thin graphite grills.

contact between the grills and the original grills. Their direct connection could not keep good electric contact because the original grill surfaces were definitely rough. Therefore very thin stainless steel base grills (10 mm deep) were welded onto the original grills in the condition where the launcher was set at the port. Then, the grills were bolted to the original grills with copper shims for improving electric contact in order to be able to change the grill that would be damaged.

After the grills were connected, the initial launcher conditioning was carried out for about 20 operation days. The injected energy has been increased up to 5 MJ without severe troubles, which was about a half of the normal injected energy value with the original LH launcher before the modification. The injected power level is about 1MW and hence the maximum pulse width reached to 5 s. Figure I.2.5-3 shows the relation between the injected power and reflection coefficient obtained in the initial conditioning phase. The launcher position is set at d = 8 - 12 mm back from the first wall of the JT-60U. The injected energy seems to be increased more at lower reflection coefficient. The reflection coefficient can be controlled mainly by the gap between the first wall and plasma surface as well as the set back depth d. The reflection coefficient was less than 10 % when the gap was set at less than about 10 cm. Further launcher conditioning is necessary to achieve 10 MJ of the tentative objective and therefore is planed to be done at lower reflection coefficient by keeping the gap less than 10 cm.

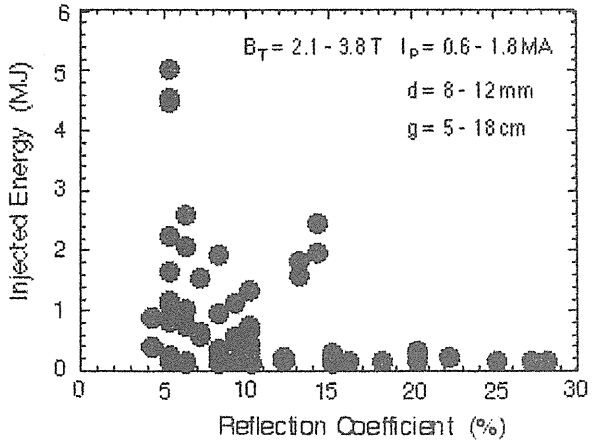

Fig. I.2.5-3 Relation between the injected energy and reflection coefficient obtained in the initial launcher conditioning.

References

2.5-1 Moriyama, S., et al., *J. Plasma Fusion Res.*, **79**, 935 (2003) (in Japanese).

2.5-2 Seki, M., et al., *Fusion Science Technology* **42**, 452 (2002).

2.5-3 Fujii, T., et al., *Proc. 20th SOFE*, (2003).

2.6 Diagnostic System

2.6.1 Time-resolved Measurement of Neutron Yield with Micro Fission Chamber

Time-resolved measurement of the neutron yield is essential to evaluate the fusion power in the fusion reactors. As it has thick components such as the blankets, vacuum vessel, diagnostic systems and the heating systems. Therefore, the neutron detectors have to be placed inside the vacuum vessel for the accurate measurement of the neutron source strength. As a neutron flux monitor, we have developed a micro fission chamber: a pencil-sized ionization chamber with fissile material

inside [2.6-1]. We have tested the effects of the magnetic field and the electromagnetic noises in JT-60U [2.6-2].

The micro fission chamber is shown in Fig. I.2.6-1. The inner surface of the cathode is coated with 0.6-mg/cm^2 UO_2, and the total UO_2 amount is 12 mg. The ^{235}U enrichment is 90%.

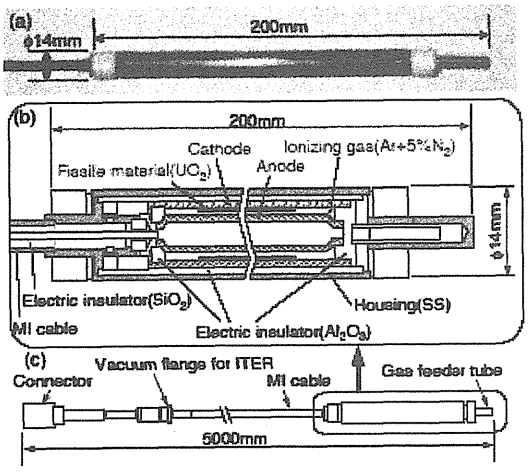

Fig. I. 2.6-1 (a) Picture and (b) cross section of the micro fission chamber. (c) Diagram of the micro fission chamber and the MI cable.

The detector is filled with 95% Ar and 5% N_2 gas at 14.6 atm. A double coaxial MI (Mineral Insulated) cable is welded to the detector. For the cable, SiO_2 is used as an electric insulator, and the cable is filled with Ar gas at 14.6 atm. The detector is set in a polyethylene block (220 x 100 x 45 mm^3) that functions as a moderator and an electric insulator. The micro fission chamber is placed between the vacuum vessel and the toroidal field coils on the torus midplane in JT-60U. At the position, the maximum magnetic field is about 2 T.

Relation between the signal of the micro fission chamber and the signal of a conventional ^{235}U fission chamber, which has been used as a neutron monitor in JT-60U, shows a good linearity, when noise signals due to NB breakdowns are removed for the micro fission chamber (Fig. I.2.6-2). The standard deviation in the neutron yields between the two detectors was 3% including stability of the electronics. Influence of the magnetic field has not been observed. Even at plasma disruptions, while change in the poloidal field was evaluated to be up to about 20 T/s, any problems have not arisen. By suppressing the electromagnetic noise due to the NB breakdowns, the micro fission chamber can be available as a neutron monitor for ITER.

2.6.2 Charge Exchange Neutral Particle Measurement with Natural Diamond Detector

Investigation of energetic ion behavior in quiescent plasmas or

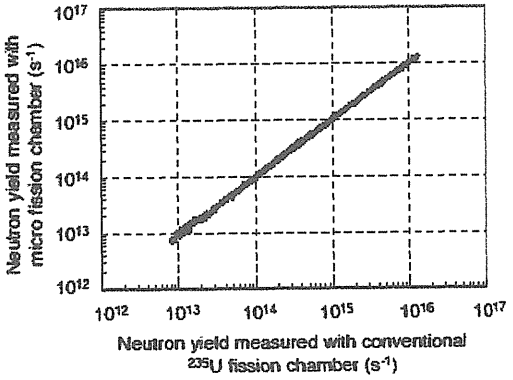

Fig. I.2.6-2 Relation between the signal of the micro fission chamber and the signal of the conventional ^{235}U fission chamber. Here, for the micro fission chamber, noise signals due to NB breakdowns are removed.

during some instabilities such as sawtooth oscillation and Alfvén eigenmodes is of great importance for burning plasmas as ITER plasmas. The charge exchange neutral particle spectrometer is one of the most effective diagnostics to investigate the energetic ion behavior, since the charge exchange neutral particles have information such as the energy distribution of the confined energetic ions. In JT-60U, a natural diamond detector (NDD) has been installed in a tangential port to measure neutralized co-going beam ions [2.6-3].

A NDD has many important advantages as a charge exchange neutral particle spectrometer; for example, a compact size, high energy resolution, high radiation resistance, and so on. An NDD has an electrode-semiconductor-electrode structure, where the electrodes are thin graphite contact layers and the semiconductor is a pure (group IIa) natural diamond. Since the number of electron-hole pairs produced by an incident fast particle inside the diamond is proportional the kinetic energy of the incident particle, the NDD can be used as a neutral particle energy spectrometer. However, since the NDD is sensitive not only to neutral particles but also to neutrons and γ-rays, reduction of the neutrons and the γ-rays background noise is necessary in JT-60 deuterium-plasma experiments. Therefore, we set up a neutron and γ-ray shield (70cm×50cm×48cm) around the NDD to reduce the background noise. The shield consists of an inner layer of lead more than 5 cm thick and an outer layer of borated-polyethylene more than10 cm thick.

Figure I.2.6-3 shows energy distribution of the neutral particles during P-NB (Positive-ion-based NB) injection and during the P-NB and the N-NB (Negative-ion-based NB)

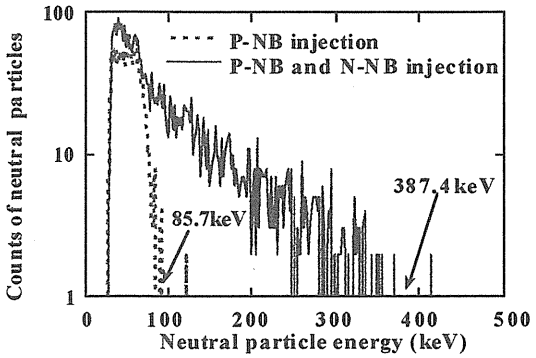

Fig. I.2.6-3. Energy distribution of charge exchanged neutral particles during P-NB injection (dotted line) and during P-NB and N-NB injection (solid line), where the P-NB and the N-NB energy were 85.7keV and 387.4keV, respectively.

injection. The energy distribution was significantly changed by the N-NB injection. The maximum energy corresponded to the NB injection energy. The time-resolved energy distribution was also obtained successfully. As to instabilities, neutral particle fluxes enhanced by sawtooth oscillation and Alfvén eigenmodes were observed with the NDD. It has been demonstrated that the NDD has high performance as a charge exchange neutral particle spectrometer.

2.6.3 Development of Analysis Methods using Electron Cyclotron Emission Signals

Singular value decomposition has been applied to analysis of magnetohydrodynamic instabilities using a set of multichannel electron cyclotron emission signals [2.6-4]. Equilibrium and perturbative terms of an electron temperature profile can be separated successfully, and structure of a magnetic island produced by a tearing mode can be revealed clearly. By neglecting components with small singular values, the signal-to-noise ratio was improved.

In order to measure electron temperature profiles with a Fourier transform spectrometer, a maximum entropy method of the nonparametric type has been developed [2.6-5]. Methods to remove ELM pulses from interferogram data and to optimize the regularization parameter using the generalized cross validation have been also developed. By the methods, the electron temperature profiles can be automatically determined using the Fourier transform spectrometer in ELMy H-mode plasmas.

References

2.6-1 Yamauchi, M., *et al., Rev. Sci. Instrum.* **74**, 1730 (2003).

2.6-2 Hayashi,T., *et al.,* "First measurement of time-resolved neutron yield on JT-60U useing a micro fission chamber," to be published in *Rev. Sci. Instrum.*

2.6-3 Ishikawa, M., *et al.*, "Charge Exchange Neutral Particle Measurements with Natural Diamond Detector under the DD Neutron Field on JT-60U Tokamak, " to be published in *Rev. Sci. Instrum.*

2.6-4 Isayama, A., *et al., Jpn J App. Phys.* **42**, L329 (2003).

2.6-5 Isayama, A., *et al., Jpn J App. Phys.* **42**, 5787 (2003).

3. Design Progress of the National Centralized Tokamak Facility

On the basis of the report issued by the Working Group on Fusion Research under Special Committee on Basic Issues of Subdivision on Science, Council for Science and Technology of MEXT in January 2003, previous design of JT-60 superconducting modification (JT-60SC) is modified to widen operation regime of high beta steady state research and is named as the National Centralized Tokamak (NCT) facility. The design requirements set by nation-wide discussion are, 1) a super-conducting device with break-even-class plasma performance, 2) capability of steady state high-β (β_N=3.5-5.5) plasma with full non-inductive current drive, required for the DEMO for more than 100 second, 3) flexibility in terms of plasma aspect ratio, plasma shaping control, and feedback control [3.1-1]. Physics and engineering designs are developed to meet these requirements, in which the technical bases developed for the previous JT-60SC design are employed.

3.1 Physics Design

Configuration optimization is one of the important research elements to achieve high beta steady state operation. Previous experiments in DIII-D show that higher beta operation becomes possible by increasing shape parameter S [$\equiv q_{95}I_p/a_pB_T \sim A^{-1}\{1+\kappa^2(1+2\delta^2)\}$] through the control of aspect ratio, A, elongation, κ, and triangularity, δ. Design studies have been made to increase operational flexibility on the plasma aspect ratio and the controllability of plasma shaping, and resulted in two machine designs, both of which have lower aspect ratio and higher S-parameter than those of ITER.

Table I.3.1-1 summarizes those machine designs [3.1-2]. Design-1 has moderate shaping flexibility with higher B_T compatible with present ECCD in JT-60. Design-2 has higher shaping flexibility with lower B_T. Both designs allow single and double null divertor operations.

Operational points of two designs are plotted in Fig.I.3.1-1 as a function of aspect ratio and shape parameter as compared with those for previous JT-60SC concept. As clearly seen in the figure, the flexibility in those parameters is remarkably extended in NCT. For medium aspect ratio of A>3.1 the shape parameter is in the range of 4-5.5, while, for low aspect ratio of A<3.0 shape parameter extends to 5-7. The enlargement of the capability in the shape parameter will contribute to extend the ideal MHD stability limit.

Table I.3.1-1 Main parameters of two machine designs

	Design-1		Design-2	
	mid-A	low-A	mid-A	low-A
I_p (MA)	4.00	4.00	4.00	5.5
B_T (T)	3.63	3.40	2.96	2.76
A	3.27	2.81	3.10	2.62
S	4.16	5.06	5.26	6.81
κ_{95}	1.82	1.70	1.83	1.84
δ_{95}	0.39	0.53	0.45	0.52
q_{95}	3.39	4.81	3.48	3.87
V_p (m^3)	80.9	122.8	77.7	132.4
R_p (m)	2.94	3.13	2.77	2.97
a_p (m)	0.90	1.11	0.89	1.13
Divertor	Single Null Closed	Double Null Open	Single Null Closed	Double Null Closed

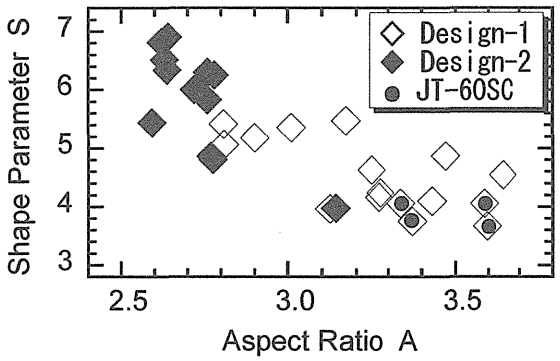

Fig.I.3.1-1 Operational points of two designs as a function of aspect ratio and shape parameter as compared with those for previous JT-60SC concept.

In order to estimate the feasibility for high plasma pressure beyond the free-boundary MHD stability limit (β_N=3.5-5.5), numerical analysis considering the 3-dimensional structure of vacuum vessel and the stabilizing plates, which is called 'VALEN code', is started under the collaboration with Columbia university and PPPL. A preliminary analysis with conformal conducting wall and up-down symmetrical plasma shaping indicates that the growth of the MHD instability with toroidal mode number of n=1 is suppressed for β_N<5 at the location of ideal wall radius at r<1.4a [3.1-3]. The controllability of in-vessel sector coils for resistive wall mode will be also analyzed by the code which contributes to optimize the design of in-vessel coils and stabilizing plates.

3.2 Engineering Design

Based on the two designs of machine specification, structures of superconducting coils, vacuum vessel and divertor are further investigated [3.2-1,2,3]. Whole assemble of the tokamak is illustrated in Fig.I.3.2-1.

The overall assembling process of toroidal field coils and the vacuum vessel in the torus hall is briefly investigated. In order to give an efficient working performance, it is investigated that the vacuum vessel is divided to two halves during the drawing of the toroidal field coils into the torus formation.

CS-Conduit: 3D finite element method analysis is performed to clarify the characteristics of the fracture toughness in the welded part of CS-conduit after the heat treatment process of superconducting conductor. Stress enlargement factor is compared to that calculated by the Newman-Raju solution, which is usually adopted for the estimation of CS conductor. The 3D analysis for the crack at the welding part on the plane plate with the thickness of 3 mm gives a 5% higher value than that by the solution. The growth of crack at the front is almost the same both in the analysis and the solution.

Radiation shield: Support of radiation shielding plates for neutron emission, which was located at the outer wall of vacuum vessel in the previous design of JT-60SC, is changed to be located at the coil-case of toroidal field (TF) coils. The change contributes to the reinforcement of the TF coils-case against the shear stress by electromagnetic forces during plasma operation, and to the reduction of the load on the vacuum vessel for the improved proof against the earthquake.

Vacuum vessel: "C-shaped" rib is adopted for the joint-support structure between outer and inner vacuum vessel, in order to reduce the interval of the ribs, which brings the hard structure of vacuum vessel. The welding method for the support rib is investigated on the viewpoint of the accessibility for work of welding and testing, and it is concluded to adopt plug welding, and fillet welding at the inner, and outer vacuum vessel, respectively.

Divertor: Unit structure of the outer divertor is designed taking into account the electromagnetic force at the plasma operation, thermal expansion during the baking, and the manufacturing. Each unit, divided by a 5° segment in the toroidal direction, has a flat heat deposition plate and 8 pieces of heat-sink. Each end of the coolant channel of the heat-sink is not turned back for keeping the coolant pressure. In order to optimize the cooling efficiency of heat deposition plate, thermal analysis for the coolant channel is made for the several cases of screw size, return-pass, and flow velocity. As a result, it is shown that the header of the return pass is removed, and that the coolant flow velocity of about 4 m/s is expected in the case of the M10-screw channel.

Cryostat: As a result of stress analysis for cryostat performed by a 3D-model, it is confirmed that each part of the cryostat satisfies the structural strength against the complex load from electromagnetic force and seismic force. A manufacturing plan of the cryostat in the torus hall is also investigated in which the clearance with the existing facilities, such as connecting port with NBI, is taken into account.

Shielding material: Development of high performance boron-doped resin [3.2-4] for neutron shield is initiated, which has sufficient mechanical strength and thermal resistance in order to extend the applicability for the shielding structure such as nuclear reactors. Several types of boron-doped resin, which are applicable at the temperature higher than 250 °C with much higher mechanical strength than that of polyethylene, are developed.

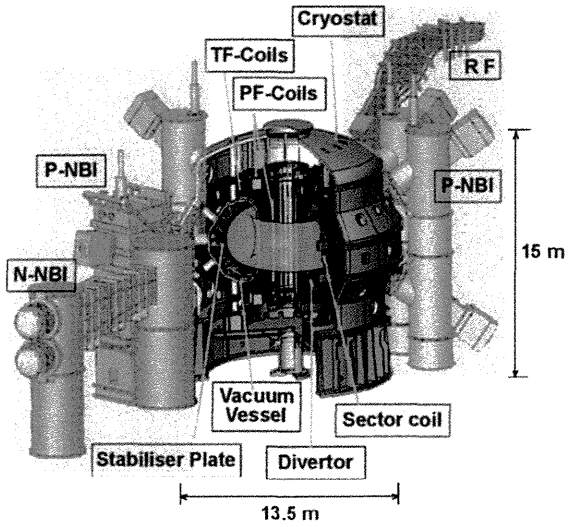

Fig.I.3.2-1 Birdseye view of the National Centralized Tokamak Facility

References

3.1-1 Tamai, H., *et al.*, *Plasma Science & Technology* **6**, 2141 (2004).

3.1-2 Matsukawa, M, *et al.*, *IEEE Transactions on*

Plasma Sciences **32**, 135 (2004).

3.1-3 Kurita, G., *et al.*, *Annual APS DPP Meeting, Oct. (2003) Albuquerque, USA.*

3.2-1 Kizu, K., *et al.*, *18th Int. Conf. on Magnet Technology, Oct. (2003), Morioka, Japan.*

3.2-2 Tsuchiya, K., *et al.*, *18th Int. Conf. on Magnet Technology, Oct. (2003), Morioka, Japan.*

3.2-3 Sakurai, S., *et al.*, *4th APFA Conf., Oct. (2003), Hangzhou, China.*

3.2-4 Morioka, A., *et al.*, *Journal of Nuclear Science & Technology*, Supplement **4**, 109 (2003).

II JFT-2M PROGRAM

On JFT-2M, advanced and basic research for the development of high performance tokamak plasma is being promoted, making use of the flexibility as a medium-sized device and the research cooperations with universities and other institutions. Recently, the Advanced Material Tokamak Experiment (AMTEX) program has been carried out in JFT-2M. The low activation ferritic steel (F82H) has been tested for the development of the structural material for a fusion reactor. In this fiscal year, the third stage test of AMTEX was conducted with the Ferritic Inside Wall (FIW) covering full inside wall of the vacuum vessel in order to investigate the compatibility of ferritic steel with high performance plasmas.

The influence of the FIW on the plasma stability and the MHD activity has been investigated under the close wall condition. In the case of optimum electron density and low impurity release from the first wall, high normalized beta of $\beta_N = 3.5$ has been kept almost constant even at the close wall condition of $r_{wall}/a \sim 1.3$. It has shown good compatibility between FIW and the high β_N plasma close to an operation regime of a fusion demonstration reactor (DEMO). The observed time constant of the growth rate of MHD activity for close wall case was a few milliseconds, which is the same order of the wall time constant as well as the time constant with normal resistive wall without ferromagnetism. The effect of the boronization on the hydrogen retention in the ferritic steel was studied with small test pieces exposed to JFT-2M plasmas.

In parallel with the AMTEX program, the advanced and basic study on H-mode plasmas and a Compact Toroid (CT) injection, etc. have been performed. The operational boundary of the ELMy H-mode and the High Recycling Steady (HRS) H-mode is found to exist at the normalized electron collisionality of about unity in the plasma edge region. In relation to the H-mode confinement, density and magnetic fluctuations have been measured. Characteristic fluctuations in a range of 20 – 300 kHz were observed, accompanied with the change in the H-mode property. The characteristics of the scrape-off and divertor plasma have been investigated with electrostatic probes and fast framing camera. It has been confirmed that the CT plasma can be transported with a curved drift tube,

keeping spheromac configuration.

A series of the experimental programs on the JFT-2M was completed at the end of this fiscal year after the 21 years operations since 1983, with the significant contribution to the controlled nuclear fusion research.

1. Advanced Material Tokamak Experiment (AMTEX) Program

The low activation ferritic steel is a leading candidate of structural material for the blanket of a fusion demonstration reactor (DEMO). However, it is ferromagnetic material and it easily rusts in the air. Thus the investigation of the compatibility of the ferritic steel with plasma is important and has been investigated on the JFT-2M tokamak step by step. Since the last year, the compatibility tests have been performed with the full covering ferritic inside wall (FIW). Engineering design of FIW was summarized in reference [1-1] and [1-2]. It had been demonstrated that both magnetic effect [1-3~1-6] and impurity desorption [1-3, 1-7, 1-8] is not so severe for relatively far wall position (distance of wall divided by plasma minor radius; $r_{wall}/a \sim 1.6$). Among the remaining subjects, the most important one in this year was the compatibility of the ferritic wall with high normalized beta plasma at closer wall position because high normalized beta (β_N) plasma of β_N = 3.5~5.5 realized by improving the beta limit due to the wall stabilization effect will be employed in a commercially attractive fusion reactor.

It was difficult to produce the plasma near the wall until last year because 1) graphite tiles were located at 7 cm from the surface of the FIW for the ripple loss measurement, 2) impurity release was significant when the plasma position was shifted outward. Before a start of the experiments, the graphite tiles were removed. The space in the weak field side was increased by ~2 cm. In addition, some of the in-vessel components were removed to reduce impurity release. Owing to this modification, the scan of plasma position was carried out with keeping low impurity level.

As for the operation scenario, similar procedure with high beta experiments in 2002 [1-3, 1-9] was used as shown in Fig. II.1-1. The neutral beam of co-direction to I_p (co-NB) was injected during current ramp-up phase (350 ms) and the neutral beam against I_p (ctr-NB) was injected from 450 ms. The toroidal field was typically 0.8 T, which is slightly lower than the typical operation region in 2002 (>1.0T). High beta collapse was observed reproducibly. The electron density was a key parameter. When the density is lower than n_e/n_{GW}~0.4, the large ELM was observed and the normalized beta was limited β_N <3. When the density is too high (n_e/n_{GW} >1), strong MHD instability was observed and the normalized beta did not increase well. In the optimum case in Fig. II.1-2, density is limited around n_e/n_{GW} ~0.4 in the co-NB phase. A transition to High Recycling Steady H-mode [1-9] occurs just after the ctr-NB injection and intensity of the soft X-ray emission increases sharply in the center code, and the plasma collapses finally.

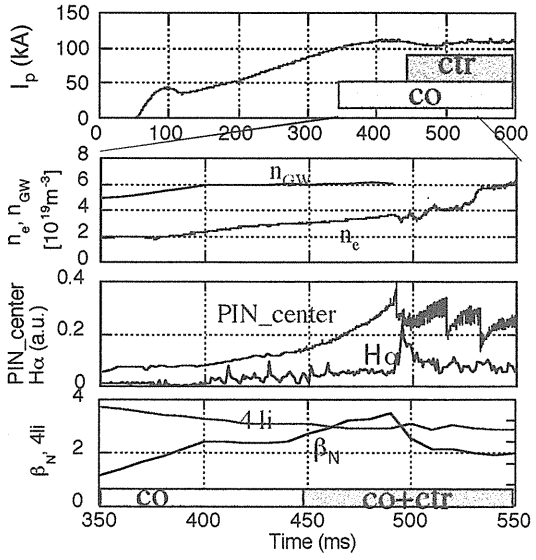

Fig. II.1-1 Typical time evolutions of the high beta

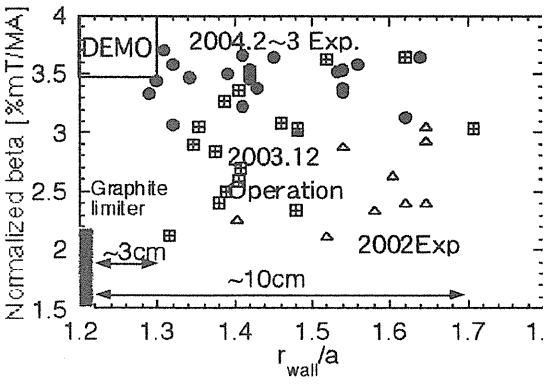

Fig. II.1-2 Maximum normalized beta against the normalized wall position.

The maximum β_N in a discharge is plotted as a function of normalized wall position in Fig. II.1-2. Due to the reduction of impurity release and the optimization of the operation scenario, the maximum beta value was improved gradually and it was not degraded even at r_{wall} /a ~1.3. Thus the operation region showing good compatibility was extended to higher normalized beta and closer wall position.

An important indicator of the wall stabilization effect is reduction of growth rate of MHD instability. Figure Fig. II.1-3 shows typical magnetic probe behavior for the close wall case (r_{wall} /a~1.4). Toroidal rotation was locked and the instability grew in a time

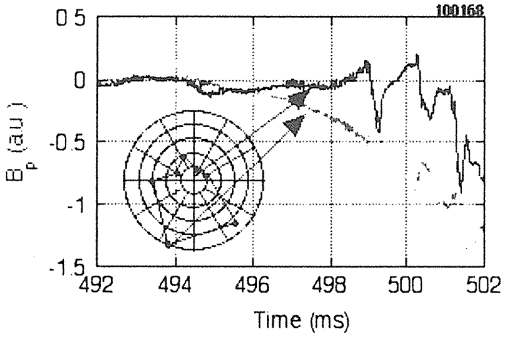

Fig. II.1-3 Typical B_q probe signal for close wall case. Toroidal mode number is estimated to be 1 by toroidally distributed B_q probes.

constant of ~1 ms. The toroidal mode number n is evaluated to be n=1 from the 8 B_θ probes distributed in the toroidal direction as shown in the figure. The position of the locking was reproducible, which means that the locking is related to external error field. The MHD behavior also depends strongly on electron density, wall condition, etc. Such n=1 mode was typically observed in closer wall case. On the other hand, fast disruptions without remarkable precursor were typically observed in far wall case. The time constant of the growth rate for close wall case was a few milliseconds, which is the same order as the wall time constant. Thus, the similar behavior as normal resistive wall without ferromagnetism was observed with the ferritic wall.

Plasma wall interaction is also one of the important issues for the application in DEMO. Since the last year, hydrogen retention characteristics have been investigated as a collaboration work with Hokkaido University [1-8, 1-10]. Small pieces of F82H (1 cm × 1 cm) were exposed to JFT-2M plasmas using sample load lock system located on a horizontal port (the sample was located at a few cm behind FIW). After the exposure, the samples were analyzed with the following methods at Hokkaido University; 1) Thermal Desorption Spectroscopy (TDS) for hydrogen retention, 2) Auger Electron Spectroscopy (AES) for atomic concentration and depth profile, and 3) Scanning Electron Microscope (SEM) and Atomic Force Microscope (AFM) for surface morphology. This year, the characteristics of boron films deposited on the F82H samples were mainly investigated. Figure II.1-4 shows outgas rate during TDS in the cases of with and without boron coating film. The deuterium atoms are desorbed in the form of D_2, HD, D_2O, C_xD_y in both cases. Deuterium concentration with boron film was almost 2 times as large as that without boron film. Required temperature for D release was higher with boron film. It is probably because the D atoms are well trapped by carbon atoms in the boron film. Helium glow discharges cause higher shift of desorption temperature,

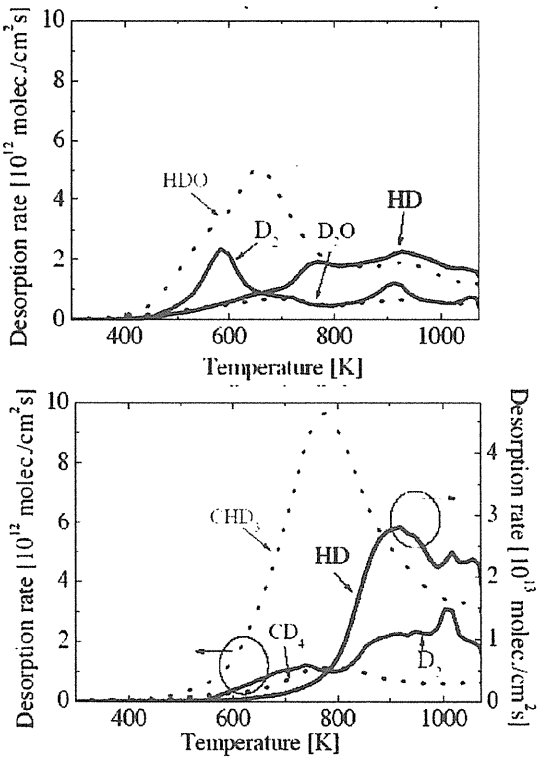

Fig. II.1-4 Thermal desorption spectra for the samples with and without boron films. Both were exposed for ~300 shots in JFT-2M tokamak.

namely, the weakly trapped D atoms were desorbed by the helium glow discharge.

The blistering was observed on F82H surface after exposure to the helium glow discharge. The blistering was relatively small for the samples with boron coating.

We have performed another collaboration work concerning with plasma wall interaction with TEXTOR. Limiter head made of F82H and SUS304 was fabricated and exposed to TEXTOR plasmas by using limiter lock system. Release of metal impurity was investigated mainly from the spectroscopic measurement. The results showed that the metal impurity desorption from F82H and SUS304 was comparable even for high heat load. Thus good prospects are given for applicability of F82H to the fusion reactor.

References

1-1 Suzuki, S., *et al.*, "Engineering Design in Installation of Fully Covering Ferritic Inside Wall on JFT-2M", to be published in *Proceedings of 20th IEEE/NPSS Symposium on Fusion Engineering* (2003).

1-2 Sato, M., *et al.*, "Design of fully covering ferritic inside wall to reduce toroidal ripple in JFT-2M", to be published in *Proceedings of 20th IEEE/NPSS Symposium on Fusion Engineering* (2003).

1-3 Tsuzuki, K., *et al.*, *Nucl. Fusion*, **43**, 1288 (2003).

1-4 Shinohara, K., *et al.*, *Nucl. Fusion*, **43**, 586 (2003).

1-5 Tsuzuki, K., *et al.*, "Investigation of compatibility of low activation ferritic steel with high performance plasma by full covering of inside vacuum vessel wall on JFT-2M", to be published in *J. Nucl. Mater.*

1-6 Bahktiari, M. *et al.*, *Phys. Plasma*, **10**, 3212 (2003).

1-7 Tsuzuki, K., *et al.*, *J. Nucl. Mater.*, **313-316**, 177 (2003).

1-8 Ogawa, H., *et al.*, "Impurity Release and Deuterium Retention Properties of Ferritic Steel Wall in JFT-2M", to be published in *J. Nucl. Mater.*

1-9 Kamiya, K., *et al.*, *Nucl. Fusion*, **43**, 1214 (2003).

1-10 Yamaguchi, K., *et al.*, *J. Vac. Soc. Jpn.*, **46**, 339 (2003).

2. High Performance Experiments

2.1 High Recycling Steady H-Mode

A new attractive operational regime without any large ELMs, "High Recycling Steady (HRS)" H-mode regime, has been discovered in the JFT-2M tokamak [2.1-1]. It is easily reproduced with the NB heating of any co-, counter- and balanced-injection under the wall

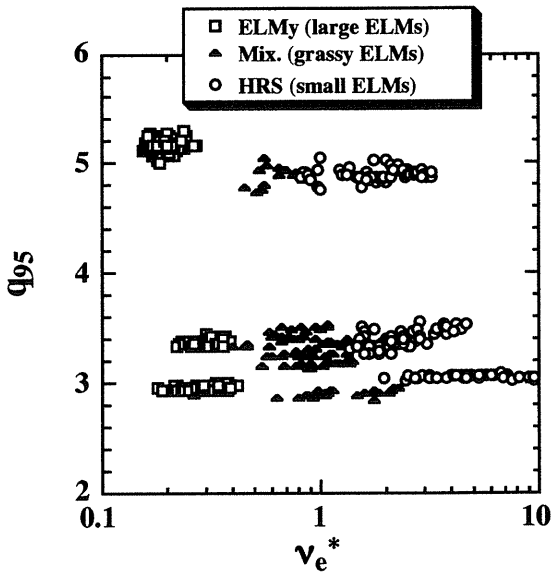

Fig.II.2.1-1 Plot of ELMy (squares), Mix. (triangles), and HRS (circles) operational regimes in safety factor at the 95% flux surface q_{95} versus edge normalized electron collisionality ν_e^*.

fueling from the boronized first wall. Recent experiments in the JFT-2M tokamak have concentrated on the studies of the access condition for the HRS H-mode regime in terms of the pedestal parameters. The HRS regime is more likely at the higher edge density and lower edge temperature, while the ELMy H-mode having large ELMs occurs at the lower edge density and higher edge temperature. It is found that the ELMy/HRS operational boundary exhibits at the normalized electron collisionality of $\nu_e^* \sim 1$ ($\propto q_{95} n_e / T_e^2$ at fixed shape) in the plasma edge region (r/a~0.85-0.9, typically), depending slightly on the safety factor at 95% flux surface q_{95}. A key feature of the HRS H-mode is the presence of the coherent magnetic fluctuations in the frequency range of the order of 10-100 kHz [2.1-2]. It is suggested that the edge MHD activities may keep an edge pressure below a certain level needed to induce a large ELM.

References

2.1-1 Kamiya, K., *et al.*, *Nucl. Fusion*, **43**, 1214 (2003).

2.1-2 Kamiya, K., *et al.*, *Plasma Phys. Control. Fusion*, **46**, A157 (2004).

2.2 Study of H-Mode Physics

The study of the stability/instabilities of the edge

transport barrier (ETB) made progress in the JFT-2M [2.2-1, 2.2-2, 2.2-3]. The instabilities at ETB seems to degrade the quality of the ETB.

After the application of the boronization and helium glow discharge cleaning (GDC) as the wall conditioning in JFT-2M, we get discharges with very low recycling just after the GDC. But after several discharges, the recycle rate increases, and fueling rate (deuterium gas puff) is decreased to almost zero during the neutral beam heating. In such conditions, we observe enhanced edge D_α intensity during the H-mode. The ETB shows typical successive time evolution, such as ELM-free state, H' state [2.2-4] and enhanced D_α state [2.2-5] (which is similar to the EDA-mode found in Alcator C-Mod) in D_α signal as shown in Fig.II.2.2-1. The transport, in another words, the quality of the ETB changes between these states.

During the H' state, a characteristic coherent density oscillation ~100 kHz was observed in the ETB by the reflectometer measurement [2.2-4]. Recently by the HIBP (Heavy Ion Beam Probe) measurement [2.2-6], coherent potential fluctuation as well as the density fluctuation localized in the ETB has been observed during the H' state with smaller radial electric field (~1/2) compared to the radial electric field during the ELM-free state [2.2-2]. Thus the instability seems to decrease the radial electric field and degrade the ETB.

Frequency spectrum of the instability as well as the background turbulent fluctuations in the ETB was measured by 38 GHz reflectometer (n_e~$1.8\times10^{19}m^{-3}$), magnetic probe and fast reciprocate probe. These spectra are characterized by the instabilities and turbulent fluctuations as follows; (1) ELM-free H-mode state: Both of the background density fluctuations and the electromagnetic fluctuations decrease much below ~100kHz. Coherent electrostatic multi-modes (high mode numbers) appear in 150~200 kHz region (one candidate may be the drift ballooning mode [2.2-7]). (2) H' state: An electrostatic quasi-coherent mode of ~80 kHz with full half width ~20 kHz appears first, then electromagnetic mode of ~300 kHz appears. (3) Enhanced D_α sate: The quasi-coherent electrostatic mode and background electrostatic turbulence becomes the same level. The width of the electromagnetic high frequency mode (300 kHz) increases. In this case, the improvement of the transport may due to the decrease (~1/2) in the low

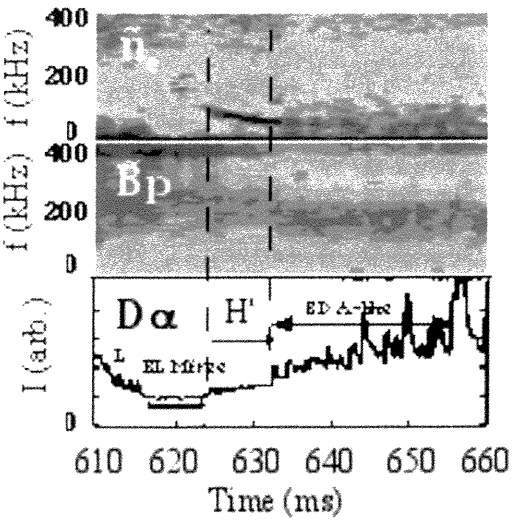

Fig.II.2.2-1 The spectrum of density fluctuations (n_e) by 38GHz reflectmeter, electromagnetic fluctuation by magnetic probe and intensity of the edge D_α signal during L-mode, ELM-free H-mode, H' mode and EDA-like mode during the neutral beam heating. Multi-modes and quasi-coherent modes are found in the ETB region.

frequency electrostatic turbulence (<40 kHz) compared to the turbulence level during the L-mode [2.2-2]. It is important to study these instabilities to control the ETB of the H-mode. Further study of plasma rotation may be important to identify the modes.

At last, in the course of the edge fluctuation study by the reciprocate electrostatic probe, we found a low frequency electrostatic mode of ~10 kHz [2.2-3] (One candidate is the geodesic acoustic mode (GAM)), which has a possibility to be used for the identification of the outermost magnetic surface.

References

2.2-1 Nagashima, Y., *et al.*, *Plasma. Phys. Control. Fusion* **46**, A381 (2004).

2.2-2 Hoshino, K., *et al.*, "On MHD Oscillations in High Beta H-mode Tokamak Plasma in JFT-2M", in *Proc. 13th Int. Toki. Conf. Toki, Japan 2003* , to be published in *J. Plasma Fusion Research* (2004).

2.2-3 Nagashima, Y., *Ph.D Tesis, The Univ. of Tokyo* (2004).

2.2-4 Shinohara, K., *et al.*, *J. Plasma Fusion Research* **74**, 607 (1998).

2.2-5 Kamiya, K., *et al.*, *Nucl, Fusion,* **43**, 1214 (2003).

2.2-6 Ido, T., *et al.*, *Phys. Rev. Lett.* **88**, 055006-1 (2002).

2.2-7 Hastie, R. J., *et al.*, *Phys. Plasmas,* **10**, 4405 (2003).

2.3 Study on Divertor and Scrape-Off Plasma

2.3.1 Structure of magnetic field line with the step probe

The magnetic surface is estimated by using the data of the magnetic probes, which are located on the FIW, however, the absolute location of the magnetic field line has some ambiguity. The absolute location of the separtrix is directly measured by the two systems of step probe, which consist of two long and short electrostatic double probes and are exactly located between the core and SOL plasma. The stationary positive and negative bias voltage are applied to the long and small pin, respectively. When the probe crosses the separatirx, the probe signal will respond to its location. The results indicate that the location of the separatrix is about 10 mm outward from those of the calculation by the equilibrium code (EQFIT), which is probable if we consider that the effect of the FIW may attract the field lines to the wall. On the other hand, we have observed that the correlation of the floating potential fluctuation disappears at the separatrix and this observation supports above result [2.3-1].

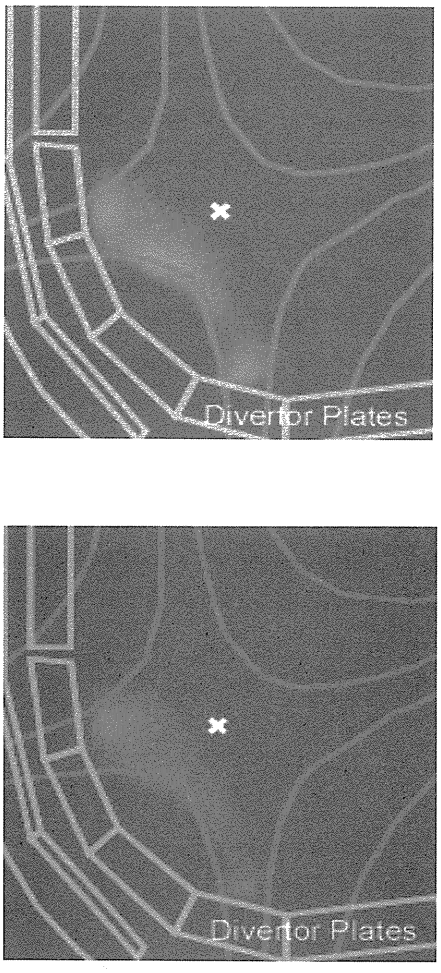

Fig.II.2.3-1 D_α emission from ELMy H-mode (top) and HRS H-mode (bottom).

2.3.2 Two dimensional D_α emission measurement by fast framing camera in ELMy H-mode and HRS H-mode

A comparison of divertor recycling between ELMy H-mode and HRS H-mode discharges [2.3-2] was made by fast measurement of two dimensional (2D) D_α (656 nm) emission profiles. It can be achieved by a new installation of fast framing camera system (30-40,500 frames/s) [2.3-3], which tangentially views the lower divertor region in this time.

Figure II.2.3-1 shows one frame picture during an ELM event (~1ms) (top) and HRS H-mode (bottom) taken at 4,500 frame/s. Plasma parameters are I_p =0.24-0.27 MA, B_T =1.6T, q_{95} =2.6-2.7, $\overline{n_{e\text{-target}}}$~$1.5\cdot10^{19}$ m^{-3}, balanced NBI of 1.0-1.4MW under the lower single null configuration. During an ELM event, D_α is strongly increased around the strike points on inner divertor plates. It indicates that the pulsed ELM heat and particle fluxes hit the divertor plates along the field line and the recycling is enhanced locally. Although D_α emission is also enhanced in the HRS H-mode, it is expanded uniformly in space. In this case, conditions of low temperature and high particle flux on the divertor plates were observed by measurement with the divertor electrostatic probes [2.3-4], indicating the recycling enhancement in the HRS H-mode due to the increase of particle loss dominantly.

2.3.3 Ion temperature measurement during ELMs

To characterize the pulsed ELM behavior in the SOL and divertor regions, the fast measurements of temperature, electron density, ion saturation current and floating/space potential in the SOL/divertor plasmas have been carried out by some unique electrostatic probes on JFT-2M. In this series of experiments, the ion temperature (T_i) is successfully measured for the first time during ELMs by the asymmetric double probe fixed in the SOL on the outer mid-plane. Figure II.2.3-2 shows the time evolutions of D_α emission on

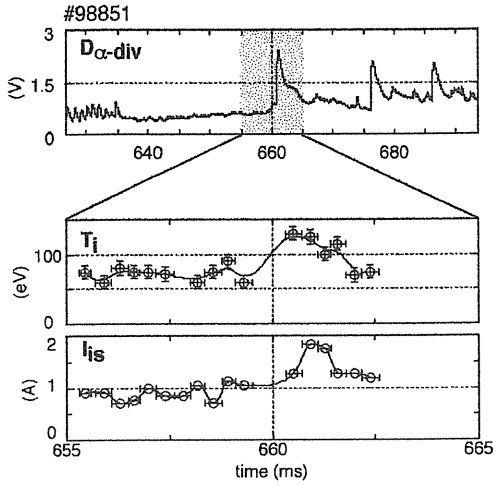

Fig.II.2.3-2 Increment of T_i and I_{is} during ELMs, where I_{is} is the ion saturation currents.

the divertor view line ($D_{\alpha\text{-div}}$) at the ELMy H-mode discharge, and T_i and ion saturation current (I_{is}) measured by the probe located at 3 cm outside the separatrix. By fast bias sweeping (250 μs), an evolution of T_i during an ELM event can be obtained and shows its twice increment by an ELM pulse. The ion saturation current also increases after a slight delay that for T_i. These results indicate that a remarkable radial loss of both heat and particles is brought at an ELM event. Further analysis is still going on to evaluate the quantity of heat and particle fluxes from the measured data.

References

2.3-1 Uehara, K., *et al.*, *Bull. Phys. Soc. Jpn.*, 31pYJ-2, 250 (2003).
2.3-2 Kamiya, K., *et al.*, *Nucl. Fusion*, **43**, 1214 (2003).
2.3-3 Kawashima, H., *et al.*, *Bull. J. Plasma Fusion*, 28aB12P, p.242 (2003).
2.3-4 Kawashima, H., *et al.*, *J. Nucl. Mater.*, **313-316**, 1338 (2003).

2.4 Compact Toroid Injection

Compact toroid (CT) injection is an advanced method of the particle fueling into the plasma, and is being investigated on JFT-2M with collaboration between JAERI and Himeji Institute of Technology (HIT), and Hokkaido University. Prior to the injection experiment in 2003, the CT transport along a curved drift tube was studied for improvement of the CT injection efficiency. The vertical injection eliminates the drug force due to the gradient in the magnetic pressure along the path [2.4-1] and thus would be more advantageous for fuelling to the fusion reactor. To apply a vertical injection, extension of a drift tube by the combination of a straight and a curved one on a CT injector was more flexible than the establishment of the injector in vertical direction for the design of the fusion reactor in the future. It was successfully demonstrated in the proof-of-principle experiments at HIT [2.4-2] that the CT plasma could transport along the curved drift tube without no degradation of CT plasma parameters such as velocity (v_{CT}), magnetic field strength (B_p, B_t), electron density (n_{CT}) and its life time (τ_{CT}). However, this experiment was carried out under the condition that v_{CT} was about 1/10 compared to that expected in a future reactor, there was a possibility that the CT plasma could be destroyed in the case of the high v_{CT} and high n_{CT} CT plasma. Therefore, it is necessary to test the CT injector, which can make higher performance CT plasmas.

Figure II.2.4-1 shows the schematic drawing of an experimental setup. A curved drift tubes with a 90° bend, a straight drift tube and a diagnostics vacuum chamber (FC) were connected at the outlet of the CT injector. This injector consisted with two co-axial plasma gun. Obtained CT plasma parameters were as follows; v_{CT} = 150~300 km/s and $n_e = (0.2 - 1)\times10^{22}$ m^{-3}. Details of this CT injector will be appeared in Ref. [2.4-3]. Figure II.2.4-2 shows radial profiles of poloidal (B_p) and toroidal (B_t) magnetic field in the CT plasma after passing the curved drift tube, which were measured by magnetic probe array at the FC. This profile was a typical spheromac configuration. This means that the CT plasma can transport along the curved drift tube in the case of the high performance CT plasma. However, the degradation of the CT

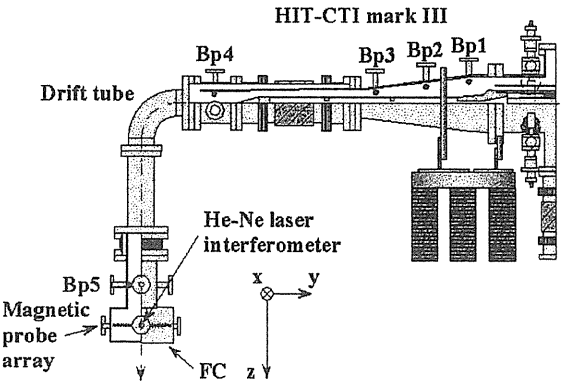

Fig. II.2.4-1 Experimental arrangement of CT injector with the curved drift tube.

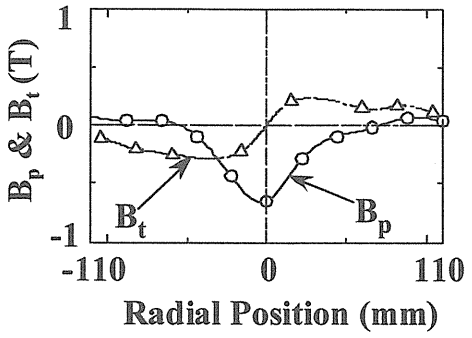

Fig. II.2.4-2 Radial profiles of B_p amd B_t in the plasma

velocity was observed, which was not observed in the previous experiments at HIT. This result has showed that the optimization of relation between CT velocity and the curvature drift tube is needed to apply to the vertical injection experiment.

References

2.4-1 Suzuki, Y., *et al.*, *Nucl. Fusion*, **41**, 873 (2001).

2.4-2 Fukumoto, N., *et al.*, "Development of curved drift tubes for improved Compact Toroid injection efficiency", to be published in *Nucl. Fusion.*

2.4-3 Fukumoto, N., *et al.*, "Characteristics of modified CT injector for JFT-2M", to be published in *Fusion Eng. and Design.*

3. Operation and Maintenance

3.1 Operation Status

In the original operation schedule of JFT-2M, there was no schedule to operate in FY2003 and planned to start operation again in FY2004. The original schedule, however, was changed in the middle of FY2003 and it had been decided that the JFT-2M would be shutdown after two weeks operation in February and March 2004. During the machine operation stop, the annual regular inspections in tokamak machine, additional heating system and power supply were carried out based on the rule and regulations in accordance with the original schedule.

During the operation stop a period, DC generator (DCG) was operated to maintain these function in the without a load every one month. In addition, the following works were carried out.

- Repair of the damaged parts inside the vacuum vessel in May and April 2003.
- Repair of the damaged protection plates at the insulated connection flanges inside the vacuum vessel in July and August 2003.

After completing the works, the vacuum vessel was pumped out and baked out for three weeks for the plasma experiments. During October and November 2003, the wall conditioning including baking, Taylor-type discharge cleaning at high temperature and boronization were carried out for 10 days. In January 2004, the same first wall conditioning operation was done again. After that, the final plasma experiments in JFT-2M were carried out in February and March 2004 for one week, respectively.

The main troubles of the equipment during the maintenance and the operation phase were listed as follows;

- Trouble of the controller of the vertical magnetic fields coil power supply, caused by electrical noise that appeared in the monitor of coil electric current.
- Differential electric current showing a sign of a flashover of the commutator of the DCG was detected. The flashover was avoided by grinding the surface of the commutator of the DCG precisely.
- Vacuum pumping system was stopped three times in the about same time. Which was caused by the noise that appeared in the controller.
- A water leakage from the ground electrode and the circuit board trouble for the control of the output of PreIonization Beam Injector (PIB) occured. The ground electrode and the circuit board were renewed for the repair.
- About Neutral Beam Injector (NBI), it was the movement defect of the control circuit board for the arc power supply of the B system, and another one a support structure short-circuited electrically. The control circuit board was replaced, and the support structure was replaced with the good material for the insulation.

The above-mentioned troubles were solved by the significant efforts although there were difficulties in finding their causes. After repairing, the plasma experiment operation in JFT-2M was carried out for one week in each of February and March. During the machine operation of JFT-2M, the following topics on the plasma diagnostic devices and the Compact Toroid (CT) injector were performed.

- Calibration of Heavy Ion Beam Probe (HIBP) under toroidal magnetic fields.

- Calibration of TeleVision Thomson Scattering （TVTS） under with and without plasma discharge.
- Experiment to evaluate the transport characteristic of CT in a curved injection pipe under the toroidal magnetic fields.

All experiments planned completed. In FY2003, the plasma discharges of 775 shots were carried out together with 137 hours of discharge cleanings, 99 shots of coil-energizing operations and two boronization operations for 13.2 hours. The experiment of JFT-2M operated for 21 years since the first plasma on April 27, 1983 was completed successfully. The final shot number of JFT-2M plasma discharge was 100,321. Participants in the final plasma experiment on March 19, 2003 are shown in Fig.II.3.1-1

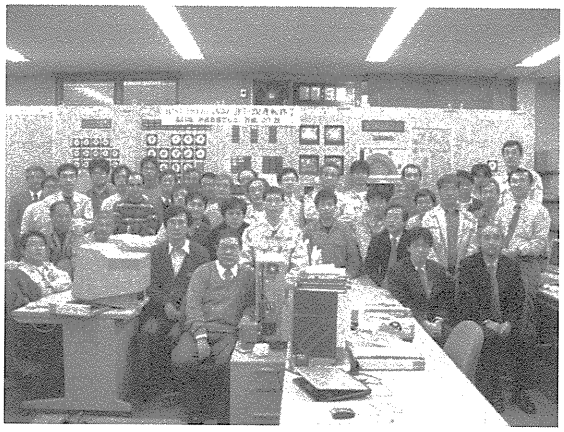

Fig.II.3.1-1 Participants in the final plasma experiment of JFT-2M on March 19. 2003

III. THEORY AND ANALYSIS

The principal objective of theoretical and analytical studies is to understand the physics of tokamak plasmas. Much progress was made in analyzing the H-mode power threshold, effects of anomalous transport phenomena on the neoclassical tearing modes (NTM), ECCD power necessary for NTM stabilization and resistive wall mode (RWM) and MHD ballooning mode stabilization by plasma rotation.

Progress has been made in the NEXT (Numerical EXperiment of Tokamak) project to investigate complex physical processes in transport and MHD phenomena. A mechanism of zonal flow saturation in the ion temperature gradient and electron temperature gradient (ITG and ETG) turbulence was examined in detail. The physics of fast magnetic reconnection events due to nonlinear destabilization of double tearing mode (DTM) was also studied by toroidal MHD simulations.

1. Confinement and Transport

1.1 Roles of Aspect Ratio, Absolute B and Effective Z for the H-mode Power Threshold

Analysis of ITPA H-mode power threshold database is advanced to study the roles of aspect ratio A, absolute magnetic field and effective charge number Z_{eff}. A new scaling expression for power threshold P_{thr} is presented;

$P_{thr,new} = 0.072\,|B|_{out}^{0.7} n_{20}^{0.7} S^{0.9}\,(Z_{eff}/2)^{0.7}\,F(A)^{\gamma}$,

where P is the power in MW, B the magnetic field in T, n_{20} the line averaged electron density in 10^{20}m^{-3}, and S the plasma surface area in m^2. Absolute B at the outer surface $|B|_{out}$ is used instead of the toroidal magnetic field B_t, and the observed dependence of P_{thr} on the plasma current I_p in low-A tokamaks is described without the explicit use of the I_p variable. This expression is naturally consistent with the full set of database. Clear and strong dependence on Z_{eff} is found; $P_{thr} \propto Z_{eff}^{0.7}$. Both the scattering nature in the data fitting and the "low-density anomaly" can be reduced. Nonlinear A dependence, $F(A) = 0.1A/\{1-(2/(1+A))^{0.5}\}$, is also suggested that is related to the untrapped-particle fraction. The dependence on this term is rather uncertain at present, $\gamma = 0\pm0.5$. Fig. III.1.1-1 shows that the new scaling fits well the experimental data better than the P_{thr0} scaling. Scattering in the data points is reduced from a previous scaling $P_{thr0} = 0.06\,B_t^{0.7} n_{20}^{0.7} S^{0.9}$ (the standard deviation σ is 0.35 for $\ln(P_{thr}/P_{thr0})$ and σ = 0.31 for $\ln(P_{thr}/P_{thr,new})$). Based on the new scaling, we estimate P_{thr} in ITER. The prediction of P_{thr} = 40 ~ 50 MW can be reliable if Z_{eff} will be kept ~2 [1.1-1].

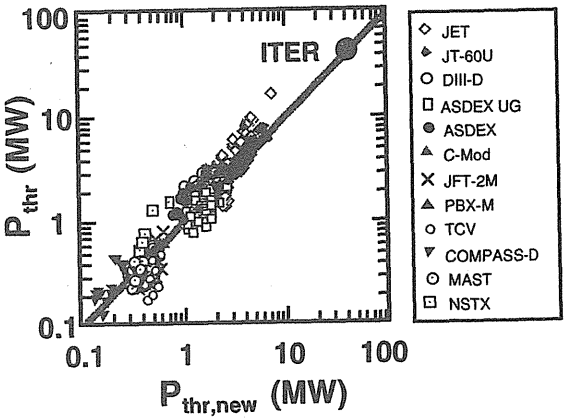

Fig. III.1.1-1 Comparison of experimental P_{thr} data with new scaling expression $P_{thr,new}$.

Reference

1.1-1 ITPA H-mode Power Threshold Database Working Group presented by Takizuka, T., *Plasma Phys. Control. Fusion*, **46**, A227 (2004).

2. MHD Stability

2.1 Improvement of the Modified Rutherford Equation of the Neoclassical Tearing Modes

The theory of the neoclassical tearing mode (NTM) based on the modified Rutherford equation has been investigated. Influence of anomalous perpendicular heat transport and anomalous perpendicular ion viscosity on the destabilizing term due to the bootstrap current of the modified Rutherford equation was studied theoretically. Importance of the two-fluid description of the perturbed plasma for evolution of the neoclassical islands was demonstrated. Series of different parallel transport mechanisms competitive to anomalous cross-island heat transport in formation of the perturbed electron and ion temperature profiles within the island are considered. The perturbed electron temperature profile is established in competition between anomalous perpendicular electron heat conduction and parallel electron heat convection or heat conduction. While in the formation of the ion perturbed temperature profile, perpendicular ion heat conduction is balanced by the parallel transports associated with ion inertia in an island. The heat balance equations were solved analytically to obtain perturbed electron and ion temperatures profiles. The partial contributions from the

electron and ion temperature perturbations in the bootstrap drive of the mode and magnetic curvature effect were then accounted in the transport threshold model of NTMs. It was found that the ion temperature contributes to weakening the bootstrap drive. It was also demonstrated that taking into account the curvature effect predicts notable improvement of NTM stability.[2.1-1, 2.1-2]

References

2.1-1 Mikhailovskii, A.B., et al., *Phys. Plasmas* **10**, 3790 (2003)

2.1-2 Konovalov, S.V., et al., *Phys. Lett. A.* **318**, 429 (2003).

2.2 Evaluation of ECCD Power Necessary for the Neoclassical Tearing Mode Stabilization

The ECCD power necessary for the neoclassical tearing mode (NTM) stabilization has been evaluated for ITER parameters by using the modified Rutherford equation coupled with the 1.5D transport code and the EC code. The EC current above a threshold value can fully stabilize the NTM (Fig. III.2.2-1 (a)). Here, the condition for the full stabilization is defined as $I_{EC} \geq I_{fs}$, where I_{fs} is the minimum EC current necessary for full stabilization. At the condition of $I_{EC}=I_{fs0}$ (Fig. III.2.2-1 (b)), there is a peak of dW/dt at $W=W_{ES}$ (~0.01), where I_{fs0} is I_{fs} for $W>W_{ES}$ and W_{ES} is an upper bound of W effective for early stabilization. If the island width is once larger than W_{ES}, the EC current of I_{fs0} is required to decrease the island width below W_{ES}, i.e., $I_{fs}=I_{fs0}$ for $W>W_{ES}$ (Fig. III.2.2-1 (c)). On the other hand, early EC injection to the growing island of $W<W_{ES}$ can reduce the necessary EC current, i.e., $I_{fs} < I_{fs0}$ for $W<W_{ES}$. The values of I_{fs0} and W_{ES} are important for the ECCD power evaluation. Necessary ECCD power on ITER is evaluated for parameters estimated from comparisons with JT-60U experiments. From I_{fs0} and EC code results, the EC power of about 30 MW is found to be sufficient for the simultaneous stabilization of both the m/n=3/2 and 2/1 mode NTM on ITER. The necessary ECCD power can be reduced to 12 MW when the EC current width is half decreased by optimizing injection angles of ECCD. Additionally, when the ECCD is injected to the growing island below W_{ES}~0.01 (~2cm), the required EC power can be lower than 12 MW[2.2-1,2.2-2].

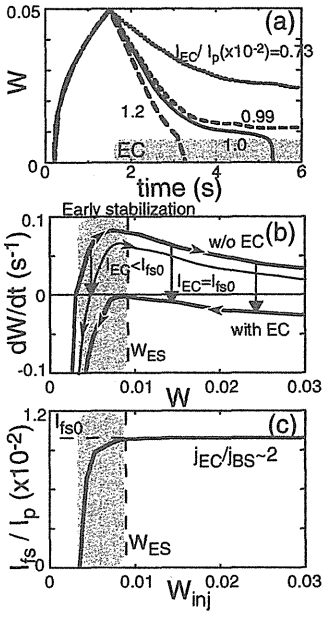

Fig.III.2.2-1 (a): Time evolution of m/n=3/2 mode NTM island width W for various values of EC current I_{EC}/I_p. (b): Growth rate dW/dt as a function of W with (lower broad and thin lines) and without (upper broad line) ECCD where I_{fs0}/I_p~0.01. (c): Necessary EC current for full stabilization, I_{fs}, as a function of island width at EC injection, W_{inj}.

References

2.2-1 Hayashi, N. et al., *J. Plasma Fusion Res.*, **80** 605 (2004).

2.2-2 Hayashi, N. et al., *Nucl. Fusion* **44** 477 (2004).

2.3 RWM Analyses with Ferromagnetic Wall and Plasma Flow Effects in a Tokamak

Stability analyses by linear MHD code including the effect of ferromagnetism using full set of resistive MHD equations find substantial influences of residual magnetism in passively stabilizing wall on ideal MHD stability, even though the ferromagnetism is sufficiently saturated at a high toroidal field, and shows the deterioration of the beta limit. The toroidal flow effect on the resistive wall mode with and without the effect of ferromagnetism is investigated, and ferromagnetic wall effect on the stability window opened by both effects of the toroidal plasma flow and the plasma dissipation will also be investigated [2.3-1].

Reference

2.3-1 Kurita, G., Tuda, T., Azumi, M. et al., "RWM Analyses with Ferromagnetic Wall and Plasma Flow Effects in a Tokamak ", *45th APS Annual Meeting of the Division*

of Plasma Physics, October 27-31 Albuquerque, New Mexico (2003).

2.4 Rotational Stabilization of High-n Ballooning Modes in Tokamaks

Linear stability of high-n (n: toroidal mode number) ballooning modes in toroidally rotating tokamaks has been studied via ideal magnetohydrodynamic (MHD) model. We have found numerically that toroidal rotation shear damps perturbation energy of ballooning modes even in a dissipationless system: a damping phase alternates with an exponentially growing phase in the time evolution and the mode is stabilized when the damping dominates the growth. As schematically shown in Fig. III.2.4-1, geometrical effects such as D-shaping of plasma cross-section reduces (1) instantaneous growth rate and (2) duration of the exponentially growing phase. Therefore, D-shaping cooperates with the toroidal rotation shear to provide efficient stabilization of the mode [2.4-1].

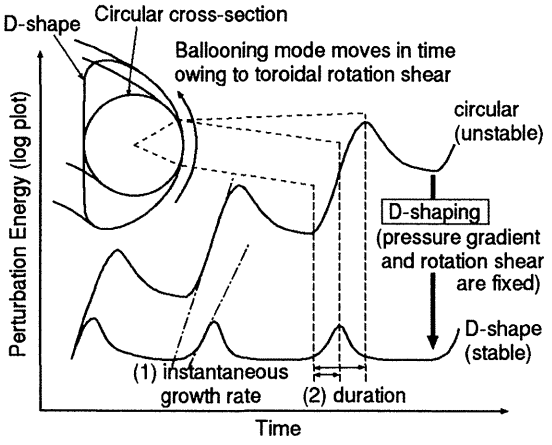

Fig. III.2.4-1 Toroidal rotation shear damps perturbation energy of ballooning modes; a damping phase alternates with an exponentially growing phase in the time evolution. D-shaping of plasma cross section reduces not only (1)instantaneous growth rate but also (2)duration of the exponentially growing phases.

In the H-mode pedestal region of a static or a toroidally rotating tokamak, we have found that the separatrix or the X-point affects the ballooning stability only in a thin layer in the pedestal region when the plasma cross section is D-shaped. Therefore, D-shaping is the dominant geometrical effect rather than the X-point in a present-day tokamak[2.4-2].

References

2.4-1 Furukawa, M., Tokuda, S. and Wakatani, M., *Nucl. Fusion* **43**, 425 (2003).

2.3-2 Furukawa, M., Tokuda, S. and Wakatani, M., *Plasma Phys. Control. Fusion* **46**, 409 (2004).

3. Numerical Experiment of Tokamak (NEXT)

3.1 Gyrokinetic Simulations of Tokamak Micro-turbulence including Kinetic Electron Effects

In order to study the ion temperature gradient driven trapped electron mode (ITG-TEM) turbulence in tokamak plasmas, a global gyrokinetic toroidal particle code for a 3-dimensional nonlinear turbulence simulation (GT3D) has been extended including kinetic trapped electron models [3.1-1,2]. In this code, a kinetic trapped electron response is solved using drift-kinetic and bounce-averaged trapped electron models [3.1-2]. A new bounce-averaged kinetic trapped electron model enables order of magnitude low cost ITG-TEM calculations. A gyrokinetic field solver with a Pade approximation for the ion polarization density is developed to capture a short wavelength unstable region. In the linear calculations, basic properties of ITG-TEM modes are confirmed. Adding trapped electrons not only increases the growth rate of the ITG mode, but also produces another unstable electron mode, the TEM mode, which is unstable even at $\eta_i \sim 0$, $\eta_i \equiv \partial \ln T_i / \partial \ln n$. The dominant mode changes from the ITG mode to the TEM mode depending on k_θ and η_i. In the linear benchmark calculations using Cyclone base case parameters, frequencies and growth rates obtained from GT3D, GTC and FULL codes show reasonable quantitative agreement [3.1-3].

References

3.1-1 Idomura, Y. , Tokuda, S. and Kishimoto, Y. , "Global Gyrokinetic Simulation of Ion Temperature Gradient Driven Turbulence in Plasmas with Canonical Maxwellian Distribution", *18th International Conference on Numerical Simulation of Plasmas, 7-10 September 2003, Cape Cod, Massachusetts.*

3.1-2 Idomura, Y., Tokuda, S. and Kishimoto, Y., "Gyrokinetic Simulations of Tokamak Micro-Turbulence including Kinetic Electron Effects", *J. Plasma Fusion Res.* **SERIES** 6, in print (2004).

3.1-3 Rewoldt, G., Lin, Z. and Idomura, Y., "Linear Comparisons of GTC, GT3D, and FULL with Trapped Electrons", *45th APS Annual Meeting of the Division of Plasma Physics, October 27-31 Albuquerque, New Mexico.*

3.2 Zonal Flow Dynamics in Gyro-fluid ETG Turbulence and its Statistical Characteristics

The amplitude level of zonal flow is important in suppressing turbulent transport. The saturation of

enhanced zonal flows in slab electron temperature gradient (ETG) turbulence with weak magnetic shear was investigated numerically. Based on gyrofluid ETG simulations, we have found that the zonal flow is drastically enhanced in high pressure gradient regime when the magnetic shear is weak (s ～0.1)[3.2-1]. In order to investigate the turbulent characteristics dominated by such a strong zonal flow, we performed the time-frequency wavelet analyses of turbulent fluctuations. As the result, we found a low frequency Kelvin-Helmholtz (KH) instability as seen in Fig. III.3.2-1, which is considered to be a plausible damping mechanism of the enhanced zonal flows [3.2-2]. Results seem to suggest a possibility of turbulence transition from the ETG-dominated one to the KH-dominated one due to the zonal flow dynamics in weak shear plasmas.

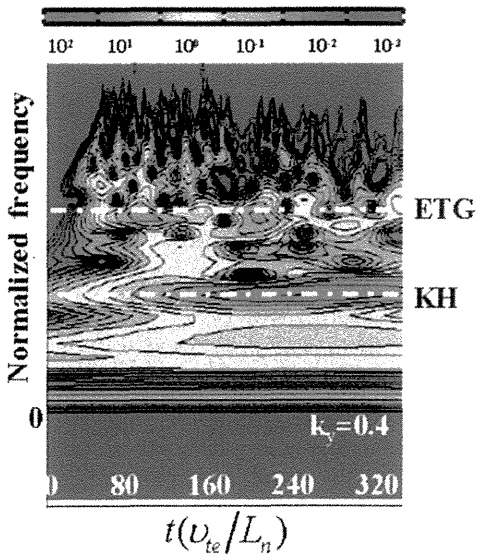

Fig. III.3.2-1 Time-frequency wavelet energy spectra of the turbulent electrostatic potential in zonal flow dominated ETG turbulence. It shows the excitation of a low frequency fluctuation (KH mode) at the end of the fast growing phase of zonal flows.

Enhanced zonal flow dynamics may affect the scaling of electron transport in toroidal ETG turbulence. Electromagnetic ETG simulations showed that while the Ohkawa's scaling of anomalous electron transport with beta, $\chi_e \propto 1/\beta_e$, is reproduced in the moderate shear plasma, the finite β_e effect may reverse the Ohkawa's scaling in weak shear ETG turbulence due to the reduction of zonal flow generation by the magnetic Reynolds stress. [3.2-1,2]. Further, it was shown that the toroidal coupling enhances the zonal flow while it destabilizes the ETG mode. Hence, the electron transport seems insensitive to the toroidicity in the weak shear plasma due to the complex destabilizing and stabilizing competitions.

Statistical description of turbulence provides a new insight to understand the transport properties in a dynamic plasma system, such as intermittency and degree of freedom of the dynamical system. Thus, statistical characteristics were analyzed against the zonal flow state, above-mentioned ETG simulation results, for different electron temperature gradient and magnetic shear. It was found that the formation of coherent structure due to zonal flows could be distinguished from the turbulent structure by investigating the correlation dimension of fluctuations because the zonal flows results in the reduction of the correlation dimension to less than 3 from around 8 in

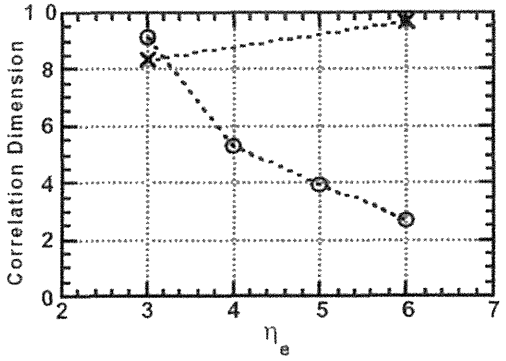

Fig. III.3.2-2 Correlation dimension of poloidal electrostatic field in weak shear ($\hat{s} = 0.1$) ETG turbulence with zonal flow (circles) and without zonal flow (crosses).

highly turbulent plasmas, as shown in Fig. III.3.2-2 [3.2-3]. It was also confirmed that the deviation of probability density function (PDF) from the Gaussian distribution, namely, the enhancement of PDF tails over those of a Gaussian PDF, means the large intermittency of heat flux.

References

3.2-1 Li, J. and Kishimoto, Y., *Phys. Plasmas* **11**, 1493 (2004).

3.2-2 Li, J. Kishimoto, Y., et al., "Saturation of Zonal Flow in Gyrofluid Simulations of Electron Temperature Gradient Turbulence", *J. Plasma Fusion Res.* **SERIES 6**, in print (2004).

3.2-3 Matsumoto, T., Kishimoto, Y. and Li, J., "Statistical Characteristics from Gyro-Fluid Transport Simulation", *J. Plasma Fusion Res.* **SERIES 6**, in print (2004).

3.3 Global Characteristics of Zonal Flows Generated by ITG Turbulence

Global structure of zonal flows driven by ion temperature gradient (ITG) driven turbulence in tokamak plasmas was investigated using a global electromagnetic Landau fluid code [3.3-1,2]. The simulation results showed that the safety factor q changes the zonal flow behavior in tokamak plasmas. In a low q region (q~1) the zonal flows are stationary, and the zonal flows in a high q region are oscillatory because of the coupling with (m, n)=(1,0) pressure perturbations, where m and n are poloidal and toroidal mode numbers, respectively (Fig. III.3.3-1).

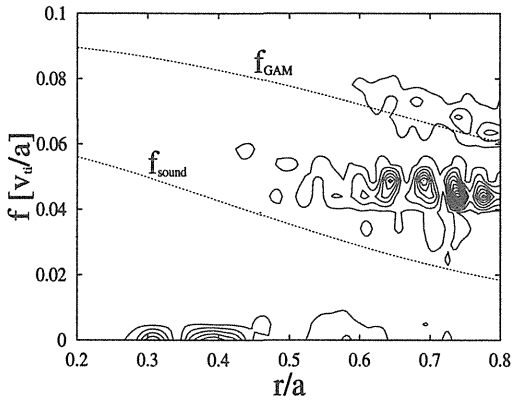

Fig. III.3.3-1 Radial variation of zonal flow frequency in the case with positive magnetic shear. In an inner low q region, the zonal flows have peaks around zero. On the other hand, the zonal flows in an outer high q region have finite frequency between the GAM frequency f_{GAM} and the sound frequency f_{sound}.

Since the coupling between the zonal flows and the (1,0) pressure perturbations is due to a geodesic curvature, the oscillation of the zonal flows with (1,0) pressure perturbations is called the geodesic acoustic mode (GAM). We found that the difference of the zonal flow behavior divides the plasma into the zonal flow dominant region with the stationary zonal flows and the turbulent region with the oscillatory zonal flows. While the stationary zonal flows suppress the turbulence effectively, the oscillatory zonal flows cannot overwhelm the turbulence due to the energy loop between the zonal flows and the ITG turbulence. The zonal flow energy supplied from the turbulence via the Reynolds stress goes to the (1,0) pressure perturbations due to the geodesic curvature. The energy of the (1,0) pressure perturbations in the high q region returns to the turbulence by nonlinear effect.

References

3.3-1 Miyato, N., Li, J. and Kishimoto, Y., "Global Simulation of Electromagnetic Microturbulence Based on Reduced Landau Fluid Model", *45th APS Annual Meeting of the Division of Plasma Physics, October 27-31 Albuquerque, New Mexico* (2003).

3.3-2 Miyato, N., Li, J. and Kishimoto Y., "Electromagnetic Effect on Turbulent Transport in Tokamak Based on Landau Fluid Global Simulation", *J. Plasma Fusion Res.* **SERIES 6**, in print (2004).

3.4 Formation of Local Current Structure and Explosive Phenomena

The explosive phenomenon caused by the local current structure (current point) formation by nonlinear simulations of the double tearing mode (DTM) has been

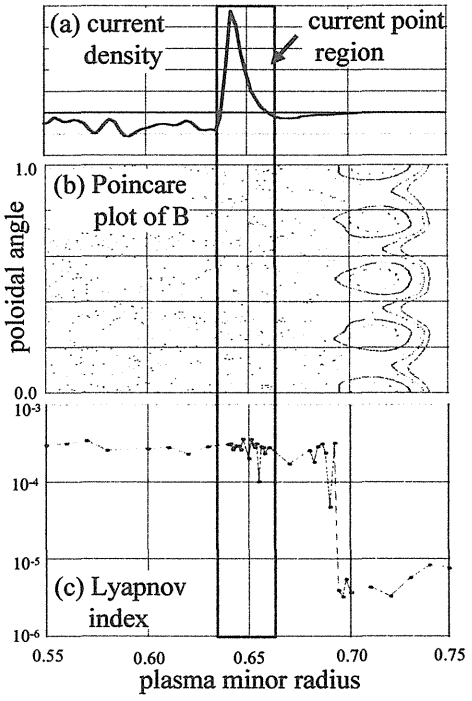

Fig. III.3.4-1 Radial profiles of (a) current density, (b) Poincare plot and (c) Lyapnov index around the reconnection region obtained by toroidal MHD simulation.

reported. Detailed process is investigated and also these results are confirmed by toroidal MHD simulations [3.4-1]. It is shown that the inverse aspect ratio of a current structure increases as the magnetic flux is pushed into the reconnection region and the explosive growth of DTM is triggered. This process is different from the ordinary reconnection theories used for fusion and space plasmas. During the increasing phase of the inverse aspect ratio, current density also increases as

almost inversely proportional to the resistivity. Because of this feature, the growth rate in the explosive phase shows the weak dependence on the resistivity. These basic features are obtained in MHD simulations with the helical symmetry. In order to investigate the toroidal coupling effects, which can cause the harmonics with the different helicity and make the magnetic fields stochastic, toroidal MHD simulations are carried out. As shown in Fig.III.3.4-1, a current point is formed under the stochastic magnetic fields. This result shows that a current point formation and explosive growth of DTM is a robust phenomenon.

References

3.4-1 Ishii, Y., Azumi, M. and Kishimoto, Y., *Physics of Plasmas* **10** 3512 (2003).

IV. TECHNOLOGY DEVELOPMENT

1. Superconducting Magnet

Superconducting magnets can generate a high magnetic field in both of steady-state and pulsed modes, and therefore, they are indispensable components in a tokamak fusion reactor, such as the ITER. JAERI has developed superconducting magnet technology required for ITER construction through the ITER Engineering Design Activity (EDA) started in 1992. In the EDA, a Central Solenoid (CS) model coil and a Toroidal Field (TF) model coil were developed and tested, and all of their development goals have been achieved, including a stable operation at the nominal magnetic field of 13 T with the nominal operating current of 46 kA. Detailed investigation of the test results, however, indicated that there was an unexpected decrease in the critical current performance of the conductors used in the model coils when a large current, such as more than 40 kA, was put in the conductors under high magnetic fields.

In 2003, JAERI has studied the cause for the decrease in the critical current with an aim to optimize the design of the ITER conductor. In line with this design optimization, an enhancement in the critical current of Nb_3Sn strand was performed based on the recent progress in superconductor technology which had been triggered by the ITER EDA. In addition, detailed characterization of structural materials to be used in the ITER magnet has been performed in order to validate design basis and to define detailed technical specifications. The following sections describe major achievements in these research activities.

1.1 Effect of Large Electromagnetic Force on ITER Superconductors

The superconductor of the CS model coil has a cable composed of about 1,000 superconducting strands (strand dia. 0.8 mm) enclosed in a metal conduit. The superconducting performance of a strand or conductor can be characterized by a critical current and n value (refer to note below), and these parameters were evaluated in detail in the model coil experiment. Results have shown that measured critical current was smaller than expected (strand critical current x number of strands) and n value of the conductor was also lower than that of the strand [1.1-1, 1.1-2]. This degradation in the superconducting performance was a new finding that appears only in the large-current high-filed conductors and could not be explained with the knowledge at that time. JAERI has then performed a study to identify a cause for this degradation as follows [1.1-3, 1.1-4].

Since strands in the cable are twisted, each strand is mechanically supported by the neighboring strands at an interval determined by a cable twist pitch. Between two supporting points, a strand is free to move under a transverse electromagnetic force, which may cause periodic and localized deformation of the strand along its length as shown in Fig.IV.1.1-1. The performance of a Nb_3Sn strand is easily degrades due to a mechanical strain, and therefore, this deformation was considered to be a cause for the degradation.

In order to verify the above consideration and to quantitatively evaluate the effect of the deformation, JAERI developed an apparatus which can simulate this periodical deformation by artificially applying a transverse load on the strand. In order to determine the load to be applied to the strands, force distributions inside the cable was estimated as follows. About 1,000 strands exist in the conductor, and each strand is supported by the neighboring strands as mentioned above and by friction force between strands as well. The friction force is small compared to the electromagnetic force and can therefore be neglected. In this case, electromagnetic force acting on the strands can be treated as an isotropic load equivalent to a hydrostatic pressure. The force f [N/m], which single

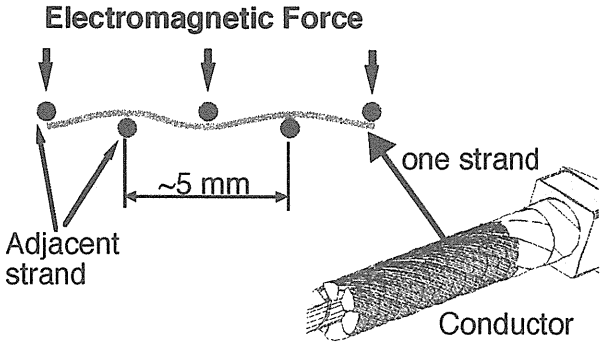

Fig.IV.1.1-1 Periodic and local deformation of a strand in the cable due to transverse electromagnetic force.

n value: When the current (I) of a superconductor increased, gradual transition from a superconducting state to a normal state occurs, resulting in the appearance and increase of normal voltage (V). The relation between V and I is empirically formulated as $V \propto (I/I_c)^n$ using a critical current (I_c) and n value. The larger n value represents the better superconducting performance.

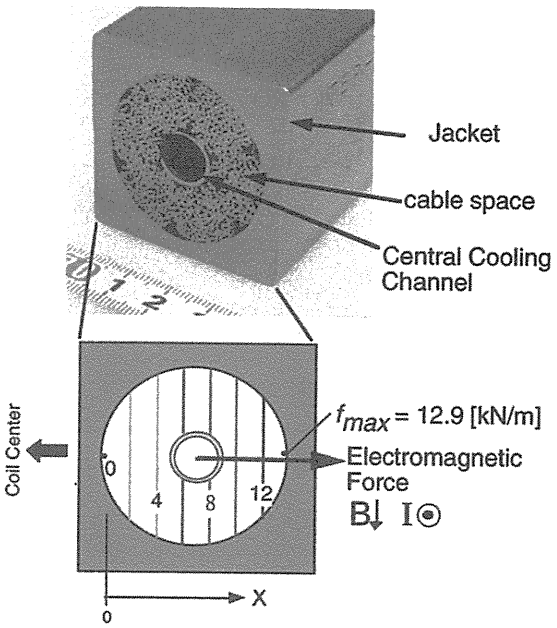

Fig.IV.1.1-2 The appearance of the conductor and distribution of transverse electromagnetic force in the cross section of the conductor. The unit of contour lines is kN/m.

strand inside the cable receives, can be formulated as follows,

$$f = 2rx\frac{IB}{\pi R^2} \qquad (1.1\text{-}1)$$

Where r, R, I, and B represent strand radius, conductor cross sectional radius, conductor current and magnetic field. x represents the coordinate of the strand location as shown in Fig.IV.1.1-2. In case of the CS model coil conductor, using the values of I=40[kA], B=13[T], R=19.25[mm] and r=0.405[mm], we get f=3.61x10^5 x [N/m] and its distribution is shown in Fig.IV.1.1-2 as contour line.

The critical current and n value of a Nb_3Sn strand were then measured by the apparatus with applying the load evaluated above. Results are shown in Fig.IV.1.1-3. Critical current decreases as the load increases and n value decreases greatly even at a small load. By this experiment it was demonstrated for the first time that the transverse electromagnetic force acting on a strand will cause degradation in superconducting performance of the high-field large-current conductor.

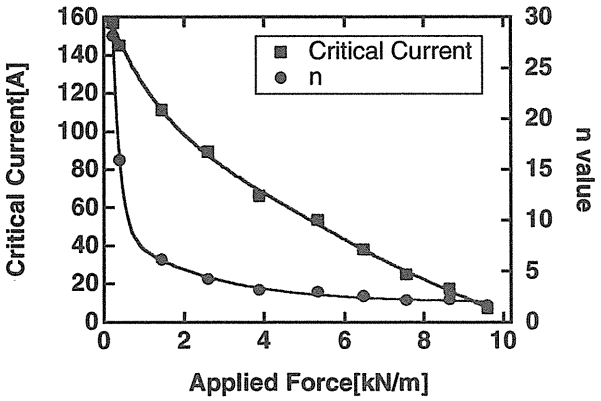

Fig.IV.1.1-3 Influence of localized periodical deformation of the critical current and n value.

References

1.1-1 Okuno, K., "Progress in the Superconducting Magnet Technology through the ITER CS Model Coil Program," to be published in *IEEE Trans. ASC* (MT18).

1.1-2 Okuno, K., *et al.*, "Test of the Nb_3Al Insert and ITER Central Solenoid Model Coil," *IEEE Trans. ASC*, 13, 1437 (2003).

1.1-3 Nunoya, *et al.*, "Evaluation Method of Critical Current and Sharing Temperature for Large-current Cable-in-conduit Conductors," *IEEE Trans. ASC*, 13, 1404 (2003).

1.1-4 Nunoya, Y., *et al.*, "Experimental Investigation on the Effect of Transverse Electromagnetic Force on the V-T Curve of the CIC Conductor," to be published in *IEEE Trans. ASC* (MT18).

1.2 Development of Advanced Bronze-processed Nb_3Sn Strand

Significant progress has been achieved in the performance of Nb_3Sn strands owing to the activities during the ITER EDA. The averaged performance of Nb_3Sn strands used in the CS model coil has reached a critical current density (J_c) of 640 A/mm^2 (at 12 T and 4.2 K) and a hysteresis loss of 110 mJ/cm^3 (at 4.2 K for a cycle of 3-T amplitude). However, as a result of the design optimization of the ITER conductor based on the model coil test results, the enhancement of Nb_3Sn strand J_c up to 700 A/mm^2 was required to compensate the degradation mentioned in the previous section. To achieve this J_c in a bronze processed Nb_3Sn strand, the following two methods were attempted: 1) increase of a tin content in bronze, and 2) modification of the temperature pattern of a heat treatment for Nb_3Sn formation.

Regarding the first method, a major concern was that higher tin content in bronze might cause strand breakage during fabrication, which set a limit of tin content at 14%(in weight) in the model coil conductors. Therefore, trial fabrication of Nb_3Sn strand using 15% and 16% tin contents in bronze was performed in order

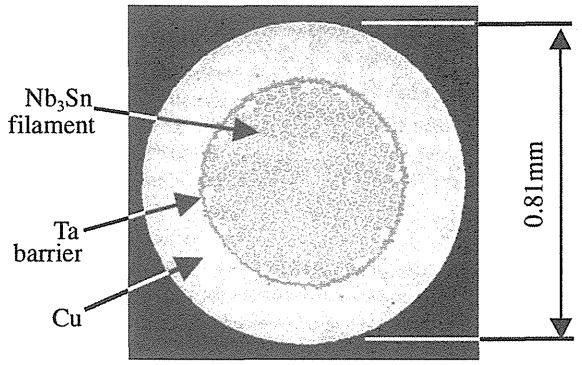

Fig.IV.1.2-1 Cross sectional view of Nb_3Sn strand made of bronze with tin content of 16% (in weight).

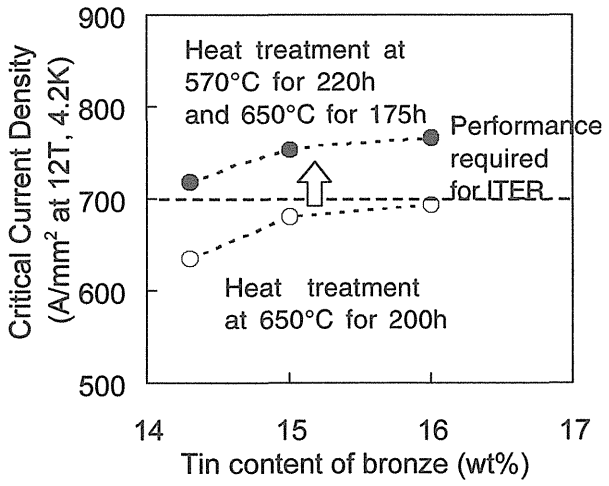

Fig.IV.1.2-2 Improvement of the critical current of bronze processed Nb_3Sn strand by increasing tin content of bronze and modification of heat treatment pattern.

to confirm productivity and performance. Cross sectional view of the strand manufactured in this trial is shown in Fig.IV.1.2-1. No breakage occurred during the fabrication. Critical current density of the strand was improved up to 690 A/mm^2 under the heat treatment in a conventional pattern (650°C x 200h). The second method was planned since additional heat treatment at an intermediate temperature prior to the main heating at 650°C provides a possibility to obtain higher J_c by making a grain size of Nb_3Sn smaller. Measured critical current is shown in Fig.IV.1.2-2 for the strands having tin content of 14% to 16% which were heat treated in two steps at 570°C for 220 hours and at 650°C for 175 hours. This figure indicates that the critical current has increased by 11% from that heat treated with the conventional pattern. From these results, we concluded that a bronze processed Nb_3Sn strand can

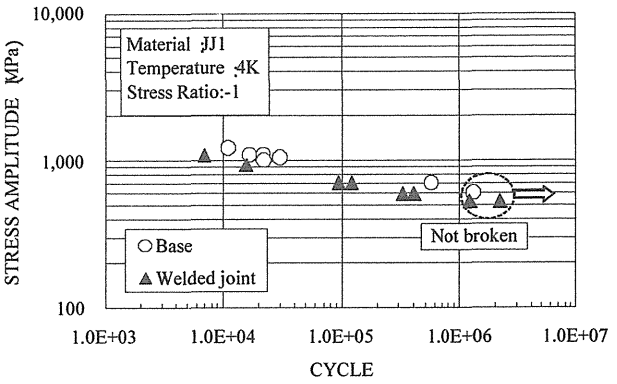

Fig.IV.1.3-1 Fatigue (S-N) characteristics of JJ1 base metal and welded joint at 4 K.

satisfy the new ITER requirement on J_c of more than 700 A/mm^2 at 12 T.

1.3 Development of Cryogenic Structure Materials for ITER Superconducting Magnets

A new cryogenic structural material JJ1 (0.03C - 10Mn - 12Cr - 12Ni - 5Mo - 0.24N) has been developed by a collaboration between JAERI and Japan Steel Works. JJ1 will be applied to the high stress portion of the ITER TF coil case, whereas SS316LN (0.03C - 2Mn - 17Cr - 12Ni - 2Mo - 0.16N) will be applied to the low stress portion. Detailed characterization was performed on these materials to validate the design of the TF coil case.

Fatigue characteristics of JJ1 base metal and welded joint have been measured at liquid helium temperature. Figure IV.1.3-1 shows fatigue curve (S-N curve) obtained by strain controlled tension-compression fatigue tests. Measurements were performed in the range from 10,000 to 1,200,000 cycles, and the test was terminated at 1,200,000 cycles, if a sample was not broken, which corresponds to the design condition defined by the operation cycles of the TF coil case (60,000 stress cycles) with a design margin of 20 [1.3-1]. The result justifies the design basis of the TF coil case.

Hot rolled plates of SS316LN having a high nitrogen content (N>0.16%) with a thickness up to 200mm will be used in the TF coil case. There was no production experience of a SS316 plate with a thickness of more than 100 mm. So as to confirm the mechanical properties of such a thick plate, a SS316LN hot rolled plate with a thickness of 200 mm was manufactured and mechanical tests were performed at 4 K. As a result, 0.2%-offset yield strength was

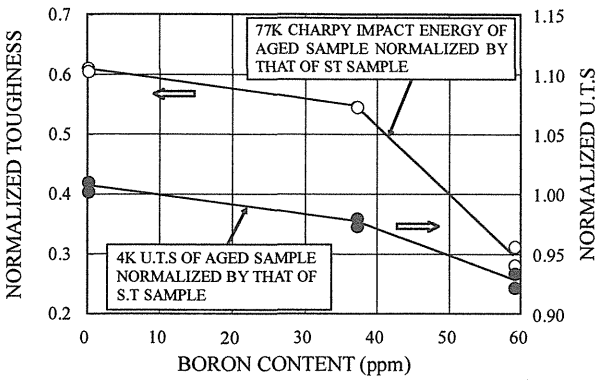

Fig.IV.1.3-2 Degradation of toughness and ultimate tensile strength (U.T.S.) of JK2LB after heat treatment (aged). Vertical axis indicates a ratio of values between after and before heat treatment.

measured to be more than 850MPa, which exceeds the required value of 750MPa, and its strength distribution along the through-thickness direction was confirmed to be uniform. Thus, the 200-mm-thick SS316LN plate was qualified for the use in the TF coil case.

JAERI has also developed high manganese stainless steel containing very small quantity of boron, named JK2LB (0.03C - 22Mn- 13Cr -9Ni -1Mo - 0.2N - 0.003B), in collaboration with Kobe Steel Ltd. [1.3-2]. This material can withstand the heat treatment for Nb_3Sn formation, and is therefore applied to the ITER conductor. The addition of boron is indispensable to improve productivity, but the effect of boron on mechanical properties at cryogenic temperature was not known. In addition, carbon promotes degradation due to embitterment during the heat treatment and its content had to be limited. Because of these, an optimization of chemical composition of JK2LB has been performed together with the assessment of the mechanical properties. As an example of the results, degradation ratios of toughness and tensile strength of JK2LB after heat treatment are shown in Fig.IV.1.3-2 as a function of boron content. It is found that the toughness and tensile strengths decrease as boron content increases, and the degradation become significantly large in the range of boron content of more than 40 ppm. On the other hand, the degradation of toughness of JK2LB with carbon content of 200 ppm is smaller than that with 500ppm. From these results, we have concluded that the upper limits of boron and carbon contents to be 40 ppm and 300 ppm, respectively.

References

1.3-1 Hamada, K. *et al.* "Fatigue Assessment of the ITER TF Coil Case based on JJ1 Fatigue Tests," to be published in *Proceedings of the 23rd Symposium of Fusion Technology* (2004).

1.3-2 Nakajima, H., *et al.* "Development of Low Carbon and Boron Added 22Mn-13Cr-9Ni-1Mo-0.24N Steel (JK2LB) for Jacket which Undergoes Nb_3Sn Heat Treatment," to be published in *IEEE Trans. ASC* (MT-18).

2. Neutral Beam Injection Heating

2.1 1-MeV Class Beam Acceleration [2.1-1]

One of the key components of the ITER Neutral Beam (NB) system is a high energy and high current beam source, which is designed to produce 1-MeV, 40-A D^- ion beams for 16.5-MW neutral beam injection per module. Its R&D is in progress at present toward the demonstration of 1 A class H^- ion acceleration at a current density of 200 A/m^2 up to 1 MeV as a "Proof-of-Principle (PoP)" of the ITER accelerator.

In conventional accelerators, pressurized SF_6 gas is used for high voltage insulation. However, in the ITER NB system, it was clarified that the gas insulated beam source (GIBS) cannot be adopted because the Radiation-Induced Conductivity (RIC) of the gas causes a power loss of MW order. To avoid this problem, a Vacuum Insulated Beam Source (VIBS), where the whole beam source is immersed in vacuum, has been developed (Fig.IV.2.1-1). To develop the VIBS, there were several subjects to be confirmed and improved as follows; 1) Voltage holding of long vacuum gap: The FRP (fiber reinforced plastic) insulator stack, as a vacuum boundary, surrounds the accelerator. There is a vacuum gap of 50 mm wide all around the accelerator to the insulator stack. This vacuum gap allows direct line of sight from -1 MV to the ground (in distance ~ 1.8 m). Vacuum insulation through this long gap was examined based on insulation criteria for both glow and vacuum arc discharges. It was confirmed that glow discharge could not be generated in the operating pressure region. 2) Improve the voltage holding of the FRP insulator: To avoid surface flashover along the insulator, electric field concentration at the negative side triple junction was reduced to 1.2 kV/mm by installing new stress rings. As a result, the accelerator sustained the rated voltage of -1 MV for 8,500 s continuously without breakdown [2.1-2].

Having improved the voltage holding capability of the FRP insulator stack, the H^- ion beams were extracted with seeding cesium to enhance the negative ion currents. The H^- ion beam current as a function of extraction voltage at the acceleration energy of 900 keV is shown in Fig.IV.2.1-2. The ion extraction current increases in proportional to 3/2 power of the extraction voltage (Child-Langmuir law). The H^- ion beam of 110 mA (80 A/m^2) was stably accelerated at the extraction voltage of > 5 kV. Saturation of the current indicates that almost all ions near the extraction apertures are extracted (emission limit). By increasing the negative ion production in the source, the current density required for ITER will be attained at the extraction voltage of 9 kV, which is within the test facility capability and also the design value of the ITER power supply. Since the KAMABOKO source itself has already achieved 300 A/m^2 H^- ion production, further increase of the current density is possible by optimization of cesium condition and arc discharge power input.

The beam acceleration up to1 MeV and a current of 0.1-A level was quite stable and accomplished for several hundreds shots in two experimental campaigns. The breakdown due to photoelectrons generated by bremsstrahlung was not observed during the beam acceleration. Thus the development of vacuum insulated accelerator has solved technical issues of high voltage insulation of 1 MV level in long vacuum gaps under presence of the H^- ion beams.

References

2.1-1 T.Inoue, *et al.*, *Rev.Sci.Instr.* 75 (5), 1813-1815 (2004).

2.1-2 M. Taniguchi *et al.*, *Nucl. Fusion* 43, 665-669 (2003).

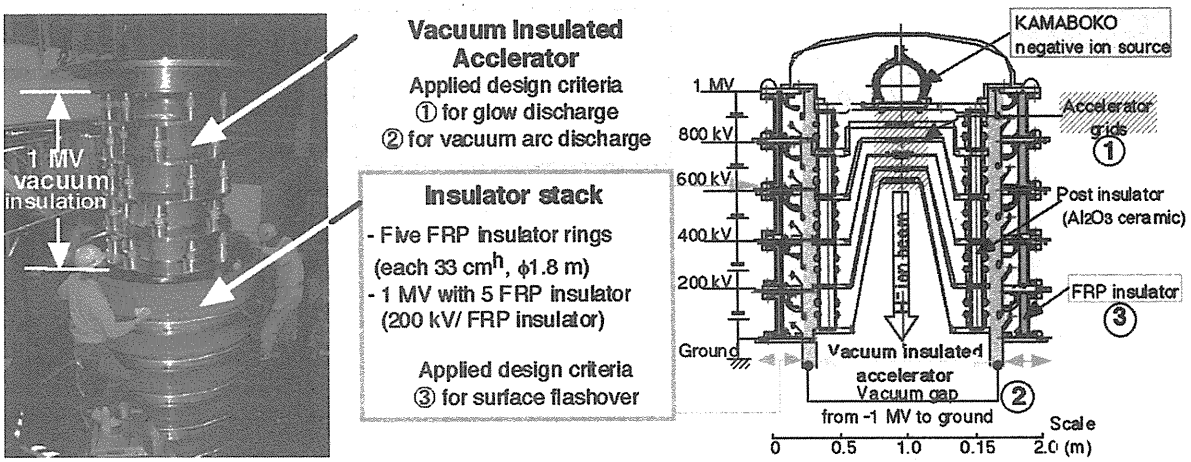

Fig.IV.2.1-1 JAERI vacuum insulated accelerator.

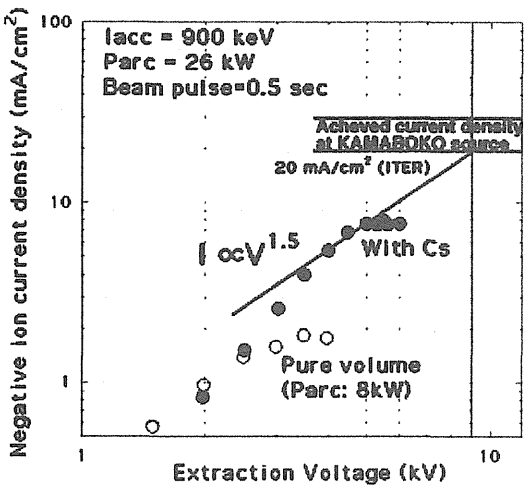

Fig.IV.2.1-2 The dependence of negative ion current density on the extraction voltage.

2.2 Improvement of Negative Ion Uniformity in Large Ion Sources [2.2-1]

In the Negative ion Neutral Beam Injector (N-NBI) for JT-60U, a high current negative ion beams of >20A have been already produced through a large extraction area of 45cm x 120cm. However, the beam pulse length at high current operation is limited due to the high power loadings on acceleration grids and on beamline components [2.2-2]. One of the possible reasons for the high power loading is the non-uniformity of the negative ion density in longitudinal direction of the extraction area. Therefore, the improvement of the non-uniformity of negative ion production is one of the critical issues for expanding the performance of the NBI.

To investigate origins of non-uniformity in the large negative ion source, measurement of plasma parameters by Langmuir probes and the extracted beam profile measurements were performed in the JAERI 10 A source. Typical results of the Langmuir probe measurements are shown in Fig.IV.2.2-1. The probe was scanned in the extraction region where the negative ions were produced. The result revealed strong gradient in electron temperature (Te, open circles) even with uniform magnetic filter field, which divides the plasma generator into two regions, namely, the driver region (main arc discharge region with fast electron) and the negative ion production region (with Te < 1 eV). A measured Te reached ~5 eV at the bottom of the ion source (Fig.IV.2.2-1c). The H^- ion beam intensity was lower at the bottom (Fig.IV.2.2-1d). The negative ion destruction reaction, $H^- + e^- > H_0 + 2e^-$, has a large cross section at higher electron temperature (Te > 1 eV), for example, the cross section increases ~5 times larger only with the temperature increase from 1 eV to 2 eV. This suggests that the high Te is one of the main reasons of local reduction in the H^- ion current.

Based on the above investigation, we firstly tested to lower the Te at the bottom by increasing the magnetic filter field to 130% from the former strength at the bottom half of the source (Fig.IV.2.2-1a). As a result, Te was reduced at the bottom (closed circles), and the recovery of the H^- ion current was observed. This shows that the origin of the non-uniformity of the negative ion production is partial increase of Te at the extraction region of the ion source.

To identify possible leakage path of the fast electrons from the driver region to the extraction region, a molybdenum plate of 50 mm x 50 mm was inserted in the source to intercept the leaking fast electron. A reduction of Te followed by the recovery of the H^- ion current was also observed when the plate was placed at the center of the

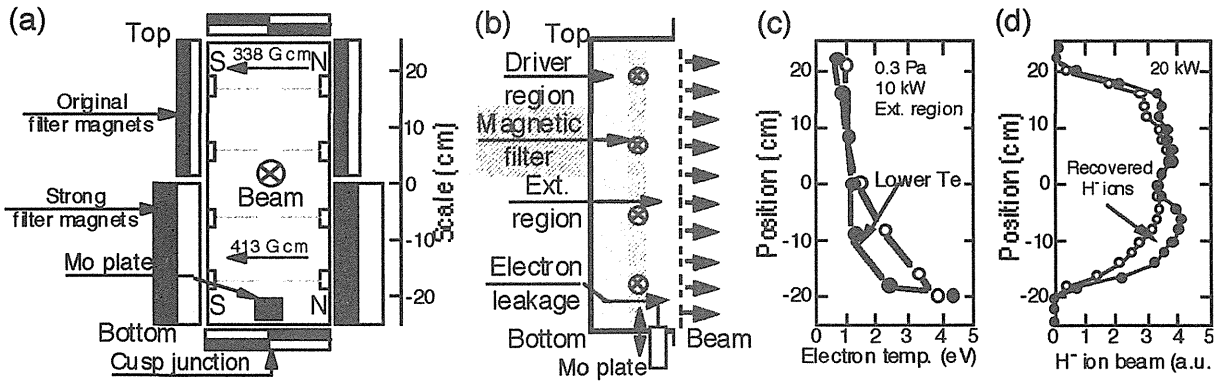

Fig.IV.2.2-1 A change of electron temperature and H^- ion current recovery. (a) The source plan view with the filter magnet configuration, (b) the source side view, and variation of (c) electron temperature, and (d) H^- ion beam intensity, before (open circles) and after (close circles) filter field enhancement.

bottom source wall, where a junction of cusp magnetic field was located. Thus one of the dominant mechanisms of the local H^- ion reduction was revealed to be the leakage of fast electrons through the junction of cusp magnetic field.

References

2.2-1 Hanada M., *et al.*, " Experimental study on uniformity of H^- ion beam in a large negative ion source ", submitted to *23rd Symp. on Fusion Technology* (2004).

2.2-2 Umeda N. *et.al., Nucl. Fusion* 43, 522 (2003).

2.3 Plasma Neutralization of High Energy Negative Ion Beams [2.3-1]

A system efficiency of high energy negative-ion-based NBI is limited to be 40% by using the existing gas neutralizer. To obtain higher system efficiency, neutralization efficiency needs to be improved. This can be achieved by adopting plasma neutralizer, where a dense ($> 5 \times 10^{18}$ m^{-3}) and highly ionized plasma is required for 1 MeV-class negative ion beams.

A plasma neutralizer was experimentally studied in the JAERI 400 keV Negative Ion Acceleration Stand (NIAS) (Fig.IV.2.3-1). An arc discharge type plasma generator was installed in the beamline for the plasma neutralization. Dimensions of the plasma generator are 600 mm in diameter, and 2000 mm in length. It has large openings for beam path with a diameter of 200 mm. The anode wall of the plasma generator is surrounded by the cusp magnetic field, which is generated by the neodymium permanent magnets. Sixteen tungsten filament cathodes were installed. At the chamber openings, the transverse magnetic field is applied to suppress the fast electron leakages [2.3-2]. Hydrogen plasma with an ionization degree of 10-15 % was produced at a lower gas pressure of < 0.05 Pa by arc discharge. A negative ion beam (H^-, 200 keV, 4 mA) was passed through the plasma generator and was converted to the H_0 or H^+. Neutrals and residual ions (H_0, H^-, H^+) were separated by the electro-magnet and were calorimetrically measured at the targets, respectively. The neutralization loss of the H^- before the plasma neutralizer could be suppressed to be less than 20% by using strong pumping system (22 m^3/s by two cryopumps and one turbo molecular pump).

Fig.IV.2.3-2 shows the neutralization efficiencies of the H^- for hydrogen gas and plasma targets. The maximum neutralization efficiency was 65% at 5×10^{15} cm^{-2} (molecular density) in plasma (filled circles) with 10% ionization degree compared with 59% at 7×10^{15} cm^{-2} in gas (opened circles). These experimental results agreed well with the theoretical ones (solid lines), which were obtained from the cross section data. As expected in the theoretical neutralization efficiency, it was experimentally confirmed that the plasma target has the higher neutralization efficiency in the lower line density than the gas target.

References

2.3-1 Hanada M. *et al., Rev. Sci. Instr.*, 75 (5), 1813 (2004).

2.3-2 Section I.2 of this *Annual Report*

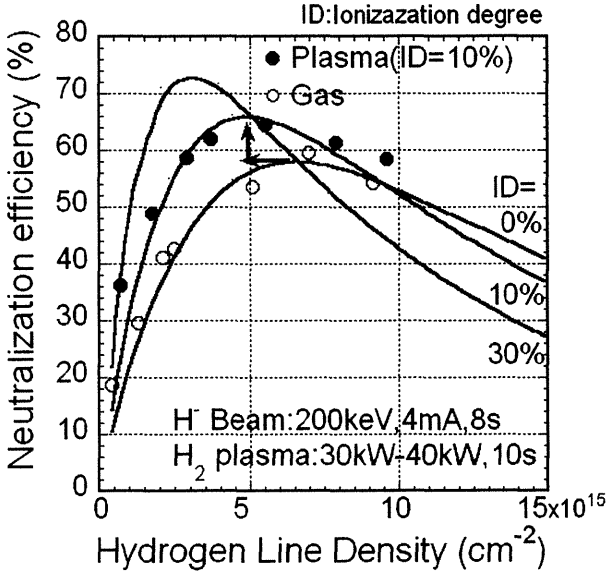

Fig.IV.2.3-2 Neutralization efficiency as a function of the gas line density.

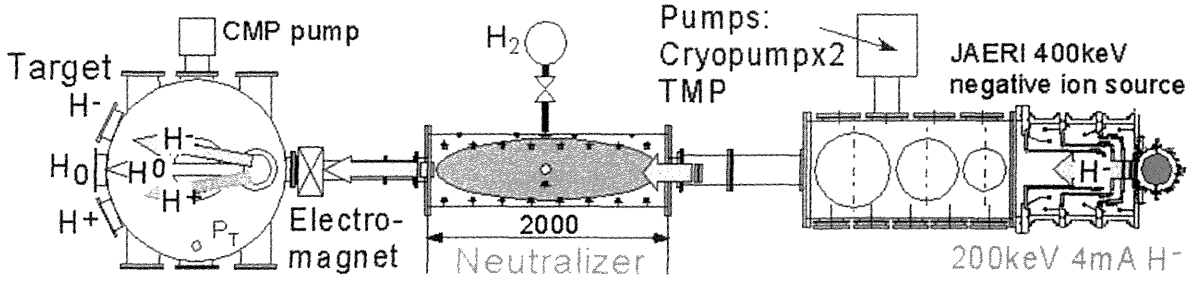

Fig.IV.2.3-1 Schematics of the plasma neutralizer equipped in the 400 keV negative ion acceleration test stand at JAERI.

3. Radio Frequency Heating

3.1 High Power Output of 0.5MW/100sec by a 170GHz Gyrotron

ITER requires a 170-GHz high-power gyrotron system with a total power of 24 MW, for electron cyclotron heating (ECH), current drive (ECCD) and suppression of plasma instabilities. Intensive development of a 170-GHz gyrotron (1 MW, continuous wave (CW) operation and 50% efficiency) is under way for ITER. In this gyrotron, 170-GHz millimeter wave with $TE_{31,8}$ mode oscillates in a cylindrical open cavity with the magnetic field of ~6.7T. The power is delivered as the Gaussian beam through the artificial diamond window.

Integration of breakthrough technologies had been achieved by 2002; i.e. 1 MW oscillation at high order mode cavity, energy recovery by a depressed collector, and a synthetic diamond window. However, the extension of the pulse duration with high power was limited by a sudden pressure increase in the gyrotron due to overheating of the bellows section attached to the mirror steering for adjusting the RF beam direction to the output window. It was also clarified that the heating of the bellows was caused by a power deposition of the stray radiation due to diffraction loss corresponding to the mode conversion loss from $TE_{31,8}$ to Gaussian beam [3.1-1].

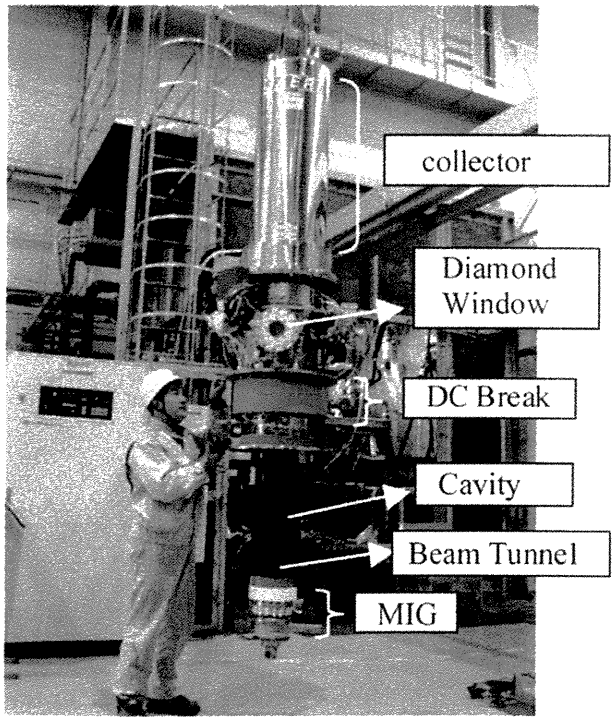

Fig. IV.3.1-1 A 170-GHz gyrotron that operates at 0.5 MW for 100 sec.

The countermeasures for local power deposition on the bellows are the followings:

(1) Reduction of the ohmic loss by RF shield and Cu coating on the bellows.

(2) Enhancement of forced water cooling.

As an effect of the Cu coating on the bellows, the heating rate of the bellows was reduced to less than 1/10 of the original rate, and the sudden pressure increase was suppressed by bellows cooling in addition to Cu coating. Consequently, 0.5 MW power level operation for 100 s was demonstrated without significant conditioning [3.1-2].

Furthermore the temperature of the major components reached the steady state within the 100 s operation. Fig.IV.3.1-2 shows an example of time evolution of (a) the temperatures at the collector surface, (b) the center of the output diamond window cooled by fluorinate liquid at the edge, and (c) fluorinate liquid for DC break cooling in the 100 s operation with 0.5 MW level. The collector temperature was 120 °C in steady state, which indicates the temperature increase (ΔT) is acceptable for 1 MW operation even though the power becomes double. The edge of the diamond window is cooled by the fluorinate liquid. Temperature increase of the center of the disk measured by an IR camera was

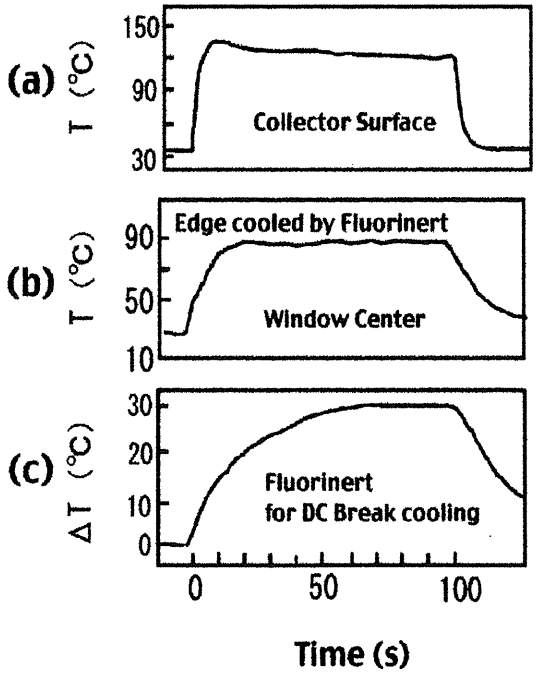

Fig. IV.3.1-2 Time Evolution of temperature change in the gyrotron during a 0.5-MW, 100-s pulse operation. (a) collector surface, (b)center of the output window, (c)fluorinert for DC break cooling.

~60 °C, and it is possible to transmit the 1 MW power by the enhancement of flow velocity. The DC break for depressed collector operation, whose temperature increases due to the absorption of the stray radiation, is cooled by the fluorinate liquid. The temperature of the fluorinate liquid was acceptable value, ΔT~30 °C. These results indicate that the 1 MW-CW operation is possible [3.1-3].

References

3.1-1 Sakamoto, K., *et al.*, "Development of 170GHz and 110GHz Gyrotron for Fusion Devices", *Nucl. Fusion* 43 (2003) 729.

3.1-2 Sakamoto, K., *et al.*, "Development of ECRF Technology in JAERI", *Proc. of IAEA Technical Meeting on ECRH Physics and Technology for ITER*, (2003).

3.1-3 Kasugai, A., *et al.*, "Study of millimeter wave high-power gyrotron for long pulse operation", *Nucl. Inst. Methods in Phys. Res.* A528 (2004)110.

3.2 Development of RF Launcher for mm Wave Steering

3.2.1 Transmission experiment of RS launcher

A Remote Steering (RS) launcher has been developed as an advanced mm-wave-injecting antenna on Electron Cyclotron Heating and Current Drive (ECH/ECCD) for the ITER and a future DEMO reactor[3.2-1]. The RS launcher consists of a square or rectangular corrugated waveguide and a steering mirror installed at the inlet of the waveguide. Therefore, neutron irradiation and high heat flux from plasma onto the mirror can be reduced to the negligibly small level, compared to a Front Steering (FS) type launcher. In 2003, the transmission experiments of the new prototype RS launcher with a high precision of the corrugations were carried out.

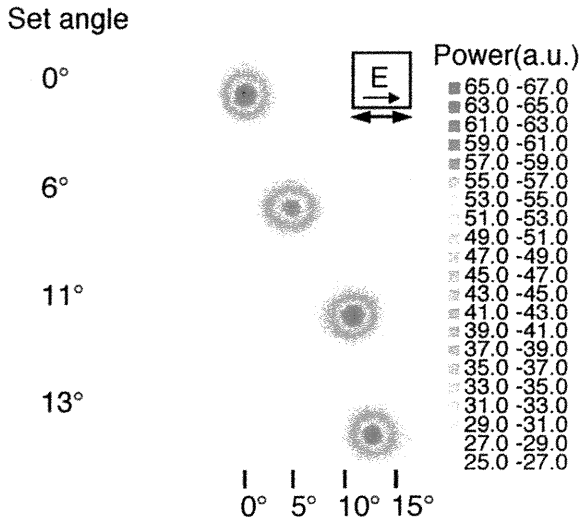

Fig. IV.3.2-1 Radiation Pattern of RF beam.

In the low power experiment, the radiation patterns of RF beams were measured by a X-Y scanner. The RF beams with both polarizations vertical and parallel to the steering plane were radiated in the experiment. It was confirmed that the radiation pattern with the E-field polarization both perpendicular and parallel to the steering plane agreed with theory for both polarization.

The high power experiment was also carried out to investigate the capability of high power transmission. The RF beam pattern radiated from the waveguide outlet onto a screen (RF absorber) was measured by an infrared camera. The example of the patterns is shown in Fig. IV.3.2-1[3.2-2, 3.2-3]. The patterns also agreed with theory. The radiation power was calorimetrically measured using a dummy load. It was verified that the transmission loss in the waveguide was less than 5% in the steering range from −12° to 12°. The principle of the remote steering concept with high power and efficient transmission was confirmed.

3.2.2 Development of reliable diamond window

A torus diamond window is located at the inlet of a launcher and takes a role of vacuum and tritium barrier between the launcher (vacuum vessel) and the transmission line. Therefore, the reliable window structure is required.

A heat deposition when RF passes the diamond window is removed at the disk edge by water in the conventional window structure. In this case, the ingress of water into the launcher (vessel) is concerned if a crack was produced at the edge. In order to eliminate the possibility of water ingress at the edge, a diamond window with Cu-coated edge was developed. The thickness of the coating is 0.5mm. The aluminum blaze between the diamond and the inconel cuff is covered by the Cu coating layer. Therefore, the coating layer is effective for avoiding the aluminum corrosion. The conceptual drawings of the conventional and Cu-coated window are shown in Fig. IV.3.2-2(a) and (b), respectively. The photograph of the diamond window with Cu-coated edge is shown in IV.3.2-3. The RF transmission experiment of the

window has been started to investigate the capability to remove the RF power deposition.

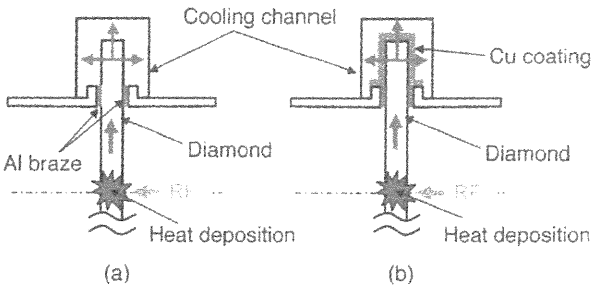

Fig. IV.3.2-2 Conceptual drawings of (a) conventional and (b) Cu-coated window.

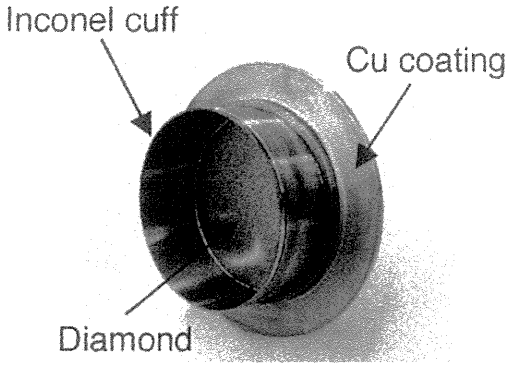

Fig. IV.3.2-3 The photograph of the diamond window with Cu-coated edge.

References

3.2-1 Takahashi, K., *et al.*, "High power experiments of remote steering launcher for electron cyclotron heating and current drive", *Fusion Eng. Des* 65. (2003) 589.

3.2-2 Takahashi, K., *et al.*, "Transmission experiments of a 170GHz remote steering EC launcher", *Proc. of The 28th International Conference on Infrared and Millimeter Waves*, (2003).

3.2-3 Takahashi, K., *et al.*, "Development of EC Launcher and Diamond Window for ITER", *Proc. of IAEA Technical Meeting on ECRH Physics and Technology for ITER*, (2003).

3.3 Application of High Power RF

3.3.1 Study of IFMIF RFQ

International Fusion Materials Irradiation Facility (IFMIF) is an accelerator-based neutron irradiation facility employing the deuteron-Lithium (D-Li) stripping reaction, to produce the neutron field similar to the D-T Fusion reactor. In the IFMIF, two D-beams of 125mA will be accelerated up to 40MeV using linearly combined accelerators of a radio-frequency quadrapole linac (RFQ) and a drift tube linac (DTL). The output energies at injector, the RFQ linac and the DTL are designed to be 0.1, 5 and 40 MeV, respectively.

In the RFQ linac, the operation frequency of 175MHz was selected to accelerate the large current of 125mA. For this low frequency, the rectangular waveguide with a cross-sectional size of 1.0 x 0.5m is needed, and the conventional RF-Input coupler using Iris type becomes large to inject RF power into RFQ. Therefore, an RF-Input coupler with multi-loop antennas has been newly designed for the input of RF power of 2.3MW level. The high power RF is fed from four coaxial waveguides, which are connected to loop antennas in the RFQ cavity. Important issue is a demonstration of excitation of quadruple operation mode (TE_{210}) using the multi-loop antenna structure, since the loops may disturb the phases and power balance among the loops. The R&D of the RF coupling section, therefore, was indispensable for the development of RFQ.

A mock-up loop antenna using a pipe of 10mm in diameter was fabricated, and phase differences and power balances were measured among the four inputs[3.3-1, 3.3-2]. As a result, it is found that the coupling with multi-loop antennas using two or four loops is better than one loop antenna from the point views of both withstanding voltage and power balance. The phase difference and power balance were also measured in both two and four loop cases. In case of

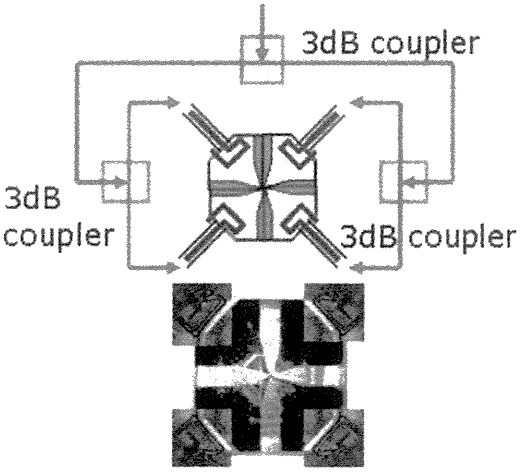

Fig. IV.3.3-1 Low-power test set-up of RF input coupler using four loop antennas.

four loops as shown in Fig.IV.3.3-1, an acceptable average phase-difference of 179° (180° of design value) was obtained. As for RF power balance, power differences among loops were within 8% deviation. These results show that the RF-Input coupler with a multi-loop antenna in the IFMIF 175MHz RFQ is feasible.

3.3.2 Microwave Beaming Propulsion

Experiments on a microwave beaming propulsion were conducted using 1-MW gyrotron in collaboration with the University of Tokyo. The concept of energy beaming propulsion is explained as follows: When electromagnetic waves are beamed from the ground intermittently and focused in the atmosphere, breakdown occurs near the focus and plasma is formed. The plasma absorbs the following part of beamed energy and expands outward generating shock waves. The shock waves reflect on a nozzle surface of a vehicle, generating impulsive thrust. Because the energy is provided from the ground and the atmospheric air is utilized as a propellant, neither energy source nor propellant need to be loaded onto the vehicle. Consequently, this type of launcher can achieve a high payload ratio at a remarkably low launch cost. We had tested a conceptual thruster using 1-MW millimeter-wave as shown in FigIV.3.3-2 and FigIV.3.3-3. As a result, the measured momentum coupling coefficient Cm, defined as a ratio of propulsive impulse to input power, was over 400 N/MW.

Both the plasma and shock wave dynamics are considered to play important role in the energy conversion process from electromagnetic energy to kinetic energy. The behavior of plasma and shock waves in a parabola reflector was observed. Plasma development in a microwave-beaming thruster was observed using 2-D and axsymmetric parabola reflectors. In the 2-D parabola reflector, plasma was found to develop in three directions during the initial plasma development stage as shown in Fig.IV.3.3-4. In the later stage, only the plasma leaving from the reflector was developed while the plasma expanding toward the reflector was not enhanced. Propagation speed of the shock wave measurement in the axsymmetric parabola reflector suggested that there might be some supersonic interaction between the shock and discharge front. [3.3-3]

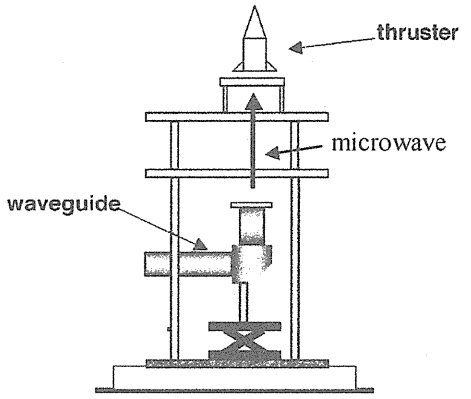

FigIV.3.3-2. Schematic of microwave-rocket launch system.

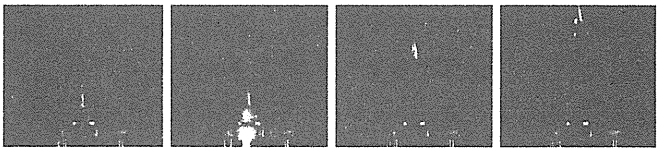

FigIV.3.3-3. High speed framing photographs of microwave-rocket model launch.

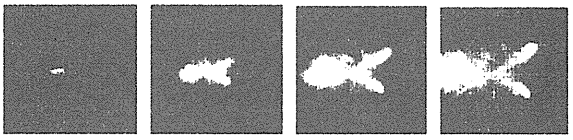

t = 0 m　t = 0.025 ms　t = 0.050 ms　t = 0.075 ms

Fig.IV.3.3-4 Plasma development in a 2-D reflector. P=1MW, 170GHz.

References

3.3-1 Maebara, S, *et al*, "Low Power Test of RFQ Mock-up modules at 175Mhz for IFMIF project", *Proc. of Particle Accelerator Conference 2003*, (2003).

3.3-2 Maebara, S, *et al*, "Development of RF-Input coupler with a multi-loop antenna for RFQ linac in IFMIF project", *Proc. of the 23rd symposium on Fusion Technology*, (2004).

3.3-3 Oda, Y, *et al*, "An observation of plasma inside of microwave boosted thruster", *Proc. 2nd Intl. Symp. Beamed Energy Propulsion, Sendai Japan*, Oct. 2003.

4. Blanket

4.1 Tungsten Armor Joining on First Wall

The first walls of breeding blanket components are required to withstand a high heat load. The structural material of the blankets, Reduced Activation Ferritic (RAF) steel, F82H must be covered by high heat flux materials. Therefore it is necessary for blanket fabrication method to develop a joint technology of two different materials. The main frame of blanket is manufactured by Hot Isostatic Pressing (HIP) method, which is one of the solid state bonding methods. In our development, the joint technology between tungsten (W) and one F82H were developed using a kind of solid state bonding method, Spark-Plasma-Sintering (SPS). The material used was F82H as a structural materials, and sintered tungsten as a armor material. The schematic illustration of the SPS system is presented in Fig. IV.4.1-1. The SPS method is a uni-axial hot pressing method, and the specimens were heated by direct current. The joining temperature was determined to be 960 °C, in order to obtain fine grained F82H [4.1-1]. The joining condition is summarized in Table IV.4.1-1.

The optical micrograph of joined interface is presented in Fig. IV.4.1-2. As shown in this figure,

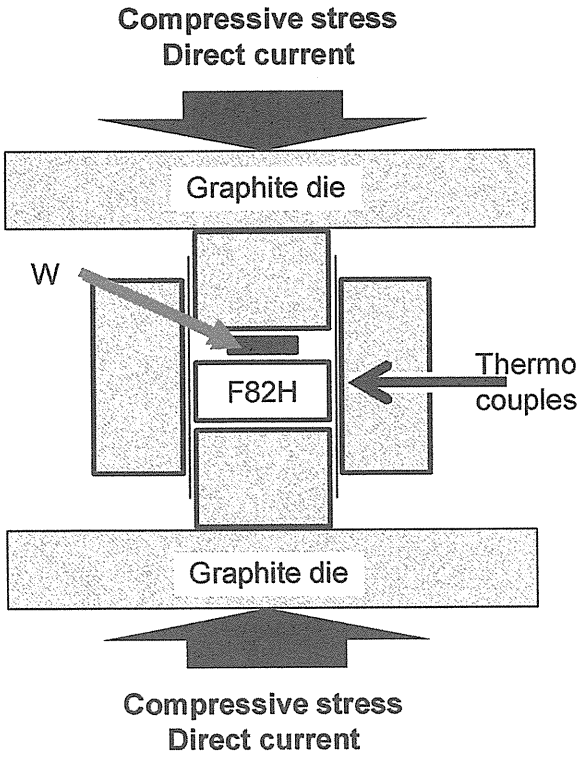

Fig. IV.4.1-1 Schematic illustration of SPS joint method.

Table IV.4.1-1 SPS joint conditions

High heat flux material	Sintered tungsten
	2^{T} x 5^{W} x 10^{L} mm
Structural material	F82H
	ϕ15 x 20 mm
Joining temperature	960 °C
Compressive stress	20 MPa
Atmosphere	10^{-1} Pa
Voltage/Current	3 V / 1000 A

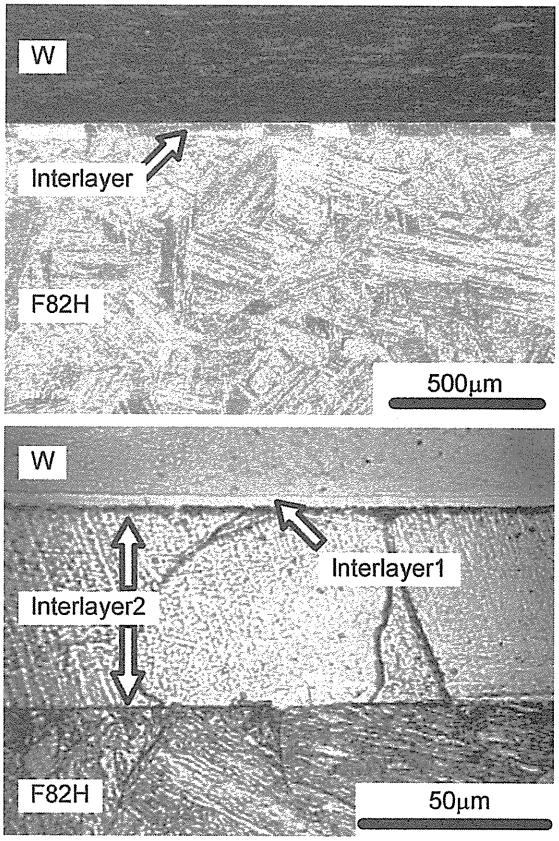

Fig. IV.4.1-2 Optical micrographs of SPS joint.

reaction bands were observed along with the interface, but no defects were observed. Energy dispersion X-ray analysis revealed that the thin reaction layer nearby W (Interlayer 1) consisted of micro-grain of tungsten carbide and some intermetallic compounds, such as Fe_2W and Cr_2W. And the thick reaction layer nearby F82H (Interlayer 2) was identified to be ferrite phase. It is considered that the interlayer 2 is formed by decarburization from F82H during the joining process (Fig. IV.4.1-3, Table IV.4.1-2).

According to the results of Nano-indentation tests, the interlayer 2 was very soft before tempering heat

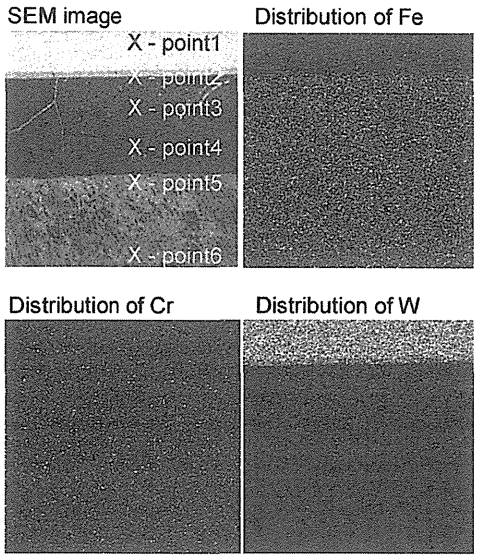

Fig. IV.4.1-3 Elemental distribution mapping o f the interface .

Table IV.4.1-2 Chemical compositions of the interface.

Analysis point	Fe (wt. %)	Cr (wt. %)	W (wt. %)
1	100	0	0
2	39	4	57
3	87	2	11
4	89	6	5
5	89	8	3
6	90	8	2

treatment (Fig. IV.4.1-4). Although the thermal expansion coefficient of F82H is three times larger than that of W, the soft interlayer 2 played as a buffer layer.

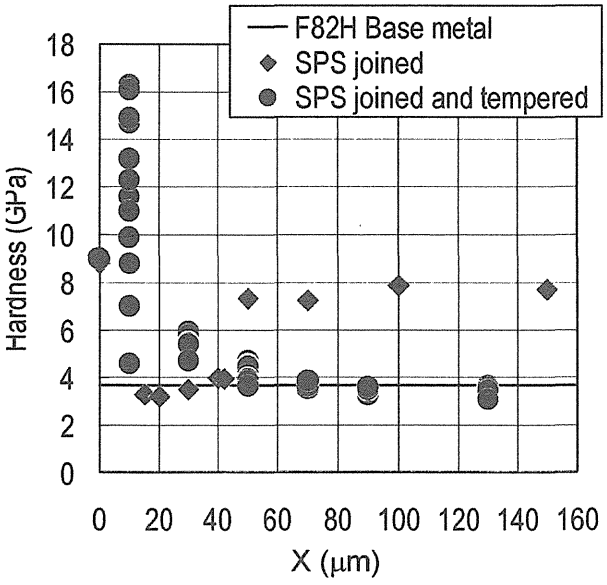

Fig. IV.4.1-4 Hardness distribution across the bonding line.

After the tempering heat treatment at 750 ℃, the hardness of interlayer 2 was the same as F82H and the tempering condition did not have significant impacts on the hardness of tungsten. According to these results, W and F82H could be joined by the solid-state-bonding without any insert material [4.1-2].

Refereces

4.1-1 Hirose, T., et al., *J. Nucl. Mater.*, **329-333**, 324 (2004).

4.1-2 Hirose, T., et al., *JAERI-Conf 2004-012*, 203 (2004).

4.2 Corrosion of Cooling Channel at High Temperature

In the blanket design of a fusion DEMO plant, it is planned that pressured water of high temperature is used as a coolant. In order to establish a reliable blanket system, corrosion phenomena of structural materials should be studied. A weight measurement is a conventional way for an estimation of corrosion behavior. In this method, a sample is maintained under a controlled corrosive condition for a certain period. Usually before the weight measurement, the sample need to be moved to a different place where atmosphere is not corrosive, because most of the weight valance cannot be used in a corrosive environment. Therefore, it is difficult to obtain continuous change of the sample weight during the corrosion test. In the present study, a new method, continuous weight measurement, was developed for analysis of corrosion behavior.

Fig. IV.4.2-1 shows the developed measurement

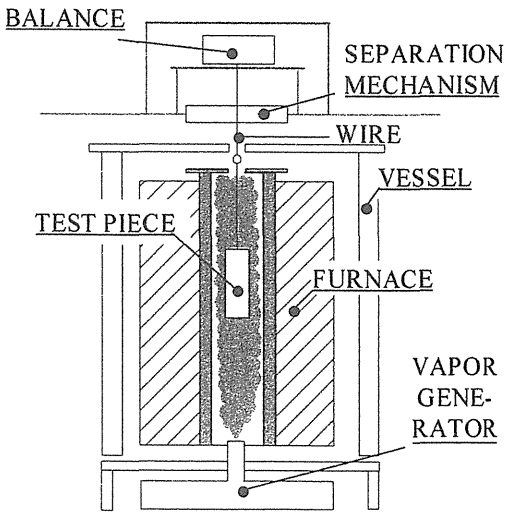

Fig. IV.4.2-1 The Configuration of the developed apparatus for the continuous weight measurement in the corrosion test.

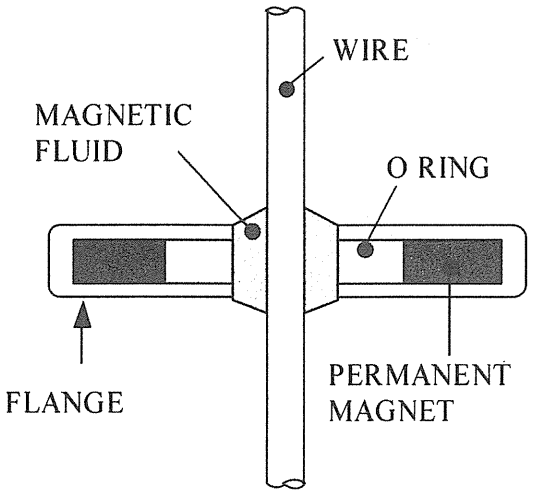

Fig. IV.4.2-2 Separation mechanism using magnetic fluid.

system that has a separation mechanism between a test furnace for a corrosion test and a weight balance. The configuration of the separation mechanism is shown in Fig. IV.4.2-2. The magnetic fluid was maintained by a permanent magnet of 0.2 T. The wire connecting the test piece with a balance was sealed by the magnetic fluid. It was confirmed that the wire could move without friction. The sample in the furnace could be heated up to 900°C. At the bottom of the furnace, a vapor generator was located and the furnace was filled with vapor. It is possible to observe a time dependence of the sample weight during a corrosion process using this system.

RAF steel (F82H) is a candidate of the structural material of a fusion DEMO blanket. The test piece was a tube of F82H, internal diameter of 2.2×10^{-2} m, 2.5×10^{-3} m thick and 0.1 m in height. Total surface area was 0.16 m^2. Before the sample was installed in the system, generation ratio of vapor was measured. Fig. IV.4.2-3 shows the generation ratio of vapor at testing temperatures. The generated vapor passed through the furnace and escaped to ambience from the top of the furnace. During the experiment, partial pressure of vapor was kept at 80 kPa.

Table IV.4.2-1 Coefficients of fitting curves from vapor corrosion test of F82H

Temperature [°C]	$y=Ax^B$		
	A	B	R
406	3.472×10^{-5}	0.5664	0.9901
490	1.765×10^{-4}	0.4759	0.9953
500	2.759×10^{-4}	0.4190	0.9987
585	5.964×10^{-4}	0.4067	0.9986

R: Correlation coefficient

Fig. IV.4.2-4 shows increases in the weights of the samples corroded in water vapor at 400 to 590°C. In the all cases, obtained curves could be fitted by a parabolic formula. The parameters is summarized in Table IV.4.2-1 when the experimental curves are fitted by the formula, $y=A\cdot x^B$. In addition, it was found that the observed weights did not increase following ideal parabolic curves and had successive scatterings. This means that observed changes of the weight correspond to not only generation of corrosion products but also absorption or desorption of corrosive gases. Probably,

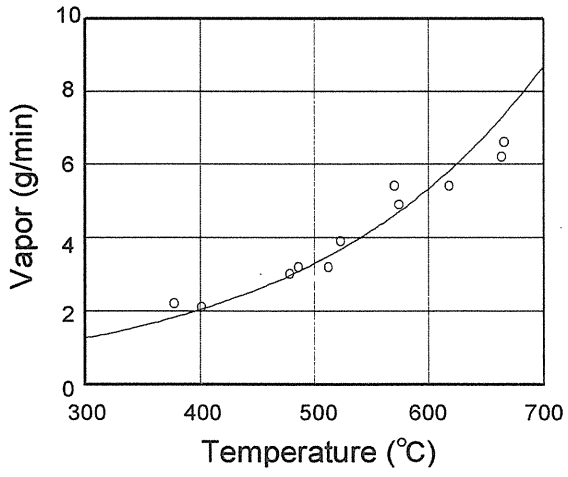

Fig. IV.4.2-3 Generation ratio of vapor at testing temperatures.

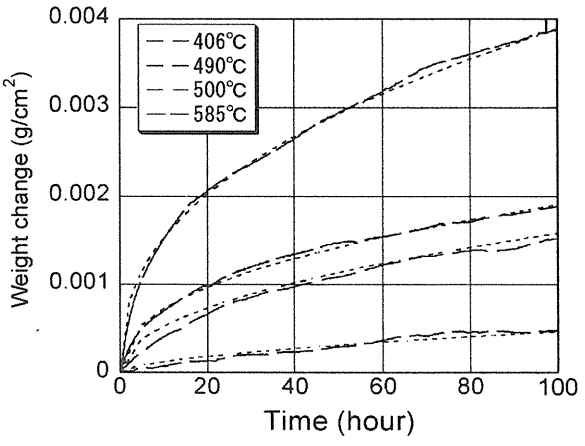

Fig. IV.4.2-4 Variation from initial weight of test pieces and fitting curves.

separation of the corrosion products from the surface is contained too.

From the continuous weight measurement, it was suggested that weight changes due to corrosion of F82H included absorption or desorption of corrosive gases. The released gases from the sample were analyzed using quadrupole mass spectrometer (QMS). For analysis on composition of gases, QMS is a useful tool, however, it should be used in a vacuum under 10^{-2}Pa. In order that the sample gas of ambient pressure could be analyzed, a new system consisting QMS and differential pumping was built up. Fig. IV.4.2-5 shows the system developed in the present study for gas analysis. The sample gas of ambient pressure was introduced to the system by a syringe and was regulated to suitable pressure for QMS measurement. From the furnace for the corrosion test, water vapor was picked up by a pump and moved to the syringe for QMS analysis. When water oxidized metal and metal oxide is produced, hydrogen is released from the metal surface. Therefore, hydrogen was analyzed in the present study.

Fig. IV.4.2-6 shows measured generation rate of hydrogen gas in the corrosion test at 500 °C. The weight of the sample and increasing rate of the weight are shown too. It was found that behavior of generation ratio of hydrogen and increasing rate of the weight was similar. This means that released hydrogen gas due to the corrosion process could be measured by the developed system. It is difficult to analyze detailed behavior of the released hydrogen gas, because the furnace for the corrosion test is not sealed and opened to ambient environment. In the next stage, a sealed test chamber will be necessary in order to interpret the detailed relationship between the scattering in weight change and the hydrogen release.

In the present study, continuous change of the sample weight during the corrosion tests was observed using a newly developed system. The applicability of the developed measurement technique was clarified.

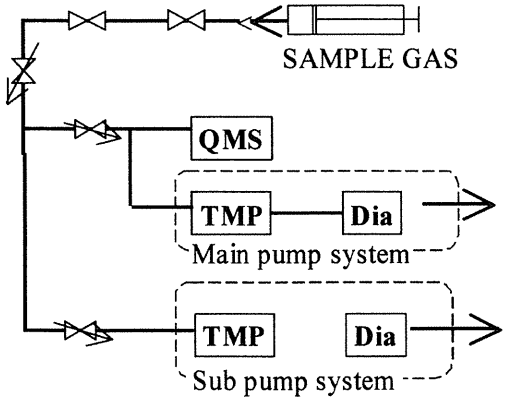

QMS: QUADRUPOLE MASS SPECT-ROMETER
TMP: TURBO-MOLECULAR PUMP
Dia: DIAPHRAGM PUMP

Fig. IV.4.2-5 Combined QMS with a differential pumping.

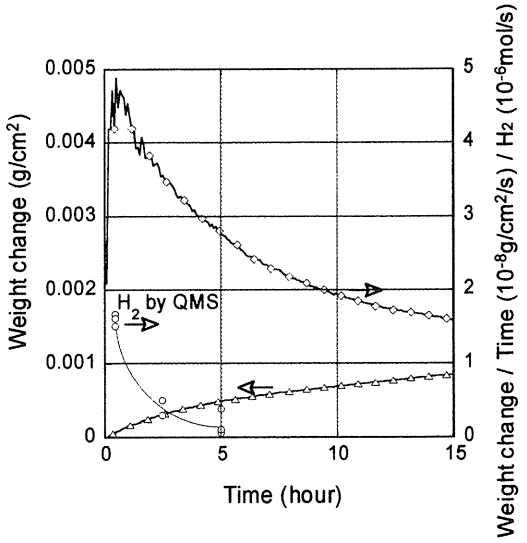

Fig. IV.4.2-6 Weight change of the sample and released hydrogen gas during corrosion test at 500°C.

References

4.2-1 Hatano, T., "Corrosion behavior studied by combination of continues corrosion measuring balance and measurement of released hydrogen gas," to be published in *Trans. At. Energy Soc. Jpn.*

4.3 Thermo-mechanical Performance of Breeder Pebble Bed

In order to establish a reliable and efficient design of the blanket system, it is necessary to elucidate properties of heat transfer in the breeder/multiplier pebble beds. During operations, deformation caused by different thermal expansions between the pebble beds and structural materials will result in the deviation of effective thermal conductivity of the beds. Therefore, it is important to study combination of thermal and mechanical properties [4.3-1]. In the previous work, these properties of the beds were analyzed independently. However, little is known about thermo-mechanical coupled phenomena of the beds. In 2003,

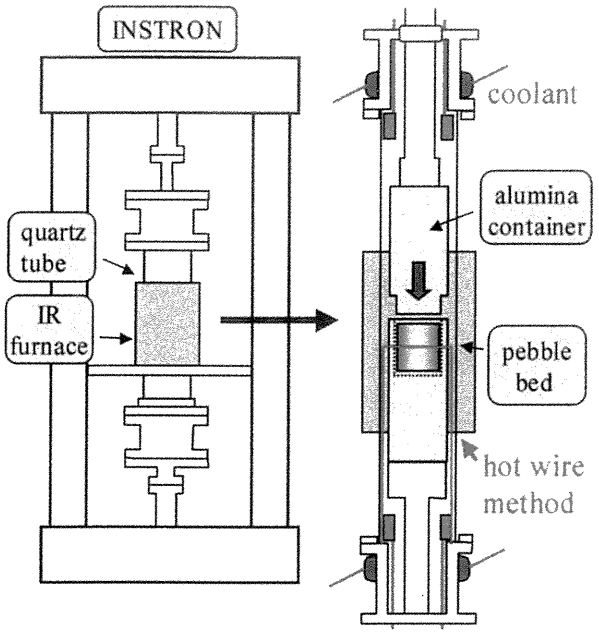

Fig. IV.4.3-1 The configuration of the developed apparatus for the effective thermal conductivity of the pebble bed.

a new apparatus for a measurement of the effective thermal conductivity of the compressed pebble bed was developed. Using the apparatus, the effective thermal conductivity and the stress-strain property can be measured simultaneously.

The configuration of the apparatus is shown in Fig. IV.4.3-1. Pebbles of Li_2TiO_3 with 2-mm diameter were packed into a container made of alumina. Diameter of the packed bed was 75 mm and height 60 mm. The initial packing fractions of the beds were 65 to 67%. The container was inserted into a quartz tube, which was located on a tensile test-apparatus, INSTRON. The atmosphere in the tube could be controlled from vacuum of 10^{-3}Pa to He gas of 0.2MPa. Temperature of the pebble beds was regulated from room temperature to 700°C by an infrared furnace. Under compression up to 10 MPa, the effective thermal conductivity of the bed was measured by the hot wire method.

In the first stage of the investigation, stress-deformation property of the pebble beds was measured during several cycles of compressions up to 10 MPa. Fig. IV.4.3-2 shows the stress-deformation curves of the compressed bed at 500°C. In the first compression, a large and irreversible displacement was observed. After the second cycle, stress-deformation curves had a good repeatability. The irreversible displacement in the first compression corresponds to a dislocation of the pebbles and decrease of pores in the bed. Because of the friction between the pebbles, these pores remained after the initial packing. The purpose of the study is to obtain basic correlation between the effective thermal conductivity and deformation of the bed. Therefore, thermal conductivity was measured after the third cycle of the compressions.

As shown in Fig. IV.4.3-3, increases of effective thermal conductivity due to the compressive deformation were confirmed at temperatures ranging from 400 to 700 °C. This is a preliminary result and enough numbers of data points are not obtained. After a series of experiments with the regulated condition, accuracy of the measurement and correlation between

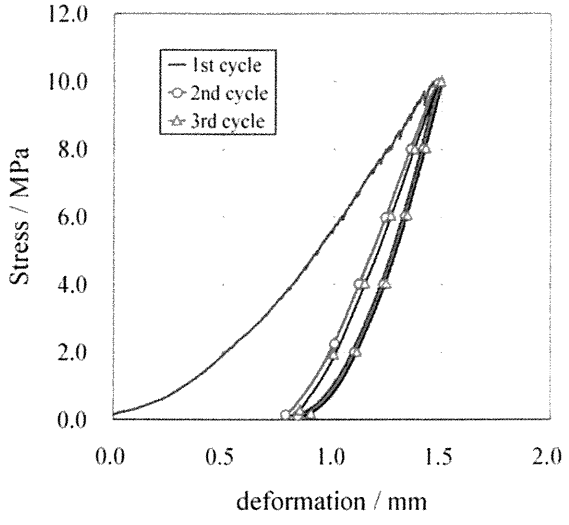

Fig. IV.4.3-2 Stress-deformation curves of the compressed Li_2TiO_3 pebble bed at 500°C.

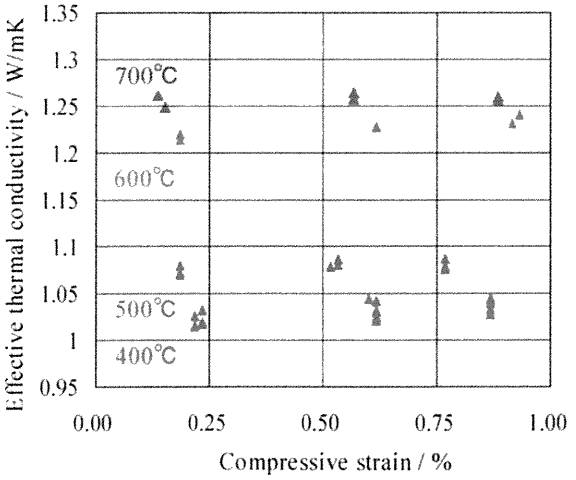

Fig. IV.4.3-3 Effective thermal conductivity of the compressed Li_2TiO_3 pebble beds.

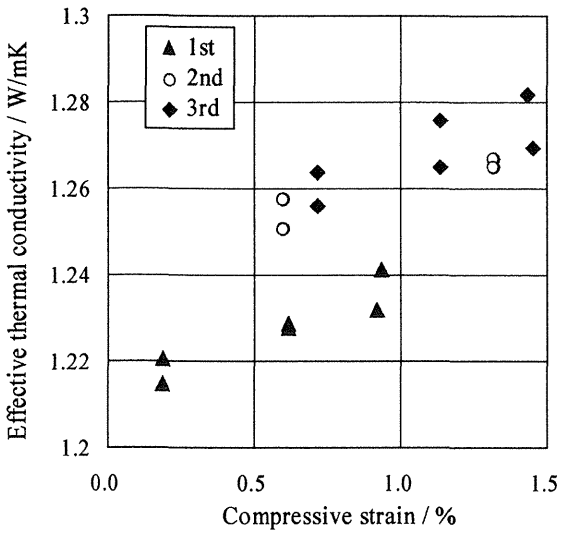

Fig. IV.4.3-4 Effective thermal conductivity of the compressed Li_2TO_3 pebble beds at 600°C.

the effective thermal conductivity and deformation of the bed will be analyzed. Fig. IV.4.3-4 shows the observed effective thermal conductivity from three measurements at 600°C. The procedure was as follows.

1. measurement at 600°C ; dots of triangle
2. measurement at 700°C
3. measurement at 600°C ; dots of circle
4. measurement at 400°C and 500°C
5. measurement at 600°C; dots of square

In each measurement, the pebble bed was compressed up to 10 MPa for several times. It was found that both compressive strain and the effective thermal conductivity increased when the thermal and/or mechanical loads worked on the bed. This means that history of the loads on the bed affect the thermo-mechanical properties of the bed. The history of the loads in the experiment includes several processes, for examples, heating and cooling, mechanical compression and thermal creep. It is necessary to make clear which process has dominant effects on the change of thermo-mechanical properties.

In the previous calculations for the thermo-mechanical design, the effect of compressive deformation on the effective thermal conductivity has been neglected. The increase in the effective thermal conductivity of the compressed bed, which was confirmed in the present study, was so small. This supported that the previous approximation is reasonable for a rough estimation. In addition, the present results suggested that the history of the mechanical and thermal loads to the pebble beds affected the effective thermal conductivity. The phenomena were found for the first time and considered important in the view of an aged deterioration [4.3-2].

References

4.3-1 Hatano, T., et al., *Fusion Sci. Technol.*, **44**, 94 (2003).
4.3-2 Tanigawa, H., et al., *JAERI-Conf 2004-012*, 178 (2004).
4.3-3 Tanigawa, H., "Effective thermal conductivity of a compressed Li_2TiO_3 pebble bed," to be published in *Fusion Eng. Des.*

4.4 Structure Design of Blanket

In this year, the performance analyses of the breeding blanket of ITER have been extensively performed [IV.4.4-1].

A Test Module of ITER Breeding Blanket is designed to use the same module support mechanism and coolant manifolds and coolant system as the shielding blankets as shown in Fig. IV 4.4-1. It has slits by applying facet structure for the breeding cells which are attached to the shield block. Internal design of the breeding cell applies pebble bed Breeder In Tube (BIT) surrounded by multiplier pebble bed as shown in Fig. IV 4.4-2. For the breeder material, Li_2TiO_3 was applied and for the multiplier material, Be was applied. The analyses performed in 2003 were neutronics analysis, tritium release analysis and thermo-mechanical analysis, which are essential performances of the

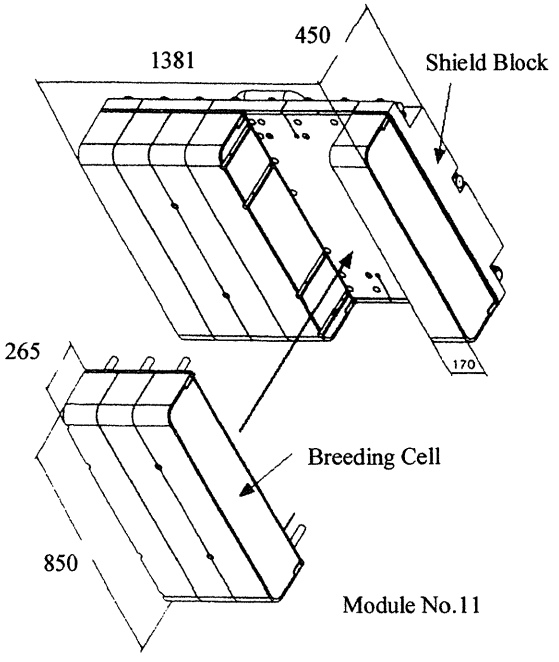

Fig. IV.4.4-1 Isometric view of the ITER breeding blanket.

breeding blanket.

With respect to the neutronics analysis, the detailed analyses of the distribution of the nuclear heating rate and TBR have been performed in 2D model using MCNP to clarify the input data for the tritium inventory and release rate analyses and thermo-mechanical analyses. Tritium Breeding Ratio (TBR) of one module was estimated 1.003.

With respect to the tritium inventory and release behavior analysis, the parametric analyses for selection of purge gas flow rate were carried out from the view point of pressure drop and the tritium inventory/release performance for Li_2TiO_3 breeder. The analysis result concluded that purge gas flow rate can be set to 88 l/min per module that reduces the purge gas flow rate down to 1/10 of that designed before and minimize the size of purge gas pipe.

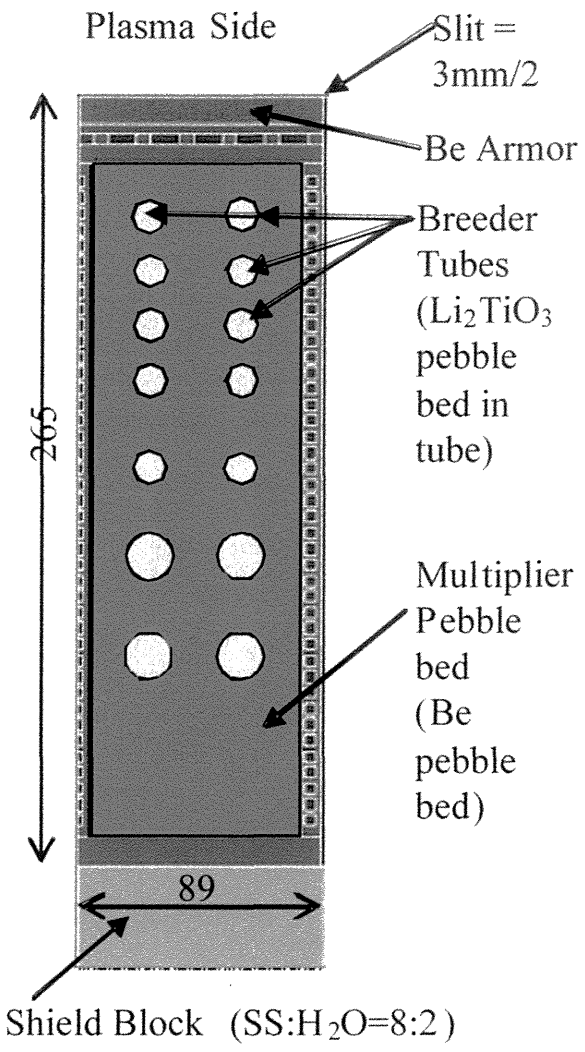

Fig. IV.4.4-2 Calculation model for nuclear analysis of a slit structure unit of blanket by MCNP.

With respect to the thermo-mechanical analyses of the pebble bed blanket structure, the analyses have been performed by ABAQUS with 2D model derived from one of eight facets of a blanket module, based on the reference design. Analyses were performed to identify the temperature distribution incorporating the pebble bed mechanical simulation and influence of mechanical behavior to the thermal behavior. The result showed that the maximum temperature in the breeding material was 617 °C in the first row of breeding rods and the minimum temperature was 328 °C in the seventh row of breeding rods. The temperature range in the Be pebble bed region ranges between 141 °C and 503 °C. The temperature ranges of breeder and multiplier pebble beds were certified to be acceptable from the view points of material integrity.

In conclusion, the analyses performed in this study showed a validity of the design of an ITER breeding blanket, from the view points of tritium breeding performance, tritium release performance and thermo-mechanical performance.

References

4.4-1 Kosaku, Y., et al., *JAERI-Tech 2003-058* (2003).

4.5 Development of Tritium Breeder and Neutron Multiplier Materials

4.5.1 Development of Tritium Breeder

Li_2TiO_3 is one of the most promising candidates for solid breeder materials. In order to keep the stability of its crystal structure at high temperatures, Li_2TiO_3 with oxide additive has been being developed.

For Li_2TiO_3 which was added with 0 – 14 mol% TiO_2, no phase transition was observed at temperatures up to 1100°C. This result indicates that the Li_2TiO_3 added with TiO_2 can be used stably, since the highest temperature of a breeder blanket is 900°C in a JAERI design for a power plant demonstration reactor [4.5-1].

Moreover, Li_2TiO_3 doped with a different oxide additive (CaO, ZrO_2, Sc_2O_3) is being developed in order to control the growth of the grain size at the time of high temperature use. Li_2TiO_3 powder and each oxide powder of small quantity were mixed to form a pellet. Measurement of the pellet density revealed that these oxide additives were effective in controlling the grain growth. For subsequent thermal property measurements, Li_2TiO_3 powder and oxide powder were mixed in the

following proportions: CaO = 0.1wt% (0.20 mol%), ZrO_2 = 0.5wt% (0.44 mol%) or Sc_2O_3 = 0.5wt% (0.40 mol%). Thermal diffusivities obtained are shown in Fig.IV.4.5-1. The values for the CaO-added Li_2TiO_3 are slightly higher (at maximum by 5% from room temperature to 400°C) than those for Li_2TiO_3 without additive, and similar results were obtained for ZrO_2 and Sc_2O_3 addition. The overall results suggest that the oxide addition is effective not only in controlling the growth of the grain size but also in improving the thermal properties. Thus, validity of oxide addition to Li_2TiO_3 has been confirmed.

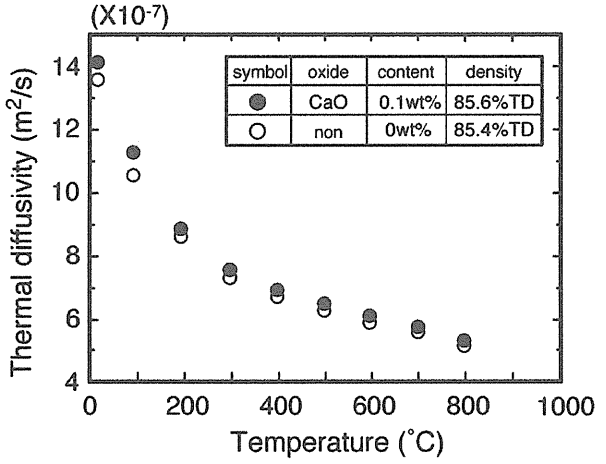

Fig. IV.4.5-1 Thermal diffusivity of Li_2TiO_3 added with CaO, and Li_2TiO_3 without additive.

In a related work, heavy-ion irradiation to Li_2TiO_3 ceramics was performed to investigate the mechanisms of disordering and creation of another phase such as TiO_2 due to irradiation [4.5-2, 4.5-3]. The extent of disordering in Li_2TiO_3 ceramics caused by ion irradiation was found to be less dependent on the accumulated radiation dose and closely related to the electronic stopping power.

Furthermore, tritium release behavior from Li_2O was studied by annealing it after neutron irradiation in the JRR-4 reactor, and the activation energies for the tritium release processes were estimated [4.5-4]. It was found that the tritium release behavior consists of two different processes, and that their activation energies were about 92 and 139 kJ/mol. From analysis of the trapping mechanism of tritium in the materials, it was found that the F center, which is a kind of oxygen vacancy, is the main trapping site of the tritium.

4.5.2 Development of Neutron Multiplier

Beryllides (i.e. Be-Ti alloy) are candidate materials for advanced neutron multiplier to be employed in the blanket of a fusion DEMO plant, and characterization of the Be-Ti alloy was performed in cooperation with some universities in Japan [4.5-5, 4.5-6].

In a study of phase equilibrium in the Be-Ti binary system for pebble fabrication technology and characterization, the microstructure of Be-Ti alloy and composition of the multi-phase alloy were analyzed by Scanning Electron Microscopy (SEM) and Electron-Probe Microanalyzer (EPMA), respectively. From the data, the phase diagram of the Be-Ti binary system was obtained.

In-situ observation of $Be_{12}Ti$ under D_2^+ ion irradiation was conducted using a Transmission Electron Microscope (TEM) equipped with a low-energy ion accelerator. The results indicate that deuterium trapping efficiency of cavity in the $Be_{12}Ti$ is much lower than that in pure beryllium.

Mechanical properties of $Be_{12}Ti$ were evaluated by nano-indentation tests before and after simultaneous irradiation of 1.25MeV electrons and 50 keV He ions at 300 and 500°C. The hardness of $Be_{12}Ti$ after irradiation was decreased compared with that before irradiation, but it was still larger than that of pure beryllium.

As a part of the program on an IEA international cooperation (HIDOBE), Be-Ti alloys (Ti content: 5at% and 7at%) were fabricated, and characterization of these specimens were performed under un-irradiated condition. These specimens will be irradiated for about 4 years in a research reactor, HFR, at Petten, the Netherlands, and the material data of the Be-Ti alloys will be obtained, in which 6000 appmHe is expected to be generated due to neutron irradiation.

References

4.5-1 Kawamura, H., *et al., Nuclear Fusion,* **43,** 675 (2003).

4.5-2 Nakazawa, T., *et al., Nucl. Instrum. Methods Phys. Res., B,* **206,** 166 (2003).

4.5-3 Nakazawa, T., *et al, 2000 Int. Conf. on Ion Implantation Technology Proc.*, 753 (2000).

4.5-4 Tanifuji.T., *et al,* "Tritium Release from Neutron-Irradiated Li_2O Sintered Pellets: Isothermal Annealing of Tritium Trap," to be published in *J. Nucl. Mater.*.

4.5-5 Kawamura, H., *et al.,* "Present Status of Beryllide R&D as Neutron Multipler," to be published in *J. Nucl. Mater.*.

4.5-6 Kawamura, H., *et al., JAERI-Conf* 2004-006 (2004).

4.6 Irradiation Technology Development for In-pile Functional Tests

In development of a small motor for in-pile mockup tests to simulate the ITER pulse operation, a new-type of small Alternating Current (AC) servomotor was developed and irradiated in the JMTR.

The previously devised servomotor (2.5 cm diameter and 3.6 cm length) was fabricated by using radiation-resistant materials for 21 of the 44 motor elements. For example, polyimide-insulated copper wire was used for the motor coil. In developing a new-type of radiation-resistant servomotor, further changes of the structure were made to eliminate organic lubricant. The stainless steel (SUS440C) bearing ball was replaced by ceramics (Si_3N_4), which do not need organic lubricant. As for the lubricant for gear, the polyphenylether oil was changed to the MoS_2 chief ingredient lubricant. In an irradiation test using JMTR, the rotation of the previously devised servomotor stopped at about 130 h (gamma-ray dose: $3x10^7$Gy, fast-neutron fluence: $3x10^{20}n/m^2$, E>1MeV) [4.6-1]. In contrast, the new-type servomotor survived under a similar irradiation for more than 2000 h. Thus, it is clear that the above-described changes have brought about improvement in the survival time by several times.

As for analysis of in-pile data, tritium release from a Li_2TiO_3 pebble bed was measured by continuing the mockup irradiation using JMTR [4.6-2]. It was clarified that the fraction of HT of the total amount of tritium, HT/(HT+HTO), increased with increasing the hydrogen content in the sweep gas, when the center temperature of the pebble bed was 400°C. On the other hand, the fraction was almost constant independently of the hydrogen contents, when the center temperature was 600°C (see Fig.IV.4.6-1). These results suggest that the tritium release was controlled by the surface reaction, because the surface reaction is influenced by the pebble bed temperature and the hydrogen content.

Effective thermal diffusivity of the pebble bed was estimated under neutron irradiation by the constant temperature raising method. The effective thermal diffusivity obtained was $2\text{-}3x10^{-7}$ m^2/s, for a pebble-bed center temperature of 400°C, and the diffusivity has not changed so far up to a fast neutron fluence of $1.5x10^{23}$ n/m^2 (E > 1MeV).

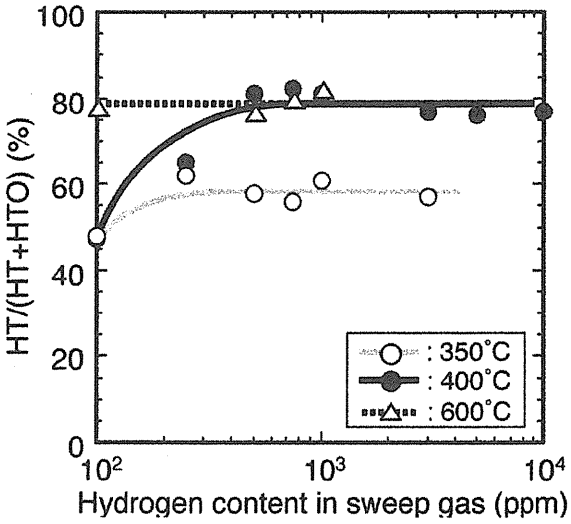

Fig. IV.4.6-1 Influence of hydrogen content in the sweep gas on the fraction of HT for a sweep-gas flow rate of 200 cc/min ($2x10^{-4}$ m^3/min).

References

4.6-1 Ishitsuka E., *et al.*, *Fusion Eng. Des.*, **58-59**, 517 (2001).

4.6-2 Tsuchiya, K., *et al.*, "In-situ Tritium Recovery Behavior from Li2TiO3 Pebble Bed under Neutron Pulse Operation," to be published in *J. Nucl. Mater.*.

5. Plasma Facing Components

Plasma Facing Components (PFCs) are one of in-vessel components of a fusion machine with the function to protect other components such as blanket and super-conducting magnet from heat, particle and neutron flux from core plasma. PFCs include first wall and divertor. In particular, divertor that locates across the magnetic field lines confining the core plasma is exposed to intense heat and particle flux directly flowing from the plasma. Development of PFCs which can endure these loadings is one of key issues for a fusion DEMO plant as well as in ITER. In 2003, in part of developments of PFCs for a fusion DEMO plant, the following activities were carried out.

5.1 Thermal Fatigue Behavior of Divertor Mockups with F82H Cooling Tubes

As part of development of PFCs for fusion machines, JAERI has been developing high performance cooling tubes with pressurized water flow. Along this line, a cooling tube with a helical triangular fin on its inner surface has recently been proposed for the application to a fusion DEMO plant. Since the triangular fin can be machined by a simple mechanical threading, this tube is known as a "screw tube". In our previous experiments, it was found that heat removal performance of the screw tube made of pure copper is as high as that of a swirl tube that is a reference cooling tube of the ITER divertor.

To examine applicability of the screw tube to a fusion DEMO plant, thermal fatigue experiment of divertor mockups with the screw tube made of Reduced Activation Ferritic (RAF) steel, F82H,

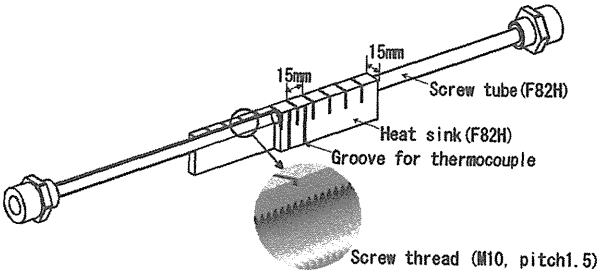

Fig. IV.5.1-1 Divertor mockup with screw tube made of F82H

has been performed. The screw tube was directly machined from an F82H plate, which indicates that there is no bonding/welding part in the test section of the mockups. Figure IV.5.1-1 shows a schematic of the mockup.

On the heated-side surface of the heat sink, slits were machined, as is the case in the divertor configuration. Thermal fatigue experiment of the mockups was carried out under one-sided cyclic heating condition by using an electron beam. The loaded surface heat fluxes were 5 and 3 MW/m^2. At a heat flux of 5 MW/m^2, water leakage due to fatigue crack occurred at the heated surface of the cooling tube of the mockup at about 650 cycle. On the other hand, the mockup did not suffer from water leakage even in 10^4 cycle in the latter condition, although several fatigue cracks at the surface of the cooling tube were observed as a result of a microscopic observation. Fig. IV.5.1-2 shows an SEM image of fracture surface of the mockup tested at 5 MW/m^2. As shown in this figure, several fatigue cracks can be found at a single slit between the heat sinks.

Fatigue lifetime estimation using numerical analysis agrees with the experiments with an error of three.

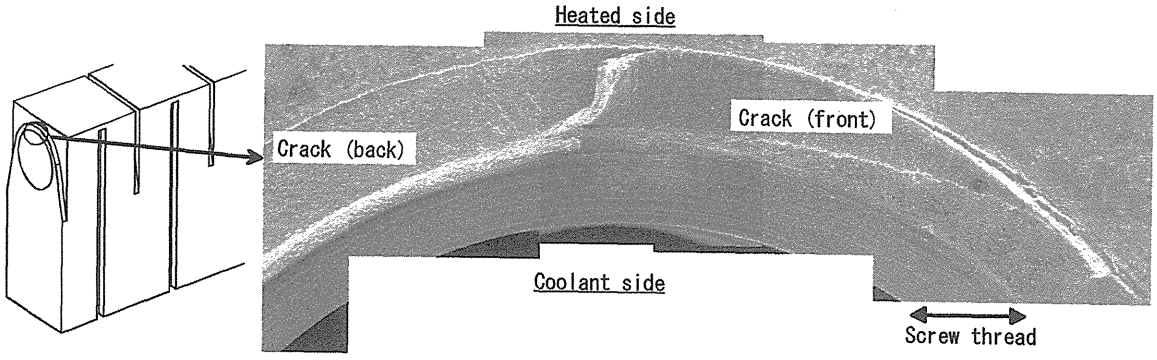

Fig. IV.5.1-2 SEM image of the fatigue crack obtained from the mockup tested at a heat flux of 5 MW/m^2

The numerical analysis predicts qualitatively longer lifetime of the cooling tube than the experiments because of stress relaxation by multiple fatigue cracks at the slit of the cooling tube. Notice that the fatigue cracks of the F82H screw tubes propagated from the outer surface of the cooling tube, not from the inner surface of the tube, which are the same results of the experiments using copper alloy screw tube. This indicates that there is less possibility for fatigue crack initiation at the screw threads on the inner surface of the screw tube used in the divertor geometry.

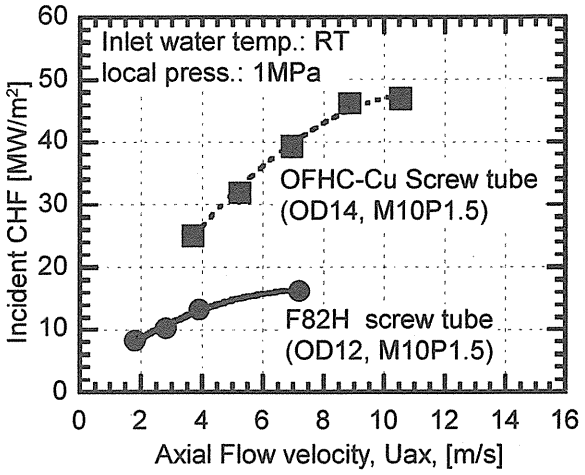

Fig. IV-5.2-1 Incident critical heat flux (CHF) of screw tubes made of F82H and pure copper (OFHC-Cu)

Reference

5.1-1 Suzuki S., *et. al.*, "Key achievements in elementary R&D on water-cooled solid breeder blanket for ITER Test Blanket Module in JAERI", to be presented in *the 20th IAEA FEC* (2004)

5.1-2 Ezato K., *et al.*, "Thermal fatigue experiment of screw cooling tube under one-sided heating condition," *Journal of Nuclear Materials* 329-333 (2004) 820-824

5.2 Critical Heat Flux of a F82H Cooling Tube for Divertor Application

Critical Heat Flux (CHF) testing using a screw tube made of F82H has been carried out in an ion beam irradiation facility in JAERI. In our previous experiments, it was reported that heat removal performance of the screw tube with M-10 screw thread and the pitch of 1.5 mm made of pure Cu is twice as high as that of a smooth tube. As the thermal conductivity of F82H is about ten times smaller than that of Cu-alloy, this study is intended to examine heat removal capability of the screw tube made of F82H.

As shown in Fig. IV.5.2-1, Incident CHF (ICHF) of the F82H screw tube is reduced to about a half of the OFHC-Cu tube. For instance, ICHF of the F82H tube is 13 MW/m^2 at a flow velocity of 4 m/s and that of the Cu tube is 25MW/m^2. To investigate the reduction of ICHF for the F82H screw tube, numerical analyses were also performed. Heat flux distributions in the tube wall of F82H and pure copper shown in Fig. IV.5.2-2 show that the incident heat flux is highly concentrated in the F82H tube because of its low thermal

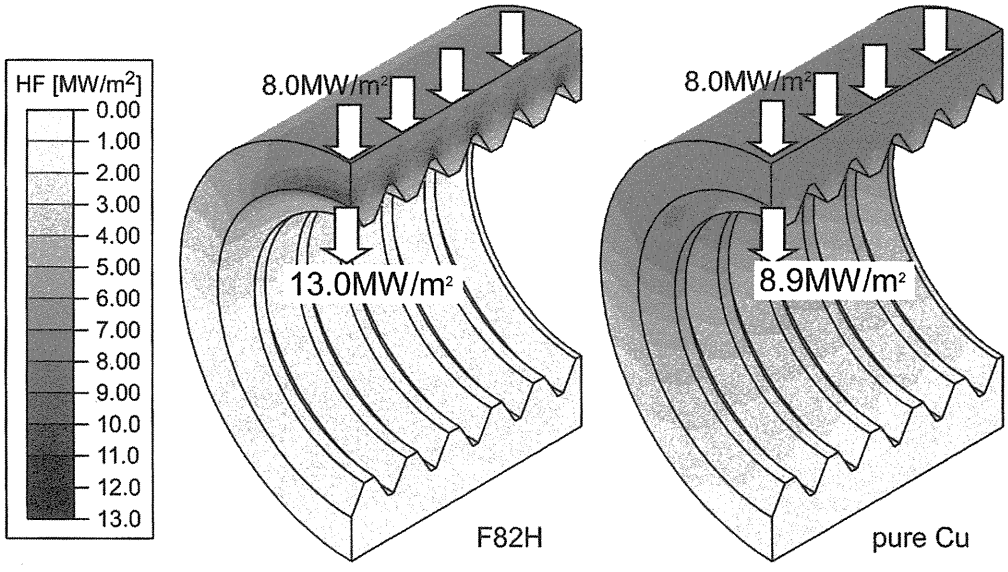

Fig. IV-5.2-2 Heat flux distribution inside the tube walls made of F82H and pure copper.
(Cooling conditions are the pressure of 1MPa, the axial flow velocity of water of 2 m/s.)

conductivity. It is also found that the ratios of the heat flux at the inner surface of the cooling tube to the incident heat flux are around 1.6 for the F82H tube and 1.1 for the copper tube. Based on these results it turns out that application of F82H to PFC cooling structures needs to enhance dispersion of the incident heat flow, for example, to be covered with refractory material with higher heat conductivity such as tungsten.

Reference

5.2-1 Ezato K., *et. al.,* "Critical Heat Flux testing on screw cooling tube made of RAF-steel F82H for divertor application," to be presented in the 23rd Symposium on Fusion Technology (SOFT) 2004, Italy, and to be published in *Fusion Engineering and Design*

5.2-2 Boscary J., *et al.,* "Critical Heat Flux in Subcooled Water Flow of One-Side-Heated Screw Tubes," *Fusion Technology* 35 (1999) 289-296

5.3 Synergistic Effects of Heat and Particle Loads on Tungsten

To investigate synergistic effects of simultaneous loads of heat and particle flux on tungsten which is one of candidate materials of a fusion DEMO plant, hydrogen ion beam irradiation experiments have been performed in collaboration with Kyushu University. Repetitive pulse loads on a tungsten sample with a duration of 2 s and the fluence of about 10^{24} ion/m^2 caused blister formation to the surface of the sample at the maximum temperature of 1000°C. At this high temperature, blister formation on a tungsten surface has not been observed as the results of continuous hydrogen ion irradiation so far. This is ascribed to that the diffusion of hydrogen atom in tungsten is suppressed and its accumulation is enhanced during the cooling phase of the repetitive pulse loads. Microscopic observation also indicates such blister formation caused by hydrogen ion irradiation depends on crystal orientation of tungsten as shown in Fig. IV.5.3-1.

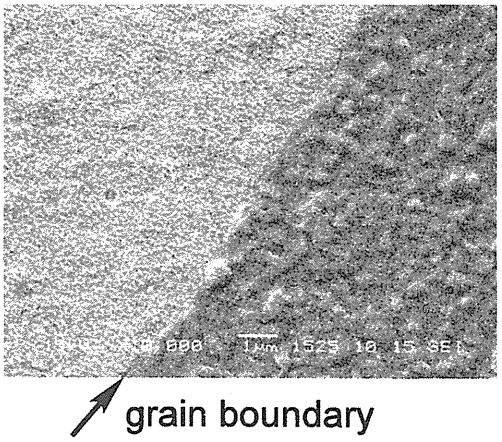

Fig. IV.5.3-1 SEM image of blister formation of tungsten surface. Blister is formed only in the lower right region of which crystal orientation is different from upper left region

Reference

5.3-1 Tokunaga K., *et al.,* "Synergistic effects of high heat loading and helium irradiation of tungsten," *Journal of Nuclear Materials* 329-333 (2004) 757-760

6. Structural Material

6.1 Development of Structural Materials for Blanket

Reduced Activation Ferritic/martensitic (RAF) steel, F82H is one of the most promising candidates as the structural materials for the ITER breeding blanket modules and DEMO blankets. In 2003, neutron and ion irradiation experiments using HFIR, JMTR, TIARA and so on were performed to investigate its irradiation properties. A basic research of oxide dispersion strengthened (ODS) steels based on F82H has been also performed to survey its high tensile strength at higher temperature.

6.1.1 Neutron Irradiation Experiments in HFIR

Neutron irradiation experiments based on Japan-US collaboration are in progress using HFIR in ORNL. In 2003, neutron irradiation cycles of a target capsule (JP26) and rabbit capsules have started. JP26 mainly includes samples for the research of fracture toughness of F82H. The fabrication of another target capsule (JP27) and design of two target capsules (JP28 and 29) have been performed.

In order to investigate the reason of radiation hardening of F82H, precipitation behaviors of various kinds of RAFs, JLF-1, ORNL9Cr, F82H+2Ni and F82H, under irradiation have been examined with extraction residue method. Major results were as follows:

i) increase of precipitation of RAFs, of which radiation hardening was extreme, was large;

ii) radiation hardening of JLF-1, which was tempered at low temperature, was small because of progress of irradiation enhanced recovery, i.e. coarsening and decrease of precipitate; and

iii) large radiation hardening of Ni doped F82H was related with increase of small precipitate (see Fig.IV.6.1-1).

6.1.2 Neutron Irradiation Experiments in JMTR

Tensile tests of F82H irradiated up to 2dpa at 250 °C in JMTR were performed to investigate the effects of the tempering temperature and time on the tensile strength. The following results were obtained:

i) tensile strength of irradiated F82H was increased with an elevation of the tempering temperature;

ii) no tendency was found between the tensile strength and tempering time, although the tempering time affects the tensile strength (see Fig.IV.6.1-2).

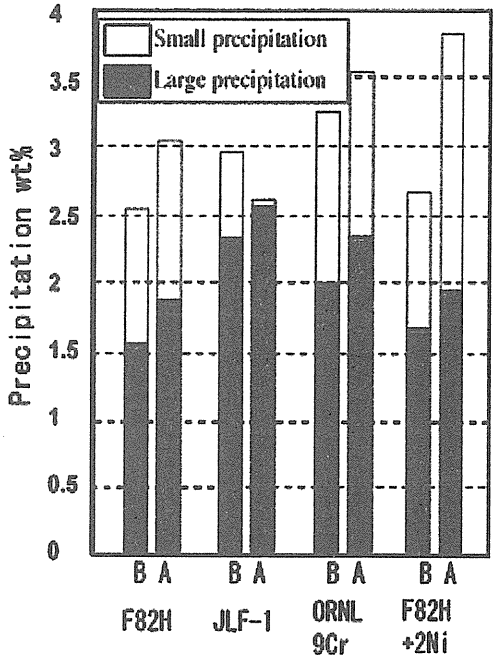

Fig. IV.6.1-1 Change of precipitation quantity of irradiated F82H (B: before irradiation, A: after irradiation)

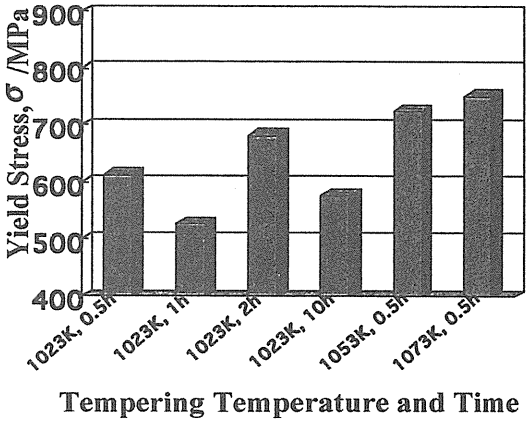

Fig. IV.6.1-2 Effects of tempering temperature and time on the tensile strength of F82H irradiated in JMTR up to 2dpa at 250°C

6.1.3 Ion Beam Irradiation Experiments in TIARA

Irradiation experiments by multiple ion beams at TIARA have been performed up to 100dpa to investigate the radiation hardening of F82H at high doses. Followings are the major observations;

i) radiation hardening with increasing dose was almost saturated at around 30dpa;

ii) dose dependence of radiation hardening is quite similar in both of neutron and ion irradiation cases within the available neutron irradiation dose data. It is expected that hardness change due to neutron irradiation at higher doses would be small (see

Fig.IV.6.1-3).

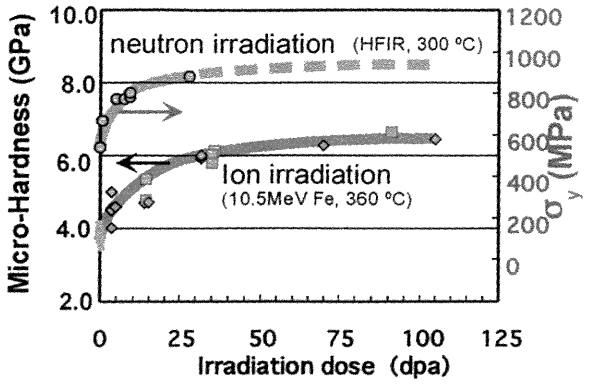

Fig. IV.6.1-3 Radiation hardening behavior of F82H irradiated at TIARA and HFIR.

6.1.4 Oxide Dispersion Strengthened (ODS) Steel

Creep tests of an ODS steel have been performed at 550°C and 650°C in 2003. The ODS steel has a high tensile strength at high temperature by including the micro-particle of Y_2O_3 in RAF matrix, and HIP method (1150°C, 1hour, 190MPa) was used to produce the material. It was found that the creep strength increased from that of F82H by more than 50 and 150MPa at 550 and 650°C, respectively (see Fig.IV.6.1-4). It is expected that blanket system with high durability for the creep deformation at high temperature will be available by using the ODS steel.

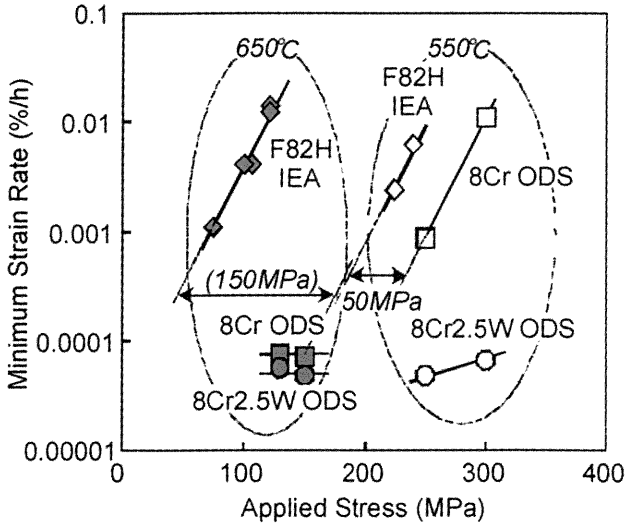

Fig. IV.6.1-4 Creep property of ODS steel produced by HIP method

References

6.1-1 Tanigawa, H., Hashimoto, N. et al., "Microstructure Property Analysis of HFIR Irradiated Reduced-Activation Ferritic/Martensitic Steels," Proc. 11th Int. Conf. on Fusion Reactor Materials, Dec.7-12, 2003, Kyoto, Japan.

6.1-2 Wakai, E., Taguchi, T. et al., "Effect on Tempering Treatment on Mechanical Properties of F82H Irradiated by Neutrons," Proc. 134th JIM Meeting, Mar.30-Apr.1, 2004, Tokyo, Japan.

6.1-3 Ando, M., Tanigawa, H. et al., "Reduction Method of Radiation Hardening in F82H Steels by Heat Treatments," Proc. 11th Int. Conf. on Fusion Reactor Materials, Dec.7-12, 2003, Kyoto, Japan.

6.1-4 Nakamura, K., Shiba, K. and Hishinuma, A., "Effects of Y_2O_3, Ti and W on Mechanical Properties of 8Cr based ODS Steels for Blanket Structures," Proc. 11th Int. Conf. on Fusion Reactor Materials, Dec.7-12, 2003, Kyoto, Japan.

6.2 Comprehensive Design Report for International Fusion Materials Irradiation Facility

IFMIF is an accelerator-based D-Li neutron source designed to produce an intense neutron field that will simulate the neutron environment of a D-T fusion reactor. IFMIF will provide a neutron flux equivalent to 2 MW/m^2 in a volume of 500 cm^3 and will be used in the development and qualification of materials for fusion systems. In 2003, "Comprehensive Design Report (CDR)" has been published to dedicate judgment of decision maker for promotion of IFMIF project in each party [6.2-1]. This report aims at (1) summarizing the present technology level and costs of major systems based on the results of the "Conceptual Design Activity (CDA)" during 1995-1996, the "Conceptual Design Evaluation (CDE)" during 1997-1998, and "Key Element Technology Phase (KEP)" during 2000-2002, (2) showing the necessity of the next R&D program, Engineering Validation and Engineering Design Activity (EVEDA) and (3) outlining scope of Construction, as well as Operation and Decommissioning Activity (CODA). Major conclusions of the CDR are summarized as follows.

6.2.1 Mission, User's and Operational requirements

(1) The primary mission of IFMIF will be to generate a materials database for the design, construction, licensing and safe operation of a DEMO. This will be achieved through testing and verifying materials performance under neutron irradiation that simulates fusion reactor service up to the full lifetime of anticipated service in DEMO. Medium fluence irradiation tests of high heat flux materials for divertors, ceramic materials for a

variety of uses, and functional tests of small blanket elements, complementing the tests of blanket test modules in ITER, are also considered important uses of such a facility. In support of these missions, IFMIF will also provide calibration and validation of data from fission reactor and accelerator-based irradiation tests.

(2) User's requirements for an intense neutron source are neutron flux/volume relation equivalent to 2 MW/m^2 in 0.5 L volume (1 MW/m^2, 4.5×10^{17} n/m^2s; E = 14 MeV, 3×10^{-7} dpa/s for Fe), neutron spectrum similar to a neutron spectrum at the inner wall of fusion reactors as near as possible, neutron fluence accumulation with DEMO-relevant fluences of 150 dpa in a few years, neutron flux gradient less than 10%/gage volume, machine availability more than 70%, time structure of quasi continuous operation, and a good accessibility of irradiation volume for experimentation and instrumentation.

(3) IFMIF shall be available for use by a wide variety of material scientists from the international community. The facility shall provide all necessary services to support the research activities including complete facility access with an office space and laboratory support, appropriate scheduling of experimental and irradiation time, fabrication support for the preparation of specimens and test fixtures, assistance and support for data retrieval and storage, and comprehensive set of equipment for in-situ and post irradiation testing.

6.2.2 System Design Requirements and Description

IFMIF consists of three major subsystems - the Test Facilities, the Target Facility, and the Accelerator Facility - in addition to the Post Irradiation Experiment (PIE) facilities and other conventional facilities shown in Fig.IV.6.2-1. Each of the two accelerators produces a 40-MeV, 125-mA deuteron beam, directed to completely overlapping footprints on the target. The lithium loop and lithium processing system are located below the main level of the facility.

(1) Test Facilities: The IFMIF Test Cell and specimen irradiation areas must be capable of accommodating the wide range of environments associated with fusion reactor materials including ferritic-martensitic steels, vanadium alloys, SiC/SiC composites, refractory metals, brazing materials & joints, ceramic insulators, Radio Frequency (RF) windows, ceramic breeder materials, neutron mulitipliers and

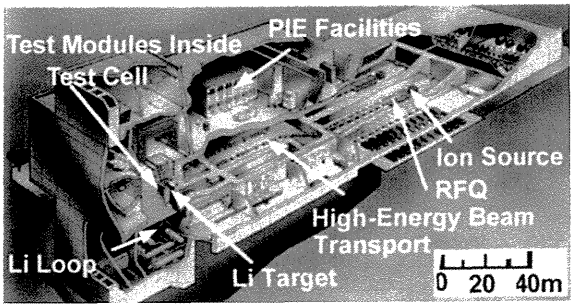

Fig.IV.6.2-1 Overview of the present IFMIF design with major subsystems

superconducting materials. The necessary versatility in experimentation leads to various technical requirements, including efficient access to the Test Cell, shape of usable irradiation volumes, maximum temperature variation within specimen capsules, flexibility in loading schemes for different irradiation rigs, and accommodation of the complex instrumentation.

(2) Target Facility: Major functions of the target facilities are to provide a stable lithium jet for production of an intense neutron flux and to remove the heat load generated in stopping the 10 MW deuteron beam. The target system consists of the target assembly and the Li loop, where an electromagnetic pump circulates the Li through the target assembly, the impurity purification system, and the heat exchange system. The purification system maintains tritium, ^7Be, activated corrosion products and other impurities below permissible levels.

(3) Accelerator Facility: The requirement for 250 mA of deuteron beam will be met by two CW 175 MHz linear accelerators (linac), each providing a 125-mA deuteron beam and operating in parallel. This approach is cautiously aggressive with respect to the current capabilities of RF linac technology and provides operational redundancy by allowing operation to continue at 125-mA when either of the two accelerators is temporarily removed from service for maintenance or repair. The reference design utilizes the room-temperature 5-MeV Radio Frequency Quadrupole (RFQ) linac and Alvarez type Drift-Tube Linac technologies.

6.2.3 Major R&D Requirements

The IFMIF conceptual design is based, to the maximum extent feasible, on the use of existing, proven technology. With this approach, there are no

requirements for basic research to validate any of the processes or test systems. Development activities have been planned to improve or adapt the technologies selected for IFMIF. In addition, a limited development effort is directed at evaluating alternative accelerator configurations, which may offer improved performance.

It is recognized that some development activities and some detailed preliminary design efforts are still required to provide the basis for making a decision on IFMIF construction. Therefore, a new phase, the Engineering Validation and Engineering Design Activity (EVEDA), is planned to focus on the detailed engineering design and the associated prototypical component tests, e.g. full-scale mockup of High Flux Test Module, Li test loop with purification system, high-power RFQ-type load cavity used for high power RF test, and beam matching diagnostics. EVEDA will be organized under a new organizational structure to allow for enhanced joint team design work and for a smooth transition to subsequent construction.

6.3.4 Project Schedule, Organizations and Cost

(1) Schedule : The long range schedule for the IFMIF program is shown in Fig.IV.6.2-2. The EVEDA is assumed to start in 2005 and complete in 2009. The construction will start immediately after the approval of CODA, and last 7 years for the first half-power operation phase using one accelerator only. The first operation phase lasts about three years and the second accelerator is built during that same time period. After the commissioning of the full-power operation using both accelerators, the steady mode operation will continue for 20 years, with possible extension for an additional 10 years.

(2) Organizations: Functions and responsibilities of the EVEDA organization are to be provided in a new Agreement of IEA and its Annex for EVEDA. The proposed EVEDA organization consists of Executive Committee, Operating Agent, Joint Team and Home Teams. The Executive Committee can establish a subsidiary body such as Users Group for management, administration and for technical matters. The User Group is responsible for examining and defining user requirements and testing plan. Tasks of engineering validation are performed in each Home Team in each participant party. The engineering design is performed in Joint Team established at the Operating Agent and in each Home Team.

(3) Cost: The best estimate of the cost of EVEDA is 86 MICF and the cost for construction is 540 MICF, which includes an allowance for indeterminates of 75 MICF. (Million IFMIF Conversion Factor, a cost unit defined for this project. The unit ICF corresponds to $1 US as of July 2003.) The cost of installation and checkout phase is estimated to be 117 MICF. The operation cost including the start-up and commissioning operation and the steady operation for 3 years with a single 125-mA beam and 20 years with a double 125-mA beam is estimated to be 1,825 MICF. The decommissioning activity cost is estimated to be 50 MICF, after which the host country must manage the remaining waste in an appropriate storage or disposal facility.

References

6.2-1 IFMIF International Team, IFMIF Comprehensive Design Report (2003).

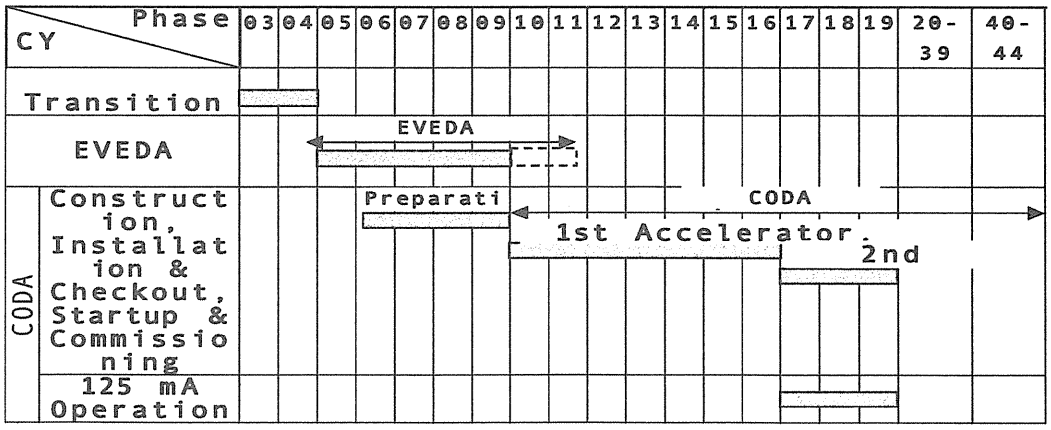

Fig.IV.6.2-2 IFMIF main schedule.

7. Tritium Technology

7.1 Tritium Processing Technology Development for Breeding Blanket

A cryogenic molecular sieve bed (CMSB) has been developed as a tritium recovery method from helium with a small amount of tritium, which is needed for the processing of exhaust gas at helium glow discharge cleaning (HeGDC) and for the processing of helium sweep gas coming out from the breeding blanket. The CMSB consists of molecular sieve cooled by liquid nitrogen, on which hydrogen isotopes are adsorbed but helium is not. Therefore, hydrogen isotopes can be recovered by heating up the molecular sieve after adsorbing process.

Following the basic experiment of the CMSB using protium and deuterium, its system experiment using tritium was planned and carried out connecting the fuel cycle model system with which the gas was purified as fuel. In the present experiment, the stream of hydrogen isotopes and helium was supplied to the CMSB, whose flow rate and concentration of hydrogen isotopes were chosen similar to those of the current ITER test blanket design conditions (6000 cm^3/min, 1% of hydrogen isotopes, and 3-10 ppm of tritium). Molecular sieve 5A was used as the adsorbent and 2.5 kg was packed in the present CMSB.

The first step of the experiment, adsorption process, was continued till the breakthrough of tritium was observed, and then, the CMSB was disconnected from the supply system of helium with hydrogen isotopes and was connected to the fuel cycle model system. The second step was the regeneration of the CMSB, that is, evacuating in the CMSB and heating up the CMSB. A mixture stream of desorbed hydrogen isotopes and helium remained in the CMSB was sent to the fuel cycle model system where pure hydrogen isotope could be get by the palladium diffuser.

The breakthrough curve observed in the first step of the experiment was well explained from the basic characteristics of the CMSB obtained in the previous work. Fig. IV.7.1-1 shows a process response obtained in the regeneration stage of the CMSB. An early stage of the regeneration up to 250 minutes is the evacuation stage of the CMSB, and only helium was sent to the palladium diffuser. Following stage after 250 minutes is the heating up stage of the CMSB, in which the adsorbed hydrogen isotopes were rapidly released and were sent to the palladium diffuser. The fuel cycle model system worked well even in the condition where the supplied gas was changed drastically in their conditions. The amount of hydrogen isotopes finally recovered by the palladium diffuser was in good agreement with that adsorbed by the CMSB. It has thus been demonstrated that the CMSB worked well together with the fuel cycle system for the tritium recovery from the blanket sweep gas or the HeGDC exhaust gas.

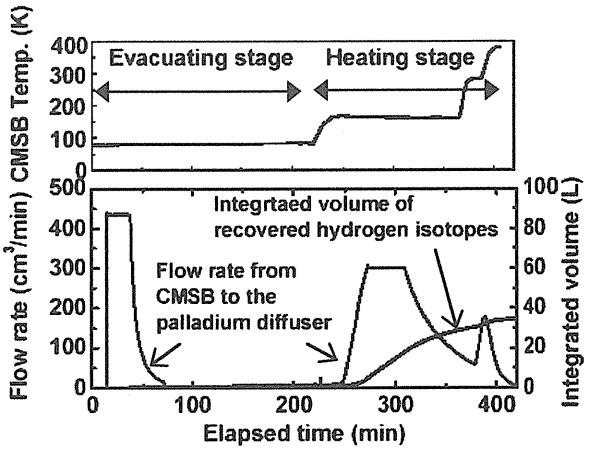

Fig. IV.7.1-1 Regeneration behavior of CMSB after the adsorption process of hydrogen isotopes.

As the development of an advanced economical method for tritium removal from blanket sweep gas necessary for fusion power plant, basic research on electrochemical hydrogen pump using ceramic protonic conductor has progressed [7.1-1]. It was verified that higher pumping speed could be obtained by adding water vapor, and it was obtained the result that the concentration of charge carrier seemed to become higher by the water vapor.

For the tritium removal from a large amount of cooling water of the blanket, the pressure swing adsorption method has been studied. This method utilizes the isotopic effect on vapor adsorption together with quick desorption by reducing atmospheric pressure instead of reducing temperature. As a result of basic experiment using Nax zeolite as an adsorbent, feasibility of this method was verified.

Reference

7.1-1Kawamura, Y., *et al.*, *Fusion Sci. Tech.*, **45**, 33 (2003).

7.2 Tritium Accounting Technology Development

The tritium accounting technique detecting brems-strahlung X-rays of ray of with a NaI (Tl) scintillation counter has been examined with pure tritium in a concentration range of 10^2~10^8 GBq/m^3. The principle of this technique is observing the bremsstrahlung X-rays generated by the interaction between beta particles from tritium and a gold film coated on the inner surfaces of a tritium-containing small measuring cell. A linear relationship between the counting rate of bremsstrahlung X-rays and the tritium concentration was observed for the concentration range of 10^2~10^6 GBq/m^3 (Fig. IV.7.2-1), and the sensitivity was determined to be about 0.5 GBq/m^3 per cpm in this concentration range. The performance of this tritium monitor was also investigated with tritium mixtures diluted with deuterium or hydrogen, and the linear relationship between the counting rate of bremsstrahlung X-rays and the tritium concentration was observed for the two mixtures at tritium concentrations smaller than 10^4 GBq/m^3 (Fig. IV.7.2-1). In addition, as an example of its practical use, this monitor was applied to the purity measurement of tritium released from a tritium storage bed, and the trace of ^{3}He release was successfully measured during heating

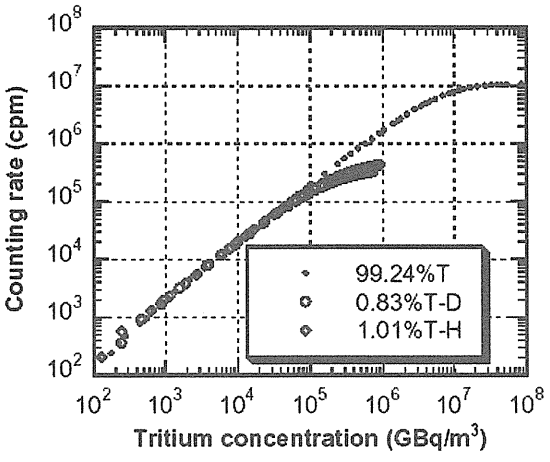

Fig. IV.7.2-1 The relationship between X-ray counting rate and tritium concentration for pure tritium and tritium mixtures diluted with deuterium or hydrogen.

the bed for the release of tritium. These results show that this technique is promising for tritium accountancy in the fuel processing system of fusion reactors [7.3-1, 7.3-2].

In order to confirm long-term reliability of the developed tritium storage bed having self tritium accounting function with in-bed gas flowing calorimetry method, its tritium accounting function was investigated after 5-years stable storage of about 5 g of tritium. As the result, its long-term reliability was confirmed by finding that its sensitivity and its accuracy were well maintained.

References

7.3-1 Shu, W. M., *et al., J. Nucl. Mater.*, **313-316**, 584 (2003)
7.3-2 Shu, W. M., *et al., J. Nucl. Sci. Technol.*, **40**, 1019 (2003).

7.3 Basic Study on Tritium Behavior

As a part of the collaboration program with universities utilizing the Caisson Assembly for Tritium Safety Study (CATS) of JAERI which consists of a 12 m^3 airtight enclosure (caisson) for tritium release, application of bio-reactor utilizing hydrogen oxidation bacteria on the tritium removal from the air has been studied under the collaboration with Ibaraki University. As a result of a series of experiment, it was succeeded to remove more than 85% of tritium from the air in the caisson, the conditions of which were the flow rate of 100 cm^3/min, tritium concentration of around 200 Bq/cm^3 and at the room temperature. This result encourages the study of hydrogen oxidation bacteria for its practical applications. In the collaboration with Kyushu University, the interaction study between tritium vapor and cement paste has been carried out for the estimation of tritium behavior in the concrete wall of tritium handling rooms and its efficient removal. The results revealed that the fundamental mechanism of tritium vapor penetration into the cement paste could be explained combination of adsorption process of tritium vapor on the cement surface and the isotope exchange reaction of hydrogen on the surface.

As a part of tritium inventory control study, the removal experiment of carbon/hydrogen co-deposited layer generated on plasma facing tiles of JT-60 and TFTR has been performed by means of KrF excimer laser (wave length: 192 nm) pulse irradiation for developing an effective removal technique of tritium involved in co-deposited layer. The results showed that the excimer laser irradiation could remove the co-deposited layer with tritium with almost no damage on the base material of the tile. In addition, it was revealed that the excimer laser irradiator coupled with a

tritium monitor could be used for analyzing the depth profiles of tritium in materials because a pulse of excimer laser removed quite a thin layer of the surface by ablation.

Under the collaboration with department of fusion plasma research and some universities, tritium behavior in the JT-60 vacuum vessel has been investigated. In this study, the tritium exhaust amount and its chemical form from the vacuum vessel were measured for all JT-60 operation stages, i.e. air vent, vacuum pumping, wall cleaning and tokamak discharge stages. The results at the air vent stage revealed that the tritium was exhausted as water form when the vacuum vessel atmosphere contained vapor, and tritium exhaust amount was proportional to the vapor concentration as shown in Fig. IV.7.3-1. During the wall conditioning and plasma experiment, ratio of water form in exhausted tritium was observed to decrease from almost 100% to a negligibly small level with the progress of the wall conditioning of JT-60.

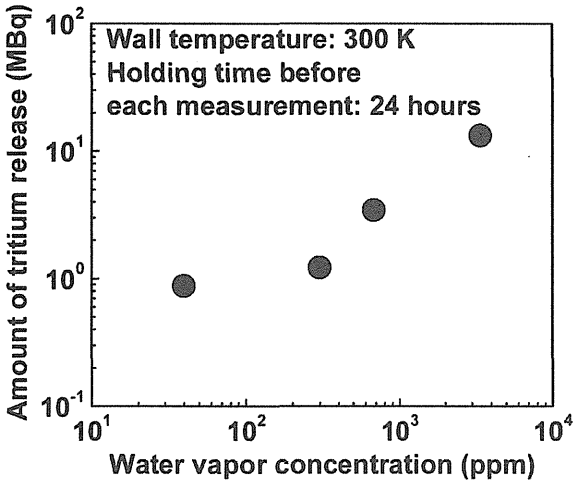

Fig. IV.7.3-1 Dependence of tritium release amount on vapor concentration in the air introduced to JT-60 vacuum vessel at the air vent stage.

7.4 Successful Operation Results of Tritium Safety Systems in TPL

The safety system of Tritium Process Laboratory (TPL) consists of Glove Box Gas Purification System (GPS), Air Cleanup System (ACS), Effluent Tritium Removal System (ERS) and Dryer Regeneration System (DRS). The GDS was operated for about 8,000 hours by controlling tritium concentration in the glove boxes, in which experimental apparatus are installed. The ACS was operated for cleaning 150,000 m^3 of air during the experiments of Caisson Assembly and maintenance of the glove boxes, experimental apparatus and other tritium operations. The ERS removed about 13 TBq of tritium mainly out of the exhaust gas from the experimental apparatus. The DRS removed 80 liters of tritiated water (180 GBq) from the GPS and ACS dryers.

The tritium safety system of TPL has been in service to support operations with use of tritium since 1988. Some maintenance work such as periodical inspection or replacement have been carried out in this fiscal year for some rotating machines. Fig. IV.7.4-1 shows monthly environmental tritium release from the stack of TPL during this fiscal year. Total amount of released tritium was 33 GB, which is sufficiently lower than the target value at TPL.

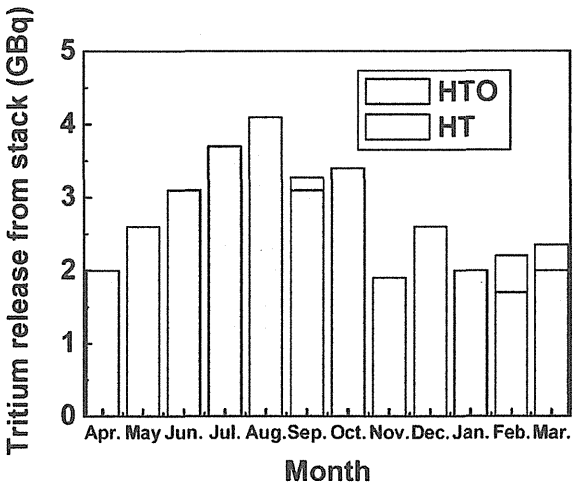

Fig. IV.7.4-1 Monthly environmental tritium release from the stack of TPL during this fiscal year.

8. Fusion Neutronics

8.1 Blanket Neutronics Experiments

8.1.1 Analysis of Three Layers Experiment

In order to examine the accuracy of the Tritium Breeding Ratio (TBR) of the blanket design proposed by JAERI, D-T neutronics experiments of blanket mock-up assemblies were performed at JAERI FNS. The mock-up assemblies consisted of lithium-6 enriched Li_2TiO_3 (40 atom%), beryllium, the ferric steel F82H and a SS-reflector. The densities of main atoms and impurities in the component materials were carefully analyzed by the Inductively Coupled Plasma (ICP) mass-spectroscopy up to the order of ppm. Neutron absorption effect of impurities in the beryllium block was investigated by a pulsed neutron experiment [8.1-1]. The Tritium Production rates (TPR) in the enriched Li_2TiO_3 of the mock-up were measured by Li_2CO_3 pellet detection method. The measured TPR was analyzed by the Monte Carlo codes MCNP-4C with the nuclear data libraries JENDL-3.2, and FENDL-2. Figure IV.8.1-1 shows a result of TPRs obtained from the experiment and the calculation as a function of the depth of Li_2TiO_3 layer. It was found that the values agreed each other within 10 %. In addition, the accuracy of TPR was significantly influenced by the accuracy of the Li-isotope density in the Li_2TiO_3.

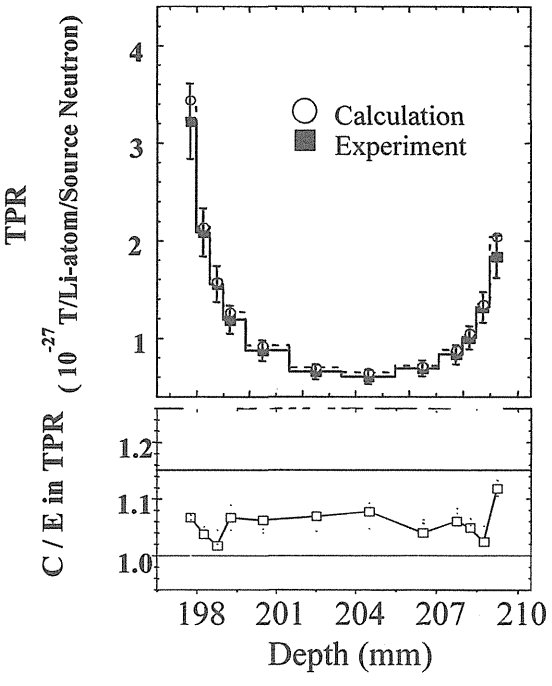

Fig. IV.8.1-1 Tritium production rate (TPR) and C/E value on the 3rd Li_2TiO_3 layer.

8.1.2 Tungsten Armor Effect on TBR

In the blanket design proposed by JAERI, the local TBR is around 1.4 - 1.5 for the case without an armor on the first wall. It is expected that tungsten (W) armors may reduce the TBR to less than unity. In order to evaluate the tungsten armor effect on TBR experimentally, neutronics experiments have been performed by using DT neutrons. A breeding blanket mockup, composed of 16-mm thick F82H, 12-mm thick Li_2TiO_3 and 200-mm thick Be with about 660 mm in height and about 660 mm in width, was installed about 450 mm apart from the DT neutron source. In the experiments three types of mockups were tested: without the armor; with 12.6-mm thick W armor; and with 25.2-mm thick W armor. Fifteen pieces of Li_2CO_3 pellets were embedded in the Li_2TiO_3. After the irradiation, induced radioactivities were measured by beta ray intensity of these pellets with a liquid scintillation counter, and TPR was evaluated. Figure IV.8.1-2 shows the ratio of TPR in the mock-up with the W armor to that without the armor. By installing 25.2-mm and 12.6-mm thick W armors, TPRs were reduced by 14 and 12 %, at the maximum, respectively, and integrated TPRs in the Li_2TiO_3 layer were reduced by 8 and 3 % compared with TPR obtained without the armor, respectively. In the blanket design proposed by JAERI, it is expected that the reduction of the TBR is less than 2 % as the thickness of the W armor is less than 5 mm.

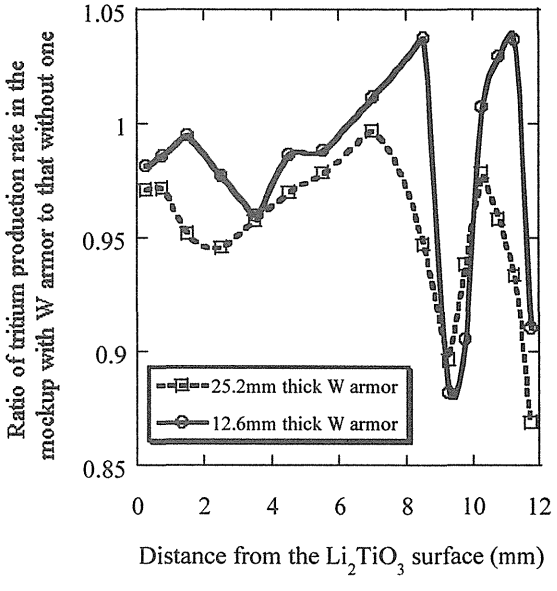

Fig. IV.8.1-2 Ratio of the tritium production rate in the mock with the W armor to that without one.

8.1.3 Impact of the D-T Source Reflector on TPR in One-breeder Layer Mock-up Experiments

In the fusion reactor, the neutron spectrum incident on the blanket contains two components: high-energy neutrons from the D-T plasma, and low energy neutrons, reflected on the opposite side of the reactor vacuum chamber. The stated situation was simulated in two integral experiments on the blanket mock-up irradiated by neutrons from the D-T source; the first experiment was performed with the reflector, and the second one without the reflector. The integral experiments were performed with the mock-up comprising F82H, lithium titanate, and beryllium layers, with a thickness of 16 mm, 12 mm and 200 mm, respectively.

A reasonable agreement between experimental and calculated results exists for tritium production via the $^{6}Li(n,\alpha)^{3}H$ reaction in the experiment with the mock-up irradiated by neutrons from the pure D-T source. The ratio of calculated to experimental TPR-6 value was about 1.02. Analysis of the data obtained in experiments with the mock-up irradiated by neutrons from the D-T source with a reflector, show that the calculation overestimates the tritium production data. The average ratio of the calculated to experimental TPR value was about 1.14. The source reflector drastically changes the incoming neutron spectrum for the blanket mock-up with an increase in the tritium production rate by more than two times. Analysis indicates that one of the possible reasons for the observed overestimation in the experiment with the source reflector is an inadequate description of the backward scattering neutron contribution from the SS316 source reflector. Obtained results demonstrated the importance of an adequate description of backward scattering neutrons for accurate tritium breeding predictions in layers located near the first wall of the blanket.

References

8.1-1 Verzilov Y., *et al., J. Nucl. Mater.*, **329-333**, 1337 (2004).

8.2 Shielding Experiments

In the fusion reactor, a personnel access outside the biological shield composed of concrete is required for maintenance several days after shutdown. It is important to reduce the decay gamma-ray dose rates to make this work possible. Of equal importance is the reduction of the residual radioactive nuclei from the viewpoint of the radioactive waste management. By modifying the low activation concrete Wide-use type 1 for the fission reactor [8.2-1], the boron-doped low activation concrete was developed for the D-D fusion device [8.2-2]. In the present study, the application of this boron-doped low activation concrete to the D-T fusion reactor was examined experimentally.

The induced radioactivities were evaluated by the DT neutron irradiation test for 12 hours using FNS. Figure IV.8.2-1 shows the induced radioactivities measured in the standard sample and the low activation concrete, and the ratio of the radioactivities of the standard sample to those of the low activation concrete. Radioactivities are reduced drastically in the boron-doped low activation concrete compared with those in a standard sample except in the case of a short period of cooling 7 - 10 days after irradiation. It is concluded that the boron-doped low activation concrete used in the present study is highly useful as a shielding material [8.2-3].

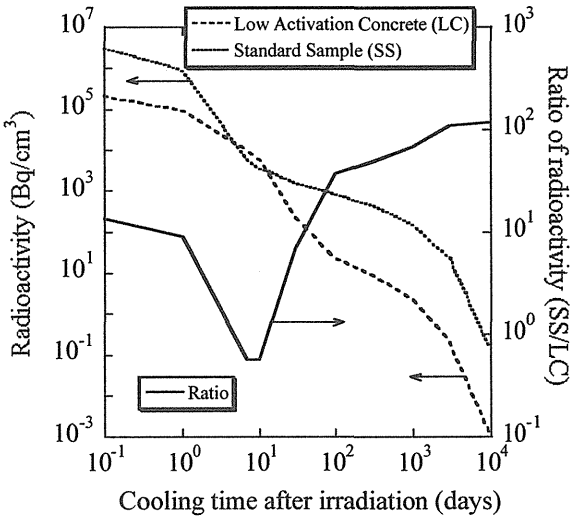

Fig. IV.8.2-1 Induced radioactivities detected in the standard sample and the low activation concrete, and the ratio of the radioactivities of the standard sample to those of the low activation concrete.

References

8.2-1 Kinno, M., *et al., J. Nucl. Sci. Technol.*, **39**, 1275 (2002).
8.2-2 Morioka, *Fus. Eng. Des.*, **63-64**, 115 (2002).
8.2-3 Sato, S., *et al., J. Nucl. Sci. Technol.*, **Suppl.4**,66 (2004).

8.3 Cross Section Measurements of Fusion Materials

8.3.1 Charged-particle Emission DDX Measurement

It is important to measure Double-Differential Cross sections of charged particles (DDXc) induced with DT neutron for evaluations of the Kinetic Energy Released in Materials (KERMA) and the Primary Knock-on Atom (PKA) spectrum in fusion reactor materials. However, only a few data have been obtained because of the difficulty for a high background condition of radiation and small cross sections.

A development of a new spectrometer for measurement of DDXc has been carried out using a DT neutron beam source, which closely realizes a collimated neutron beam with the diameter of 2 cm under a very low background condition. A telescope system consisting of two silicon surface barrier diodes of ΔE and E, and a two-dimensional Multi-Channel Analyzer (MCA) were employed for an identification of charged-particle species. As the first step, we measured α-particle emission DDX of aluminum in order to confirm the validity of the new spectrometer. In the spectrometer we eliminated almost all noise signals using coincidence detection technique and statistically accurate DDXc data were successfully obtained with relatively short measurement time and good energy resolution.

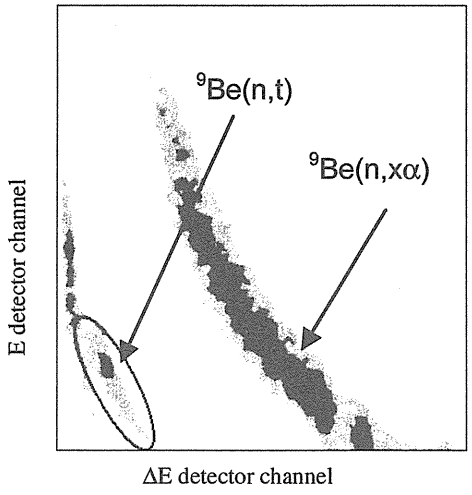

Fig.IV.8.3-1 Measured 2D-spectrum of emitted charged-particle from ^{9}Be at 30 deg.

Then, we measured DDXc of beryllium because of its importance for a fusion reactor design, especially in the blanket field. The measured 2D-spectrum at a scattering angle of 30 degree in Lab. system is shown in Fig. IV.8.3-1. We could clearly derive α energy spectrum from ^{9}Be(n,xα) reactions and tritium energy spectrum from ^{9}Be(n,t) reaction distinguished from α signals. The fact that we can measure such a small DDXc for ^{9}Be(n, t) reaction suggests the superiority of the present method to other conventional methods. We are continuing the measurements of DDXc for important fusion materials using the spectrometer.

8.3.2 Activation Cross Sections of IFMIF Accelerator Structural Materials

In the design of IFMIF (International Fusion Materials Irradiation Facility), long-term operation with more than 70 % total facility availability is required. However, the activation of structural materials composing the IFMIF accelerator due to the bombardment by deuteron beam limits the maintenance time and makes the long-term operation difficult. Therefore, the accurate estimation of deuteron-induced radioactivity and the selection of low activation structural materials are important. Thus, measurements of deuteron-induced activation cross sections for main structural materials (aluminum, copper and tungsten) were performed on the basis of a stacked-foil technique at TIARA. As a result of the experiment, we have obtained the activation cross sections for the reactions ^{27}Al(d,x)^{27}Mg or ^{24}Na, ^{nat}Cu(d,x)^{62,63}Zn or ^{61,64}Cu, and ^{nat}W(d,x)^{187}W or $^{181-184,186}$Re in 22-40 MeV range. These results were compared with another experimental cross sections and estimated data in the ACSELAM library. Figure IV.8.3-2 shows the cross sections for the ^{nat}Cu(d,x)^{64}Cu.

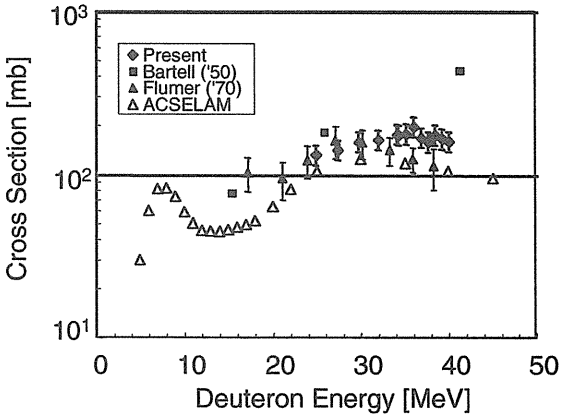

Fig. IV.8.3-2 Cross sections for the ^{nat}Cu(d,x)^{64}Cu reaction.

8.4. Water Cherenkov Detector with WLS Fiber

Further research of the water Cherenkov detector as a D-T fusion power monitor [8.4-1] requires development

of an efficient light collection system which will be able to function in a radiation environment.

The present detector design consists of a water radiator, a light collection system, an optical fiber bundle and a remotely located light detector. A water radiator is a quartz tube surrounded by the Teflon reflector, which is being filled with water flowing from the vicinity of the D-T neutron source. Two light collection systems were tested in conditions that were created by operation of the neutron source in direct and pulse modes. The first light collection system is based on the wavelength shifting fiber BCF-91 (Bicron) twined around the quartz tube as shown in Fig.IV.8.4-1, and the second system is based on quartz fibers overlooking the quartz tube. It was discovered that the first system has a reasonable light collection efficiency and a temporal resolution as well. Nevertheless, due to high sensitivity of the Wave Length Shifting (WLS) fiber to external radiation, it is not appropriate to use this system in the vicinity of the neutron source. The second system appears to be more suitable for this purpose, although further improvements of the light collection efficiency are essential. A new design of the system is in progress.

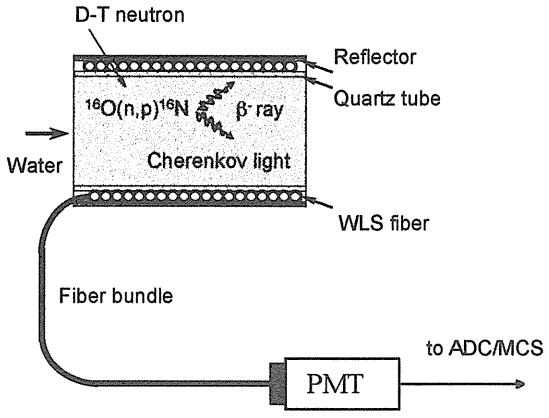

Fig.IV.8.4-1 Water Cherenkov detector with WLS fiber.

References

8.4-1 Verzilov Y., *et al., J. Nucl. Sci. Technol.*, **Suppl.4**, 395 (2004).

8.5. Operation of the FNS Facility

Operation of the FNS facility has been carried out to cope with various operation patterns in a variety of experiments requested by JAERI and the other collaborative parties. The total operation time was 786 hours in the fiscal year 2003. In those experiments, seven fixed targets containing 370 GBq tritium in total were consumed for the 80° beam line. In addition, two rotating targets containing 33 TBq tritium were for the 0° beam line. The amount of tritium processed by the Tritium Adsorption Processor (TAP) system reached 7.58 TBq.

Maintenance activities performed during the fiscal year are as follows. As a result of the periodic check-up, the oil-free vacuum pumps and CRYO pump for 80° beam line were overhauled. The control circuit of the accelerator was inspected every six months.

Since FNS handles tritiated titan type tritium target and processes many tritium contaminated wastes, it is important to know the amount of tritium activity in the target and the tritium wastes for radioactivity control. The dose rate of X-rays from the fixed tritiated titanium target was measured using an ion chamber to evaluate the tritium activity. The tritiated titanium of the large rotating tritium target and a contaminated waste were measured by changing the distance between the detector and the sample. The ion chamber (Aloka ICS313) that has the effective volume of 300 cm^3 and a carbon coated polyethylene window 5 mg/cm^2 in mass thickness was used for the measurement.

Figure IV.8.5-1 shows the relation between the dose rate of the X-ray emitted from the tritiated titanium and the tritium activity. The dose rate in logarithmic scale shows a good linearity to the tritium activity in logarithmic scale. As the result, it was made clear that the tritium activity can be measured in the range from 40MBq to 40TBq.

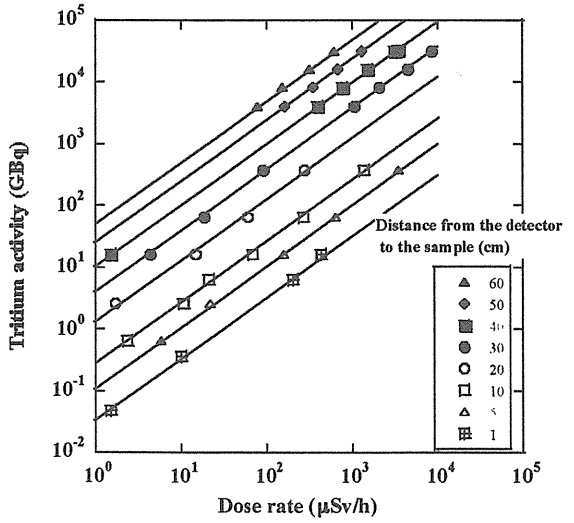

Fig.IV.8.5-1 Relation of the X-ray dose rate from the tritiated titan and the tritium activity.

9 Vacuum Technology

9.1 Performance Test of New Vacuum Pump with Transfer- Coating Technique

In the study on the vacuum pumping system of the fusion reactor, development of a new type roughing vacuum pump has been continued. This pump is a scroll type vacuum pump [9.1-1] with the complete dry-sealed performance, and has a special bearing system by the transfer coating technique in order to improve the lubrication characteristics. The performance tests for about 300 hours have been performed following single-handed tests for about 1,000 hours. In this tests, this pump was installed in the vacuum pumping system of JVX apparatus (Fig, IV.9.1-1) in order to simulate the operational condition. The results showed that the new type scroll pump had almost the same vacuum performance (ultimate pressure : 1 Pa , slight increase of friction noise～5 dB) as the conventional type pump in the operational condition as well as those demonstrated by the previous single-handed tests.

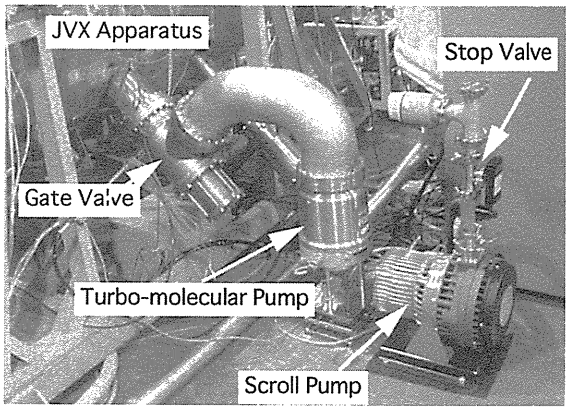

Fig. IV.9.1-1 Installation of the new type scroll pump in the vacuum Pumping system of JVX apparatus.

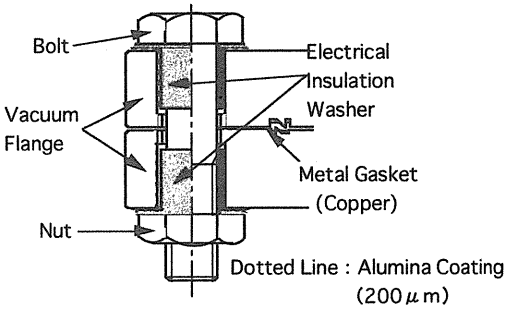

Fig. IV.9.1-2 Bolting of vacuum vessel flange with a new electrical insulation washer

References

9.1-1 Abe T., *et al.*, "Double Wrap Dry Scroll Vacuum Pump Having a Compressed Gas Cooling Passage Disposed in the Scroll Shaft", *US Patent* (US006249405A), Nov.21, 2000.

9.2 Development of an Electrical Insulation Washer Coated by Alumina Film

In the study on the prospective technique to improve surface condition [9.2-1], an electrical insulation washer with alumina film coated by plasma spraying method was developed. This washer was used for bolting the flange of vacuum vessel (Fig. IV.9.1-2). It passed more than 5 years after bolting, and no remarkable decrease of electrical insulation (more than 1,000MΩ /1,000V) was observed.

References

9.2-1 Kanari, M., *et al.*, "Repeated Impact Test on Plasma Sprayed Alumina Insulation Film for Fusion Reactor", *J. At. Energy Soc. Japan* ,Vol.43, No.12 (2001) 1228.

V. International Thermonuclear Experimental Reactor (ITER)

1. Overview of the ITER Program and Activities

1.1 ITER Transitional Arrangements (ITA)

In January 2003 the ITER Transitional Arrangements (ITA) started under the auspices of the IAEA, following the successful completion of the Coordinated Technical Activities (CTA). The purpose of the ITA is to prepare for an efficient start of the Agreement, if and when so decided, and to maintain the integrity of the ITER Project. Along the work plan approved by the ITER Preparatory Committee (February 2003), the Design and R&D Task works started among the Participant Teams (PTs). Based on the task agreement between the International Team (IT) and each PT, these shared works make the implementation of preparing the procurement documents for facilities and equipments that are so scheduled as to be ordered at the early stage of ITER construction such as superconducting magnets and vacuum vessel sectors. Since 2003 JAERI has been in charge of seventeen Design Task works which are described in 2.1.

1.2 Progress of Negotiations and Prospective Schedules

Governmental Negotiation meetings among Canada, China, the European Union, Japan, the Russian Federation and the United States of America were held continuously to reach an agreement on the joint implementation of ITER project. In June 2003 the Republic of Korea also joined the Negotiation. The delegates discussed the structure and management system of the international organization that will implement the ITER project, the staffing and resources of the organization, the procurement allocation of ITER components, etc., as well as the siting of ITER. Four candidate sites had been proposed at Clarington in Canada, Vandellos in Spain, Cadarache in France, and Rokkasho in Japan. In November 2003 Cadarache was chosen as EU's preferred site, and Canada withdrew from the Negotiations in December 2003. Then the two candidate sites, Cadarache and Rokkasho, have been put forward. The schedule for ITER construction is shown in Table V.1.2-1 with recent progress as of March 2004.

Table V.1.2-1 Schedule for ITER Construction

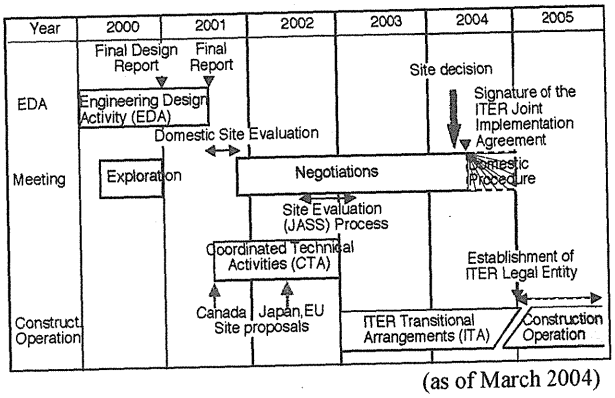

(as of March 2004)

2. Domestic Activities

2.1 ITA Design Task

2.1.1 Vacuum Vessel

Four fabrication procedures of the VV sector have been considered and compared between them. One is a procedure of completing inner shell firstly. The others are methods of connecting poloidal segments. It is recommended that an inboard complete segment and the other segments with inner shell and ribs are assembled to the poloidal cross section then outboard outer shells are welded. For the welding of the VV fabrication, electron beam weld or tungsten inert gas weld (TIG) / narrow gap TIG can be applicable for the inner shell and TIG for outer shell. As a non-destructive test (NDT) method, radiographic test can be applicable for inner shell, but some modification of NDT method may be required for outer shell.

Fabrication procedures of field joints between VV sectors and between a VV sector and ports in the tokamak pit have been tabled including adjusting jigs, weld joints and leak test methods. Progress penetrant test is proposed for testing outer-shell welds and PPT and ultrasonic test for inner shell welds. For leak test of the field joints of VV sector and port, sniffer method is applied for outer shell, and vacuum method for inner and outer shells, respectively.

Reinforcements of the lower port stub region and FEM structural analyses have been performed for the independent VV supports located under the lower ports. As a result, the stresses are within the allowable values for eighteen VV supports, but further study will be required for nine VV supports.

2.1.2 Structural Analysis of the Central Solenoid

The detailed design of the Central Solenoid (CS) and its

procurement specification are being prepared by the ITER IT and PTs. The reference design of the CS is to use single jacket made of stainless steel (JK2LB, see section IV.1.3) that has been developed by JA PT. The CS consists of six identical winding modules and preload structure composed of tie plates, key blocks, wedge blocks, shims and buffer zones, as shown in Fig. V.2.1-1. The preload structure is required to keep the contact between modules and to maintain modules in compressive stress during ITER plasma operations. JA PT performed detailed stress analyses on the CS to validate the design including the preload structure.

The preload structure produces compressive load on the CS modules during assembly at room temperature and an additional load is obtained during cooldown to 4 K. Preloading at room temperature is performed as follows: the tie plates are heated up to a certain temperature to create a gap between the top/bottom structure and module, shims are inserted into the gap, and then the tie plates are cooled to room temperature, resulting in producing a compressive load to the modules. Additional load is produced during cool down by thermal contraction difference between the winding pack (dominated by JK2LB that shrinks less than stainless steel) and tie plates (stainless steel). Stress analyses using axisymmetric 2D model were preformed with simulating this preloading procedure in order to confirm that sufficient compressive load can be obtained.

A preliminary analysis indicated that unexpected partial tensile stress occurs in the CS module, which may damage insulation material in the winding pack. To eliminate the partial tensile stress, we tried to obtain as much preload as possible with the preload structure. In case that the heating temperature of the tie plates is 130℃, axial compressive stress of 96 MPa can be obtained at the equatorial plan, as shown in Fig. V.2.1-2. Above this heating temperature, the stress of the tie plates was found to exceed the allowable value of stainless steel. As shown in the figures, compressive stress dominates in all CS modules, and the area of the axial tensile stress was estimated to be only 6% of the upper-most module, but still remained. Further detailed stress analysis indicated that the partial tensile stress in the winding pack was caused by the difference of the thermal contractions between the insulation and winding pack. To completely eliminate the local tensile stress at this region, the use of debonding layer was suggested.

In these analyses, the maximum Tresca stress of the conductor was calculated to be 545 MPa which is lower than the acceptable value of 667 MPa. Thus the detailed stress analyses are almost complete to validate the ITER CS design.

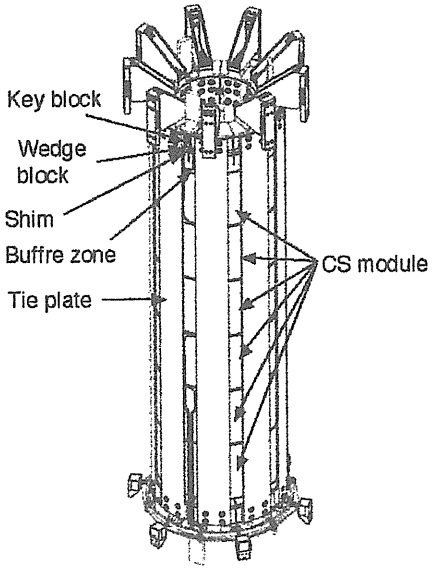

Fig. V.2.1-1 ITER CS consisting of six modules and preload structure.

2.1.3 Development of Detailed Neutral Beam Interfaces with Buildings and Site

The ITER neutral beam (NB) system is a large system with a considerable impact on the design and layout of

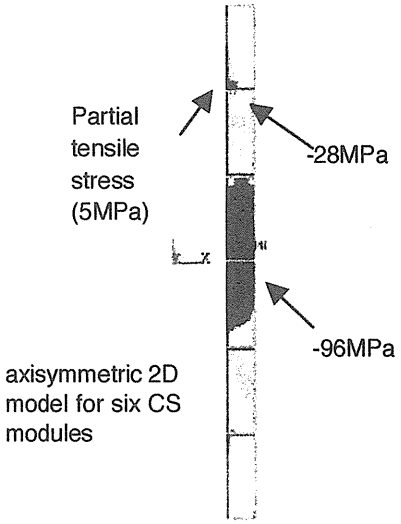

Fig. V.2.1-2 Axial stress distribution in the CS at the severest condition during the plasma operation in case that heating temperature of the tie plates is 130℃. Positive stress indicates tension.

the main tokamak complex and the site layout. The present work provides further detailed information of the NB power supply design sufficient to develop the layout in the NB power supply yard, to be done by the International Team. A skeleton of the NB power supply system has been drawn with identification codes of major components. Lists of the major components of the power supply with dimensions were also produced. The NB power supply layout in the power supply yard has been reviewed based on the major components. A vertical view of the layout with connection of the transmission line 1 has been designed.

Expert advices for the design improvement activities by the IT have been provided from the JA PT. Especially for the analysis of the neutron streaming under the new layout of the power supply yard proposed by the IT. The simulation was carried out by the IT with advices of the JA PT for the model.

2.1.4 Participation of Benchmarking of ECCD Codes

In ITER inductive scenarios, neoclassical tearing modes (NTMs) is estimated to emerge in the low normalized pressure, b, and to suppress the further increase of b. Therefore, it is important to control NTMs by the localized current, and electron cyclotron (EC) waves are planed to be launched for the local current drive in ITER. In order to control the NTMs by EC current drive (ECCD), it is required to estimate the key parameters of EC wave launching, such as the position of the mirror, the launching angles, the beam width, the beam divergence, and the beam power. As the first step in the study of launching parameters of EC waves for the NTMs control, benchmarking has been performing among the ECCD codes in the world: ECWGB, OGRAY, BANDIT-3D, TORAY-GA, TORAY-FOM, TORBEAM and RADAR which is developed in JAERI. A method of benchmarking is to search the relation between toroidal and poloidal injection angle for current drive on q=3/2 and q=2/1 magnetic surfaces. By comparing the results of all codes, it is found that the obtained total driven currents are almost similar but the injection angles are distributed in a range of about 5 degrees.

2.1.5 Blanket

Based on updated disruption scenarios, detailed 3-D EM analyses have been performed for linear current decay with 40 ms quench time. Almost all EM forces due to eddy currents are kept below the design allowable limits except for the radial force acting on the flexible support of module #5 under major disruption (MD), the poloidal force on the key of module #9 also under MD and the poloidal force on the key of module #9 under fast upward vertical displacement event. For module #5, design improvement to reduce the eddy current has been made by the IT through deeper slots and higher water ratio in the SS block. This feature increases the effective electrical resistivity of the shield block and applies to all modules.

On the design of module #4, structures and fabrication methods to simplify the back shape of the module and improve the flow distribution and pressure loss within the module have been investigated based on the concepts developed by the IT. As for module #10, a modified design developed by the IT has been examined, which progressively incorporated toroidal slots to reduce the EM loads with preventing the interference with the manifold.

With dynamic analyses considering several gap combinations between the key and the key groove, damping effects and EM load waveforms, the dynamic amplification factors for the inter-modular key of module #1 and the stub key of module #18 have been estimated. Load distributions on the inter-modular key have been analyzed taking the gap condition between the key and the key groove into account. The moment around radial axis (Mr) with inclined gap width (inclined module attachment) is 50 % higher than that with uniform gap width. Based on these results, detail stress analyses of the inter-modular key have been performed with thermal load due to nuclear heating, EM moment and the force due to TF coil fast discharge. The EM moment around radial axis is dominant for the primary stress.

2.1.6 Operation Scenario

The following four subtasks has been studied; 1) the analyses of coil currents, magnetic field configurations, electromagnetic forces and available flux for burn, considering the recent design improvement of PF and CS coils, 2) the plasma start-up scenario from the divertor region, 3) the early divertor scenario in order to reduce the thermal load on the limiter, and 4) the possibility of reduction of the length of the outer

blanket support in the buffle region. The results of the subtasks are summarized as follows:

1) The maximum magnetic field of CS coil is reduced compared with the previous design. However, by increasing the radius and the current of CS coils, the burn flux of the present design can be larger than that of the previous CS design.
2) The start-up of plasma from the divertor region is studied. In case that the stray field at the initial magnetization is less than 1mT and the currents of the coils are maintained within the limits, the magnetic flux available at the initial magnetization is reduced to about 90Wb. Then, the 15MA operation scenario is not possible due to insufficient flux for the operation. However, even with these limitations, there is possibility of low current plasma operation (10-13MA).
3) A new scenario with the formation of the divertor configuration at a lower plasma current of 4.5 MA was examined. It was found that the currents, the operation voltages, the maximum fields and electro magnetic forces of the coils were within their design limits and the plasma current can be possible up to 15MA. This scenario may be more effective to reduce the thermal load on the limiter.
4) In order to reduce the length of the outer blanket support in the buffle region, the thickness of this support should be larger than or equal to 60mm and the copper cladding with 1.2mm thickness have to be attached on the surface of the support, to maintain the same level of the plasma controllability as FDR design in 2001.

2.1.7 Tokamak Assembly

ITER toroidal field coil (TF coil) is composed of 18 coils. The wedges of the adjacent TF coils have to be assembled with a target gap less than 0.3 mm between them. This is the most critical for ITER tokamak assembly. The followings are therefore studied.

Flange surface of the gravity support of the TF coil is proposed as a reference surface in order to specify the tolerance for the manufacturing of the TF coil in the factory. The basic tolerances of manufacturing in the factory and assembly in the tokamak pit are expected 0.005 mm/m and 1.0 mm including measuring error, respectively.

Minimization of the deformation of the TF coil during lifting by the crane is required in order to meet the requirement of the target gap of 0.3 mm between the wedges of the TF coils for final installation. FEM analysis shows the deformation of the TF coil is reduced to 0.2 mm in the toroidal direction, by proposing a temporary lower support for vacuum vessel (VV) and a modified lifting tool for VV.

Clockwise assembly procedure is proposed for 18 TF coil. The wedge of a new TF coil is adjusted on that of the adjacent TF coil already assembled in the pit one by one. The last TF coil only is assembled from the radial and outer direction into the space between the first and 17th TF coils. The assembly direction of the last TF coil agrees that of the crane traveling for precise positioning. The shim plates on the both wedge surfaces of the last TF coil for the gap control are customized after measurement of the gaps between the last TF coil and two adjacent TF coils.

2.1.8 Remote Maintenance

Remote handling scenario/procedure for blanket maintenance are studied to improve the major interfaces between blanket module and remote handling equipment, such as key configuration and end-effector, based on the latest IT design.

According to the change of blanket segmentation proposed by the IT in 2002, the remote handling scenario/procedure for blanket maintenance is reexamined. To avid the interference between modules and remote handling equipment, kinematic (CAD) analyses are performed. As a result, some dimensions of the remote handling equipment, such as arm length, rotational mechanism around the rail and height of end-effector, are modified, in addition to the proposal of the module configuration changes.

Design of the front access holes of the modules for module gripping and electrical strap connection is also changed. In this case, an integrated mechanism composed of three degrees of freedom is required in the strict space for 1) sliding the gripper for grasping the module, 2) locking the gripper for fail safe and 3) fixing the bolt for temporally module fixing. Independent front access holes for module gripping and electrical strap connection are proposed based on the latest module design and space limitation so as to solve the problem.

As for coaxial cooling pipe proposed by the IT, the assembly tolerance has to be controlled to keep the required quality because the coaxial pipe is composed of a multi-alignment structure. The final assembly tolerance of the edges for welding is required less than the target 0.3 mm based on the R&D result using YAG laser. Sensitivity study of the assembly tolerance of the coaxial pipe is performed so as to assess the feasibility of the multi-alignment structure. As a result, the machining tolerance of each assembly element is required less than 0.1 mm in order to satisfy the target gap less than 0.3 mm for YAG laser welding.

2.1.9 Tokamak Building

The penetration of NB ports through the bio shield wall intersects the load path for dead weight and other loads from the top of the bio shield wall to the basement. The FEM analysis of the bio shield wall was carried out by the JA PT during EDA, indicating that the excess of in-plane shear stress around the NB cells penetrations was large and might require significant structural improvement. The purpose of this task is to develop the feasible and cost-effective design improvement. The results are summarized bellow.

According to the latest design, although some conditions are improved to reduce the local stress concentration, the maximum shear stress in the vertical direction around the NB cells penetrations still exceeds the allowable shear stress of concrete for long term loading case. Therefore, a certain reinforcement around the NB cells penetrations is still required. The excess of shear stress in the vertical direction around the NB cells penetrations is about 13% for the allowable shear stress of concrete (specified concrete strength: $Fc=300kg/cm^2$).

As for long term loading cases, the following schemes may be effective; a) Increasing concrete section area (increasing thickness of wall and/or reducing size of penetrations), b) Increasing concrete strength (use of high strength concrete), c) Increasing section strength with mixed structure (steel reinforced concrete structure (SRC), steel plate reinforced concrete structure, etc.). As for short term loading cases, the reinforcing with additional steel rebars may be effective.

As an example, the reinforcement using SRC was evaluated based on the Japanese design codes for reference. It is confirmed that the strength around penetrations will be increased appropriately and the value of stress may be lower than the allowable one in this plan.

2.1.10 Neutronics

Three dimensional Monte Carlo shielding analyses are conducted on the ITER NBI duct for the nuclear and bremsstrahlung radiation. The detailed distribution is evaluated about the nuclear heating rate and surface heat load of the NBI duct wall by the neutron and photon transport calculation. The analytical representations of these nuclear responses are established as a function of the distance from the blanket surface. It is clarified that these are different between the duct wall facing the plasma and that hidden from the plasma, and also between the blanket and vacuum vessel region.

Neutron streaming effects were analyzed with a simple design code DUCT-III for several designs of the pressure relief line that is connected to the NBI duct. The cross section, length and the number of bends of the line were examined in the analysis to suppress the activation of the rupture disk installed on the way of the line. The dose rate around the disk in the proposed design condition of the line is considered to be low enough so that workers can get access to the disk for the maintenance.

2.2 Site Related Activities

2.2.1 Transportation

Transportation of components is one of the highly important issues for smooth construction of ITER. At that stage very frequent transportation of materials and components of regular size and weights would be required as well as heavy and large components during the construction. The impact of the transportation issue to the execution of the ITER project is therefore quite strong. In particular, the transportation of more than 300 ITER components, such as vacuum vessel sector (550 ton) and TF coil (400 ton), over the weight of 40 ton is critical, so that it will be therefore a key item for the ITER site selection. In Japan, Rokkasho candidate site is located near seashore, resulting in no limitation for ground transportation and no potential problem for unloading. If the heaviest component of PF-3 coil (750 ton) can be transported to Rokkasho

candidate site, it is attractive for the project compared with on-site fabrication planed in Cadarache candidate site. Here the weight in the parentheses is based on the latest information from the IT, including additional weight for packing.

Therefore, the manufacturing, transportation and assembly of PF-3 coil have been examined, taking into account of quality control, factory fabrication, transportation, construction and operation of on-site factory, based on our experience of large devices such as JT-60, Large Helical Device, superconducting magnets and vacuum vessel. The detailed results are described below.

After manufacturing, PF coil is temporarily supported and packed as a package, considering prevention of excessive deformation due to the dead weight and forces applied during transportation such as vibration. The packed PF coils is put on a platform or dolly at lay down condition and the platform or dolly with the PF coil is transported using a regular barge to the port near Rokkasho candidate site. The dolly can transport heavy component with a weight of about 3,000 ton by combination of several standard units: this has enough capacity to transport the PF coil. At the port near the site, the platform or dolly is unloaded using roll-on/roll-off method and transports the PF coil to the site.

There are two possible routs from the port to Rokkasho candidate site, depending on the size of PF coils, which are the existing road (route R2) and the dedicated road (route R1) planned for transportation of heavy component such as PF-3 coil, as shown in Fig. V2.2-1. The distance and slope of these routes are 7 km and 2.8 %, 4 km and 4 %, respectively, which are suitable for the dolly transportation.

Based on the above result, we have concluded that off-site fabrication of PF-3 coil has significant technical benefits. In addition, off-site fabrication provides significant schedule saving of around 2 years for the coil construction, and it also avoids the project risks in schedule delay by the independent fabrication without any interaction to the on-site construction of the other facilities.

2.2.2 Seismic Issues

Following the discussion in the 1st Ministerial Meeting on 20th December 2003, additional investigation and assessment on seismic issues have been made for the Rokkasho candidate site and prepared for the site technical assessment among the ITER Parties. The investigation covers a wide range of technical data and evaluation in addition to those presented in the Joint Specific Site Assessment (JASS). The main results confirmed are summarized below.

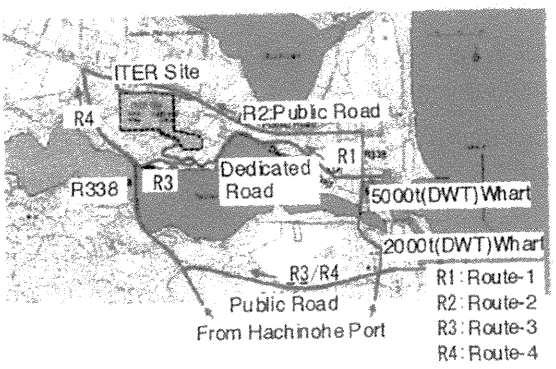

Fig. V.2.2-1 Transportation routes to Rokkasyo candidate site

(1) Soil Characteristics

The soil property and structure of the basement were confirmed from the comprehensive test results, as presented in JASS.

- The Takahoko stratum of Miocene epoch (firm rock of the Tertiary era) is distributed widely with an enough thickness, continuously expanded from the adjacent site for the Nuclear Fuel Cycle facilities.
- The allowable bearing capacity of the Takahoko stratum is at least 200 ton/m^2 and sufficiently enough for supporting the ITER buildings.
- The Takahoko stratum appears from relatively shallow depth (GL-20 m), which is fully consistent with the current layout of the ITER tokamak building.

(2) Intensity of Earthquakes at the Rokkasho Candidate Site

The data of past earthquakes and active faults within 400 km from the Rokkasho candidate site have been investigated, including the KiK-net database of the latest earthquakes.

- Possibility of large earthquakes above JMA-scale V (corresponding to about 80 – 250 gal) is very small.
- In the latest major earthquake (2003 Tokachioki), the maximum ground acceleration measured in the Kik-

net Rokkasho station is 100 gal at most.
- There is no remarkable active fault, near the Rokkasho candidate site.
- The statistics of the past earthquakes for 329 years predicts the 35-year return period velocity of about 3 cm/s (corresponding to about 50 gal), which is very small.

(3) Seismic/Isolation Design

Considering potential radiological impact, the ITER tokamak is conservatively designed to withstand the design basis earthquake: the design basis earthquake would be defined as the largest one estimated from the past earthquakes and active faults with a recurrence period of less than 10,000 years.
- The intensity of the design basis earthquake is estimated to be about 230 gal on the free bedrock surface from the practice of the Nuclear Fuel Cycle facilities.
- Facilitating unique ITER structures, seismic isolation is proposed and this results in a sufficient margin even for larger earthquakes than the design basis earthquake.
- Seismic isolation has been utilized widely and the rubber bearings are applicable to ITER within the currently proven technology.

General buildings or houses are also conservatively designed in accordance with the Building Standard Law, although the possibility of large earthquake is very small.
- To assure structural integrity of the major structural members against a large earthquake (above JMA-scale V), assuming once a life time.
- To prevent collapse or breakage of the buildings against a severe earthquake (above JMA-scale VI or VII), assuming an extremely unlikely occurrence.

(4) Seismic Hazard Assessment

In accordance with the IAEA Safety Guide (NS-G-33 "Evaluation of Seismic Hazards for Nuclear Power Plants"), a seismic hazard analysis has been made to assess the level of seismicity at the Rokkasho candidate site. In this analysis, the seismic hazard curves are calculated using the probabilistic models of seismic source zone and propagation of motion. A logic tree analysis is introduced to evaluate the modeling uncertainties. Based on the natures of earthquakes within and around Japan islands, three types of seismic source zones are identified; active faults, zone corresponding to in-cluster earthquakes, and zone corresponding to inter-plate earthquakes. The relationship between the seismic magnitude and its annual frequency of occurrence is given by Gutenberg-Richter equations [2.2-1] using the historical earthquake databases. Attenuation relation is given in accordance with Nishimura et al [2.2-2].

Figure V.2.2-2 shows the uniform hazard spectra calculated from the probabilistic seismic hazard curves. In Fig. V.2.2-2 dotted lines correspond to the median (50 percentile) hazard curves with annual frequencies of 10^{-2} and 10^{-3} for design basis earthquakes. Solid line corresponds to the design basis earthquake at the Rokkasho candidate site estimated from the practice of the Nuclear Fuel Cycle facilities. From this, it can be found that the Japanese design basis earthquake envelops the IAEA requirements.

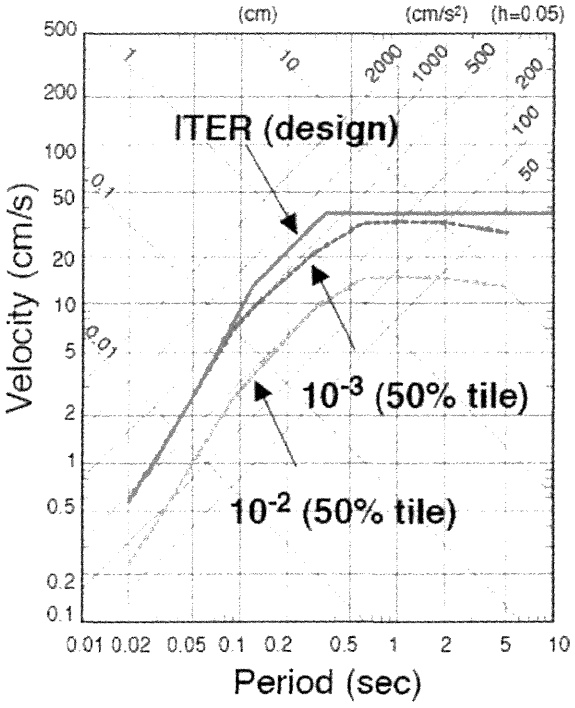

Fig. V.2.2-2 Uniform Hazard Spectra and JA Design Spectra defined at Free Bedrock Surface

2.2.3 Licensing Including Codes and Standards

Concerning the safety regulation of ITER, at requests through the examination proceeded at the Ministry of Education, Culture, Sports, Science and Technology (MEXT), JAERI addressed technical information related to the safety evaluation and the plan of

operational & decommissioning stage, for completion of the final report "Basic Policy of ITER Safety Regulation" (2003 November), which reflected public opinions to the draft report. In addition, JAERI worked for the preliminary safety review carried out by MEXT within the scope of the ITER Final Design Report according to "Guide for Review of Safety Design and Assessment" (a part of the "Basic Policy of ITER Safety Regulation"). Concerning structural codes for ITER, the code structure and the draft articles of technical rules, which relates to conformity assessment, quality assurance and, design, manufacture and inspection of the vacuum vessel and, design of the superconducting magnets, were drawn up and reviewed in detail by the code specialists of the Thermal and Nuclear Power Engineering Society (TENPES) and the American Society of Mechanical Engineers (ASME). A Subcommittee on Fusion Reactors organized in the Japan Society of Mechanical Engineers (JSME) has started to review the draft articles for development of fusion code. In addition, ASME has approved to create a new Division 4 for fusion code under the Section III of the ASME Boiler and Pressure Vessel Code. Justification of the project guideline related to the safety design and safety evaluation was examined by the Ad-hoc Committee with authorities and experts at specialists group of the Nuclear Safety Research Association and reflected in the project guideline. A series of experiments was carried out using JFT-2M to show conservatism of the design basis required as described in 2.4.2.

2.2.4 Site Preparation

For hosting ITER in the Rokkasho candidate site, JAERI has contributed to the joint works on site preparation and support together with MEXT and Aomori Prefecture, placing a special emphasis on the flexibility of the site throughout the construction, operation and decommissioning.

Concerning the on-site preparation, the following issues have been considered and evaluated especially in terms of technical aspect; 1) land development, 2) foundation work for buildings, 3) seismic isolator, 4) facilities for water supply and drain inside the site, 5) heat rejection system, 6) active/reactive electric power compensation system, 7) electric power receiving systems, 8) external works (cafeteria, road, car parks, outdoor lighting, fences, rain-water drainage pipes, etc.), 9) countermeasure for snow fall, 10) secondary storage building for radioactive waste, 11) environmental monitoring facilities, etc. Regarding the off-site preparation, on the other hand, 1) facilities for water supply and drain outside the site, 2) power transmission lines, 3) routes, cost and schedule of transportation for large and heavy instruments, and so on.

Temporal buildings are available at the establishment of the ITER Organization (for 40-300 people in time to the build-up the staff). Preparation needed for the start of construction will be finalized before the start of the excavation of the tokamak building.

References

2.2-1 Gutenberg, B. and Richter, C. F., "Earthquake Magnitude, Intensity, Energy and Acceleration," *Bulletin of the Seismological Society of America*, **32**, 163 (1942).

2.2-2 Nishimura, I. et al., "Response Spectra for Design Purpose of Stiff Structures on Rock Site," *Proc. 16th Int. Conf. on Structural Mechanics in Reactor Technology*, (CD-ROM) (2001).

2.3 Contributions to International Tokamak Physics Activity (ITPA)

JAERI continued to contribute to all the aspects of International Tokamak Physics Activity (ITPA). Its contribution to ITPA is highlighted by long pulse operation and sustainment of high β_N in I.1.1, achievement of high fusion triple product under full non-inductive current drive in I.1.2.1, confinement improvement at high density in I.1.2.3, NTM stabilization in I.1.3.1, energetic ion transport by TAE modes in I.1.3.2, effect of toroidal rotation on ELM in I.1.4.2, plasma transport at ELM in I.1.6.1, sol flow studies in I.1.6.2, development of advanced diagnostics in I.2.6 and high recycling steady (HRS) H-mode in II.2.1. In this section, cross-machine comparison studies of key plasma characteristics carried out under ITPA are summarized.

2.3.1 H-Mode Threshold Power [2.3-1]

An analysis of the ITPA H-mode power threshold database is advanced to study the roles of the aspect ratio, A, the absolute magnetic field and the effective charge number, Z_{eff}. A new scaling expression for the power threshold, P_{thr}, is presented. A clear and strong dependence on Z_{eff} is found; $P_{thr} \sim Z_{eff}^{0.7}$ The prediction of P_{thr} = 40-50 MW in ITER can be reliable if Z_{eff} is kept ~2. For more details, please refer III 1.1.

2.3.2 H-Mode Pedestal Physics [2.3-2]

Dimensionless identity experiments have been carried out for the first time in JT-60U and JET, achieving a very good match in the plasma geometry, with the exception of aspect ratio, which differs by ~16%. Contrary to expectations, a match of the pedestal pressure (or $\beta_{p,ped}$) is not obtained in the two devices in the same ELM regime. In the Type I ELM regime, T_e gradients and widths are very close in the two devices for similar T_{ped}, whilst density profiles tend to be steeper in JET. This result is discussed more in detail in I.1.4.

2.3.3 ITB Physics [2.3-3~5]

A dimensionless figure of merit, $(H_{HITER\text{-}89\text{-}P} \times \beta_N)/q_{95}^2$ has been proposed. In advanced regimes, this figure of merit has reached a value $(H_{HITER\text{-}89\text{-}P} \times \beta_N)/q_{95}^2$ ~0.4 at $q_{95} < 5$ and at a β_p exceeding unity, required for their extrapolation to ITER steady state operation with $Q > 5$ for at least ten confinement times. Densities in the range of $n_e/n_G \sim 0.8$ or $n_e > 6\text{-}7 \times 10^{19}$ m^{-3} have not been obtained at $H_{HITER\text{-}89\text{-}P}$ ~3 in advanced regimes, as required in non-inductive current drive operation in ITER.

A review paper has been published on ITB physics [2.3-4]. There is considerable experimental support for the E x B flow shear paradigm, namely that when the flow shear exceeds the linear growth rate of ITG instabilities, transport is suppressed and an ITB can form, particularly for ITBs in the ion channel. ITBs in the electron channel tend to require the stabilizing effects of negative magnetic shear and Shafranov shift. The local diffusivities at ITBs can be comparable with neoclassical predictions. Analysis of multi-tokamak ITB database indicates significant density dependence for ion barriers, almost linear, but a weaker dependence on magnetic field, in contrast to theoretical expectations based on the ρ^*_T criterion. While plasmas with positive magnetic shear indicated that the threshold power per particle increases with $1/\rho^*$, in accord with theoretical predictions for the sheared ExB flow model, this power can be substantially reduced for smaller values of ρ^* in negative magnetic shear plasmas. This is a desirable regime for achieving ITB plasmas in ITER. Electron barriers can appear at much lower powers than ion barriers, although negative magnetic shear appears to be required. Impurity accumulation and insufficient He exhaust in the presence of ITBs is a potential threat.

Critical values of temperature scale length L_T for ITB formation have been investigated in various devices using the ITPA international ITB Database [2.3-5]. Large variations in the ratio of ion gyroradius ρ_s or ρ_i to L_T are found in some cases. This suggests that the critical values of ρ_s/L_{Te} and ρ_s/L_{Ti} depend on plasma parameters or quantities other than ρ_s (ρ_i) should be introduced to normalize L_T.

2.3.4 Diagnostics [2.3-6]

Individual diagnostic systems for performing the measurements in ITER have been selected and the conceptual design of many of these systems has been completed. It is expected that most measurement requirements will be satisfied; especially those for basic control and machine protection are well covered. However, the precise performance of the various diagnostic systems will not be known until the designs are further developed and the outstanding R&D has been done. Two areas where there is a substantial short fall in the measurement capability are the measurement of the alpha particle birth profile, and the measurement of the confined and escaping alphas.

References

2.3-1 Takizuka, T., et al., *Plasma Phys. Control. Fusion*, **46**, A227 (2004).

2.3-2 Saibene, G., et al., *Plasma Phys. Control. Fusion*, **46**, (2004).

2.3-3 Litaudon, X., et al., *Plasma Phys. Control. Fusion*, **46**, A19 (2004).

2.3-4 Connor, J.W., et al., *Nucl. Fusion*, **44**, R1 (2004).

2.3-5 Fujita, T., et al., *Proc. 30th EPS Conference on Contr. Fusion and Plasma Phys.*, **27A**, P2.131 (CD-ROM) (2003).

2.3-6 Donné, A.J.H. and Costley, A.E., *IEEE Trans. Plasma Sci.*, **32**, 177 (2004).

2.4 Engineering Safety Demonstration

2.4.1 Dynamic Test on Vibration for Tokamak Structure

The main components of the ITER tokamak structure are superconducting magnets and a vacuum. The supports of these components are flexible in the radial direction in order to mitigate the thermal load due to thermal contraction or expansion. Such flexible type supports are not usually used to support the large and heavy structures. It is therefore necessary to verify the dynamic response of the ITER tokamak structure by experimental and analytical ways [2.4-1].

The assembly of the 1/5.8 sub-scale magnet structure model shown in Fig. V.2.4-1 was used in the dynamic test including static loading and excitation tests. The following technical findings were obtained by comparing the experimental results with the analytical ones:

1) From the static loading test, it was found that the deformation of the base plate and the elongation of the bolts joining the base plate to the foundation were not so small. The global deformation calculated from the modified FEM model, which included the base plate and the bolts, was almost the same as the experimental result.
2) The fundamental frequency calculated from the modified FEM model was also almost the same as measured in the excitation test.
3) For higher modes, the frequencies calculated from the modified FEM model disagreed with the measured ones. The calculated values were about 15% higher than the measured ones.

To calculate the dynamic response of the magnet structure covering higher modes more accurately, the more precise FEM model is required and it will be important how to simulate the rigidity of the internal joints of the magnet structure.

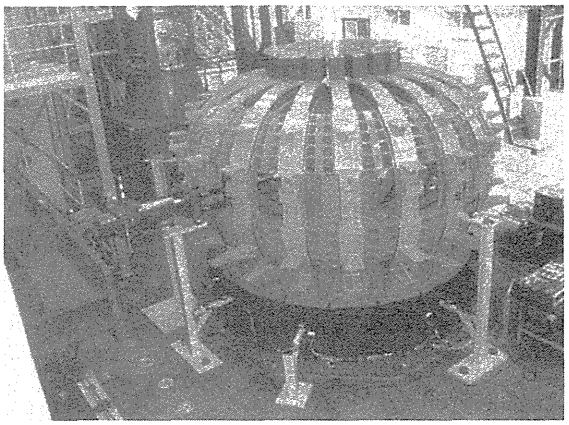

Fig. V.2.4-1 Assembly of the 1/5.8 sub-scale magnet structure model during static loading test.

2.4.2 Experiment of Disruptions under the Condition of Simulated ICE using JFT-2M

The blankets and divertors in ITER are experimental components without safety functions to demonstrate and optimize their performance including plasma surface interaction and accumulate engineering database through the ITER operation for the following fusion reactors. From viewpoint of safety design, therefore, it is assumed a priori their damage or failure, resulting in ingress of cooling water into the vacuum vessel and consequently plasma disruption. This is called "Ingress of Coolant Event" (ICE). Electromagnetic force due to the disruption acts on the surrounding structures, such as the vacuum vessel. Since ICE is one of the normal conditions by definition, the electromagnetic force caused by ICE must be considered as the design loads for the vacuum vessel. The electromagnetic force depends on the decay time constant of the plasma current. However, the present database on the decay time constant does not cover the ICE condition. Accordingly, experiment of disruptions under the condition of simulated ICE has been performed using JFT-2M to validate the design conditions.

To estimate the electromagnetic force due to disruption caused by ICE, plasma current decay time at the current quench (τ_{cq}) was measured as an indicator. Here, τ_{cq} is estimated by exponential fitting on the decay curve from 80% to 20% of initial plasma current during current decay. Disruption caused by ICE was simulated by injecting large amount of gases (Nitrogen and Argon), and compared to the present disruption database of τ_{cq}.

The L/R decay time of plasma, is mainly determined by the plasma electron temperature (T_e) and the effective charge of plasma ($\langle Z \rangle$). Where L and R are inductance and resistance of plasma after thermal quench and $\langle Z \rangle = \Sigma(Z_i n_i)/\Sigma n_i$, i=0,1,2,···, including neutral atoms. The L/R decay time decreases with the decrease in T_e and the increase in effective charged number $\langle Z \rangle$. The T_e during current quench depends on a balance between radiation power and ohmic heating power. In case of massive gas injection (or

ICE), the T_e becomes low (below ~1eV), and <Z> also becomes small, resulting that a small change of τ_{cq} would be expected by compensating each other.

Rupture disk was used for the rapid injection of large amount of gas. Pressure vessel with the volume of 0.028m^3 and the operation gas pressure of 0.6MPa was connected to JFT-2M, through the rupture disk followed by an orifice to adjust the gas flow rate, restricting by the critical flow rate of the orifice (from 3.5kPa·m^3/s to 242Pa·m^3/s).

Before gas injection experiment, characteristics of current decay time in JFT-2M were confirmed. The dataset of RMSE for the fit exponential of less than 2% were selected for the database. From this database, lower bound of τ_{cq} on JFT-2M was found to be 0.5ms.

In ICE simulated experiments, gas was injected to OH plasma of I_p=140kA, q_{95}=3~4. Gas flow rate was scanned to change the orifice diameter of 6mm, 12mm and no orifice case (effective diameter of rupture disk of 50mm). These gas injection rates were roughly equivalent to double ended break of cooling pipes at the diameter of 10mm to 50mm in ITER. In addition, argon gas was used for the estimation of gas species dependence.

Table V.2.4-1 Experimental conditions

	Case (1)	Case (2)	Case (3)	Case (4)
Orifice diameter (mmΦ)	6	12	No orifice	No orifice
Gas flow rate (kPam^3/s)	3.5	13.8	242	215
Gas species	N_2	N_2	N_2	Ar

From the experimental results, τ_{cq} was decreased with the increasing in gas flow rate. However, the change of τ_{cq} with different gas flow rate was not so large, as expected. The reduction in τ_{cq} was only ~ 30% even if the amount of injected gas increased by one or two order of magnitude. The current decay times were 0.7 to 1.1ms,which was within the range of current decay time of JFT-2M database as shown in Fig.V.2.4-2.

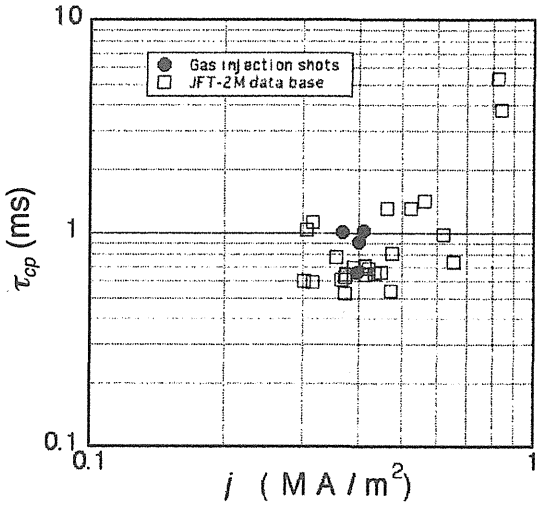

Fig. V.2.4-2 Current decay time of simulated ICE disruption compared to the JFT-2M disruption database.

2.4.3 Tritium Handling

(1) Demonstration of Tritium Removal Facility under Unusual Conditions

Oxidation performance of the detritiation system has been verified using a 1/1,000 scale model detritiation system of ITER (~2.64m^3/hr in gas flow) in order to clarify the detritiation efficiency in ITER in case of fire. The model detritiation system consists of two oxidation catalyst beds (473K and 773K for oxidation of hydrogen isotopes and hydrocarbons in the ventilation gas, respectively) and a vapor adsorber column with molecular sieve for removing water vapor as well as the detritiation system of ITER. In this experiment, the performance of oxidation catalyst bed for hydrogen and methane with coexistence of carbon monoxide or carbon dioxide which simulating the ventilation gas in fire has been investigated.

Oxidation efficiency of this model detritiation system for hydrogen (2%) and methane (2%) in air was more than 99.99% for hydrogen and more than 99.9% for methane, respectively, in normal operating condition. These performances have been maintained even under the coexistence of carbon dioxide up to 20%, and carbon monoxide up to 10% as long as enough oxygen for oxidation existed in the ventilation gas. Those results proved the integrity of the oxidation catalyst of the detritiation system in case of fire.

(2) Evaluation of Interactions between Tritium and Materials of Facilities

Tritium permeation evaluation through the plasma facing components (PFC) has been carried out with newly obtained experimental results such as transport properties in the PFC materials and permeability of tritium through heat exchanger material when tritium contacts with it as water form.

Results indicate that tritium permeation through the

PFC is mainly attributed through the first wall region due to its large surface area and tritium generation by nuclear reaction of $^{9}Be(n, t)^{7}Li$. Tritium concentration in the primary cooling water was estimated to reach about 1.5 TBq/m^3, which was within the acceptance criteria of the tritium concentration (1.8 PBq/m^3) as indicated in Fig. V.2.4-3. On the other hand, tritium permeation amount through the wall of heat exchanger from the primary to the secondary cooling water was estimated to be negligibly small (about 0.4GBq after 20 years operation as shown in Fig. V.2.4-3). Therefore, it could be concluded that tritium permeation through the PFC would not be serious issue in a viewpoint of safety in ITER [2.4-2].

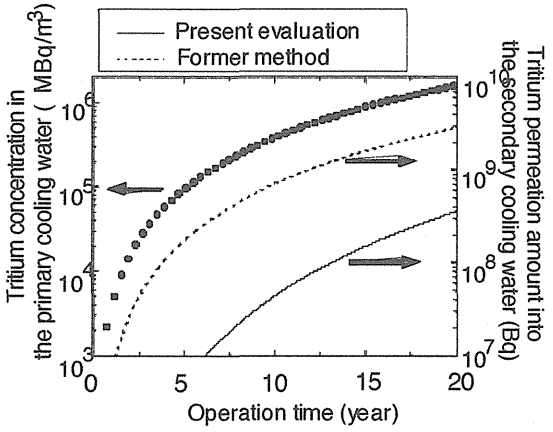

Fig. V.2.4-3 Time evolution of tritium concentration in the primary cooling water and tritium permeation amount from the primary cooling water to the secondary cooling water through the heat exchanger.

A series of irradiation tests has been carried out for polymerized compounds used in the electrolysis cell of ITER WDS (Water Detritiation System). The cell is designed to use for two years in water with a tritium concentration of 9.25TBq/kg (530kGy). While no serious change was observed for the tensile strength and an ion exchange capacity of membrane materials (Nafion) of the cell up to 850 kGy of gamma irradiation, a kind of poly-tetra-fluoro-ethylene as the insulator lost their tensile strength at around 300 kGy. This problem can be solved to replace the insulator with polyimide resin, whose high durability for irradiation is well demonstrated. It can thus be expected that the electrolysis cell would hold two years use under the ITER condition with changing sulator materials.

(3) Decontamination Technique for Construction Materials of ITER

In order to investigate effective tritium removal method from a room, intentional tritium release and its removal experiments have been carried out with the Caisson Assembly for Tritium Safety Study (CATS) of 12m^3 gas-tight box (Caisson).

As to the residual contamination of tritium on the wall of CATS, it was found that existence of small amount of tritiated water (~ppm) in the released tritium enhanced the residual contamination, and that high humidity in the CATS reduced the residual contamination. On the other hand, addition of water vapor into the ventilation airflow of the CATS contaminated by the tritiated water accelerated the removal of the residual contamination. For example, about 95% of the residual tritium contamination on the wall of the CATS was removed by the addition of water vapor of 600ppm into the ventilation flow. Those results indicate the effectiveness of water vapor addition on the tritium removal. Those behaviors have been well explained with the newly developed analytical code assuming the adsorption and desorption reaction of tritiated water on the wall and isotope exchange reaction between water vapor and tritium on the wall.

References

2.4-1 Onozuka M., et al., *Fusion Eng. Des.*, **69**, 757 (2003).

2.4-2 Nakamura, H., et al., to be published in *J. Nucl. Mater.* (2004).

VI. FUSION REACTOR DESIGN

1. Design and Physics of Fusion Reactor

1.1 Design of VECTOR

The optimization of the VECTOR design parameters led to a fusion output of 2.5 GW with a small reactor weight of 8,000 tons. Because of its compactness, CO_2 emission in the life cycle of the VECTOR power plant was estimated to be as low as 2.9 g-CO_2/kWh, being lower than that of an ITER-sized DEMO reactor (4.9 g-CO_2/kWh). As to the waste management of VECTOR, on the basis of reactor design and radiological considerations, we suggested reusing a liquid metal breeding material (PbLi) and a neutron shield material (TiH_2) in successive reactors. According to this waste management, the disposal waste would be reduced to as low as 3,000-4,000 tons, which is comparable with the radioactive waste of a light water reactor (4,000 tons in metal). Furthermore, it was numerically confirmed that such a low-A reactor would have an advantage over α-particle confinement.

VECTOR is an economical and compact reactor concept featuring the combination of low aspect ratio (A~2) and superconducting toroidal field coils [1.1-1] shown as VECTOR'02 in Fig.VI.1.1-1. In the VECTOR'02, a single null divertor (SND) configuration and A=2 were chosen. The SND configuration requires relatively low elongation plasma shape less than 2.0~2.1 for avoiding an equilibrium bifurcation problem. These design conditions have been repealed for VECTOR'03 and the new parameters have been recently optimized to maximize (fusion output) /(reactor weight) with feasible engineering and plasma parameters: $B_{max} \leq 19$ T, the neutron wall load ≤ 5 MW/m^2, $f_{GW} \leq 1$, HH ~ 1.3, $\beta_N \leq 5.5$, etc. As a result, we reached an optimal design with R = 3.2 m, a = 1.4 m, A = 2.3, $\kappa = 2.35$, $I_p = 14$ MA, $f_{bs} = 0.83$ and $P_{fus} = 2.5$ GW. The reactor weight is reduced to 8,800 tons, being a half or one third of that of other tokamak reactors.

As to the physics aspect, it is numerically confirmed that VECTOR has an advantage over α-particle loss originating from ripple transport [1.1-2]. In order to clarify this, numerical result for a wide current hole (the hole radius of 0.6a) is compared between VECTOR and A-SSTR2 in Fig. VI.1.1-2.

Comparing at a same toroidal magnetic field (TF) ripple, low-A shows lower α-particle loss. The main reason for such a small loss in low-A is that TF ripple amplitude sharply damps along R in low-A. From the point of view of the resulting peak heat load on the first wall, the allowable α-particle loss fraction is 2-3% for A-SSTR2, which is satisfied at the TF ripple of 0.3% at the plasma surface. In contrast, since the heat load distribution tends to expand and thus the peak heat load is reduced in low-A, higher α-particle loss fraction (~5%) is acceptable for VECTOR. As a result, the TF ripple of VECTOR can be designed at as high as 1.5% even for such a wide current hole [1.2-3].

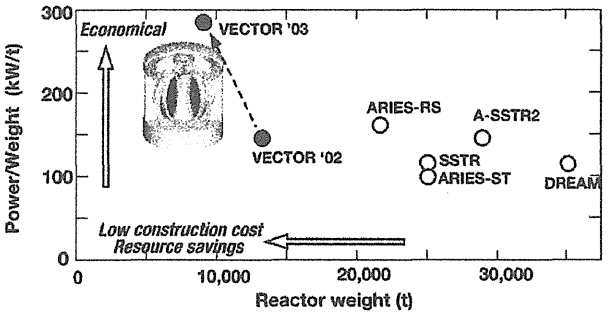

Fig. VI.1.1-1 Comparison between VECTOR and other reactors

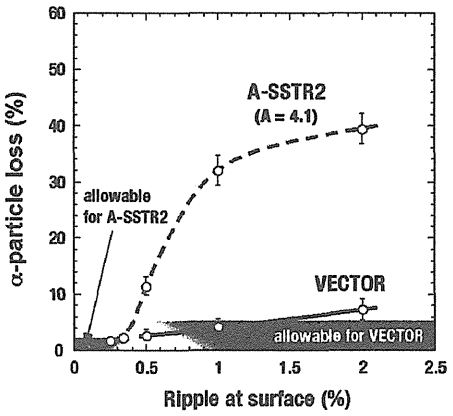

Fig. VI.1.1-2 Calculated α-particle loss for wide current hole

References

1.1-1 Nishio, S., *et al.*, *Proc. 19th IAEA Fusion Energy Conf. (Lyon)* FTP1/21 (2002).

1.1-2 Tobita, K., *et al.*, *Plasma Phys. Control. Fusion* **46**, S95 (2004).

1.1-3 Tokimatsu, K., *et al*, *Nucl. Fusion* **40**, 653 (2000).

1.2 Physics Related to Reactor Design

1.2.1 Dynamics of High β Reversed Shear Plasmas

Characteristics and underlying mechanisms for plasma current spikes frequently observed at the thermal quench of JT-60U disruptions were investigated through

TSC simulations. It was first clarified that shell effects play an important role in the current spikes of high β_p plasmas according to the initial position of the plasma and the vacuum vessel [1.2-1]. As a consequence, a negative current spike appears when the plasma is located close to the outboard of the vacuum vessel.

1.2.2 Non-inductive Current Ramp-up Scenarios

Slow current ramp-up was investigated by the TSC code. The result indicates that a cooperative linkage between non-inductively driven and ITB-generated bootstrap (BS) currents exhibit a self-organized recurrence of positive shear (PS) and negative shear (NS) profiles [1.2-2]. Figure VI.1.2-1 shows the time evolution of the magnetic shear, indicating the recurrence of the magnetic shear between PS and NS.

References

1.2-1 Takei, N., *et al.*, *30th EPS Conference on Controlled Fusion and Plasma Physics, St Petersburg*, 2003 ECA **27A**, P-2.127 (2003).

1.2-2 Nakamura, Y., *et al.*, *30th EPS Conference on Controlled Fusion and Plasma Physics, St Petersburg*, 2003 ECA **27A**, P-2.128 (2003).

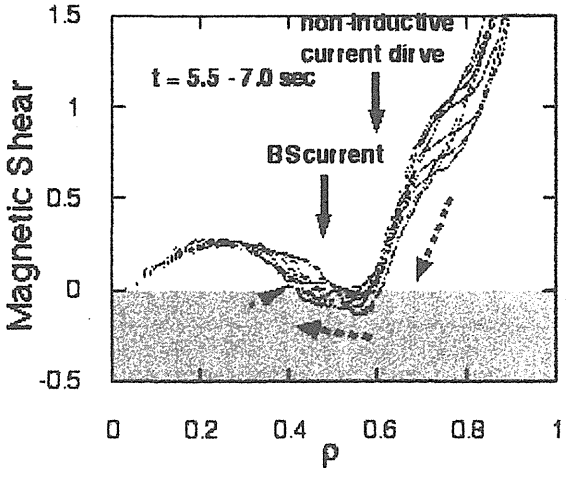

Fig.VI.1.2-1 Evolution of the magnetic shear profile. Non-inductive current is driven around $\rho \sim 0.6$, while BS current distributed around $\rho < 0.6$ just inside the ITB. Positional difference between non-inductive and BS currents leads to an inward drift of the magnetic shear, possibly resulting in disappearance of an internal transport barrier.

1.3 Analysis of Liquid Wall Divertor

A concept of liquid wall divertor was examined in terms of heat removal by simulations using the computational fluid dynamics (CFD) analysis codes. In the concepts, liquid such as Flibe is introduced along the divertor plate to remove heat flux from the plasma [1.3-1]. The CFD codes, STAR-CD and FLUENT based on the finite volume analysis method and ADINA-F based on the finite element analysis method, were used to model the flowing liquid wall divertor. It was indicated that STAR-CD and FLUENT tend to result in a lower value than the true heat flux, because the heat flux is applied to the free liquid surface via a gaseous layer. On the other hand, ADINA-F has a problem in modeling the secondary flow in the flowing liquid, which is required to improve heat removal.

References

1.3-1 Kurihara, R., *Fusion Eng. Des.* **61-62**, 209 (2002).

2. Assessment of Fusion Energy

2.1 Impact of Hydrogen Production by Fusion

In order to assess the potentiality of fusion as a future energy source, a simulation until the end of 21st century was carried out. The simulation is based on a World integrated model in which energy demand in the world is determined by considering population, population growth, personal income, GDP, GDP growth, etc. When the regulation of CO_2 emission is globally strengthened and fusion energy is succeeded in reducing the cost-of-electricity (COE) to 7 cent/kWh in 2050 and 3 cent/kWh in 2100, the share of fusion energy in the primary energy sources is about 14% in 2100. In the case that the future energy market widely accepts hydrogen fuel, the share of fusion energy will increase to about 17% in 2100 if fusion is used for hydrogen production as shown in Fig VI.2.1-1.

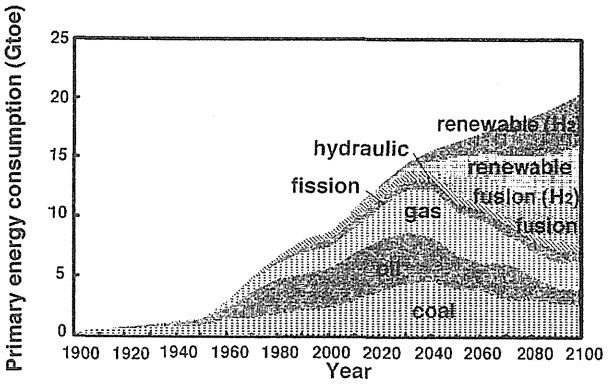

Fig. VI.2.1-1 Expected share of fusion energy in the future energy market. Gtoe means 10^9 tons-oil-equivalent.

2.2 Waste Management

Waste management strategy for a compact fusion reactor such as VECTOR was investigated from a point of view of reducing disposal waste. Such a compact reactor has a great impact on reducing the total quantity of waste although the quantity of radioactive waste is as large as that of a conventional fusion reactor. One of the waste management strategies to reduce the amount of disposal waste is recycling of radioactive waste under regulatory control. However, this strategy has difficulties in a demand-supply balance of recycled materials in nuclear facilities only, economical control of deleterious impurities in recycled materials, special chemical processing, precision machining and complicated installation work by fully remote handling.

Considering the situation, we propose to design a fusion reactor suitable for reuse. Promising reuse components are neutron shield and liquid metal tritium breeding material. In VECTOR, LiPb is used as the tritium breeding and neutron multiplying material. At the decommissioning, LiPb is collected in a storage tank to cool down the radioactivity. The material for neutron shield adopted in VECTOR is TiH_2. The shield is composed of the assembly of steel (or SiC/SiC composite material) containers filled with TiH_2. As to the neutron shield, processes needed for the installation to the next generation reactor are also expected to be simple, being suitable for reuse. Along the strategy, the

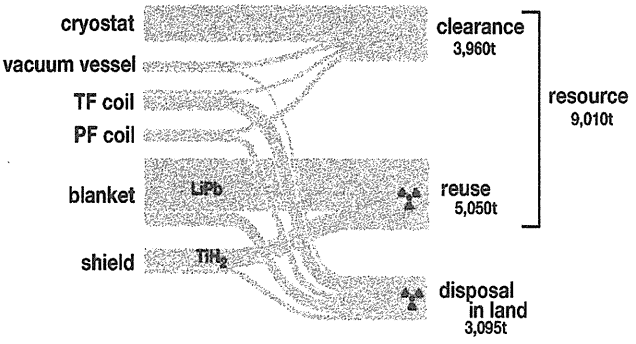

Fig. VI.2.2-1 Classification of waste from VECTOR.

weight of disposal waste from a low aspect ratio reactor VECTOR is as low as 3,000 t as illustrated in Fig.VI.2.2-1. The radioactive waste of ports and subsystems around the reactor, which are not included in the estimation, is expected to be a few thousands of tons [2.2-1]. To include the additional radioactive waste, the total weight of disposal waste comparable with the metal radioactive waste from a light water reactor (4,000 t for metal).

References

2.2-1 Tobita, K., *et al.*, "Waste managament for JAERI fusion reactors", *J. Nucl. Mater.* **329-333**,1610 (2004).

Appendix A.1 Publication List (April 2003 – March 2004)

A.1.1 List of JAERI Report

1) Department of Fusion Engineering Research,(Ed. Nishitani, T.), "Report of the 13th IEA Workshop on Radiation Effects on Ceramic Insulators, December 9, 2003, Kyoto," JAERI-Review 2004-004 (2004).

2) Department of JMTR, "Summary of the Symposium on Beryllides as Advanced Nuclear Functional Material," JAERI-Review 2003-026 (2003) (in Japanese).

3) Ezato, K., Dairaku, M., Taniguchi, M., et al., "Quantitative Experiments on Thermal Hydraulic Characteristics of an Annular Tube with Twisted Fins", JAERI-Tech 2003-084 (2003).

4) IFMIF International Team, "Minutes of the IFMIF Technical Meeting December 4-5, 2003, Kyoto, Japan", JAERI -Review 2004-008 (2004).

5) Ishii, K., Seki, M., Shimono, M., et al., "Measures against the Damage of the Antenna Mouth of JT-60U LHRF System", JAERI-Tech 2003-079 (2003) (in Japanese).

6) Horikawa, T., Kaminaga, A., Nakamura, H., et al."Analysis of Exhaust Gas Composition in JT-60U Discharge Cleaning Experiments", JAERI-Tech 2003-12 (2003).

7) JT-60 team, "Review of JT-60U Experimental Results in 2001 and 2002", JAERI-Review 2003-11 (2003).

8) Kawamura, H., Tanaka, S., Ishitsuka, E., (ed.), "Proceedings of the Sixth IEA International Workshop on Beryllium Technology for Fusion", JAERI-Conf 2004-006 (2004).

9) Kikuchi, T., Yamada, H., Saito, T., et al., "Development of Sealing Plug for Sweep Gas Line", JAERI-Tech 2004-026 (2004) (in Japanese).

10) Kosaku, Y., Kuroda, T., Enoeda, M., et al., "Nuclear, Thermo-mechanical and Tritium Release Analysis of ITER Breeding Blanket", JAERI-Tech 2003-058 (2003).

11) Kurihara, R., Watanabe, K., Konishi, S., et al." Literature Survey of Thermalhydraulic Studies on Supercritical Pressurized Water", JAERI-Review 2003-7 (2003).

12) Luo, G. -N., Shu, W. M., Nakamura, H., et al., "Characteristics of a Low Energy and High Flux Compact Plasma Source and Preliminary Results in Studying Surface Modification of Tungsten Irradiated by the Source", JAERI-Research 2004-031 (2004).

13) Matsuhiro, K., Ando, M., Nakamura, H., et al., "Estimation of Tritium Permeation through Reduced-Activation Ferritic Steel at IFMIF Target Back-Wall Damaged by Neutron Irradiation", JAERI-Research 2004-003 (2004).

14) Minami, R., Kobayashi, N., Sakamoto, K., et al., "Control of Electron Beam Current of High Power Gyrotron for CW Operation", JAERI-Research 2004-006 (2004).

15) Nakahira, M., "Evaluation of Susceptibility on Crevice Corrosion for ITER Vacuum Vessel", JAERI-Tech 2003-083 (2003)(in Japanese).

16) Nakahira, M., "Applicability of LBB Concept to Tokamak-type Fusion", JAERI-Tech2003-087 (2003) (in Japanese).

17) Nakamura, H., Nishi, M., Morita, K., "Chemical State of Tritium in Sr-Ce Oxide Ceramics and its Removal

Characteristics", JAERI-Research 2003-016 (2003) (In Japanese).

18) Nakamura, H., Nishi, M., Sugisaki, M., "Measurement and Evaluation of Isotope Effect between Tritium and Deuterium on Diffusion and Surface Recombination in/on Nickel using Ion Driven Permeation Method", JAERI-Research 2003-018 (2003) (In Japanese).

19) Nakamura, H., Nishi, M., "Tritium permeation evaluation through vertical target of divertor based on recent tritium transport properties", JAERI-Research 2003-024 (2003).

20) Neudatchin, S. V., Takizuka, T., Shirai, H., et al., "Dynamics and Interplay of L-H-L Transitions and ITB-events in Reversed Shear Plasma with Internal Barriers in JT-60U", JAERI-Review 2003-029 (2003).

21) Oikawa, T., "Study of Non-Inductive Current Drive using High Energy Neutral Beam Injection on JT-60U", JAERI-Research 2004-1 (2004).

22) Oikawa, T., Tsuchiya, K., Kurihara, K., et al., "Development of Plasma Stored Energy Feedback Control and its Application to High Performance Discharges on JT-60U", JAERI-Reserch 2004-12 (2004).

23) Okano, F., Suzuki, S., et al., "The Control system of JFT-2M tokamak Auxiliary subsystem", JAERI Tech 2003-059 (2003) (in Japanese).

24) Sato, S., "Study on Shielding Design Method for Radiation Streaming in a Tokamak-Type Fusion Reactor based Monte Carlo Calculation", JAERI-Research 2003-014 (2003).

25) Senda, I., Fujieda, H., Neyatani, Y., Tda E., Shoji T., "Revised Version of Tokamak Transient Simulation Code SAFALY (1)", JAERI-Data/Code 2002-008 (2003).

26) Senda, I., Fujieda, H., Neyatani, Y., Tda E., Shoji T., "Revised Version of Tokamak Transient Simulation Code SAFALY (2)", JAERI-Data/Code 2002-012 (2003).

27) Shimono, M., Seki, M., Terakado, M., et al., "Low-Power and Long-Pulse Test of a Klystron of the JT-60U LHRF Heating System", JAERI-Tech 2003-075 (2003) (in Japanese).

28) Tabata, T., Kubo, H., Sadaka, M., "Formulating Analytic Expressions for Atomic Collision Cross Sections", JAERI-Research 2003-8 (2003)

29) Takahashi, M., Seki, M., Shimono, M., et al., "Performance and Experience of a 110GHz Gyrotron Operation on the JT-60U ECH System", JAERI-Tech 2003-080 (2003) (in Japanese).

30) Takase, H., Tobita, K., Nishio, S., "Pellet Injection and Plasma Behavior Simulation Code PEPSI", JAERI-Date/Code 2003-8 (2003).

31) Takase, Y. and JT-60 team, "Plasma Current Initiation and Ramp-up without Use Ohmic Heating Center Solenoid and Formation of High Confinement Plasma", JAERI-Review 2003-029 (2003).

32) Takizuka, T., Arakawa, K., Shimizu, K., et al., "Development of Database for the Divertor Recycling in JT-60U and its Analysis", JAERI-Research 2003-010 (2003) (in japanese).

33) Takizuka, T., Sakamoto, Y., Fukuda, T., et al., "Energy Confinement Scaling for Reversed-shear Plasmas with Internal Transport Barrier in JT-60U", JAERI-Review 2003-029 (2003).

34) Tanaka, R., Ochiai, K., Nakao, M., et al., "Secondary Gamma-ray Measurements on the D-T Neutron Skyshine Experiments", JAERI-Tech 2003-063 (2003) (in Japanese).

35) Terakado, M., Seki, M., Shimono, M., et al., "Power Modulation by Changing Anode Voltage on JT-60U ECH System", JAERI-Tech 2003-053 (2003) (in Japanese).

36) Urata, K., Shinohara, T., Suzuki, M., et al., "Fast Ion Loss Calculation in the Ripple Compensation Magnetic Field by Ferritic Steel Insertion using the FEMAG/OFMC code", JAERI-Data/Code 2004-007 (in Japanese).

37) Verzilov, Y. M., Ochiai, K., Nishitani, T., "Feasibility Study of the Water Cherenkov Detector as a D-T Fusion Power Monitor in the System using Neutron Activation of Flowing Water -First Experimental Phase-", JAERI-Research 2003-019 (2003).

38) Verzilov, Y.M., Ochiai, K., Sato, S., et al., "Analysis of Impurities in Beryllium, affecting Evaluation of the Tritium Breeding Ratio", JAERI-Research 2004-004 (2004).

39) Yamada, H., Kawamura, H., Tsuchiya, K., et al., "An Investigation of Post-Irradiation Examination Facility for Fusion Blanket Materials", JAERI-Tech 2004-036 (2004) (in Japanese).

40) Yokokura, Y., Hiranai, S., Sibayama, M., et al., "Transmission System in JT-60U Electron Cyclotron Heating System", JAERI-Tech 2003-047 (2003) (in Japanese).

41) Yoshida, K., Isono, T., Sugimoto, M., et al., "Analysis Program for Magnetic Field, Inductance of Air-core Coils: COIL", JAERI-Data/Code 2003-014 (2002) (in Japanese).

A.1.2 List of papers published in journals

1) Aiba, N., Tokuda, S., Hayashi,et al., M., "Simulation Study on the Motion of the Pressure Perturbation in an Axisymmetric Toroidal System", J. Phys. Soc. Japan, **73**, 364 (2003).

2) Akiba, M., Ishitsuka, E., Enoeda, M., "Development of Supercritical Water Cooled Solid Breeder Blanket in JAERI", J. Plasma Fusion Res., **79**, 929 (2003).

3) Akiba, M., Jitsukawa, S., Muroga, T., "Blanekt Technology Development Using ITER for Demonstration and Commercial Fusion Power Plant", J. Plasma Fusion Res., **79**, 672-677, (2003).

4) Aoki, Y., Nishijima, S. Koizumi, N., et al., "Monte Carlo simulation of Strand Position in CIC Conductor", IEEE Trans. ASC, **13**, 1744 (2003).

5) Bakhtiari, M., Azumi, M., Tsuzuki, K., et al., "Effect of a Ferromagnetic Wall on Low β Tearing Modes in the JapanAtomic Research Institute Fusion Torus-2 Modified", Phys. Plasmas, **10**, 3212(2003).

6) Bandourko, V., Jimbou, R., Nakamura, K., et al., "Erosion of CFC under simultaneous bombardment by helium and deuterium ions", J. Nucl. Mater., **313-316**, 413 (2003).

7) Bruskin, L. G., Mase, A., Oyama, N., et al., "Reflectometry Study of Mode Coupling in Fusion Plasma Turbulence",Plasma Phys. and Control. Fusion, **45**, 1227(2003).

8) Davies, A., Field, J., Takahashi, K., et al., "The toughness of free-standing CVD diamond", J. Mater. Sci., **39**, 1571 (2004).

9) Enoeda, M., Kosaku, Y., Hatano, T., et al., "Design and technology development of solid breeder blanket cooled by supercritical water in Japan", Nucl. Fusion, 43, issue 12, 1837 (2003).

10) Fujita, T. and JT-60 team, "Overview of JT-60U Results Leading to High Integrated Performance in Reactor-Relevant Regimes", Nucl.Fusion, **43**, 1527(2003).

11) Furukawa, M., Tokuda, S., Wakatani, M., "Geometrical Improvements of Rotational Stabilization of High- n Ballooning Modes in Tokamaks", Nucl. Fusion, **43**, 425(2003).

12) Furukawa, M., Tokuda, S., Wakatani, M., "Stability of Ideal MHD Ballooning Modes and its Stabilization by Toroidal Rotation Shear near Separatrix" ,Plasma Phys. and Control. Fusion, **46**, 409(2004).

13) Furuya, K., Wakai, E., Ando, M., et al., "Tensile and Impact Properties of F82H Steel Applied to HIP-Bond Fusion Blanket Structures",Fusion Eng. Des., **69**, 385 (2003).

14) Gotoh, Y., Masaki, K., Kizu, K., et al., "Analyses of Erosion and Re-deposition Layers on Graphite Tiles Used in the Wshaped Divertor Region of JT-60U", J. Nucl. Mater., **313-316**, 370 (2003).

15) Hamada, K., Matsui, K., Takahashi, Y., et al., "Pressure Drop Characteristics of Nb_3Al Cable-in-conduit Conductors under Electromagnetic Force –Relation between Pressure Drop Characteristics and Cable Stiffness–," Cryogenic Eng., **38**, 417 (2003).

16) Hamada, K., Takahashi, Y., .Matsui, K., et al., "Effect of Electromagnetic Force on the Pressure Drop and Coupling Loss of Cable-in-Conduit Conductor", Cryogenics, **44**, 45 (2004).

17) Hatano, T., Enoeda, M., Suzuki, S., et al., "Effective thermal conductivity of a Li_2TiO_3 pebble bed for a DEMO blanket", Fusion Sci. Technol., **44**, 94 (2003).

18) Hayashi, N., Ozeki, T., Hamamatsu, K., et al., "ECCD Power Necessary for the Neoclassical Tearing Mode Stabilization on ITER", Nucl. Fusion, **44**, 477(2004).

19) Hayashi, N., Ozeki, T., Hamamatsu, K., et al., "Simulation on Neoclassical Tearing Mode Stabilization by ECCD for JT-60 Superconducting Tokamak", J. Plasma Fusion Res. ,**SERIES 5**, 519 (2003).

20) Hayashi, N., Takizuka, T., Hosokawa, M., et al., "Asymmetry of Dense Divertor Plasmas Infuluenced by ThermoelectricPotential and Charge-exchange Momentum Loss", J. Nucl. Mater. **313-316**, 1041(2003).

21) Hirohata, Y., Motojima, T., Sengoku, M., et al., "Suppression of hydrogen absorption to V-4Cr-4Ti alloy by TiO2/TiC coating", J. Nucl. Mater., **313-315**, 172 (2003).

22) Hirohata, Y., Oya, Y., Kodama, K., et al., "The Depth Profiles of Deuterium and Hydrogen in Graphite Tiles Exposed toDD Plasma Discharges of JT-60U", Physica Scripta, **T103**, 19 (2002).

23) Hirose, T., Tanigawa, Y., Ando, M., et al., "Neutron Irradiation Effects on Fatigue Crack Initiation Points in a Reduced Activation Steel," Materia Japan, **39**, 902 (2003).

24) Horiike, H., Ida, M., Iida, T., et al., "Lithium Free Surface Flow Experiment for IFMIF", Fusion Eng. Des., **66-68**, 199 (2003).

25) Ida, M., Nakamura, H., Nakamura, H., et al., "Design of Contraction Nozzle and Concave Back-Wall for IFMIF Target", Fusion Eng. Des., **70**, 95 (2004).

26) Ide, S., Suzuki, T., Sakamoto, Y., et al., "Studies of the Influence of Electron Heating on ITB subject to AdvancedTokamak Operation in JT-60U", Nucl. Fusion, **44**, 87(2004).

27) Idomura, Y., Tokuda, S., Kishimoto,Y., "Global Gyrokinetic Simulation of Ion Temperature Gradient Driven Turbulence in Plasmas using a Canonical Maxwellian Distribution", Nucl. Fusion, **43**, 234(2003).

28) Inaguchi, T., Hasegawa, M., Koizumi, N., et al., "Quench Analysis of an ITER 13T-40kA Nb_3Sn coil (CS Insert)", Cryogenics, **44**, 121 (2004).

29) Inoue, T., Hanada, M., Iga, T., et.al., "Accelerator R&D for JT-60U and ITER NB systems", Fusion Eng. Des., 66-68, 597 (2003).

30) Ioki, K., Barabaschi, P., Barabash, V., et al., "Design Improvements and R&D Achievements for VV and In-vesselComponents towards ITER Construction", Nucl. Fusion, **43**, 268 (2003).

31) Isayama, A., Iwama,N., Hosoda, Y., et al., "Singular Value Decomposition Analysis of Multichannel Electron Cyclotron Emission Signals of Tokamak Plasma", J.J.A.P, Part 2, **42**, L329(2003).

32) Isayama, A., Iwama,N., Showa,T., et al., "Maximum Entropy Estimation of Electron Cyclotron Emission Spectra from Incomplete Interferograms in ELMy H-Mode Tokamak Experiment", J.J.A.P., Part 1, **42**, 5787(2003).

33) Isayama, A., Kamada, Y., Hayashi, N., et al., "Achievement of High Fusion Triple Product, Steady-State Sustainment and Real-Time NTM Stabilization in High-β ELMy H-Mode Discharges in JT-60U", Nucl. Fusion, **43**, 1272(2003).

34) Ishida, S., K, Abe., Ando, A., et al., "Objectives and Design of the JT-60 Superconducting Tokamak" ,Nucl. Fusion, **43**, 606(2003).

35) Ishii, Y., Azumi, M., Kishimoto, Y., " Long Timescale Plasma Dynamics and Explosive Growth Driven by the Double Tearing Mode in Reversed Shear Plasmas", Nucl. Fusion, **43**, 539(2003).

36) Ishii, Y., Azumi,M., Kishimoto, Y., "Current Point Formation and Magnetic Reconnection Process in Nonlinearly Destabilized Double Tearing Modes", Phys.Plasmas, **10**, 3512(2003).

37) Isono, T, Hamada, K., Kawano, K., et al., "Development and Test Results of 69 kA HTS Current Lead for Fusion Application," Cryogenic Eng., **39**, 122 (2004).

38) Isono, T., Kawano, K., Hamada, K., et al., "Test Results of 60-kA HTS Current Lead for Fusion Application," Physica C, **392-396**, 1219 (2003).

39) Isono, T., Nunoya, Y., Ando, T., et al., "Development of 10kA Bi2212 Conductor for Fusion application", IEEE Trans. ASC, **13**, 1512 (2003).

40) Itoga, T., Kawata, N.,(Nishitani, T.), "Development of Thermal Neutron Profiling Method using an Optical Fiber", J. Nucl. Sci. Technol., Suppl. **4**, 403 (2004).

41) Kajiwara, K., Ikeda, Y., Sakamoto, K., et al., "High Power Operation of 110GHz Gyrotron at 1.2MW on the JT60ECRF System",Fusion Eng. Des., **65**, 493 (2003).

42) Kamiya, K., Kimura, H., Ogawa, H., et al., " Observation of High Recycling Steady H-Mode Edge and Compatibility with Improved Core Confinement Mode on JFT-2M", Nucl. Fusion, **43**, 1214(2003).

43) Kamiya, K., Miura, Y., Ido, T., et al., "Calibration of Heavy Ion Beam Probe Energy Analyzer using Mesh Probe in the JFT-2M Tokamak", Rev.Sci.Instrum., **74**, 4206(2003).

44) Kaneko, J.H., Tanaka, T., (Nishitani, T.), et al., "Radiation Detector Made of a Diamond Single Crystal grown by a Chemical Vapor Deposition Method", Nucl. Instrum. Methods in Phys. Res. A **505**, 187 (2003).

45) Kaneko, O., Yamamoto, T. "Heating and current drive by N-NBI in JT-60U and LHD", Fusion Sci. Technol., **44**,503(2003).

46) Kawai, M., Akino, N., Ebisawa, N., et al., "Progress of negative ion source improvement in N-NBI for JT-60U",FusionSci. Technol., **44**, 508 (2003).

47) Kawamura, H., Ishitsuka, E., Nakazawa, T., et al., "Development of advanced blanket materials for a solid breeder blanket of a fusion reactor", Nucl. Fusion, **43**, 675 (2003).

48) Kawamura, H., Kikukawa, A., Tsuchiya, K., et al., "Evaluation of Effective Thermal Diffusivity of Li_2TiO_3 Pebble Bed under Neutron Irradiation", Fusion Eng. Des., **69**, 263 (2003).

49) Kawamura, Y., Konishi, S., Nishi, M., "Extraction of hydrogen from water vapor by hydrogen pump using ceramic protonic conductor", Fusion Sci. Technol., **45**, 33 (2003).

50) Kawano, Y., Chiba, S., Inoue, A., "Application of Diamond Window for Infrared Laser Diagnostics in a Tokamak Device", Rev.Sci.Instrum., **75**, 279(2003).

51) Kikuchi, M., Ando, T., "Superconducting Coil with Pure Copper Wires for Thermal Protection Outside Cable-In Conduit Conductors", Fusion Eng. Des., **66-68**, 1097(2003).

52) Kishimoto, Y., "Numerical EXperiment of Tokamak (NEXT) Prospect for "Multiple-Hierarchical Complex Plasma Research"," J. Japan Soc for Simulation Tech., **22**, 89 (2003).

53) Kobayashi, S., Sakasai, A., Koide, Y., et al., "Development of Fast Charge Exchange Recombination Spectroscopy by using Interference Filter Method in JT-60U", J. Plasma Fusion Res. (in Japanese),

79,1043(2003).

54) Koizumi, N., Nunoya, Y., Matsui, K., et al., "Evaluation of Strain Applied to Strands in a 13 T – 46 kA Nb_3Al Cable-in-conduit Conductor", Super. Sci. Tech., **16**, 1092 (2003).

55) Koizumi, N., Nunoya, Y., Takayasu, M., et al., "Evaluation of the Critical Current Performance of the Nb_3Al Insert," Cryogenic Eng., **38**, 399 (2003).

56) Koizumi, N., Okuno, K., Nakajima, H., et al., "Development of a Nb_3Al Conductor to be Applied to a Fusion Reactor and Its Application to a Large Superconducting Coil," Cryogenic Eng., **38**, 391 (2003).

57) Konishi, S., Okano, K., Tokimatsu, K., et al., " Socio-Economic Study of Fusion Energy at the Japan Atomic Energy Research Institute", Fusion Eng. Des., **69**, 523(2003).

58) Konovalov, S., Mikhailovskii, A. B., Tsypin, V. S., et al., "Drift Stabilization of Internal Resistive-Wall Modes in Tokamaks",Plasma Physics Rep., **29**, 779(2003).

59) Konovalov, S.V., Mikhailovskii, A.B., Tsypin, V.S., et al., "Effects of Parallel Viscosity on Rotation of Magnetic Islands in Tokamaks", Phys. Lett. A. , **318**, 429 (2003).

60) Kudo, Y., Sakurai, S., Masaki, K., et al., "Design and Structural Analysis for the Vacuum Vessel of SuperconductingTokamak JT-60SC", Fusion Sci. Technol., **44**, 333 (2003).

61) Kurita, G., Tsuda, T., Azumi, M., et al., "Ferromagnetic and Resistive Wall Effects on the Beta Limit in a Tokamak", Nucl. Fusion, **43**, 949(2003).

62) Kusakabe, T., Miyamoto, Y., Ishida, R., et al., "Total Cross Sections for Charge Transfer by Multiply Charged Neon and Argon Ions Colliding with Various Hydrocarbons at keV Energies", Nucl. Instrum. Meth. in Phys. Res. B, **205**, 600 (2003).

63) Laesser, R., Gruenhagen, S., Kawamura,Y., "Use of micro gas chromatography in the fuel cycle of fusion reactors",Fusion Eng. Des., **69**, 813 (2003).

64) Lang, P. T., Cierpka, P., Maruyama, S., et al., "A System for Cryogenic Hydrogen Pellet High Speed Inboard Launchinto a Fsion Device via Guiding Tube Transfer", Rev. Sci. Instrum., **74**, 3974 (2003).

65) Loarte, A., Shimada, M., Sugihara, M., et al., "Characteristics of Type I ELM Energy and Particle Losses in ExistingDevices and Their Extrapolation to ITER", Plasma Phys. Control. Fusion, **45**, 1549 (2003).

66) Masaki, K., Sugiyama, K., Tanabe, T., et al., "Tritium Distribution in JT-60U W-shaped Divertor", J. Nucl. Mater., **313-316**, 514 (2003).

67) Matsuda, N., Nakashima, H., (Ochiai, K.), "A Study on Induced Activity in the Low-activationized Concrete for J-PARK", J. Nucl. Sci. Technol., Suppl. **4**, 395 (2004).

68) Matsui, K., Takahashi, Y., Koizumi, N., et al., "AC Loss Performance of Cable-in-conduit Conductors –Influence of Cable Mechanical Property on Coupling Loss Reduction–," Cryogenic Eng., **38**, 410 (2003).

69) Matsukawa, M. and JT-60SC Design team "Recent Results and Modification Program of JT-60 towards High IntegratedPerformance", IEEE Trans. Plasma Sci., **32**, 135(2004).

70) Matsukawa, M., Ishida, S., Sakasai, A., et al., "Design and Analysis of Plasma Position and Shape Control in Superconducting Tokamak JT-60SC" ,Fusion Eng. Des., **66-68**, 703(2003).

71) Mikhailovskii, A. B., Kovalishen, E. A., Shirokov, M. S., et al., "Microislands in Tokamaks" ,Phys.Plasmas, **11**, 666 (2004).

72) Mikhailovskii, A. B., Shirokov, M. S., Tsypin, V. S., et al., "Fluid Treatment of Convective-Transport Threshold Model of Neoclassical Tearing Modes in Tokamaks", Phys.Plasmas, **10**, 3790(2003).

73) Mikhailovskii, A. B., Shirokov, M. S., Tsypin, V. S., et al., "Transport Threshold Model of Subsonic Neoclassical Tearing Modes in Tokamaks", Phys.Plasmas, **10**, 3975(2003).

74) Mikhailovskii, A., Churikov, A. Konovalov, S., et al., "Possible Nature of Nonideal Perturbations, Limiting PlasmaPressure in a Tokamak", Doklady Phys., **48**, 156(2003).

75) Mikkelsen, D. R., Shirai, H., Urano, H., et al., "Stiff Temperature Profiles in JT-60U ELMy H-mode Plasmas" ,Nucl.Fusion, **43**, 30(2003).

76) Miura, Y. and JT-60 team "Study of Improved Confinement Modes with Edge and/or Internal Transport Barriers on the Japan Atomic Energy Research Institute Tokamak-60 Upgrade (JT-60U)",Phys.Plasmas, **10**, 1809(2003).

77) Morimoto, Y., Ochiai, K., Nishio, T., et al., "Dogleg Duct Streaming Experiment with 14 MeV Neutron Source", J. Nucl. Sci. Technol., Suppl. **4**, 42 (2004).

78) Morimoto, Y., Ochiai, K., Sato, S., et al., "Shutdown Dose Evaluation Experiment for ITER", Fusion Eng. Des., **69**, 643 (2003).

79) Morioka, A., Sato, S., Ochiai, R., et al., "Neutron Transmission Experiment of Boron-Doped Resin for the JT-60SC Neutron Shield using 2.45MeV Neutron Source", J.Nucl. Sci. Tech., **Supplement 4**, 109(2004).

80) Mukhovatov, V., Shimada, M., Shimomura, Y., et al., "Overview of Physics Basis for ITER", Plasma Phys. Control. Fusion, **45**, A235 (2003).

81) Mukhovatov, V., Shimomura, Y., Shimada, M., et al., "Comparison of ITER Performance Predicted by Semi-empiricaland Theory-based Transport Models", Nucl. Fusion, **43**, 942 (2003).

82) Nagasaki, K., Isayama, A., Ide, S., et al., "Stabilization Effect of early ECCD on a Neoclassical Tearing Mode in the JT-60U Tokamak", Nucl. Fusion, **43**, L7(2003).

83) Nagashima,Y., Shinohara,K., Hoshino,K., et al.," Coherent Edge Fluctuation Measurements in H-Mode Discharges in JFT-2M", Plasma Phys. Cntl. Fusion, **46**, A381 (2004).

84) Nakagawa, T., Mihara, Y., Takahashi, K., et al., "Propulsive impulse measurement of a microwave-boosted vehicle in the atmosphere", J. Spacecraft and Rockets **41**, 151 (2004).

85) Nakahira, M., "Structual Safety Assessment of a Tokamak-type Fusion Facility for a Through Crack to Cause Cooling Water Leakage and Plasma Disruption", J. Nucl. Sci. Technol., **41**, 226 (2004).

86) Nakahira, M., "Technical Code Issues of ITER Vacuum Vessel and Their Resolutions",J. Nucl. Sci. Technol., **40**, 687 (2003).

87) Nakamichi, M., Kawamura, H., Uchida, M., "Compatibility Test between $Be_{12}Ti$ and Li_2TiO_3", Fusion Eng. Des., **69**, 257 (2003).

88) Nakamura, H., Higashijima, S., Isobe, K., et al., "Application of glow discharges for tritium removal from JT-60U vacuum vessel", Fusion Eng. Des., **70**, 163 (2004).

89) Nakamura, H., Shu, W. M., Hayashi, T., et al., "Tritium permeation study through tungsten and nickel using pure tritium ion beam", J. Nucl. Mater., **313-316**, 679 (2003).

90) Nakamura, H., Riccardi, B., Ara, K., et al., "Latest Liquid Lithium Target Design during the Key Element Technology Phase in the International Fusion Materials Irradiation Facility (IFMIF)", Fusion Eng. Des., **66-68**, 193 (2003).

91) Nakazawa, T., Grismanovs, V., Yamaki, D., et al., "Disordering in Li2TiO3 irradiated with high energy ions", Nucl. Instrum. Methods Phys. Res. B, **206**, 166 (2003).

92) Neudatchin, S., Takizuka, T., Hayashi, N., et al., "Instantaneous Correlation between ELM-Like MHD Activity and Abrupt Non-Local Reduction of Transport at Internal Transport Barrier Formation in JT-60U High-β_p Plasmas", J. Plasma Fusion Res. (in Japanese), **79**, 1218(2003).

93) Ninomiya, A., Araia, K., Takano, K., et al., "Experimental Results of ITER Nb_3Al Insert –Characteristics of Acoustic Emission–," Cryogenic Eng., **38**, 425 (2003).

94) Nishitani, T., Ochiai, K., Yoshida, S., et al., "D-T Neutron Skyshine Experiments and the MCNP Analysis", J. Nucl. Sci. Technol., Suppl. **4**, 58 (2004).

95) Nunoya, Y., Isono, T., Sugimoto, M., et al., "Evaluation Method of Critical Current and Sharing Temperature for Large-current Cable-in-conduit Conductors", IEEE Trans. ASC, **13**, 1404 (2003).

96) Oda., Y., Nakagawa, T., Takahashi, K., et al., "Plasma behavior in a microwave beaming rocket", J. Inst. Appl. Plasma Sci., **11**, 47 (2003).

97) Oikawa T., Tsuchiya, K., Kurihara, K., "Development of Plasma Stored Energy Feedback Control and its Application to High Performance Discharges on JT-60U", Fusion Eng. Des., **70**, 175(2004).

98) Oka, K., "A New Optical Fiber System with Hybrid Functions of Power Delivery and Real-Time Remote Observation for YAG Laser Welding," Rev. Laser Eng., **31**(9), 612 (2003).

99) Oka, K., "Robot for the nuclear energy disaster ~Development of a Radiation-Proof Robot~," J. Japan Soc. Mech. Eng., **106**, 765 (2003).

100) Okuno, K., Martovetsky, N., Koizumi, N., et al., "Test of the Nb_3Al Insert and ITER Central Solenoid Model Coil", IEEE Trans. ASC, **13**, 1437 (2003).

101) Onozuka, M., Takeda, N., Nakahira, M., et al., "Numerical Evaluation of Experimental Models to Investigate the Dynamic Behavior of the ITER Tokamak Assembly", Fusion Eng. Des., **69**, 757 (2003).

102) Oya, Y., Hirohata, Y., Kizu, K., et al., "Hydrogen Isotope Behavior in In-vessel Components Used for DD Plasma Operation of JT-60U by SIMS and XPS technique", J. Nucl. Mater., **313-316**, 209 (2003).

103) Oyama,N., Bruskin,L.G., Takenaga,H., et al., "Density Fluctuation Measurement at Edge and Internal Transport Barriers in JT-60U", Plasma Phys. Cntl. Fusion, **46**, A355 (2004).

104) Ozeki, T. and JT-60 team "Studies of MHD Behaviour in JT-60U", Plasma Phys. Control. Fusion, **45**, 645(2003).

105) Polevoi, A., Sugihara, M., Takenaga, H., et al., "Pellet Injection as a Possible Tool for Plasma Performance Improvement", Nucl. Fusion, **43**, 1072 (2003).

106) Sagara, A., Enoeda, M., Nishio, S., et al., "Blanket Designs in Fusion Power Reactors", J. Plasma Fusion Res., **79**,

663-671, (2003).

107) Sakamoto K., Kasugai A., Ikeda Y., et al., "Development of 170 and 110GHz gyrotrons for fusion devices", Nucl. Fusion, **43**, 729 (2003).

108) Sakasai, A., Ishida, S., Matsukawa, M., "Advanced Fusion Technologies Developed for JT-60 Superconducting Tokamak", Nucl. Fusion, **44**, 329(2003).

109) Sakurai, S. and JT-60 team "Results and Future Plan of JT-60U towards Steady-State Tokamak Reactor", Plasma Sci. Tech., **6**, 2151(2004).

110) Sato, S., Kawasaki, N., Kume, E., Nishitani, T., "Development of Combined System of Monte Carlo Calculation with Activation Calculation for Evaluation of Decay Gamma Ray Dose Rate in Nuclear Fusion Reactor",J. Nucl. Sci. Technol., Suppl. **4**, 62 (2004).

111) Sato, S., Maki, K., "Analytical Representation for Neutron Streaming through Slits in Fusion Reactor Blanket by Monte Carlo Calculation", Fusion Eng. Des., **65**, 501 (2003). Hou, L., Ishii, T., (Hori, J.), et al., "Measurement of $B(M1)$ for the $pp_{3/2}$ $np^{-1}{}_{/1/2}$ Doublet in ^{68}Cu," Physical Rev. C **68**, 054306 (2003) .

112) Sato, S., Morioka, A., Kinno, M., et al.,"Experimental Study on Induced Radioactivity in Boron-doped Low Activation Concrete for DT Fusion", J. Nucl. Sci. Technol., Suppl. **4**, 66 (2004).

113) Sato, S., Nakamura, T., Nishitani, T., "Helium Production due to Neutron Streaming through Small Circular Ducts in Fusion Reactor Blanket by Analytical Fitting from Monte Carlo Calculation Results",Fusion Sci. Technol., **43**, 559 (2003).

114) Sato, S., Nishitani,T., "Impact of Armor Materials on Tritium Breeding Ratio in the Fusion Reactor Blanket", J. Nucl. Mater., **313-316**, 690 (2003).

115) Sato,S., Ochiai, K., Hori, J., et al., "Neutronics Experiments for DEMO Blanket at JAERI/FNS", Nucl. Fusion, **43**, 527 (2003).

116) Shikama, T., Nishitani, T., Kakuta, T., et al., "Irradiation Test of Diagnostic Components for ITER Application in a Fission Reactor, Japan Materials Testing Reactor", Nucl. Fusion, **43**, 517 (2003).

117) Shimada, M., Mukhovatov, V., Federici, G., et al., "Performance of ITER as a Burning Plasma Experiment",Nucl.Fusion, **44**, 350 (2004).

118) Shimizu, K., Takizuka, T., Sakurai, S., et al., "Simulation of Divertor Detachment Characteristics in JT-60 with Superconducting Coils", J.Nucl. Mater., **313-316**, 1277(2003).

119) Shimomura, Y., "Status and Prospect of the ITER Project", Fusion Sci. Technol. **44**, 3 (2003).

120) Shimotono, H., Nishio, S., Kondoh, S., "Feasibility of D^3He / ST Fusion Power Reactor", Fusion Eng. Design, **69**, 675(2003).

121) Shinohara, K., Kawashima, H., Tsuzuki, K., et al., "Effects of Complex Magnetic Ripple on Fast Ions in JFT-2M Ferritic Insert Experiments", Nucl. Fusion, **43**, 586(2003).

122) Shiraiwa, S., Ide, S., Ito, S., et al., "Formation of Advanced Tokamak Plasmas without the Use of an Ohmic-Heating Solenoid", Phys. Rev. Lett., **92**, 035001-1(2004).

123) Shu, W. M., Kawakubo, Y., Luo, G. N., et al., "Removal of co-deposited layers by excimer lasers", J. Nucl. Sci. Technol., **40**, 1019 (2003).

124) Shu, W. M., Kawakubo, Y., Masaki, K., et al., "Ablative removal of codeposits on JT-60 carbon tiles by an excimer laser", J. Nucl. Mater., **313-316**, 584 (2003).

125) Shu, W. M., O'hira, S., Suzuki, T., et al., "Radiochemical reactions between tritium oxides and carbon monoxide", Fusion Eng. Des., **70**, 123 (2004).

126) Sugie, T., Costley, A., Malaquias, A., et al., "Spectroscopic Diagnostics for ITER", J. Plasma Fusion Res., **79**, 1051 (2003).

127) Sugie, T., Kasai, S., Taniguchi, et al., "Irradiation Test of Mo- and W-Mirrors for ITER by Low Energy Deuterium Ions", J. Nucl. Mater., **329-333PB**, 1481 (2004).

128) Sugihara, M., Lukash, V., Kawano, Y., et al., "Wave Form of Current Quench during Disruptions in Tokamaks",J.Plasma Fusion Res., 79, 706 (2003).

129) Sugihara, M., Mukhovatov, V., Shimada, M., et al., "Scaling of H-mode Edge Pedestal Pressure for a Type-I ELMRegime in Tokamaks",Plasma Phys. Control. Fusion, 45, L55 (2003).

130) Sugiyama, K., Miyasaka, K., Masaki, K., et al., "Tritium Profiles on the Surface of Graphite Tiles Used in JT-60U", Physica Scripta, T103, 56 (2002) .

131) Suzuki, S., Ueda, Y., Tokunaga, K., et al., "Present Research Status on Divertor And Plasma Facing Components for Fusion Power Plants", Fusion Sci. Technol., 44, 41 (2003).

132) Takahashi, K., Ishitsuka, E., Hayashida, K., et al., "Development of ECH&CD launcher components for fusion device", Fusion Eng. Des., 66-68, 589 (2003).

133) Takahashi, K., Moeller, C. P., Sakamoto, K., et al., "High power experiments of remote steering launcher for electron cyclotron heating and current drive", Fusion Eng. Des., 65, 589 (2003).

134) Takenaga, H., Higashijima, S., Oyama, N., et al., "Relationship between Particle and Heat Transport in JT-60U Plasmas with Internal Transport Barrier", Nucl. Fusion, **43**, 1235(2003).

135) Takizuka, T., Hosokawa, M., Shimizu, K., "Two-dimensional Particle Simulation of the Flow Control in SOL and Divertor Plasmas", J. Nucl. Mater.,**313-316**, 1331 (2003).

136) Tamai, H., Kurita, G., Sakurai, S., et al., "Progress in Physics and Technology Developments for the Modification of JT 60", J.Plasma Sci.Tech., **6**, 2141(2004).

137) Tanabe, T., Berkis, N., Miya, N., et al., "Tritium Retention of Plasma Facing Components in Tokamaks", J. Nucl Mater, **313-316**, 478 (2003).

138) Tanaka, T., Sato, F., (Nishitani, T.), et al., "Electrical Properties of Mineral-insulated Cable under Fusion Neutron Irradiation", Fusion Eng. Des., **66-68**, 837 (2003).

139) Tanigawa, H., Ando, M., Sawai, T., et al., "Microstructure and Hardness Variation in a TIG Weldment of Irradiated F82H", Fusion Sci. Technol., **44**, 219 (2003).

140) Tanigawa, H., Shiba, K., Sokolov, M. A., et al., "Charpy Impact Properties of Reduced-Activation Ferritic/ Martensitic Steels Irradiated in HFIR up to 20 DPA", Fusion Sci. Technol., **44**, 206 (2003).

141) Taniguchi, M., Hanada, M., Inoue, T., et al., "Development of high performance negative ion sources and accelerators for MeV class neutral beam injector",Nucl. Fusion, **43**, 665 (2003).

142) Taniguchi, M., Sato, K., Ezato, K., et al., "Sputtering of carbon-tungsten mixed materials by low energy deuterium", J.Nucl.Mater., **313-316**, 360 (2003).

143) Tobita, K., Nishio, S., Konishi, S., et al., "Design Choice and Radioactive Waste of Fusion Reactor," J. Nucl. Mater. **129-333** 1610 (2004).

144) Tobita, K., Nishio, S., Konishi, S., et al., "First Wall Issues related with Energetic Particle Deposition in a Tokamak Fusion Power Reactor", Fusion Eng. Des., **65**, 561(2003).

145) Tobita, K., Ozeki, T., Nakamura, Y., "Alpha Particle Confinement and Neutral Beam Current Drive in Fusion Plasma with a Current Hole," Plasma Phys. Control. Fusion 46 (2004) S95.

146) Tsuchiya, K., Alvani, C., Kawamura, H., et al., "Effect of TiO_2 on the Reduction of Lithium Titanate Induced by H_2 in the Sweep Gas", Fusion Eng. Des., **69**, 443 (2003).

147) Tsuchiya, K., Kawamura, H., Uchida, H., et al., "Improvement of Sintered Density of Li_2TiO_3 Pebbles Fabricated by Direct-Wet Process", Fusion Eng. Des., **69**, 449 (2003).

148) Tsuchiya, K., Kizu, K., Miura, Y., et al., "Design of Toroidal Field Coil for the JT-60 Superconducting Tokamak", IEEE Trans. Appl. Superconductivity, **13**, 1480(2003).

149) Tsuchiya, K., Kizu, K., Miura, Y.M., et al., "Development of a 30 m Long Nb_3Al Superconducting Conductor Jacketed with a Round-In-Square Type Stainless Steel Conduit for the Toroidal Field Coils in JT-60SC", Fusion Eng. Des., **70**,131(2004).

150) Tsuzuki, K., Kimura, H., Kawashima, H., et al., "High Performance Tokamak Experiments with Ferritic Steel Wall on JFT-2M", Nucl. Fusion, **43**, 1288 (2003).

151) Uchida, M., Ishitsuka, E., Kawamura, H., "Thermal Conductivity of Neutron Irradiated $Be_{12}Ti$", Fusion Eng. Des., **69**, 499 (2003).

152) Uchida, M., Kawamura, H., Uda, M., et al., "Elementary Development for Beryllide Pebble Fabrication by Rotating Electrode Method", Fusion Eng. Des., **69**, 491 (2003).

153) Ueda, Y., Tobita, K., Kato, Y., "PSI Issues at Plasma Facing Surfaces of Blankets of Fusion Reactors", J. Nucl. Mater, **313-316**, 32 (2003).

154) Uehara, K., Fukumoto, R., Tsushima, A., et al., "Evaluation of Ion Temperature using Ion Sensitive Probe in the Boundary Plasma of the JFT-2M Tokamak", J.Phys. Soc. Jpn, **72**, 2804(2003).

155) Umeda, N., Grisham, L. R., Yamamoto, T., et al., "Improvement of beam performance in the negative-ion based NBI system for JT-60U", Nuclear Fusion, **43**, 522 (2003).

156) Verzilov, Y., Ochiai, K., Nishitani, T., "A new Approach to the D-T Neutron Monitor using Water Flow", J. Nucl. Sci. Technol., Suppl. **4**, 395 (2004).

157) Wakai, E., Ando, M., Tanigawa, H., et al., "Swelling behavior of F82H steel irradiated by triple/dual ion beams", J. Nucl. Mater., **318**, 267 (2003).

158) Wakai, E., Sato, M., Sawai, T., et al., "Mechanical properties and microstructure of F82H steel doped with boron or boron and nitrogen as a function of heat treatment", Materials Transactions, JIM, **45**, 407 (2004).

159) Yamada, H., Nagao, Y., Kawamura, H., et al., "Preliminary Neutronic Estimation for Demo Blanket

withBeryllide", Fusion Eng. Des., **69**, 269 (2003).

160) Yamaguchi, K., Yamauti, U., Hirohata, Y., et al.,"Deuterium Retention of Low Activation Ferritic Steel F82H" , J.Vac.Soc. Jpn, **46**, 449(2003).

161) Yamamoto, T., Umeda, N., Kuriyama, M., et al., "Improving the performance of a negative-ion based neutral beam injector for JT-60U", J. Plasma Fusion Res. SERIES, **5**, 474 (2002).

162) Yoshida, S., Nishitani, T., K. Ochiai, et al., "Measurement of radiation skyshine with D-T neutron source", Fusion Eng. Des., **69**, 637 (2003).

163) Yoshino, R., "Neural-net disruption predictor in JT-60U", Nucl. Fusion, **43**, 1771 (2003).

A.1.3 List of papers published in conference proceedings

1) Aiba, N., Tokuda, S., Ishizawa, T., et al., "The Effect of the Aspect Ratio on the External Kink-Ballooning Instability in High-Beta Tokamaks," Proc. 13th Int. Toki Conf. on Plasma Phys. and Control. Nucl. Fusion, 44, J. Plasma Fusion Res., in print (2004).

2) Ando, M., Tanigawa, H., Wakai, E., et al., "Reduction Method of Radiation Hardening in F82H Steels by Heat Treatments," 11th Int. Conf. on Fusion Reactor Materials (2003), to be published in J. Nucl. Mater..

3) Ando, M., Wakai, E., Tanigawa, H., et al., "Synergistic Effect of Displacement Damage and Helium Atoms on Radiation Hardening inF82H at TIARA Facility," 11th Int. Conf. on Fusion Reactor Materials (2003), to be published in J. Nucl. Mater..

4) Asakura, N., Takenaga, H., Nakano, T., et al., "Parallel and Drift Plasma Flows in SOL, and Influence on Impurity Transport in JT-60U Tokamak", Proc. 30th EPS Conf. on Control. Fusion and Plasma Phys., 27A, P-2.153 (CD-ROM) (2003).

5) Bakhtiari, M., Tamai, H., Kawano, Y., et al., "Disruption Mitigation using Gas Puffing in the JT-60U Tokamak," to be published in Proc. 45th Annual Meeting of the Division of Plasma Physics of APS (2003).

6) Bruskin, L. G., Oyama, N., Mase, A., et al., "Theoretical Modeling and Application of Microwave Reflectometry to Plasma Turbulence Study", to be published in Proc. 13th Int. Toki Conf. on Plasma Phys. and Control. Nucl. Fusion (2003).

7) Chankin, A. V., Stangeby, P. C., "Global Circulation of Drift Flows in the SOL and Divertor and its Impact on Divertor Asymmetries," Proc. 30th EPS Conf. on Control. Fusion and Plasma Phys., 27A, O-4.1C (CD-ROM) (2003).

8) Costley, A. E., Itami, K., Kondoh, T., et al., "Long Pulse Operation in ITER: Issues for Diagnostics" Proc. 30th EPS Conf. on Contr. Fusion and Plasma Phys., 27A, O-4.1D (CD-ROM) (2003).

9) Fujita, T., Sakamoto, Y., Suzuki, T., et al., "Key Quantities for ITB Formation and Sustainment," Proc. 30th EPS Conf. on Control. Fusion and Plasma Phys., 27A, P-2.131 (CD-ROM) (2003).

10) Furukawa, M., Tokuda, S., Wakatani, M., "A Model Equation for Ballooning Modes in Toroidally Rotating Tokamaks," Proc. 13th Int. Toki Conf. on Plasma Phys. and Control. Nucl. Fusion, 40, J. Plasma Fusion Res., in print (2004).

11) Furuya, K., Walai, E., Takada, F., et al., "Tensile Property in Neutron-Irradiated HIP-Bond F82H Steel," to be published in Proc. AESJ Fall Meeting (2003).

12) Gotoh, Y., Arai, T., Yagyu, J., et al., "Transmission Electron Microscopy of Redeposition Layers on Graphite Tiles Used for Open Divertor Armor of JT-60," 11th Int. Conf. on Fusion Reactor Materials (2003), to be published in J. Nucl. Mater..

13) Hanada, M., Kashiwagi, M., Inoue, T., et al., "Experimental comparison between plasma and gas neutralization of high-energy negative ion beams," 10th Int. Conf. on Ion Sources (2003), to be published in Rev. Sci. Instrum..

14) Heidinger, R., Danilov, I., Takahashi, K., et al., "Performance and conceptual studies of diamond windows for high power gyrotrons and EC launchers," Proc. IAEA Technical Meeting on ECRH Physics and Technology for ITER (2003), to be published on CD-ROM (IAEA, Vienna).

15) Heinzel, V., Bem, P., (Sugimoto, M.), et al., "Overview on the IFMIF Test Cell Development," 11th Int. Conf. on Fusion Reactor Materials (2003), to be published in J. Nucl. Mater..

16) Higashijima, S., Nakamura, H., Horikawa, T., et al., "Tritium Removal using Wall Conditioning Discharges in JT-60U," Proc. 30th EPS Conf. on Control. Fusion and Plasma Phys., 27A, P-2.126 (CD-ROM) (2003).

17) Hino, T., Yamaguchi, K., Yamauchi, Y., et al., "Deuterium Retention and Physical Sputtering of Low Activation Ferritic Steel," to be published in Proc. 4th General Sci. Assembly of Asia Plasma & Fusion Association on

New Develop. of Plasma Phys. and Fusion Tech. (2003).

18) Hirohata, Y., Oya, Y., Yoshida, H., et al., "Depth Profile and Retention of Hydrogen Isotopes in Graphite Tiles Used in the W-shaped Divertor of JT-60U," 11th Int. Conf. on Fusion Reactor Materials (2003), to be published in J. Nucl. Mater..

19) Hobirk, J., Oikawa, T., Fujita, T., et al., "Off-Axis Neutral Beam Current Drive Experiments on ASDEX Upgrade and JT-60U," Proc. 30th EPS Conf. on Control. Fusion and Plasma Phys., **27A**, O-4.11B (CD-ROM), (2003).

20) Hoshino, K., Nagashima, Y., Ido, T., et al., "On MHD oscillations in high beta H-mode Tokamak Plasma in JFT-2M," 13th Int. Toki Conf. on Plasma Phys. and Control. Nucl. Fusion (2003), to be published in J. Plasma Fusion Research.

21) Idomura, Y., Tokuda, S., Kishimoto, Y., "Gyrokinetic Simulations of Tokamak Micro-Turbulence including Kinetic Electron Effects," Proc.13th Int. Toki Conf. on Plasma Phys. and Control. Nucl. Fusion, 7, J. Plasma Fusion Res., in print (2004).

22) Inoue, T., Taniguchi, M., Dairaku, M., et al., "Acceleration of 1 MeV, 100 mA class H^- ion beams in a proof-of-principle accelerator for ITER," 10th Int. Conf. on Ion Sources (2003), to be published in Rev. Sci. Instrum..

23) Isayama, A., Nagasaki, K., Ide, S., et al., "Stabilization of Neoclassical Tearing Mode by Electron Cyclotron Wave Injection in JT-60U," Proc. 15th Topical Conf. on Radio Frequency Power in Plasmas, 321 (2003).

24) Itami, K., Sugie and T., Vayakis, G., "Study of Multiplexing Thermography for ITER Divertor Targets" Proc. 30th EPS Conf. on Contr. Fusion and Plasma Phys., **27A**, P-4.62 (CD-ROM) (2003).

25) Itoh, T., Itoh, K., (Ida, M.), et al., "Optical Measurement of Waves on High-Speed Lithium Jet Simulating IFMIF Target Flow," to be published in Proc. 11th Int. Conf. on Nuclear Engineering (2003).

26) Jameson, R. A., Ferdinand, R., Klein, H., et al., "IFMIF Accelerator Facility Reference Design," 11th Int. Conf. on Fusion Reactor Materials (2003), to be published in J. Nucl. Mater..

27) Kagei, Y., Kishimoto, Y., Nagata, M., et al, "MHD Relaxation to a Flipped State in Low Aspect Ratio Toroidal Plasmas," Proc. 13th Int. Toki Conf. on Plasma Phys. and Control. Nucl. Fusion, 99, J. Plasma Fusion Res., in print (2004).

28) Kaminaga, A., Horikawa, T., Nakamura, H., et al., "Analysis of Exhausted Gas in JT-60 Deuterium Operation," Proc. 20th IEEE/NPSS Symp. on Fusion Eng. (2003).

29) Kamiya, K., Bakhtiari, M., Kasai, S., et al., "High Recycling Steady H-mode Regime in the JFT-2M Tokamak," 9th IAEA Technical Meeting on H-mode Physics and Transport Barriers (2003), to be published in Plasma Phys. Control. Fusion.

30) Kasugai, A., Sakamoto, K., Minami, R., et al., "Study of millimeter wave high power gyrotron for long pulse operation," Proc. 25th Int. Free Electron Laser Conf. (2003), to be published in Fusion Eng. Des..

31) Kasugai, A., Sakamoto, K., Takahashi, K., et al., "Development of gyrotron system for high frequency power modulation," Proc. 8th Int. Conf. on Infrared and Millimeter Waves, 127 (2003).

32) Kawamura, H., Takahashi, H., Yoshida, N., et al., "Present status of beryllide R&D as neutron multiplier," Proc. 11th Int. Conf. on Fusion Reactor Materials (2003), to be published in J. Nucl. Mater..

33) Kawano, Y. and JT-60 team "Diagnostics for Fusion Plasma Control in JT-60U," Proc. 30th EPS Conf. on Control. Fusion and Plasma Phys., **27A**, O-3.5C (CD-ROM) (2003).

34) Kawano, Y., Chiba, S, Inoue, A., et al., "Application of CVD Diamond Window in Infrared Laser Diagnostics for Fusion Plasmas," Proc. 30th EPS Conf. on Control. Fusion and Plasma Phys., **27A**, P-4.66 (CD-ROM) (2003).

35) Kawano, Y., Sugihara, M., Ozeki, T., et al., "Characteristics of Current Quenches of Major Disruption in JT-

60U," Proc. 30th EPS Conf. on Control. Fusion and Plasma Phys., 27A, P-2.129 (CD-ROM) (2003).

36) Kishimoto, H., Shirai, H., "Recent Progress in Tokamak Physics toward ITER," Proc. 3rd Int. Sakharov Conf. on Physics, 185 (2003).

37) Kitaide, Y., Hatayama, A., Inoue, T., et al., "Numerical analysis of plasma, uniformity un negative ion sources by a fluid model," 10th Int. Conf. on Ion Sources (2003), to be published in Rev. Sci. Instrum..

38) Kizu, K., Miura, Y.M., Tsuchiya, K., et al., "Development of the Nb_3Al D-Shape Coil Fabricated by React-And-Wind Method for JT-60 Superconducting Tokamak," to be published in Proc. 6th Europ. Conf. on Appl. Superconductivity (2003).

39) Kondo, H., Fujisato, A., (Ida, M.), et al., "High Speed Lithium Flow Experiments for IFMIF Target," 11th Int. Conf. on Fusion Reactor Materials (2003), to be published in J. Nucl. Mater..

40) Kondoh, T., Richards, R. K., Hutchinson, D. P., et al., "Prospects for alpha-particle diagnostics by CO_2 laser collective Thomson scattering on ITER," Proc. 30th EPS Conf. on Contr. Fusion and Plasma Phys., 27A, P-4.65 (CD-ROM) (2003).

41) Kudo, Y., Sakasai, A., Nakajima, H., et al., "Mechanical Tests on the Welding Part of SS316LN after Heat Treatment for Nb3Sn Superconducting Conductor," 11th Int. Conf. on Fusion Reactor Materials (2003), to be published in J. Nucl. Mater..

42) Kusama, Y. and JFT-2M group "Advanced Material and High Performance Experiments on JFT-2M," Proc. 30th EPS Conf. on Control. Fusion and Plasma Phys., 27A, P-2.143 (CD-ROM) (2003).

43) Li, J., Kishimoto, Y., Miyato, N., et al., "Saturation of Zonal Flow in Gyrofluid Simulations of Electron Temperature Gradient Turbulence," Proc. 13th Int. Toki Conf. on Plasma Phys. and Control. Nucl. Fusion, 99, J. Plasma Fusion Res., in print (2004).

44) Loginov, N., Nakamura, H., Shishulin, V., et al., "Some Technological Aspects of IFMIF Liquid Lithium Target," 11th Int. Conf. on Fusion Reactor Materials (2003), to be published in J. Nucl. Mater..

45) Maebara, S., Morishita, T., Sugimoto, M et al., "Low Power Test of RFQ Mock-up modules at 175MHz for IFMIF Project," Proc. 2003 Particle Accelerator Conf., 2829 on CD-ROM (2003).

46) Masaki, K., Yagyu, J., Miyo, Y., et al., "In-out Asymmetry of Low-Z Impurity Deposition on the JT-60 Divertor Tiles," 11th Int. Conf. on Fusion Reactor Materials (2003), to be published in J. Nucl. Mater..

47) Matsui, H., and IFMIF team, "Outcome from the Key Element Technology Phase in IFMIF," 11th Int. Conf. on Fusion Reactor Materials (2003), to be published in J. Nucl. Mater..

48) Matsumoto, T., Kishimoto, Y., Li, J., "Statistical Characteristics from Gyrofluid Transport Simulation," 13th Int. Toki Conf. on Plasma Phys. and Control. Nucl. Fusion, PII-41, J. Plasma Fusion Res., 101, in print (2004).

49) Mironov, M. I., Khudoleev, A. V., Kusama, Y., "Feasibility of Local Fast Ion Distribution Function Measurement on JT-60U by Means of Neutral Heating Beams," Proc. 30th EPS Conf. on Control. Fusion and Plasma Phys., 27A, P-4.74 (CD-ROM) (2003).

50) Mironov, M. I., Khudoleev, A. V., Kusama, Y., "Formation of Target for Fast Ions Charge-Exchange in Big Plasma Devices with Neutral Beam Heating," to be published in Proc. 10th Russian Conf. on High-Temperature Plasma Diagnostics (2003).

51) Miura, Y.M., Kizu, K., Tsuchiya, K., et al., "Development of 20-kA NbTi Cable-In-Conduit Conductors for JT-60 Modification Program," to be published in Proc. 6th Europ. Conf. on Appl. Superconductivity (2003).

52) Miya, N., "Research Activities Using Plasma Facing Materials in JT-60U under a Cooperative Program between JAERI and Universities," 11th Int. Conf. on Fusion Reactor Materials (2003), to be published in J. Nucl. Mater..

53) Miyato, N., Li, J., Kishimoto, Y., "Electromagnetic Effect on Turbulent Transport in Tokamak based on Landau

Fluid Global Simulation," Proc. 13th Int. Toki Conf. on Plasma Phys. and Control. Nucl. Fusion, 98, J. Plasma Fusion Res., in print (2004).

54) Morimoto, Y., Oya, Y., Hirohata, Y., et al., "Correlation between Hydrogen Isotope Profiles and Surface Structure of Divertor Tiles in JT-60U," 11th Int. Conf. on Fusion Reactor Materials (2003), to be published in J. Nucl. Mater..

55) Morishita, T., Inoue, T., Iga, T., et al., "High proton ratio plasma production in a small negative ion source," 10th Int. Conf. on Ion Sources (2003), to be published in Rev. Sci. Instrum..

56) Nagashima, Y., Shinohara, K., Hoshino, K., et al., "Coherent Edge Fluctuation Measurements in H-mode Discharges on JFT-2M," 9th IAEA Technical Meeting on H-mode Physics and Transport Barriers (2003), to be published in Plasma Phys. Control. Fusion.

57) Nakagawa, T., Mihara, Y., Takahashi, K. et al., "A microwave beaming thruster powered by 1MW microwave," Proc. 9th AIAA/ASME/SAE/ASEE Joint Propulsion Conference and Exhibi (2003), to be published on CD-ROM.

58) Nakamura, Y., Tsutsui, H., Takei, N., et al., "Current Profile Behavior during Ramping-up Phase in High Bootstrap Current Tokamak Plasmas," Proc. 13th Int. Toki Conf. on Plasma Phys. and Control. Fusion, 39, J. Plasma Fusion Res., in print (2004)

59) Nakamura, Y., Tsutsui, H., Takei, N., et al., "TSC Modelling of Current Ramp Scenarios with ITB-Generated Bootstrap Currents in JT-60U Reversed Shear Discharges," Proc. 30th EPS Conf. on Control. Fusion and Plasma Phys., 27A, P-2.128 (2003)

60) Nakamura, H., Riccardi, B., Loginov, N., et al., "Present Status of the Liquid Lithium Target Facility in IFMIF," 11th Int. Conf. on Fusion Reactor Materials (2003), to be published in J. Nucl. Mater..

61) Narui, M., Yamasaki, M., (Nishitani, T.), et al., "Irradiation Effects in Bolometer and Constituting Materials for ITER Application," Proc.11th Int. Conf. on Fusion Reactor Materials (2003), to be published in J. Nucl. Mater..

62) Nishitani, T., Ochiai, K., Klix, A., et al., "Initial Results of Neutronics Experiments for Evaluation of Tritium Production Rate in Solid Breeding Blanket," to be published in Proc. 20th IEEE/NPSS Symp. on Fusion Engineering (2003).

63) Nishitani, T., Vayakis, G., Yamauchi, M., et al., "Radiation-mediated Thermoelectric Potential in the Mineral-insulated Cable of Magnetic Diagnostic Coils for ITER," Proc.11th Int. Conf. on Fusion Reactor Materials (2003), to be published in J. Nucl. Mater..

64) Ochiai, K., Hayashi, T., Kutsukake, C., et al., "Measurement of Deuterium and Tritium Retention on the Surface of JT-60 Divertor Tiles by Means of Nuclear Reaction Analysis," Proc. 11th Int. Conf. on Fusion Reactor Materials (2003), to be published in J. Nucl. Mater..

65) Oda, Y., Nakagawa, T., Takahashi, K., et al., "An observation of plasma inside of microwave boosted thruster," Proc. 2nd Int. Symp. on Beamed Energy Propulsion, 399 (2003).

66) Ogawa, H., Yamauchi, Y., Tsuzuki, K., et al., "Impurity Behavior in JFT-2M with Ferritic Steel Wall," 11th Int. Conf. on Fusion Reactor Materials (2003), to be published in J. Nucl. Mater.

67) Ogiwara, H., Katoh, H., (Tanigawa, H.), et al., "Microstructural Evolution in Reduced Activation Ferritic/Martensitic Steels under Ion Irradiation and Effect on Deformation Behavior," 11th Int. Conf. on Fusion Reactor Materials (2003), to be published in J. Nucl. Mater..

68) Oka, K., Tanaka, T., (Wakai, E.), et al., "Fracture Properties of 50MeV Helium Irradiated Oxide Dispersion Strengthened Ferritic Steels," 11th Int. Conf. on Fusion Reactor Materials (2003), to be published in J. Nucl. Mater..

69) Oka, K., "Remote Handling by the Radiation-Proof Robot," Proc. Mechanical Engineering Congress, VIII, 213, 2003.

70) Oya, Y., Morimoto, Y., Oyaidzu, M., et al., "Analyses of Hydrogen Isotope Distributions in the Outer Target Tile Used in the W-shaped Divertor of JT-60U," to be published in Proc. 7th Int. Workshop on Hydrogen in Condensed Mater (2003).

71) Peterson, B. J., Ashikawa, N., Konoshima, S., et al., "Imaging Bolometer for a Burning Plasma Experiment," Proc. 30th EPS Conf. on Control. Fusion and Plasma Phys., 27A, P-4.67 (CD-ROM) (2003).

72) Saigusa, M., Takahashi, K., Ohishi, S., et al., "Study of joule loss of grooved mirror polarizer," Proc. IAEA Technical Meeting on ECRH Physics and Technology for ITER (2003), to be published on CD-ROM (IAEA, Vienna).

73) Sakamoto, K. "Development of gyrotron and application to fusion research," Proc. 8th Int. Conf. on Infrared and Millimeter Waves, 11, (2003).

74) Sakamoto, K., Kasugai, A., Takahashi, K., et al., "Development of ECRF technology in JAERI," Proc. IAEA Technical Meeting on ECRH Physics and Technology for ITER (2003), to be published on CD-ROM (IAEA, Vienna).

75) Sakasegawa, H., Tanigawa, H., Hashimoto, N., et al., "Correlation between Irradiation Creep Behavior and Microstructural Evolution of Reduced Activation Ferritc/Martensitic Steels," 11th Int. Conf. on Fusion Reactor Materials (2003), to be published in J. Nucl. Mater..

76) Sasaki, M., Morimoto, Y., Takahashi, K., et al., "Energetic deuterium and helium irradiation effects on chemical structure of CVD diamond," Proc. 11th Int. Conf. on Fusion Reactor Materials (2003), to be published in J. Nucl. Mater.

77) Sato, M., Isayama, A., Inagaki, S., et al., "Relativistic Downshift Frequency Effects on Electron Cyclotron Emission Measurement; Measurements of Electron Density in Tokamak and Electron Temperature in LHD," to be published in Proc. 13th Joint Workshop on Electron Cyclotron Emission and Electron Cyclotron Resonance Heating (2003).

78) Sato, M., Kimura, H., Tsuzuki, K., et al., "Design of Fully Covering Ferritic inside wall to reduce Toroidal ripple in JFT-2M," to be published in Proc. 20th IEEE/NPSS Symp. on Fusion Eng. (2003).

79) Sato, S., Tanaka, T., Hori, J., et al., "Radioactivity of Vanadium-alloy Induced by D-T Neutron Irradiation," Proc.11th Int. Conf. on Fusion Reactor Materials (2003), to be published in J. Nucl. Mater..

80) Sawai, T., Ando, M., Wakai, E., et al., "Microstructural Evolution and Hardening in Ion-Irradiated F82H up to 100 dpa," 11th Int. Conf. on Fusion Reactor Materials (2003), to be published in J. Nucl. Mater..

81) Seki, M., Akiba, M., Kayama, A., et al., "Overview of fusion nuclear technology in Japan," Proc. 6th Int. Symp. on Fusion Nuclear Technology (2003), to be published in Fusion Eng. Des..

82) Shiba, K., Nakamura, K. and Hishinuma, A., "Preliminary Research Results on ODS Steels for Fusion Applications," 11th Int. Conf. on Fusion Reactor Materials (2003), to be published in J. Nucl. Mater..

83) Shikama, T., Nishitani, T., Yamamoto, S., et al., "Irradiation Tests of Functional Materials for ITER Plasma Diagnostics," Proc. 11th Int. Conf. on Fusion Reactor Materials (2003), to be published in J. Nucl. Mater..

84) Shimada, M., Polevoi, A., Mukhovatov, V., et al., "High Performance Operation in ITER," Proc. 30th EPS Conf. on Contr. Fusion Plasma Phys., P3.137 (CD-ROM) (2003).

85) Shimomura, Y., "Review of the ITER project," 18th Int. Conf. on Magnet Technology (2003), to be published in IEEE Transactions on Applied Superconductivity.

86) Shimomura, Y., "Status and prospect of the ITER project," 11th Int. Conf. on Fusion Reactore Materials (2003), to be published in J. Nucl. Mater..

87) Shinohara, K., Takechi, M., Ishikawa, M., et al., "Energetic Particle Physics in JT-60U and JFT-2M," 8th IAEA Technical Meeting on Energetic Particles in Magnetic Confinement Systems (2003), to be published in Plasma Phys. Control. Fusion.

88) Sokolov, M. A., Tanigawa, H., Shiba, K., et al., "Fracture Toughness and Charpy Impact Properties of Several RAFS before and after Irradiation in HFIR," 11th Int. Conf. on Fusion Reactor Materials, (2003), to be published in J. Nucl. Mater..

89) Song, Y., Nishio, S., Konishi, S., et al., "Buckling Analysis for the Center Post of Low Aspect Ratio Tokamak," to be published in Proc. 20th IEEE/NPSS Symp. on Fusion Eng. (2003).

90) Sugie, T., Costley, A., Malaquias, A., et al., "Spectroscopic Measurement System for ITER Divertor Plasma: Divertor Impurity Monitor," Proc. 30th EPS Conf. on Contr. Fusion and Plasma Phys., **27A**, P-4.63 (CD-ROM) (2003).

91) Sugihara, M., Lukash, V., Kawano, Y., et al., "Examinations on Plasma Behaviour during Disruptions on Existing Tokamaks and Extrapolation to ITER," Proc. 30th EPS Conf. on Contr. Fusion Plasma Phys., P2.139 (CD-ROM) (2003).

92) Sugimoto, M. and Takeuchi, H., "Low Activation Materials Applicabale to IFMIF Accelerator," 11th Int. Conf. on Fusion Reactor Materials (2003), to be published in J. Nucl. Mater..

93) Sugimoto, M., Maebara, S., Moriyama, S., et al., "Behavior Analysis of RF System for Linac in International Fusion Materials Irradiation Facility (IFMIF)," to be published in Proc. 14th Symp. on Accelerator Sci. Technol. (2003).

94) Sugiyama, K., Tanabe, T., Masaki, K., et al., "Tritium Retention in Plasma-facing Components Following D-D Operation," 11th Int. Conf. on Fusion Reactor Materials (2003).

95) Suzuki, S., Tsuzuki, K., Kimura, H., et al., "Engineering Design in Installation of Fully Covering Ferritic Inside Wall on JFT-2M", 20th IEEE/NPSS Symp. on Fusion Engineering (2003).

96) T. Kondoh, Y. Kawano, A. E. Costley, et al., "Toroidal interferometer/polarimeter density measurement system for long pulse operation on ITER," Proc. 30th EPS Conf. on Contr. Fusion and Plasma Phys., 27A, P-4.64 (CD-ROM) (2003).

97) Takahashi, K., Moeller, C. P., Kasugai, A., et al., "Transmission experiments of a 170GHz remote steering EC launcher," Proc. 8th Int. Conf. on Infrared and Millimeter Waves, 385 (2003).

98) Takahashi, K., Sakamoto, K., Imai, T., et al., "Development of EC launcher and diamond window for ITER," Proc. IAEA Technical Meeting on ECRH Physics and Technology for ITER (2003), to be published on CD-ROM (IAEA, Vienna).

99) Takase, Y., Suzuki, T., Ide, S ., et al., "Profile Control and Plasma Start-Up by RF Waves towards Advanced Tokamak Operation in JT-60U," Proc. 15th Topical Conf. on Radio Frequency Power in Plasmas, 235 (2003).

100) Takatu, H., Satou, K., Hamada, K., et al., "Overview on materials R&D activities in Japan towards ITER construction and operation," Proc. 11th Int. Conf. on Fusion Reactor Materials (2003), to be published in J. Nucl. Mater..

101) Takei, N., Nakamura, Y., Kawano, Y., et al., "Axisymmetric MHD Simulation of ITB Crash and Following Disruption Dynamics of Tokamak Plasmas with High Bootstrap Current," Proc. 13th Int. Toki Conf. on Plasma Phys. and Control. Fusion, 39, J. Plasma Fusion Res., in print (2004).

102) Takei, N., Nakamura, Y., Tsutsui, H., et al., "TSC Simulation of Disruptive Current Termination on JT-60U Reversed Shear Plasmas," Proc. 30th EPS Conf. on Control. Fusion and Plasma Phys., (2003) **27A**, P-2.127 (CD-ROM) (2003).

103) Takenaga, H. and JT-60 team "Transport Study in Reactor-Relevant Regime on JT-60U towards Advanced Steady-State Tokamak Operation," Proc. 30th EPS Conf. on Control. Fusion and Plasma Phys., **27A**, O-1.1A (CD-ROM) (2003).

104) Tanabe, T., Sugiyama, K., Gotoh, Y., et al., "PMI Studies in JT-60U - Hydrogen Retention and Erosion/Deposition of Carbon-," to be published in 10th Int. Workshop on Carbon Matrerials for Fusion

Application (2003).

105) Tanabe, T., Sugiyama, K., Skinner, C. H., et al., "Tritium Retention and Carbon Deposition on Plasma Facing Materials," 11th Int. Conference on Fusion Reactor Materials (2003), to be published in J. Nucl. Mater..

106) Tanaka, T., Sato, S., Nagasaka, T., et. al., "Evaluation of Activation Properties of Fusion Candidate Vanadium Alloy NIFS-HEAT-2," to be published in Proc. 20th IEEE/NPSS Symp. on Fusion Engineering (2003).

107) Tanigawa, H., Hashimoto, N., Ando, M., et al., "Microstructure Property Analysis of HFIR Irradiated Reduced-Activation Ferritic/Martensitic Steels," 11th Int. Conf. on Fusion Reactor Materials, (2003), to be published in J. Nucl. Mater..

108) Toh, K., Shikama, T., (Yamauchi, M.), et al., "Optical Characteristics of Aluminum Coated Fused Silica Core Fibers under 14 MeV Fusion Neutrons Irradiation," Proc. 11th Int. Conf. on Fusion Reactor Materials 2003, to be published in J. Nucl. Mater..

109) Tokuda, S., Aiba, N., "Theory of the Newcomb Equation and Application to MHD Stability Analysis of a Tokamak," Proc. 13th Int. Toki Conf. on Plasma Phys. and Control. Nucl. Fusion, 39, J. Plasma Fusion Res., in print (2004).

110) Tokuda, S., "Inner Layer Problem for Ideal MHD Modes in a Toroidal System," Proc. 30th EPS Conf. on Control. Fusion and Plasma Phys., 27A, P-2.110 (CD-ROM) (2003).

111) Tsuzuki, K., Shinohara, K., Kamiya, K., et al., "Investigation of Compatibility of Low Activation Ferritic Steel with High Performance Plasma by Full Covering of Inside Vacuum Vessel Wall on JFT-2M," 11th Int. Conf. on Fusion Reactor Materials (2003), to be published in J. Nucl. Mater.

112) Verzilov, Y., Ochiai, K., Klix, A., et al., "Non-destructive Analysis of Impurities in Beryllium for Tritium Breeding Ratio Evaluation," Proc. 11th Int. Conf. on Fusion Reactor Materials (2003), to be published in J. Nucl. Mater..

113) Wakai, E., Ando, M., Sawai, T., et al., "Swelling Behavior and Controlling of F82H," 11th Int. Conf. on Fusion Reactor Materials (2003), to be published in J. Nucl. Mater..

A.1.4 List of other papers

1) Akiba, M., Jitsukawa, S., Muroga, T., "(Chapter 4) ITER and the prospects to DEMO/Commercial reactors," J. Plasma Fusion Res., **79**, 650 (2003), (in Japanese)

2) Asakura, N., Kato, T., Takamura, S., et al., "Report of the Meetings of International Tokamak Physics Activity, 8," J. Plasma Fusion Res., **79**, 1194 (2003) (in Japanese).

3) Asakura, N., "Recent Progress of Boundary Plasma Research, 1; Introduction, 3: Recent Progress of Divertor and SOL Plasma Studies in Tokamaks," J. Plasma Fusion Res., **80**, 181/190 (2003) (in Japanese).

4) Hashimoto, N., Tanigawa, H., Ando, M., et al., "Comparison of Microstructure between Neutron-Irradiated Reduced Activation Ferritic/Martensitic Steels, F82H-IEA, JLF-1 and ORNL9CR," DOE/ER-0313/35, 41 (2003).

5) Hashimoto, N., Tanigawa, H., Ando, M., et al., "TEM Observation around Crack in Fatigue-Precravked 1TCT Fracture Toughness Specimen of F82H-IEA," DOE/ER-0313/35, 67 (2003).

6) Kishimoto, Y., Idomura, Y., Li, J., "Prospect for "Multiple-Hierarchical Complex Plasma" where Turbulent and Laminar Flow Fluctuations are Mixed," J. Plasma Fusion Res., **79**, 478 (2003) (in Japanese).

7) Kishimoto, Y., "Multiple Time and Spatial Scale Plasma Simulation; Prospect Based on Current Status," J. Plasma Fusion Res., **79**, 460 (2003) (in Japanese).

8) Kubo, H., Takenaga, H., Nakano, T., et al., "Divertor Spectroscopy with Molecular Transport," Springer Series on Atoms and Plasmas (2003).

9) Kuroda, T., Enoeda, M., Akiba, M., "Test Blanket Program in ITER," The First Atomic Power Industry Group, **164** (2003-7) 17, (2003).

10) Matsumoto, T., "Status and Future Plan of Domestic Fusion Research," Text of the 42nd Summer School for Young Plasma Researchers (2003) (in Japanese).

11) Nakano, T., Kado, S., "Hydrocarbons in Divertor Plasmas; What can be Understood from Spectroscopy," J. Plasma Fusion Res., **80**, 91 (2004) (in Japanese).

12) Ninomiya, H., "Recent Results of JT-60 toward Steady-State Tokamak Reactor," J. Nucl. Sci. Tech., **45**, 243 (2003) (in Japanese).

13) Nishi, M., Yamanishi, T., Hayashi, T., et al., "Accounting and control of Tritium Process Laboratory (TPL) of JAERI-results of 15-year operation and research activity-," J. Plasma Fusion Res., **79**, 1078 (2003) (In Japanese).

14) Nishi, M., Yamanishi, T., Hayashi, T., "Tritium system of fusion reactor-Progress of technologies which made ITER plant design possible, and future perspective," J. Atomic Energy Soc. Japan, **46**, 115 (2004) (In Japanese).

15) Nishio, S., "A Bright Prospect of Low Aspect Ratio Tokamaks toward a Power Reactor," Meeting Materials from The Institute of Electrical Engineers of Japan, 1 (2003).

16) Nishio, S., "Fusion Power Reactor Designs Adopting SiC/SiC Composite as the Structural Material," J. Plasma Fusion Res., **80**, 14 (2004) (in Japanese).

17) Sakamoto, K., "Development of high power gyrotron and its application," Text. 16th Technical school of JSPF, "Production of millimeter and sub-millimeter waves and its application", 1 (2004).

18) Sakamoto, Y., Nakno, T., Oyama, N., "6th Research Meeting of Young Scientists for Plasma Physics," J. Plasma Fusion Res., **79**, 715 (2003) (in Japanese).

19) Sakata, S., Tsugita, T., Matsuda, T., "Real Time Processor in JT-60 Data Processing System," Tech. Meeting report from KEK, P-016 (2003).

20) Sato, M., Matsuda, T., "Control and Data Acquisition of CAMAC for JT-60 Data Processing System," Tech. Meeting report from KEK, P-039 (2003).

21) Sengoku, S., "Evaluatin of Plasma Current Profile on a Low-Aspect-Ratio Tokamak Reactor," Proc. Technical Meeting on Plasma Science and Technology, Inst. Electr. Eng. Jpn., PST-03, 23 (2003) (in Japanese).

22) Shimada, M., "Progress of Boundary Plasma Investigation toward ITER," J. Plasma Fusion Res., **80**, 222 (2004) (in Japanese).

23) Shimizu, K., Takizuka, T., "An Introduction to Boundary Plasma Physics, " J. Plasma Fusion Res., **80**, 183 (2004) (in Japanese).

24) Shirai, H., "Heat Transport Analyses," J. Plasma Fusion Res., **79**, 691 (2003) (in Japanese).

25) Smirnov, R., Tomita, Y., Takizuka, T., et al., "Particle Simulation Study of Dust Particle Dynamics in Sheaths," NIFS-784, 9 (2003).

26) Takahashi, K., Kasugai, A., Minami, R., et al., "Development of advanced antennas and diamond windows for ECH/ECCD in fusion reactor," Proc. JIEE Workshop (2003), NE03-1

27) Takenaga, H., "Particle Transport Analyses," J. Plasma Fusion Res., **79**, 790 (2003) (in Japanese).

28) Takizuka, T., Ogawa, Y., Miura, Y., et al., "Report of ITPA (Internationl Tokamak Physics Activity) Topical Group Meetings, 7," J. Plasma Fusion Res., **79**, 628 (2003) (in Japanese).

29) Takizuka, T., "Report for ITPA (International Tokamak Physics Activity), 9," J. Plasma Fusion Res., **81**, 60 (2004) (in Japanese).

30) Takizuka, T., "Variation of Current Profiles in Tokamaks; Formation Mechanism and Confinement Property of Current-Hole Configuration," J. Plasma Fusion Res., **79**, 1123 (2003) (in Japanese).

31) Tanabe, T., Sugiyama, K., Skinner, C. H., et al., "Review of Tritium Distribution on Plasma Facing Materials of D-D and D-T machines," 7th Int. Workshop on Hydrogen in Condensed Matter (2003).

32) Tanabe, T., Sugiyama, K., Skinner, C. H., et al., "Tritium Retention in Large Tokamak," US Workshop on High Heat Flux Components and Plasma Surface Interactions for Next Fusion Devices & High Power Density Devices and Designs (2003).

33) Tani, K., Tobita, K., Nishio, S., et al., "On the Confinement of Alpha Particles in a Low-Aspect-Ratio Tokamak Reactor," Meeting materials from the Institute of Electrical Engineers of Japan, 13 (2003).

34) Tanigawa, H., Hashimoto, N., Sokolov, M. A., et al., "On the Effects of Fatigue Precracking on the Microstructure around Precrack in 1TCT Fracture Toughness Specimen of F82H-IEA," DOE/ER-0313/35, 58 (2003).

35) Tanigawa, H., Sakasegawa, H., Hashimoto, N., et al., "Analysis of Ta-Rich MX Precipitates in RAFS" DOE/ER-0313/35, 33 (2003).

36) Tanigawa, H., Sakasegawa, H., Payzant, E. A., et al., "X-Ray Diffraction Analysis on Precipitates of 11J-Irradiated RAFS," DOE/ER-0313/35, 37 (2003).

37) Tanigawa, H., Sakasegawa, H., Zinkle, S. J., et al., "Analysis of Extraction Residue of HFIR 11J-Irradiated RAFS," DOE/ER-0313/35, 30 (2003).

38) Thoms, K. R., Heatherly, D. W., (Tanigawa, H.), et al., "Assembly of the US-Japan JP-26 Experiment and Start of Irradiation in the HFIR," DOE/ER-0313/35, 250 (2003).

39) Tobita, K., "Public Acceptance of a Low Aspect Ratio Tokamak Reactor from the Point of View of Waste," Meeting materials from the Institute of Electrical Engineers of Japan, 19 (2003).

Appendix A.2 Personnel and Financial Data

A.2.1 Charge in number of personnel and annual budget (FY1993-2003)

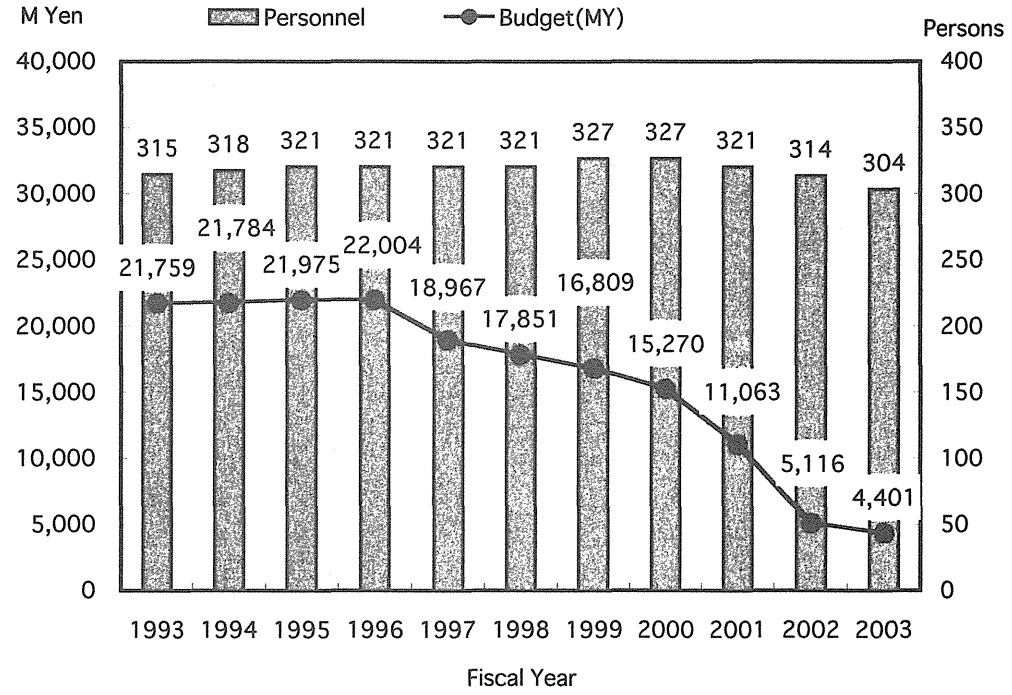

A.2.2 Organization Chart (Mar.31, 2004)

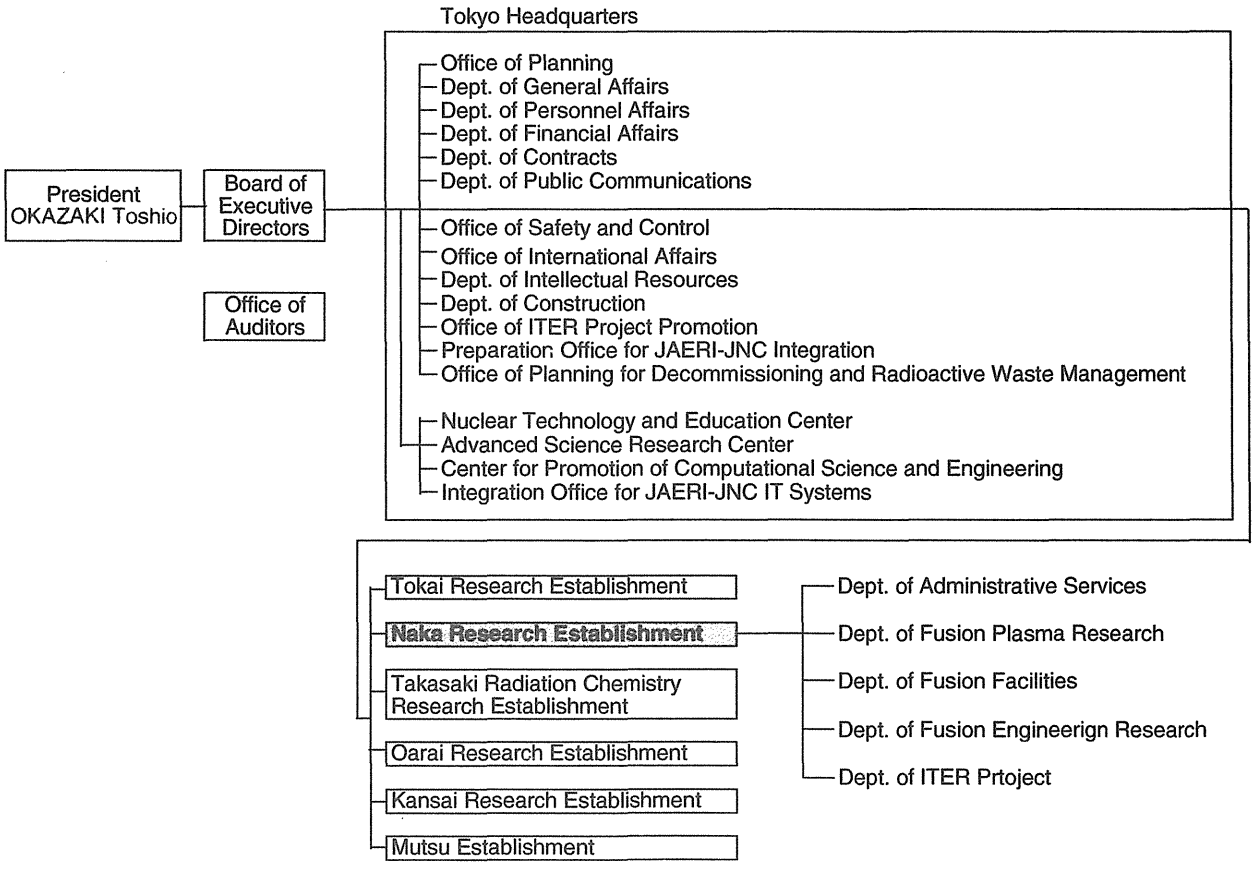

A.2.3 Scientific Staff in the Naka Fusion Research Establishment (April 2003- March 2004)

Naka Fusion Research Establishment

SEKI Masahiro	(Director General)
KIKUCHI Isao	(Vice Director General)
FUJIWARA Masami	(Scientific Consultant)
INOUE Nobuyuki	(Scientific Consultant)
SHIMOMURA Yasuo	(Scientific Consultant)
NISHIKAWA Kyoji	(Invited Researcher)
MATSUI Hideki	(Invited Researcher)
KOHYAMA Akira	(Invited Researcher)
YAMADA Hiroshi	(Invited Researcher)
AZUMI Masafumi	(Prime Scientist)
ARAKI Masanori	(Staff for Director General)
KOIDE Yoshihiko	(Staff for Director General)

Department of Administrative Services

KIKUCHI Isao	(Director)
KOBAYASHI Haruo	(Deputy Director)

Department of Fusion Plasma Research

NINOMIYA Hiromasa	(Director)
KIKUCHI Mitsuru	(Deputy Director)
NAGAMI Masayuki	(Prime Scientist)
WATANABE Tsutomu	(Administrative Manager)

Tokamak Program Division

ISHIDA Shinichi (General Manager)

ANDO Toshinari (*18)	HATAE Takaki	KAWASHIMA Hisato
KURITA Gen-ichi	KAMADA Yutaka	MORI Katsuharu (*10)
MORIOKA Atsuhiko	OGURI Shigeru (*10)	OIKAWA Akira
SAKURAI Shinji	SATO Fujio (*10)	TAKAHASHI Hiroyuki (*5)
TAMAI Hiroshi	TSUCHIYA Katsuhiko	YAMAZAKI Takeshi (*10)

Plasma Analysis Division

OZEKI Takahisi (General Maneger)

CHENG Fayin (*30)	HAMAMATSU Kiyotaka	HAYASHI Nobuhiko
IBA Katsuyuki (*24)	IWASAKI Keita (*24)	KONOVALOV Sergei (*8)
NAITO Osamu	OHSHIMA Takayuki	SAKATA Shinya
SATO Minoru	SUZUKI Masaei (*24)	SUZUKI Mitsuhiro (*1)
TAKEI Nahoko (*31)	TAKIZUKA Tomonori	TSUGITA Tomonori

Large Tokamak Experiment and Diagnostics Division

MIURA Yukitoshi (Head)

ASAKURA Nobuyuki　CHANKIN Alex V. (*8)　CHIBA Shinichi
DING Bojiang (*30)　FUJITA Takaaki　HAMANO Takashi (*20)
HIGASHIJIMA Satoru　IDE Shunsuke　INOUE Akira (*20)
ISHIKAWA Masao (*29)　ISAYAMA Akihiko　KAMIYA Kensaku
KAWANO Yasunori　KITAMURA Shigeru　KOKUSEN Shigeharu (*18)
KONOSHIMA Shigeru　KUBO Hirotaka　MIYAMOTO Atsushi (*18)
NAGAYA Susumu　NAKANO Tomohide　OYAMA Naoyuki
SAKAMOTO Yoshiteru　SAKUMA Takeshi (*20)　SUNAOSHI Hidenori
SUZUKI Takahiro　TAKECHI Manabu　TAKENAGA Hidenobu
TSUBOTA Naoaki (*18)　TSUKAHARA Yoshimitsu　UEHARA Kazuya
URANO Hajime

Plasma Theory Laboratory
KISHIMOTO Yasuaki (Head)
FURUKAWA Masaru (*22)　IDOMURA Yasuhiro　ISHII Yasutomo
KAGEI Yasuhiro (*22)　LI Jiquan (*8)　MATSUMOTO Taro
MIYATO Naoaki (*22)　SUGAHARA Akihiro (*24)　TOKUDA Shinji
TUDA Takashi　YAGI Hiroshi (*24)

Experimental Plasma Physics Laboratory
KUSAMA Yoshinori (Head)
BAKHTIARI Mohammad (*22)　HOSHINO Katsumichi　KASAI Satoshi
OASA Kazumi　OGAWA Hiroaki　SHIINA Tomio
SHINOHARA Koji

Reactor System Laboratory
TOBITA Kenji (Head)
AOKI Isao　HORIKAWA Toyohiko (*5)　KONISHI Satoshi (*14)
KURIHARA Ryoichi　NAKAMURA Yukiharu　NISHIO Satoshi
SATO Masayasu　SONG Yuntao (*6)

Department of Fusion Facilities
NINOMIYA Hiromasa　(Director)
HOSOGANE Nobuyuki　(Deputy Director)

JT-60 Administration Division
WATANABE Tsutomu　(General Manager)

JT-60 Facilities Division I
KURIHARA Kenichi (Head)
AKASAKA Hiromi　FURUKAWA Hiroshi (*20)　HOSOYAMA Hiromi (*9)
KAWAMATA Youichi　MATSUKAWA Makoto　MEGURO Kazumi (*10)
MIURA M Yushi　OHMORI Shunzo　OHMORI Yoshikazu
OKANO Jun　SEIMIYA Munetaka　SHIMADA Katsuhiro
SUEOKA Michiharu　TAKANO Shoji (*1)　TERAKADO Tsunehisa
TOTSUKA Toshiyuki　UEHARA Toshiaki (*20)　YAMASHITA Yoshiki (*10)

YONEKAWA Izuru

JT-60 Facilities Division II

MIYA Naoyuki (Head)

ARAI Takashi	GOTOH Yoshitaka (*5)	HAGA Saburo (*18)
HAYASHI Takao	HIRATSUKA Hajime	HONDA Masao
ICHIGE Hisashi	ISHIMOTO Yuki (*29)	KAMINAGA Atsushi
KIZU Kaname	KODAMA Kozo	KUDO Yusuke
MASAKI Kei	MATSUZAWA Yukihiro (*18)	MIYO Yasuhiko
NISHIMIYA Tomokazu	SASAJIMA Tadayuki	URATA Kazuhiro (*16)
YAGISAWA Hiroshi (*5)	YAGYU Jun-ichi	

RF Facilities Division

FUJII Tsuneyuki (Head)

ANNO Katsuto	HIRANAI Shinichi	HASEGAWA Koichi
IGARASHI Koichi (*18)	ISAKA Masayoshi	ISHII Kazuhiro (*20)
KASHIWA yoshitoshi	KIYONO Kimihiro	MORIYAMA Shinichi
SATO Fumiaki (*18)	SAWAHATA masayuki	SEKI Masami
SHIMONO Mitsugu	SHINOZAKI Shin-ichi	SUZUKI Sadaaki
TAKAHASHI Masami (*27)	TERAKADO Masayuki	YOKOKURA Kenji

NBI Facilities Division

YAMAMOTO Takumi (Head)

OHGA Tokumichi (Deputy General Manager)

AKINO Noboru	EBISAWA Noboru	GRISHAM Larry (*23)
HONDA Atsushi	KAWAI Mikito	KAZAWA Minoru
KIKUCHI Katsumi (*20)	KOMATA Masao	KUSANAGI Naoto (*20)
MOGAKI Kazuhiko	NOTO Katsuya (*18)	OKANO Fuminori
OSHIMA Katsumi (*18)	TANAI Yutaka (*19)	UMEDA Naotaka
USUI Katsutomi	YAMAZAKI Haruyuki (*5)	

JFT-2M Facilities Division

YAMAMOTO Masahiro (Head)

SHIBATA Takatoshi (Deputy General Manager)

KIKUCHI Kazuo	TANI Takashi	SEKI Nobuo (*20)

Department of Fusion Engineering Research

SEKI Shogo (Director)

TAKATSU Hideyuki (Deputy Director)

KATOGI Takeshi (Administrative Manager)

SHIHO Makoto

TSUJI Hiroshi

Blanket Engineering Laboratory

AKIBA Masato (Head)

ABE Tetsuya	ENOEDA Mikio	EZATO Koichro

HATANO Toshihisa　HIROSE Takanori (*22)　HOMMA Takashi
KURODA Toshimasa (*13)　SATO Kazuyoshi　SUZUKI Satoshi
TANZAWA Sadamitsu　TANGAWA Hisashi (*22)　YOKOYAMA Kenji

Superconducting Magnet Laboratory
OKUNO Kiyoshi (Head)
ABE Kanako (*7)　HAMADA Kazuya　ISONO Takaaki
KAWANO Katsumi　KOIZUMI Norikiyo　KUBO Hiroatsu (*3)
NABARA Yoshihiro　NAKAJIMA Hideo　NUNOYA Yoshihiko
OSHIKIRI Masayuki (*20)　SUGIMOTO Makoto　TAKANO Katsutoshi (*20)

Plasma Heating Laboratory
IMAI Tsuyoshi (Head)
DAIRAKU Masayuki　HANADA Masaya　IKEDA Yukiharu
INOUE Takashi　KASHIWAGI Mieko　KASUGAI Atsushi
KOBAYASHI Noriyuki (*28)　MAEBARA Sunao　MORISHITA Takatoshi (*22)
MINAMI Ryutaroh (*22)　OHUCHI Hitoshi (*20)　SAKAMOTO Keishi
SAWAHATA Osamu (*20)　SEKI Takayoshi (*5)　TAKAHASHI Koji
TANIGUCHI Masaki　WATANABE Kazuhiro　YAMANA Takashi(*2)

Tritium Engineering Laboratory
NISHI Masataka (Head)
HAYASHI Takumi　IGARI Takahiro (*20)　ISOBE Kanetsugu
IWAI Yasunori　KAWAMURA Yoshinori　KOBAYASHI Kazuhiro
LUO Guang-Nan (*8)　NAKAMURA Hirofumi　SHU Wataru
SUZUKI Takumi　TERADA Osamu (*13)　UZAWA Masayuki (*16)
YAMADA Masayuki　YAMANISHI Toshihiko

Office of Fusion Materials Research Promotion
SUGIMOTO Masayoshi (Head)
ANDO Masami　FURUYA Kazuyuki　IDA Mizuho (*7)
MATSUKAWA Shingo (*34)　MATSUHIRO Kenjiro (*22)　NAKAMURA Hiroo
NAKAMURA Kazuyuki　TAKEDA Masao (*35)　TANIGAWA Hiroyasu
YUTANI Toshiaki (*28)

Fusion Neutron Laboratory
NISHITANI Takeo (Head)
ABE Yuichi　KLIX Axel (*21)　KUTSUKAKE Chuzo
NAKAO Makoto (*13)　OCHIAI Kentaro　OGINUMA Yoshikazu (*20)
SATO Satosi　SEKI Masakazu　TANAKA Shigeru
YAMAUCHI Michinori (*28)　VERZILOV Yury (*8)

Department of ITER Project
TUNEMATSU Toshihide　(Director)
YOSHINO Ryuji　(Deputy Director)
KOIZUMI Koichi

ODAJIMA Kazuo

Administration Group
MATSUMOTO Hiroyuki (Administrative Manager)
TANAKA Fumiyo
YOSHINARI Shuji

Project Management Division
MORI Masahiro (General Manager)

ITAMI Kiyoshi	KONDO Takashi	SENGOKU Seio
SHIMIZU Katsuhiro	SUGIE Tatsuo	YOSHIDA Hidetoshi

International Coordination Division
ANDO Toshiro (Head)

HONDA Tsutomu (*28)	IIDA Hiromasa	IOKI Kimihiro (*16)
KATAOKA Yoshiyuki (*5)	MARUYAMA So	MIZOGUCHI Tadanori (*5)
MORIMOTO Masaaki (*16)	OIKAWA Toshihiro	OKADA Hidetoshi (*5)
SAKASAI Akira	SATO Kouichi (*1)	SHIMADA Michiya
SUGIHARA Masayoshi	TAKAHASHI Yoshikazu	YAMAGUCHI Kazuhiko (*26)
YOSHIDA Kiyoshi		

Plant System Division
SHOJI Teruaki (Head)

IWANAGA Kazuyuki (*32)	KASHIMURA Shinji (*12)	KATAOKA Takahiro (*15)
MATSUMOTO Kiyoshi	NAKAKURA Kensuke (*11)	OHMORI Junji (*28)
YAGENJI Akira (*4)	YAMAMOTO Shin	

Safety Design Division
TADA Eisuke (Head)

HADA Kazuhiko	HASHIMOTO Masayoshi (*7)	HIGUCHI Masahisa (*33)
MARUO Takeshi	NEYATANI Yuzuru	OHIRA Shigeru
SEO Yorimasa (*7)	TADO Shigeru (*15)	TSURU Daigo

Tokamak Device Division
SHIBANUMA Kiyoshi (Head)

KAKUDATE Satoshi	KITAMURA Kazunori (*28)	MOHRI Kensuke (*13)
NAKAHIRA Masataka	OBARA Kenjiro	

Collaborating Laboratories

Oarai Research Establishment
Department of JMTR
Blanket Irradiation and Analysis Laboratory
HAYASHI Kimio (Head)

ISHITSUKA Etsuo	KIKUKAWA Akihiro (*25)	NAKAMICHI Masaru
TSUCHIYA Kunihiko	UCHIDA Munenori (*17)	YAMADA Hirokazu (*13)

Tokai Research Establishment
Department of Material Science
Research Group for Radiation Effects and Analysis
JITSUKAWA Shiro (Group Leader)
FUJII Kimio, NAITO Akira, NAKAZAWA Tetsutya
SAWAI Tomotsugu, SHIBA Kiyoyuki, TANIFUJI Takaaki
YAMADA Reiji, YAMAKI Daiju, WAKAI Eiichi

Department of Nuclear Energy System
Research Group for Reactor Structural Materials
MIWA Yukio

Neutron Science Research Center
Research Group for Neutron Scattering from Functional Materials
IGAWA Naoki

Research Group for Nanostructure
TAGUCHI Tomitsugu

*1 Atomic Energy General Service Corporation
*2 Doshisha University
*3 Fuji Electric Co., Ltd.
*4 Hazama Corporation.
*5 Hitachi, Ltd.

*6 Institute of Plasma Physics, Academia Science (China)
*7 Ishikawajima-Harima Heavy Industries Co., Ltd.
*8 JAERI Fellowship
*9 Japan EXpert Clone Corp. (JEX)
*10 JP HYTEC Co., Ltd.

*11 Kajima Corporation
*12 Kandenko Co., Ltd.
*13 Kawasaki Heavy Industries, Ltd.
*14 Kyoto University
*15 Mitsubishi Electric Corporation

*16 Mitsubishi Heavy Industries, Ltd.
*17 NGK Insulators, Ltd.
*18 Nippon Advanced Technology Co., Ltd.
*19 Nissin Electric Co., Ltd.
*20 Nuclear Engineering Co., Ltd.

*21 Osaka University
*22 Post-Doctoral Fellow
*23 Princeton Plasma Physics Laboratory (USA)
*24 Research Organization for Information Science & Technology
*25 Sangyo Kagaku Co., Ltd.

*26 Shimizu Corporation
*27 Sumitomo Heavy Industries, Ltd.
*28 Toshiba Corporation
*29 Tsukuba University
*30 MEXT Nuclear Research Exchange Program

*31 Tokyo Institute of Technology
*32 Kounoike Construnction Co., Ltd.
*33 Japan Atomic Power Company Co., Ltd.
*34 Kokan-Keisoku Corporation
*35 Kumagai Gumi Co., Ltd.

国際単位系 (SI) と換算表

表 1　SI基本単位および補助単位

量	名称	記号
長さ	メートル	m
質量	キログラム	kg
時間	秒	s
電流	アンペア	A
熱力学温度	ケルビン	K
物質量	モル	mol
光度	カンデラ	cd
平面角	ラジアン	rad
立体角	ステラジアン	sr

表 2　SIと併用される単位

名称	記号
分，時，日	min，h，d
度，分，秒	°，′，″
リットル	l，L
トン	t
電子ボルト	eV
原子質量単位	u

1 eV = 1.60218 × 10^{-19} J

1 u = 1.66054 × 10^{-27} kg

表 5　SI接頭語

倍数	接頭語	記号
10^{18}	エクサ	E
10^{15}	ペタ	P
10^{12}	テラ	T
10^{9}	ギガ	G
10^{6}	メガ	M
10^{3}	キロ	k
10^{2}	ヘクト	h
10^{1}	デカ	da
10^{-1}	デシ	d
10^{-2}	センチ	c
10^{-3}	ミリ	m
10^{-6}	マイクロ	μ
10^{-9}	ナノ	n
10^{-12}	ピコ	p
10^{-15}	フェムト	f
10^{-18}	アト	a

表 3　固有の名称をもつSI組立単位

量	名称	記号	他のSI単位による表現
周波数	ヘルツ	Hz	s^{-1}
力	ニュートン	N	$m \cdot kg/s^2$
圧力，応力	パスカル	Pa	N/m^2
エネルギー，仕事，熱量	ジュール	J	N·m
工率，放射束	ワット	W	J/s
電気量，電荷	クーロン	C	A·s
電位，電圧，起電力	ボルト	V	W/A
静電容量	ファラド	F	C/V
電気抵抗	オーム	Ω	V/A
コンダクタンス	ジーメンス	S	A/V
磁束	ウェーバ	Wb	V·s
磁束密度	テスラ	T	Wb/m^2
インダクタンス	ヘンリー	H	Wb/A
セルシウス温度	セルシウス度	℃	
光束	ルーメン	lm	cd·sr
照度	ルクス	lx	lm/m^2
放射能	ベクレル	Bq	s^{-1}
吸収線量	グレイ	Gy	J/kg
線量当量	シーベルト	Sv	J/kg

表 4　SIと共に暫定的に維持される単位

名称	記号
オングストローム	Å
バーン	b
バール	bar
ガル	Gal
キュリー	Ci
レントゲン	R
ラド	rad
レム	rem

1 Å = 0.1 nm = 10^{-10} m

1 b = 100 fm^2 = 10^{-28} m^2

1 bar = 0.1 MPa = 10^5 Pa

1 Gal = 1 cm/s^2 = 10^{-2} m/s^2

1 Ci = 3.7 × 10^{10} Bq

1 R = 2.58 × 10^{-4} C/kg

1 rad = 1 cGy = 10^{-2} Gy

1 rem = 1 cSv = 10^{-2} Sv

（注）

1. 表1－5は「国際単位系」第5版，国際度量衡局 1985年刊行による。ただし，1 eVおよび1 uの値はCODATAの1986年推奨値によった。
2. 表4には海里，ノット，アール，ヘクタールも含まれているが日常の単位なのでここでは省略した。
3. barは，JISでは流体の圧力を表わす場合に限り表2のカテゴリーに分類されている。
4. EC閣僚理事会指令ではbar，barnおよび「血圧の単位」mmHgを表2のカテゴリーに入れている。

換　算　表

力	N(=10^5 dyn)	kgf	lbf
	1	0.101972	0.224809
	9.80665	1	2.20462
	4.44822	0.453592	1

粘度　1 Pa·s(N·s/m^2) = 10 P(ポアズ)(g/(cm·s))

動粘度　1 m^2/s = 10^4 St(ストークス)(cm^2/s)

圧力	MPa(=10 bar)	kgf/cm^2	atm	mmHg(Torr)	lbf/in^2(psi)
	1	10.1972	9.86923	7.50062 × 10^3	145.038
	0.0980665	1	0.967841	735.559	14.2233
	0.101325	1.03323	1	760	14.6959
	1.33322 × 10^{-4}	1.35951 × 10^{-3}	1.31579 × 10^{-3}	1	1.93368 × 10^{-2}
	6.89476 × 10^{-3}	7.03070 × 10^{-2}	6.80460 × 10^{-2}	51.7149	1

エネルギー・仕事・熱量	J(=10^7 erg)	kgf·m	kW·h	cal(計量法)	Btu	ft·lbf	eV
	1	0.101972	2.77778 × 10^{-7}	0.238889	9.47813 × 10^{-4}	0.737562	6.24150 × 10^{18}
	9.80665	1	2.72407 × 10^{-6}	2.34270	9.29487 × 10^{-3}	7.23301	6.12082 × 10^{19}
	3.6 × 10^6	3.67098 × 10^5	1	8.59999 × 10^5	3412.13	2.65522 × 10^6	2.24694 × 10^{25}
	4.18605	0.426858	1.16279 × 10^{-6}	1	3.96759 × 10^{-3}	3.08747	2.61272 × 10^{19}
	1055.06	107.586	2.93072 × 10^{-4}	252.042	1	778.172	6.58515 × 10^{21}
	1.35582	0.138255	3.76616 × 10^{-7}	0.323890	1.28506 × 10^{-3}	1	8.46233 × 10^{18}
	1.60218 × 10^{-19}	1.63377 × 10^{-20}	4.45050 × 10^{-26}	3.82743 × 10^{-20}	1.51857 × 10^{-22}	1.18171 × 10^{-19}	1

1 cal = 4.18605 J (計量法)

= 4.184 J (熱化学)

= 4.1855 J (15 °C)

= 4.1868 J (国際蒸気表)

仕事率　1 PS (仏馬力)

= 75 kgf·m/s

= 735.499 W

放射能	Bq	Ci
	1	2.70270 × 10^{-11}
	3.7 × 10^{10}	1

吸収線量	Gy	rad
	1	100
	0.01	1

照射線量	C/kg	R
	1	3876
	2.58 × 10^{-4}	1

線量当量	Sv	rem
	1	100
	0.01	1

（86年12月26日現在）

Annual Report of Naka Fusion Research Establishment from April 1, 2003 to March 31, 2004